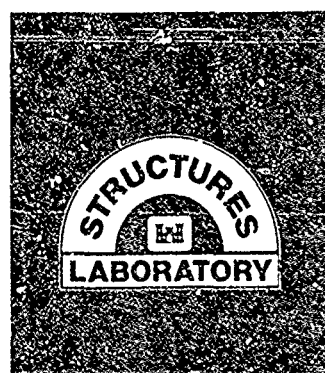
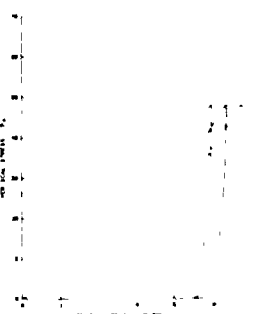
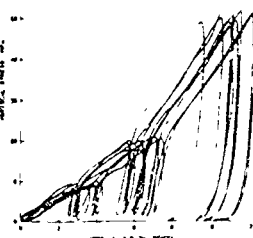
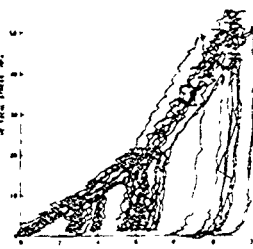




US Army Corps
of Engineers

AD-A195 698



DTIC FILE COPY (2)

TECHNICAL REPORT SL-88-25

A TECHNIQUE FOR DEVELOPING PROBABILISTIC PROPERTIES OF EARTH MATERIALS

by

James D. Cargile

Structures Laboratory

DEPARTMENT OF THE ARMY
Waterways Experiment Station, Corps of Engineers
PO Box 631, Vicksburg, Mississippi 39180-0631



April 1988

Final Report

Approved For Public Release, Distribution Unlimited

DTIC
ELECTE
JUN 03 1988
S H D

Prepared for Defense Nuclear Agency
Washington, DC 20305-1000

Under Task Code RSRB, Work Unit 00058 (Task 4)

88

Destroy this report when no longer needed. Do not return
it to the originator.

The findings in this report are not to be construed as an official
Department of the Army position unless so designated
by other authorized documents

The contents of this report are not to be used for
advertising, publication, or promotional purposes
Citation of trade names does not constitute an
official endorsement or approval of the use of
such commercial products.

Unclassified
SECURITY CLASSIFICATION OF THIS PAGE

REPORT DOCUMENTATION PAGE

1a. REPORT SECURITY CLASSIFICATION Unclassified		1b. RESTRICTIVE MARKINGS													
2a. SECURITY CLASSIFICATION AUTHORITY		3. DISTRIBUTION/AVAILABILITY OF REPORT Approved for public release; distribution unlimited.													
2b. DECLASSIFICATION/DOWNGRADING SCHEDULE															
4. PERFORMING ORGANIZATION REPORT NUMBER(S) Technical Report SL-88-25		5. MONITORING ORGANIZATION REPORT NUMBER(S)													
6a. NAME OF PERFORMING ORGANIZATION USAEWES Structures Laboratory	6b. OFFICE SYMBOL (If applicable) WESSD	7a. NAME OF MONITORING ORGANIZATION													
6c. ADDRESS (City, State, and ZIP Code) PO Box 631 Vicksburg, MS 39180-0631		7b. ADDRESS (City, State, and ZIP Code)													
8a. NAME OF FUNDING/SPONSORING ORGANIZATION Defense Nuclear Agency	8b. OFFICE SYMBOL (If applicable)	9. PROCUREMENT INSTRUMENT IDENTIFICATION NUMBER													
8c. ADDRESS (City, State, and ZIP Code) Washington, DC 20305-1000		10. SOURCE OF FUNDING NUMBERS <table border="1"><tr><td>PROGRAM ELEMENT NO</td><td>PROJECT NO</td><td>TASK NO. Code RSRB (Task 4)</td><td>WORK UNIT ACCESSION NO. 00058</td></tr></table>		PROGRAM ELEMENT NO	PROJECT NO	TASK NO. Code RSRB (Task 4)	WORK UNIT ACCESSION NO. 00058								
PROGRAM ELEMENT NO	PROJECT NO	TASK NO. Code RSRB (Task 4)	WORK UNIT ACCESSION NO. 00058												
11. TITLE (Include Security Classification) A Technique for Developing Probabilistic Properties of Earth Materials															
12. PERSONAL AUTHOR(S) Cargile, James D.															
13a. TYPE OF REPORT Final report	13b. TIME COVERED FROM TO	14. DATE OF REPORT (Year, Month, Day) April 1988	15. PAGE COUNT 257												
16. SUPPLEMENTARY NOTATION Available from National Technical Information Service, 5285 Port Royal Road, Springfield, VA 22161.															
17. COSATI CODES <table border="1"><tr><td>FIELD</td><td>GROUP</td><td>SUB-GROUP</td></tr><tr><td></td><td></td><td></td></tr><tr><td></td><td></td><td></td></tr><tr><td></td><td></td><td></td></tr></table>		FIELD	GROUP	SUB-GROUP										18. SUBJECT TERMS (Continue on reverse if necessary and identify by block number) See reverse.	
FIELD	GROUP	SUB-GROUP													
19. ABSTRACT (Continue on reverse if necessary and identify by block number) Ground shock calculation techniques currently used by analysts of explosive test events require deterministic input. In actuality, ground shock calculations should be treated probabilistically since the properties of earth materials and the characteristics of explosive blasts are dispersed random variables. A three-phase project is underway at the US Army Engineer Waterways Experiment Station to (a) develop a procedure for providing probabilistic properties of earth materials, (b) develop a probabilistic cap-type elastic-plastic constitutive model, and (c) develop a probabilistic ground shock calculation computer code. This report documents phase (a). Probabilistic properties of earth materials are developed for each layer of the sub-surface profile at a given site. One-way analysis of variance tests conducted on mass, volume, index, and seismic velocity data determine the profile. Probabilistic mechanical properties are based on covariance analysis of laboratory test results, field experiments, (Continued)															
20. DISTRIBUTION/AVAILABILITY OF ABSTRACT <input checked="" type="checkbox"/> UNCLASSIFIED/UNLIMITED <input type="checkbox"/> SAME AS RPT <input type="checkbox"/> DTIC USERS		21. ABSTRACT SECURITY CLASSIFICATION Unclassified													
22a. NAME OF RESPONSIBLE INDIVIDUAL		22b. TELEPHONE (Include Area Code)	22c. OFFICE SYMBOL												

18. SUBJECT TERMS (Continued).

Clayey sand	Rosenblueth's point
Compressibility	estimate procedures
Covariance analysis	Shear strength
Ground shock	Statistical analysis
Probabilistic properties	

19. ABSTRACT (Continued).

and engineering knowledge. A procedure for extrapolating the variance of laboratory-based recommended probabilistic mechanical properties to higher stresses is presented.

The analysis technique was applied to data obtained for two adjacent areas located near Yuma, Arizona. One-way analysis of variance of mass-volume data was very useful for developing the subsurface profile. Similar probabilistic responses were obtained by (a) applying covariance analysis to mechanical property test data plotted in forms conducive to constitutive modeling, and (b) applying the Rosenblueth procedure to results from covariance analysis of plots of "measured data." The uniqueness of a soil specimen's response during a mechanical property test was maintained by plotting stresses and strains instead of loads and deflections. The effect of correlation coefficients in the Rosenblueth procedure was evaluated. Coefficients of variation for laboratory-based recommended mechanical properties were used to extrapolate variance to higher stresses since they maximized the variance about the extrapolated mean. The recommended probabilistic properties should be used in all possible combinations since the variance was not coupled.

PREFACE

The work reported herein was funded by the Defense Nuclear Agency under Task Code RSRB, Work Unit 00058 (Task 4), "Probabilistic Constitutive Model."

This report was prepared by Mr. James D. Cargile of the Geomechanics Division (GD), Structures Laboratory (SL), US Army Engineer Waterways Experiment Station (WES). It is essentially a thesis submitted to Mississippi State University in partial fulfillment of the requirements for the degree of Master of Science in the Department of Civil Engineering. Responsibility for coordinating this program was assigned to Mr. A. E. Jackson, Jr., GD, under the supervision of Dr. J. G. Jackson, Jr., Chief, GD. Personnel of GD assisted in the preparation of this report.

COL Dwayne G. Lee, CE, was the Commander and Director of WES during the period the work reported herein was conducted. Dr. Robert W. Whalin was the Technical Director, and Mr. Bryant Mather was Chief, SL.



Accession For	
NTIS GRA&I	<input checked="checked" type="checkbox"/>
DTIC TAB	<input type="checkbox"/>
Unannounced	<input type="checkbox"/>
Justification	
By _____	
Distribution/ _____	
Availability Codes	
Dist	Avail and/or Special
A-1	

CONTENTS

	<u>Page</u>
PREFACE	i
LIST OF FIGURES	iv
LIST OF TABLES	xv
NOTATION	xvi
CONVERSION FACTORS, NON-SI TO SI (METRIC) UNITS OF MEASUREMENT ...	xviii
CHAPTER 1 INTRODUCTION	1
1.1 BACKGROUND	1
1.2 LITERATURE REVIEW	2
1.3 PURPOSE	5
1.4 SCOPE	5
CHAPTER 2 DESCRIPTION OF THE ANALYSIS TECHNIQUE	6
2.1 DETERMINATION OF THE SUBSURFACE PROFILE	6
2.2 ANALYSIS OF MECHANICAL PROPERTY TEST DATA	7
2.2.1 Data Smoothing	7
2.2.2 Covariance Analysis of Smoothed Data	8
2.2.3 Rosenblueth's Point Estimate Procedure	10
CHAPTER 3 APPLICATION OF THE ANALYSIS TECHNIQUE	13
3.1 MASS-VOLUME AND INDEX DATA	13
3.2 MECHANICAL PROPERTY DATA	15
3.2.1 Grouping of the Mechanical Property Data	15
3.2.2 Smoothing of the Data	16
3.2.3 Covariance Analysis	17
3.2.3.1 UX test results	17
3.2.3.2 Ko test results	20
3.2.3.3 HC test results	23
3.2.3.4 TXC test results	24
3.2.4 Rosenblueth Procedure	26
3.2.4.1 Equations for the function $y(x)$	26
3.2.4.2 Correlation coefficients	28
3.2.4.3 Results	30
3.2.5 Comparison of the Results from the Two Analysis Techniques	32
CHAPTER 4 FINAL PROBABILISTIC MECHANICAL PROPERTIES	184
4.1 APPLICABILITY OF THE PROBABILISTIC MECHANICAL PROPERTIES TO AREA A	184
4.2 PROBABILISTIC MECHANICAL PROPERTIES DEVELOPED FROM TEST RESULTS	184
4.3 METHODS FOR EXTRAPOLATING THE VARIANCE OF MECHANICAL PROPERTIES TO HIGHER STRESSES	187
4.4 FINAL PROBABILISTIC MATERIAL PROPERTIES	189

CONTENTS (Concluded)

	<u>Page</u>
CHAPTER 5 SUMMARY, CONCLUSIONS, AND RECOMMENDATIONS	226
5.1 SUMMARY	226
5.2 CONCLUSIONS	228
5.3 RECOMMENDATIONS	229
REFERENCES	231

LIST OF FIGURES

<u>Figure</u>		<u>Page</u>
2.1	General curves relating the random variables y and x ..	12
3.1	Summary of dry density data from Area A	43
3.2	Summary of dry density data from Area B	44
3.3	Rosenblueth procedure for calculating probabilistic values for γ , S , and V_a from probabilistic values for γ_d , ω , and G_s	45
3.4	Effect of applying the smoothing technique to noisy laboratory test responses	46
3.5	Loading dynamic UX test data	47
3.6	Results from applying COV analysis to loading dynamic UX test data	48
3.7	Composite and constructed continuous plots of the results from COV analysis of loading dynamic UX test data	49
3.8	Results from the COV analysis of unloading dynamic UX strain test data	50
3.9	Load-unload responses constructed from the results of the COV analysis of dynamic UX test data	51
3.10	Loading K_0 test data plotted in forms that are conducive to constitutive modeling	52
3.11	"Measured data" plots of the loading portion of K_0 test data	53
3.12	Results from the COV analysis of the loading portion of EXT K_0 test data plotted in forms that are conducive to constitutive modeling	54
3.13	Results from the COV analysis of "measured data" plots of the loading portion of the results from EXT K_0 tests	55
3.14	Results from the COV analysis of the loading portion of axial stress versus axial strain K_0 test data	56
3.15	Results from the COV analysis of the loading portion of PSD versus MNS K_0 test data	57
3.16	Results from the COV analysis of the loading portion of L/A_0 versus axial strain K_0 test data	58
3.17	Results from the COV analysis of the loading portion of L/A_0 versus radial stress K_0 test data	59
3.18	Composite and constructed continuous results from the COV analysis of the loading portion of K_0 test data plotted in forms that are conducive to constitutive modeling	60
3.19	Composite and constructed continuous results from the COV analysis of the loading portion of "measured" K_0 test data	61

<u>Figure</u>		<u>Page</u>
3.20	Results from the COV analysis of the unloading and reloading portions of axial stress versus axial strain K_0 test data	62
3.21	Results from the COV analysis of the unloading and reloading portions of PSD versus MNS K_0 test data	63
3.22	Results from the COV analysis of the unloading and reloading portions of L/Ao versus axial strain K_0 test data	64
3.23	Results from the COV analysis of the unloading and reloading portions of L/Ao versus radial stress K_0 test data	65
3.24	Results from the COV analysis of the unloading and reloading portions of axial stress versus axial strain EXT K_0 test data	66
3.25	Results from the COV analysis of the unloading and reloading portions of the PSD versus MNS EXT K_0 test data	67
3.26	Results from the COV analysis of the unloading and reloading portions of (UC-LC)*Ap/Ao versus axial strain EXT K_0 test data	68
3.27	Results from the COV analysis of the unloading and reloading portions of (UC-LC)*Ap/Ao versus LC EXT K_0 test data ..	69
3.28	Load-unload responses constructed from the results of the COV analysis of K_0 test data plotted in forms that are conducive to constitutive modeling	70
3.29	Load-unload-reload responses constructed from the results of the COV analysis of K_0 test data plotted in forms that are conducive to constitutive modeling	71
3.30	Load-unload-reload responses constructed from the results of the COV analysis of EXT K_0 test data plotted in forms that are conducive to constitutive modeling	72
3.31	Effect of incrementing the MNS-axis as opposed to the PSD-axis in the COV analysis of K_0 test data	73
3.32	Loading static HC test data plotted in a form that is conducive to constitutive modeling	74
3.33	"Measured data" plots of the loading portion of static HC test data	75
3.34	Loading dynamic HC test data plotted in a form that is conducive to constitutive modeling	76
3.35	"Measured data" plots of the loading portion of dynamic HC test data	77
3.36	Results from the COV analysis of the loading portion of static HC test data plotted in a form that is conducive to constitutive modeling	78
3.37	Results from the COV analysis of the loading portion of confining pressure versus axial strain static HC test data	79

<u>Figure</u>		<u>Page</u>
3.38	Results from the COV analysis of the loading portion of confining pressure versus radial strain static HC test data	80
3.39	Results from the COV analysis of the loading portion of dynamic HC test data plotted in a form that is conducive to constitutive modeling	81
3.40	Results from the COV analysis of the loading portion of confining pressure versus axial strain dynamic HC test data	82
3.41	Results from the COV analysis of the loading portion of confining pressure versus radial strain dynamic HC test data	83
3.42	Composite and constructed continuous results from the COV analysis of the loading portion of static HC test data plotted in a form that is conducive to constitutive modeling	84
3.43	Composite and constructed continuous results from the COV analysis of "measured" static HC test data	85
3.44	Results from the COV analysis of the unloading and reloading portions of static HC test data plotted in a form that is conducive to constitutive modeling	86
3.45	Results from the COV analysis of the unloading and reloading portions of confining pressure versus axial strain static HC test data	87
3.46	Results from the COV analysis of the unloading and reloading portions of confining pressure versus radial strain static HC test data	88
3.47	Results from the COV analysis of the unloading portion of dynamic HC test data plotted in a form that is conducive to constitutive modeling	89
3.48	Results from the COV analysis of the unloading portions of "measured" dynamic HC test data	90
3.49	Load-unload-reload responses constructed from the results of the COV analysis of static HC test data plotted in a form that is conducive to constitutive modeling	91
3.50	Load-unload responses constructed from the results of the COV analysis of dynamic HC test data plotted in a form that is conducive to constitutive modeling	92
3.51	Effect of incrementing the PSD-axis as opposed to the strain-axis in the COV analysis of TXC test data plotted in forms that are conducive to constitutive modeling	93
3.52	Results from the COV analysis of the loading portion of TXC test data plotted in forms that are conducive to constitutive modeling for $\sigma_c = 0$ and 0.1 MPa	94

<u>Figure</u>		<u>Page</u>
3.53	Results from the COV analysis of the loading portion of TXC test data plotted in forms that are conducive to constitutive modeling for $\sigma_c = 0.21$ and 0.35 MPa	95
3.54	Results from the COV analysis of the loading portion of TXC test data plotted in forms that are conducive to constitutive modeling for $\sigma_c = 0.7, 1.7,$ and 3.5 MPa	96
3.55	Results from the COV analysis of the loading portion of TXC test data plotted in forms that are conducive to constitutive modeling for $\sigma_c = 17.5$ MPa	97
3.56	Results from the COV analysis of the loading portion of TXC test data plotted in forms that are conducive to constitutive modeling for $\sigma_c = 20.0$ MPa	98
3.57	Results from the COV analysis of the loading portion of TXC test data plotted in forms that are conducive to constitutive modeling for $\sigma_c = 40.0$ MPa	99
3.58	Results from the COV analysis of the loading portion of TXC test data plotted in forms that are conducive to constitutive modeling for $\sigma_c = 55.0$ MPa	100
3.59	Results from the COV analysis of the loading portion of TXC test data plotted in forms that are conducive to constitutive modeling for $\sigma_c = 60.0$ MPa	101
3.60	Results from the COV analysis of the loading portion of TXC test data plotted in forms that are conducive to constitutive modeling for $\sigma_c = 80.0$ MPa	102
3.61	Results from the COV analysis of "measured data" plots of the loading portion of TXC test data for $\sigma_c = 0$ and 0.1 MPa	103
3.62	Results from the COV analysis of "measured data" plots of the loading portion of TXC test data for $\sigma_c = 0.21$ and 0.35 MPa	104
3.63	Results from the COV analysis of "measured data" plots of the loading portion of TXC test data for $\sigma_c = 0.7, 1.7,$ and 3.5 MPa	105
3.64	Results from the COV analysis of "measured data" plots of the loading portion of TXC test data for $\sigma_c = 17.5$ MPa ...	106
3.65	Results from the COV analysis of "measured data" plots of the loading portion of TXC test data for $\sigma_c = 20.0$ MPa ...	107
3.66	Results from the COV analysis of "measured data" plots of the loading portion of TXC test data for $\sigma_c = 40.0$ MPa ...	108
3.67	Results from the COV analysis of "measured data" plots of the loading portion of TXC test data for $\sigma_c = 55.0$ MPa ...	109
3.68	Results from the COV analysis of "measured data" plots of the loading portion of TXC test data for $\sigma_c = 60.0$ MPa ...	110

<u>Figure</u>		<u>Page</u>
3.69	Results from the COV analysis of "measured data" plots of the loading portion of TXC test data for $\sigma_c = 80.0$ MPa ...	111
3.70	Results from the COV analysis of the unloading and reloading portions of TXC test data plotted in forms that are conducive to constitutive modeling for $\sigma_c = 0$ and 0.1 MPa	112
3.71	Results from the COV analysis of the unloading and reloading portions of TXC test data plotted in forms that are conducive to constitutive modeling for $\sigma_c = 0.21$ and 0.35 MPa	113
3.72	Results from the COV analysis of the unloading and reloading portions of TXC test data plotted in forms that are conducive to constitutive modeling for $\sigma_c = 0.7, 1.7,$ and 3.5 MPa	114
3.73	Results from the COV analysis of the unloading and reloading portions of TXC test data plotted in forms that are conducive to constitutive modeling for $\sigma_c = 17.5$ MPa	115
3.74	Results from the COV analysis of the unloading and reloading portions of TXC test data plotted in forms that are conducive to constitutive modeling for $\sigma_c = 20.0$ MPa	116
3.75	Results from the COV analysis of the unloading and reloading portions of TXC test data plotted in forms that are conducive to constitutive modeling for $\sigma_c = 55.0$ MPa	117
3.76	Results from the COV analysis of the unloading portion of TXC test data plotted in forms that are conducive to constitutive modeling for $\sigma_c = 60.0$ MPa	118
3.77	Results from the COV analysis of the unloading and reloading portions of TXC test data plotted in forms that are conducive to constitutive modeling for $\sigma_c = 80.0$ MPa	119
3.78	Results from the COV analysis of the unloading and reloading portions of "measured" TXC test data for $\sigma_c = 0$ and 0.1 MPa	120
3.79	Results from the COV analysis of the unloading and reloading portions of "measured" TXC test data for $\sigma_c = 0.21$ and 0.35 MPa	121
3.80	Results from the COV analysis of the unloading and reloading portions of "measured" TXC test data for $\sigma_c = 0.7, 1.7,$ and 3.5 MPa	122
3.81	Results from the COV analysis of the unloading and reloading portions of "measured" TXC test data for $\sigma_c = 17.5$ MPa	123
3.82	Results from the COV analysis of the unloading and reloading portions of "measured" TXC test data for $\sigma_c = 20.0$ MPa	124

<u>Figure</u>		<u>Page</u>
3.83	Results from the COV analysis of the unloading and reloading portions of "measured" TXC test data for $\sigma_c = 55.0$ MPa	125
3.84	Results from the COV analysis of the unloading portion of "measured" TXC test data for $\sigma_c = 60.0$ MPa	126
3.85	Results from the COV analysis of the unloading and reloading portions of "measured" TXC test data for $\sigma_c = 80.0$ MPa	127
3.86	Load-unload-reload responses constructed from the results of COV analysis of TXC test data plotted in forms that are conducive to constitutive modeling for $\sigma_c = 0$ and 0.1 MPa	128
3.87	Load-unload-reload responses constructed from the results of COV analysis of TXC test data plotted in forms that are conducive to constitutive modeling for $\sigma_c = 0.21$ and 0.35 MPa	129
3.88	Load-unload-reload responses constructed from the results of COV analysis of TXC test data plotted in forms that are conducive to constitutive modeling for $\sigma_c = 0.7, 1.7,$ and 3.5 MPa	130
3.89	Load-unload-reload responses constructed from the results of COV analysis of TXC test data plotted in forms that are conducive to constitutive modeling for $\sigma_c = 17.5$ Mpa	131
3.90	Load-unload-reload responses constructed from the results of COV analysis of TXC test data plotted in forms that are conducive to constitutive modeling for $\sigma_c = 20.0$ MPa	132
3.91	Load-unload-reload responses constructed from the results of COV analysis of TXC test data plotted in forms that are conducive to constitutive modeling for $\sigma_c = 55.0$ MPa	133
3.92	Load-unload responses constructed from the results of COV analysis of TXC test data plotted in forms that are conducive to constitutive modeling for $\sigma_c = 60.0$ MPa	134
3.93	Load-unload-reload responses constructed from the results of COV analysis of TXC test data plotted in forms that are conducive to constitutive modeling for $\sigma_c = 80.0$ MPa	135
3.94	Rosenblueth equations for converting the results from the COV analysis of "measured" K_0 test data into forms that are conducive to constitutive modeling	136
3.95	Rosenblueth equations for converting the results from the COV analysis of "measured" EXT K_0 test data into forms that are conducive to constitutive modeling	137
3.96	Rosenblueth equations for converting the results from the COV analysis of "measured" HC test data into forms that are conducive to constitutive modeling	138

<u>Figure</u>		<u>Page</u>
3.97	Rosenblueth equations for converting the results from the COV analysis of "measured" TXC test data into forms that are conducive to constitutive modeling	139
3.98	Correlation coefficients for loading K_0 test data	140
3.99	Correlation coefficients for loading EXT K_0 test data	141
3.100	Correlation coefficients for loading static HC test data ..	142
3.101	Correlation coefficients for loading dynamic HC test data .	143
3.102	Correlation coefficients for loading static TXC test data for $\sigma_c = 0, 0.1, 0.21, 0.35, 0.7, 1.7,$ and 3.5 MPa	144
3.103	Correlation coefficients for loading static TXC test data for $\sigma_c = 17.5, 20.0, 40.0, 55.0, 60.0,$ and 80.0 MPa	145
3.104	Results from applying the Rosenblueth procedure to the results from the COV analysis of "measured" K_0 test data	146
3.105	Stress paths obtained from applying the Rosenblueth procedure to the results from the COV analysis of "measured" K_0 test data	147
3.106	Results from applying the Rosenblueth procedure to the results from the COV analysis of "measured" EXT K_0 test data	148
3.107	Results from applying the Rosenblueth procedure to the results from the COV analysis of "measured" static HC test data	149
3.108	Results from applying the Rosenblueth procedure to the results from the COV analysis of "measured" dynamic HC test data	150
3.109	Results from applying the Rosenblueth procedure to the results from the COV analysis of "measured" TXC test data for $\sigma_c = 0$ and 0.1 MPa	151
3.110	Results from applying the Rosenblueth procedure to the results from the COV analysis of "measured" TXC test data for $\sigma_c = 0.21$ and 0.35 MPa	152
3.111	Results from applying the Rosenblueth procedure to the results from the COV analysis of "measured" TXC test data for $\sigma_c = 0.7, 1.7,$ and 3.5 MPa	153
3.112	Results from applying the Rosenblueth procedure to the results from the COV analysis of "measured" TXC test data for $\sigma_c = 17.5$ MPa	154
3.113	Results from applying the Rosenblueth procedure to the results from the COV analysis of "measured" TXC test data for $\sigma_c = 20.0$ MPa	155
3.114	Results from applying the Rosenblueth procedure to the results from the COV analysis of "measured" TXC test data for $\sigma_c = 40.0$ MPa	156

<u>Figure</u>		<u>Page</u>
3.115	Results from applying the Rosenblueth procedure to the results from the COV analysis of "measured" TXC test data for $\sigma_c = 55.0$ MPa	157
3.116	Results from applying the Rosenblueth procedure to the results from the COV analysis of "measured" TXC test data for $\sigma_c = 60.0$ MPa	158
3.117	Results from applying the Rosenblueth procedure to the results from the COV analysis of "measured" TXC test data for $\sigma_c = 80.0$ MPa	159
3.118	Effect of including ρ in the Rosenblueth procedure for TXC test data at $\sigma_c = 17.5$ MPa	160
3.119	Effect of including ρ in the Rosenblueth procedure for TXC test data at $\sigma_c = 20.0$ MPa	161
3.120	Effect of including ρ in the Rosenblueth procedure for TXC test data at $\sigma_c = 55.0$ MPa	162
3.121	Results from applying the Rosenblueth procedure to constructed continuous results from the COV analysis of "measured" K_0 test data	163
3.122	Results from applying the Rosenblueth procedure to constructed continuous results from the COV analysis of "measured" static HC test data	164
3.123	Results from applying the Rosenblueth procedure to constructed continuous results from the COV analysis of "measured" dynamic HC test data	165
3.124	Load-unload responses constructed from the results of applying the Rosenblueth procedure to the results from the COV analysis of "measured" K_0 test data	166
3.125	Load-unload-reload responses constructed from the results of applying the Rosenblueth procedure to the results from the COV analysis of "measured" K_0 test data	167
3.126	Load-unload-reload responses constructed from the results of applying the Rosenblueth procedure to the results from the COV analysis of "measured" EXT K_0 test data	168
3.127	Load-unload-reload responses constructed from the results of applying the Rosenblueth procedure to the results from the COV analysis of "measured" static HC test data	169
3.128	Load-unload responses constructed from the results of applying the Rosenblueth procedure to the results from the COV analysis of "measured" dynamic HC test data	170
3.129	Comparison of the results from the COV and COV/Rosenblueth analysis techniques for the loading portion of K_0 test data	171
3.130	Comparison of the results from the COV and COV/Rosenblueth analysis techniques for the loading portion of EXT K_0 test data	172

<u>Figure</u>		<u>Page</u>
3.131	Comparison of the results from the COV and COV/Rosenblueth analysis techniques for the loading portion of static HC test data	173
3.132	Comparison of the results from the COV and COV/Rosenblueth analysis techniques for the loading portion of dynamic HC test data	174
3.133	Comparison of the results from the COV and COV/Rosenblueth analysis techniques for the loading portion of static TXC test data at $\sigma_c = 0$ and 0.1 MPa	175
3.134	Comparison of the results from the COV and COV/Rosenblueth analysis techniques for the loading portion of static TXC test data at $\sigma_c = 0.21$ and 0.35 MPa	176
3.135	Comparison of the results from the COV and COV/Rosenblueth analysis techniques for the loading portion of static TXC test data at $\sigma_c = 0.7, 1.7,$ and 3.5 MPa	177
3.136	Comparison of the results from the COV and COV/Rosenblueth analysis techniques for the loading portion of static TXC test data at $\sigma_c = 17.5$ MPa	178
3.137	Comparison of the results from the COV and COV/Rosenblueth analysis techniques for the loading portion of static TXC test data at $\sigma_c = 20.0$ MPa	179
3.138	Comparison of the results from the COV and COV/Rosenblueth analysis techniques for the loading portion of static TXC test data at $\sigma_c = 40.0$ MPa	180
3.139	Comparison of the results from the COV and COV/Rosenblueth analysis techniques for the loading portion of static TXC test data at $\sigma_c = 55.0$ MPa	181
3.140	Comparison of the results from the COV and COV/Rosenblueth analysis techniques for the loading portion of static TXC test data at $\sigma_c = 60.0$ MPa	182
3.141	Comparison of the results from the COV and COV/Rosenblueth analysis techniques for the loading portion of static TXC test data at $\sigma_c = 80.0$ MPa	183
4.1	Comparison of the results from the COV analysis of dynamic UX test data and the recommended laboratory response	192
4.2	Comparison of the results from the COV analysis of K_O test data and the recommended laboratory UX stress path	193
4.3	Comparison of the results from the COV analysis of EXT K_O test data and the recommended laboratory UX stress path ...	194
4.4	Comparison of the results from the COV analysis of static HC test data and the recommended laboratory HC compressibility response	195
4.5	Comparison of the results from the COV analysis of dynamic HC test data and the recommended laboratory HC compressibility response	196

<u>Figure</u>		<u>Page</u>
4.6	Results from the COV analysis of the static TXC test data and the recommended unloading response for $\sigma_c = 0, 0.1, 0.21, 0.35, \text{ and } 0.7 \text{ MPa}$	197
4.7	Results from the COV analysis of the static TXC test data and the recommended unloading response for $\sigma_c = 1.7 \text{ and } 3.5 \text{ MPa}$	198
4.8	Comparison of the results from the COV analysis of the static TXC test data for $\sigma_c = 17.5 \text{ and } 20.0 \text{ MPa}$ and the recommended laboratory response for $\sigma_c = 20.0 \text{ MPa}$	199
4.9	Comparison of the results from the COV analysis of the static TXC test data and the recommended laboratory response for $\sigma_c = 40.0 \text{ MPa}$	200
4.10	Comparison of the results from the COV analysis of the static TXC test data for $\sigma_c = 55.0 \text{ and } 60.0 \text{ MPa}$ and the recommended laboratory response for $\sigma_c = 60.0 \text{ MPa}$	201
4.11	Comparison of the results from the COV analysis of the static TXC test data and the recommended laboratory response for $\sigma_c = 80.0 \text{ MPa}$	202
4.12	Static TXC "peak" strength test data, "peak" strength values from Figures 4.6-4.11, and recommended laboratory "peak" strength envelope	203
4.13	Coefficient of variation for the results from the COV analysis of static TXC test data for $\sigma_c = 17.5 \text{ and } 20.0 \text{ MPa}$ and the recommended laboratory response for $\sigma_c = 20.0 \text{ MPa}$	204
4.14	Coefficient of variation for the results from the COV analysis of static TXC test data for $\sigma_c = 55.0 \text{ MPa}$ and the recommended laboratory response for $\sigma_c = 60.0 \text{ MPa}$	205
4.15	Comparison of the results from the COV analysis of the loading portion of TXC test data and the new recommended laboratory response at $\sigma_c = 30.0 \text{ MPa}$	206
4.16	Correlation between in situ axial strain and seismic axial strain	207
4.17	Recommended laboratory and in situ dynamic UX compressibility responses	208
4.18	Coefficient of variation for the results from the COV analysis of dynamic UX test data and the recommended laboratory UX compressibility response	209
4.19	Beta distribution parameters α and β for the results from the COV analysis of dynamic UX test data and the recommended laboratory UX compressibility response	210
4.20	Coefficient of variation for the results from the COV analysis of loading K_0 and EXT K_0 test data and the recommended laboratory stress path	211

<u>Figure</u>		<u>Page</u>
4.21	Beta distribution parameters α and β versus for the results from the COV analysis of K_0 and EXT K_0 test data and the recommended laboratory stress path	212
4.22	Coefficient of variation for the recommended laboratory TXC "peak" strength envelope	213
4.23	Beta distribution parameters α and β for the recommended laboratory TXC "peak" strength envelope	214
4.24	Recommended laboratory dynamic UX compressibility loading response extrapolated to higher stresses	215
4.25	Recommended UX stress path extrapolated to higher stresses	216
4.26	Recommended TXC "peak" strength envelope extrapolated to higher stresses	217
4.27	Low-stress laboratory and in situ probabilistic dynamic UX compressibility responses	218
4.28	Laboratory probabilistic static HC compressibility response	219
4.29	Low-stress in situ dynamic deterministic TXE "peak" strength envelope and probabilistic TXC "peak" strength envelope and UX stress path	220
4.30	Probabilistic in situ dynamic TXC shear responses for $\sigma_c = 0, 0.1, 0.21, \text{ and } 0.35 \text{ MPa}$	221
4.31	Probabilistic in situ dynamic TXC shear responses for $\sigma_c = 0.7, 1.7, \text{ and } 3.5 \text{ MPa}$	222
4.32	Probabilistic in situ dynamic TXC shear responses for $\sigma_c = 20.0, 40.0, 60.0, \text{ and } 80.0 \text{ MPa}$	223
4.33	High-stress probabilistic in situ dynamic UX compressibility responses	224
4.34	High-stress in situ dynamic deterministic TXE "peak" strength envelope and probabilistic TXC "peak" strength envelope and UX stress path	225
5.1	Discrepancy created by varying sample size	230

LIST OF TABLES

<u>Table</u>		<u>Page</u>
3.1	First attempt at the dry density-based profile for Area A ..	34
3.2	Second attempt at the dry density-based profile for Area A .	34
3.3	Third attempt at the dry density-based profile for Area A ..	35
3.4	Dry density-based profile for Area B	35
3.5	Summary of probabilistic mass-volume properties for Area A .	36
3.6	Summary of probabilistic mass-volume properties for Area B .	36
3.7	Summary of the results from dynamic uniaxial strain tests used in the analysis of mechanical properties for layer 1 of Area A	37
3.8	Summary of the results from static uniaxial strain tests with lateral stress measurements, or Kc tests, used in the analysis of mechanical properties for layer 1 of Area A	38
3.9	Summary of the results from static uniaxial strain tests with lateral stress measurements, or EXT Ko tests, used in the analysis of mechanical properties for layer 1 of Area A	39
3.10	Summary of the results from static hydrostatic compression tests used in the analysis of mechanical properties for layer 1 of Area A	40
3.11	Summary of the results from dynamic hydrostatic compression tests used in the analysis of mechanical properties for layer 1 of Area A	41
3.12	Summary of the results from static triaxial compression tests used in the analysis of mechanical properties for layer 1 of Area A	42
4.1	One-way analysis of variance test for dry density of layer 1 at Area A versus dry density for test specimens from each test type	191

NOTATION

a = minimum value for the beta distribution
 A_o = original area
 A_p = area of the piston in the triaxial extension test apparatus
 b = maximum value for the beta distribution
 C = seismic compression wave velocity
 cov = covariance
 $dV/V_o(cyl)$ = volumetric strain calculated assuming deformation as a right circular cylinder
 E = expected value
 F = ratio of the between sample variance and the within sample variance
 F_{α} = area under the right-hand tail of the F distribution
 $F_{0.05}$ = area under the right-hand tail of the F distribution for $\alpha = 0.05$
 G_s = specific gravity
 H_o = original height
 HC = hydrostatic compression
 L = load
 LC = lower chamber pressure in the triaxial extension test apparatus
 M = constrained modulus
 M_L = loading constrained modulus
 M_U = unloading constrained modulus
 MNS = mean normal stress
 n = window size in the smoothing technique and total number of curves in a set of data
 PSD = principal stress difference
 r = sample correlation coefficient
 S = degree of saturation
 S_1, S_2 = secant slopes
 S_{xx} = linear regression coefficient for the x-axis values
 S_{yy} = linear regression coefficient for the y-axis values
 S_{xy} = linear regression coefficient for the x- and y-axis values
 TXC = triaxial compression
 TXE = triaxial extension

UC = upper chamber pressure in the triaxial extension test apparatus
 UX = uniaxial strain
 V = variance
 V_a = air voids content
 \bar{x} = mean value
 $y_m(x_i)$ = measured data
 $y_s(x_i)$ = smoothed data
 α = beta distribution parameter
 β = beta distribution parameter
 β_{STRAIN} = ratio of in situ axial strain to seismic axial strain
 γ = wet density
 γ_d = dry density
 ΔH = change in height of a test specimen
 Δx = increment size along the x-axis
 Δy = increment size along the y-axis
 $\epsilon_{\text{IN SITU}}$ = in situ axial strain
 ϵ_s = seismic axial strain
 ϵ_r = radial strain
 ϵ_{r_T} = true radial strain
 ϵ_z = axial strain
 μ = number of increments in the covariance analysis
 ν_L = loading Poisson's ratio
 ν_{UN} = unloading Poisson's ratio
 $\nu_{\text{UN}1}$ = initial unloading Poisson's ratio
 ρ = correlation coefficient
 σ = standard deviation
 σ_c = confining pressure
 σ_r = radial stress
 σ_z = axial stress
 ϕ = angle of internal friction
 ω = water content
 Ω = incremental slope

CONVERSION FACTORS, NON-SI TO SI (METRIC)

UNITS OF MEASUREMENT

Non-SI units of measurement used in this report can be converted to SI (metric) units as follows:

<u>Multiply</u>	<u>By</u>	<u>To Obtain</u>
degrees (angle)	0.01745329	radians
feet	0.3048	metres
inches	25.4	millimetres
kips (force)	4.448222	kilonewtons
kips (force) per square inch	6.894757	megapascals
megatons (nuclear equivalent of TNT)	4.184	petajoules
pounds (force) per square inch	0.006894757	megapascals
pounds (mass)	0.4535924	kilograms
pounds (mass) per cubic foot	16.01846	kilograms per cubic metre

A TECHNIQUE FOR DEVELOPING PROBABILISTIC
PROPERTIES OF EARTH MATERIALS

CHAPTER 1

INTRODUCTION

1.1 BACKGROUND

The vulnerability of buried structures, such as missile silos and shelters, to nuclear blasts is assessed by conducting scaled test events using conventional explosives. The stress, velocity, and deflection of the structure and surrounding soil are measured. The response of the buried structure is significantly affected by the response of the surrounding earth media. The stress being transmitted to the structure by the soil, the friction at the soil-structure interface, the motion of the soil with respect to the structure, and the cratering characteristics of the soil are all important in the survivability of buried structures. To effectively predict or evaluate the results from a test event, the properties of the earth materials must be determined. This requires extensive soil exploration programs involving (a) drilling and sampling to obtain disturbed and undisturbed samples for identification and laboratory testing, (b) seismic surveys to determine the seismic velocity, (c) mass-volume, index, strength, and compressibility tests on disturbed and undisturbed samples, and (d) in situ compressibility tests using explosives as the loading source.

The ground shock calculation techniques currently used by the analysts of explosive test events require deterministic input parameters and provide deterministic results, i.e., single-valued quantities or functions are input and output. In actuality, the properties of earth materials and the characteristics of the explosive blasts are dispersed random variables. Since these input variables are random, the calculated stresses and ground motions are also random variables. Therefore, ground shock problems should be analyzed probabilistically. By treating a ground shock calculation probabilistically, the effect of the uncertainties in the material properties and characteristics of the explosive

blast on the dispersion of the output variables can be evaluated. Ultimately, the probability of failure for a buried structure can be assessed if the uncertainty in the input is known. To this end, a three-phase project is underway at the US Army Engineer Waterways Experiment Station to (a) develop a procedure for providing the probabilistic properties of earth materials needed as input for a probabilistic ground shock calculation, (b) develop a probabilistic cap-type elastic-plastic constitutive model that describes the probabilistic properties of the earth materials and does not require much more effort to fit than the associated deterministic model, and (c) develop a probabilistic ground shock calculation computer code and calculation procedure. This report documents the development of phase (a).

1.2 LITERATURE REVIEW

It has long been recognized that probabilistic concepts and methods should be used in geotechnical engineering to aid the development of practical procedures dealing with risk and uncertainty. Efforts have been undertaken to analyze probabilistically subgrade soil strengths (Reference 1), settlement (Reference 2), and slope stability (References 3 and 4). In developing basing concepts for ballistic missiles, it was recognized that probabilistic analysis of ground shock tests was a necessity (Reference 5). The original basing concepts for the MX missile essentially consisted of probabilistic "shell games" in which a relatively small number of missiles were concealed within a much larger number of hardened shelters. If the nuclear ground shock calculations used in shelter vulnerability analyses were to be consistent with this scenario, it was necessary that the soil profiles and properties used as input be probabilistic quantities (Reference 6).

Chou used a concept of spatial average to probabilistically model subgrade strength for pavement design (Reference 1). He pointed out that a probability-based design procedure would allow for (a) design to a level of reliability depending upon the importance and function of the pavement, (b) quantifying the design risk, and (c) optimizing design results by controlling and minimizing expenditures and early failures. The probabilistic subgrade strengths used in the procedure were based on the concept of spatial averages outlined by Vanmarcke in Reference 7.

The application of spatial averages has the advantage of reducing the variance of the variables, thereby increasing the reliability of predicted pavement performance.

Diaz-Padilla and Vanmarcke developed a probabilistic soil-structure interaction model that yields first-order probabilistic information about the differential settlements of a foundation in terms of the probabilistic input, i.e., loads and soil properties (Reference 2). The permanent loads vary due to discrepancies between specified and actual member dimensions and fluctuations in volumetric weights. The dead loads vary since the final location, composition, and weight of non-structural items is not known in the design stage. Live loads are random since they are impossible to predict with certainty. The mechanical properties of an assumed nominally homogeneous soil stratum exhibit a considerable amount of variability from point to point. The randomness is due to the natural variability of the material (the mineral composition, stratum formation process, etc.) and uncertainty introduced when measuring the soil properties (sample disturbance, human errors, and test imperfections). The means and variances of the differential settlements obtained from the application of the probabilistic model can be used to estimate the probability of exceeding specified levels.

Gilbert developed a probabilistic approach for analyzing embankment stability on soft saturated clay at the end of construction (Reference 3). The model was proposed as a supplement to the design approach based on $\phi = 0$ analyses using the undrained strength of the foundation clay. Two case studies analyzed with the proposed model indicated that bias inherent in field vane and unconfined compression testing can be the major source of uncertainty in design.

Vanmarcke presented a probabilistic approach to the classical limit equilibrium slope stability problem (Reference 4). He noted that risk analysis should be used to supplement the conventional procedures for determining the factor of safety against shear failure of earth slopes and embankments. Risk analysis permits rational consideration of factors that significantly influence the probability of failure, such as the inherent variability of soil strength, the manner in which strength values are selected, and the amount and quality of soil exploration and testing.

Since the soil parameters have a significant influence on stability calculations, they are worth quantifying. Vanmarcke noted in Reference 7 that the variability of soil properties should be considered in the design and evaluation of soil exploration programs. Three major sources of uncertainty in modeling a soil profile are: (a) the spatial in situ variability of the soil, (b) statistical uncertainty due to a limited number of soil samples, and (c) measurement errors due to sample disturbance, test imperfections, and human factors. The first source of uncertainty can be examined by considering the spatial variation of the soil properties. The effect of the second source of uncertainty can be reduced by conducting many tests. The effects of the third source can be reduced by careful monitoring to obtain high quality test data.

A significant use of probabilistic ground shock analyses is to evaluate the variability in the input parameters (blast loading and soil properties) in terms of their effects on the dispersion of the output variables (stress and motion). Using the method of partial derivatives (Reference 8), Rohani (Reference 9) developed a probabilistic solution for one-dimensional (1D) plane wave propagation in homogeneous bilinear hysteretic materials. The solution was incorporated into a computer code by Rohani and Cargile (Reference 10). The code can be used to quantitatively rank the relative effects of input variabilities on the dispersion of the output quantities. The results from 1D probabilistic calculations indicated that, at early times, uncertainty in the soil compressibility had the greatest effect on the output uncertainty. The influence of soil compressibility uncertainty decreased with increasing time while the contribution due to airblast impulse uncertainty gradually increased.

A method for objectively comparing measurements of waveforms from an explosive test event with those obtained from probabilistic prediction calculations was developed by Baladi and Barnes (Reference 11). By calculating the magnitude and phase-and-frequency errors between the measured and expected waveforms, an objective judgment of the degree of agreement or disagreement can be made.

A "simple" method was used to develop the probabilistic mechanical responses presented by Vanmarcke, Jackson, and Akers (Reference 12) and Jackson (Reference 13). The method involved calculating the mean and

standard deviation values for strain at given values of stress for a set of uniaxial strain compressibility tests.

1.3 PURPOSE

The purpose of this investigation was to document an analysis technique for developing probabilistic properties of earth materials. The technique involves (a) determining the subsurface profile for a given test site based on mass-volume relations, index parameters, seismic velocities, material type, etc., and (b) developing probabilistic values or relations for the mass-volume relations, index parameters, seismic velocities, and mechanical properties (i.e., strength and compressibility relations) for each layer of the profile. The probabilistic properties are based on laboratory test results, field experiments, and engineering knowledge. Generally, the data obtained from mechanical property tests do not extend to the stress levels required for ground shock calculations. A procedure for extrapolating the variance of the lower stress portion of the recommended probabilistic mechanical properties to higher stresses is also presented.

1.4 SCOPE

The procedures for (a) developing the subsurface profile of a given test site and (b) determining the probabilistic values and relations for the mass-volume relations, index parameters, seismic velocities, and mechanical properties for each layer of the profile are described in Chapter 2. A technique for removing the electrical noise that is often embedded in the measured data from mechanical property tests and Rosenblueth's point estimate procedure are also explained in Chapter 2. The application of the analysis technique to data obtained from two adjacent areas located near Yuma, Arizona is presented in Chapter 3. The recommended probabilistic mechanical properties are presented in Chapter 4. A method for extrapolating the variance of the lower stress mechanical properties to higher stresses is also presented in Chapter 4. A summary, conclusions, and recommendations for further study are presented in Chapter 5.

CHAPTER 2

DESCRIPTION OF THE ANALYSIS TECHNIQUE

2.1 DETERMINATION OF THE SUBSURFACE PROFILE

The subsurface profile of an area is based on changes in material type, mass-volume relations, index values, seismic velocity, etc. This data is plotted versus depth to determine trends. The mean and standard deviation values (\bar{x} and $\hat{\sigma}$, respectively) are calculated for a zone of data which appears to be different from the data above and below it. These statistics are used in a one-way analysis of variance (Reference 14) to test the null hypothesis that the apparent difference in the mean values for adjacent zones is not statistically significant.

In the one-way analysis of variance, the null hypothesis is true if the ratio of the between sample variance and the within sample variance (F) is greater than F_{α} , where

$$F = \frac{SS(Tr) \sum_{i=1}^k (m_i - 1)}{SSE (k - 1)} \quad (2.1)$$

and,

$$SS(Tr) = \sum_{i=1}^k m_i (\bar{x}_i)^2 - \frac{\left(\sum_{i=1}^k m_i \bar{x}_i \right)^2}{\sum_{i=1}^k m_i} \quad (2.2)$$

$$SSE = \sum_{i=1}^k (\hat{\sigma}^2 (m_i - 1)) \quad (2.3)$$

In equations 2.1-2.3, k is the number of samples and m is the number of data in a given sample. The value for F_{α} is obtained from the distribution of F using $k-1$ and $\sum_{i=1}^k (m_i - 1)$ degrees of freedom. If the test indicates that the means are not significantly different, i.e., F is less than F_{α} , the zone interfaces are redrawn and new mean and standard deviation values are calculated. This process is

repeated until the one-way analysis of variance test of the null hypothesis for adjacent zones is false, i.e., F is greater than F_{α} .

2.2 ANALYSIS OF MECHANICAL PROPERTY TEST DATA

Mechanical property tests (i.e., strength and compressibility tests) are conducted on undisturbed samples from each layer of the subsurface profile. The mechanical property test results for samples from a given layer are grouped together, electrical noise is removed from the data, and a covariance analysis is conducted on the data set.

2.2.1 Data Smoothing

Artificial noise created by the electronics of the measurement system used during a mechanical property test is embedded in the test data. For some tests, this noise can be severe and almost mask the measured response of the specimen. Therefore, a technique to smooth the measured data without changing the intrinsic response is needed. Such a procedure was developed by Baladi and Barnes (Reference 11) and was based on the concept of a marching mean square. If the measured value of the i^{th} data point is expressed as $y_m(x_i)$, the corresponding smoothed response $y_s(x_i)$ can be expressed as

$$y_s(x_i) = \sqrt{\frac{1}{n-1} \sum_{k=i-\frac{n-1}{2}}^{k=i+\frac{n-1}{2}} y_m^2(x_k)} \quad (2.4)$$

where $n-1$ is the window over which the marching mean square is taken (i.e., $\frac{n-1}{2}$ is the number of data points to the left and to the right of the i^{th} data point). The value of n must be an odd integer equal to or greater than 3. The degree of smoothing increases as n increases. A small value for n should be used initially. The data can be smoothed repeatedly with the same window size until a satisfactory response is produced or until further repetitions produce no change in the "smoothed" data. If additional smoothing is required, a larger window size must be used. The smoothed data should follow the general trends of the original data. The results from the smoothing process

should be compared with the original data to ensure that the general trends were not altered by excessive smoothing.

2.2.2 Covariance Analysis of Smoothed Data

A generic procedure for statistically analyzing nonlinear data was developed by Baladi and Rohani (Reference 15). The procedure is outlined in this section. The objective of the analysis is to determine the mean curve with its one standard deviation bound for a set of curves by relating the random variables y and x (Figure 2.1). This can be accomplished by applying standard statistical procedures to the slope of the random curves. The following steps should be taken to conduct the statistical analysis:

(1) For a given set of n curves, divide the x -axis into μ number of equal increments Δx . (This procedure may also be applied by dividing the y -axis into μ number of equal increments Δy .)

(2) For the i^{th} increment, determine the slope of the j^{th} curve denoted by Ω_{ij}

$$\Omega_{ij} = \frac{\Delta y_i}{\Delta x_i}, \quad j = 1, 2, \dots, n \quad (2.5)$$

(3) Determine the expected value and the standard deviation of the slope at the i^{th} increment for all the curves according to the following expressions

$$\bar{\Omega}_i = E(\Omega_i) = \frac{1}{n} \sum_{j=1}^n \Omega_{ij} \quad (2.6)$$

$$\hat{\sigma}(\Omega_i) = \sqrt{\frac{1}{n-1} \sum_{j=1}^n (\Omega_{ij} - \bar{\Omega}_i)^2} \quad (2.7)$$

(4) Next, compute the mean and the standard deviation of y . To accomplish this, the covariance and the correlation coefficient matrices of the slopes $\text{cov}(\Omega_k, \Omega_m)$ and ρ_{km} , respectively, are first calculated from the following relations:

$$\begin{aligned}\text{COV}(\Omega_k, \Omega_m) &= E[(\Omega_k - \bar{\Omega}_k)(\Omega_m - \bar{\Omega}_m)] \\ &= \frac{1}{n-1} \sum_{j=1}^n (\Omega_{kj} - \bar{\Omega}_k)(\Omega_{mj} - \bar{\Omega}_m)\end{aligned}\quad (2.8)$$

$$\rho_{km} = \frac{\text{COV}(\Omega_k, \Omega_m)}{\sqrt{E[(\Omega_k - \bar{\Omega}_k)^2] E[(\Omega_m - \bar{\Omega}_m)^2]}} \quad (2.9)$$

in which

$$E[(\Omega_k - \bar{\Omega}_k)^2] = \frac{1}{n-1} \sum_{j=1}^n (\Omega_{kj} - \bar{\Omega}_k)^2 \quad (2.10)$$

where $k = 1, 2, \dots, i, \dots, \mu$ and $m = 1, 2, \dots, i, \dots, \mu$.

Finally, the mean value and the standard deviation of y at the i^{th} increment become

$$\bar{y}_i = \sum_{j=1}^i E[\Omega_j] \Delta x_j \quad (2.11)$$

$$\hat{\sigma}(y_i) = \sqrt{\sum_{m=1}^i \sum_{k=1}^i \rho_{km} \hat{\sigma}(\Omega_k) \Delta x_k \hat{\sigma}(\Omega_m) \Delta x_m} \quad (2.12)$$

This procedure is well suited for providing probabilistic mechanical properties because the slopes of the plotted responses are used in the analysis. It is the slopes of plotted mechanical responses that are fit to constitutive models.

The covariance technique can be applied in two ways. First, the technique can be applied to smoothed data that is plotted in a form that is conducive to constitutive modeling. Or, the technique can be applied directly to the smoothed data, and the results of the analysis converted into a form that is conducive to constitutive modeling. A procedure developed by Rosenblueth can be used for the conversion. These two approaches will be applied and compared in Chapter 3.

2.2.3 Rosenblueth's Point Estimate Procedure

Rosenblueth developed a procedure for determining the moments of a dependent variable in terms of functions of the moments of its independent variables (References 16 and 17). The usual method of obtaining approximate formulas from the Taylor expansion of a function about the expectations of the random variables (Reference 8) is bound by excessive restrictions on the function, such as existence and continuity of the first few derivatives. The Rosenblueth procedure avoids such restrictions by using point estimates of the function, which leads to expressions similar to finite differences.

If Y is a function of two random variables X_1 and X_2 ,

$$Y = Y(X_1, X_2)$$

and the probability distribution functions of X_1 and X_2 are symmetrical, the expected value of Y , $E(Y)$, and variance of Y , $V(Y)$, can be estimated by the following expressions:

$$E(Y) = Y^{++} \left(\frac{1+\rho_{12}}{4} \right) + Y^{+-} \left(\frac{1-\rho_{12}}{4} \right) + Y^{-+} \left(\frac{1-\rho_{12}}{4} \right) + Y^{--} \left(\frac{1+\rho_{12}}{4} \right) \quad (2.13)$$

$$V(Y) = E(Y^2) - E^2(Y) \quad (2.14)$$

where,

$$E(Y^2) = (Y^{++})^2 \left(\frac{1+\rho_{12}}{4} \right) + (Y^{+-})^2 \left(\frac{1-\rho_{12}}{4} \right) + (Y^{-+})^2 \left(\frac{1-\rho_{12}}{4} \right) + (Y^{--})^2 \left(\frac{1+\rho_{12}}{4} \right) \quad (2.15)$$

and

$$Y^{\pm\pm} = Y(\bar{X}_1 \pm \hat{\sigma}_{X_1}, \bar{X}_2 \pm \hat{\sigma}_{X_2})$$

The terms \bar{X}_1 and \bar{X}_2 are the expected values of the variables X_1 and X_2 , respectively; likewise, $\hat{\sigma}_{X_1}$ and $\hat{\sigma}_{X_2}$ are the standard

deviations of those random variables. The term ρ_{12} is the correlation coefficient of X_1 and X_2 .

From the above equations, the expected value and the variance of Y can be calculated from four point estimates of the function Y . Each point estimate can be viewed as a deterministic calculation of the dependent random variable Y . The equations presented above can be generalized to n random variables requiring 2^n point estimates.

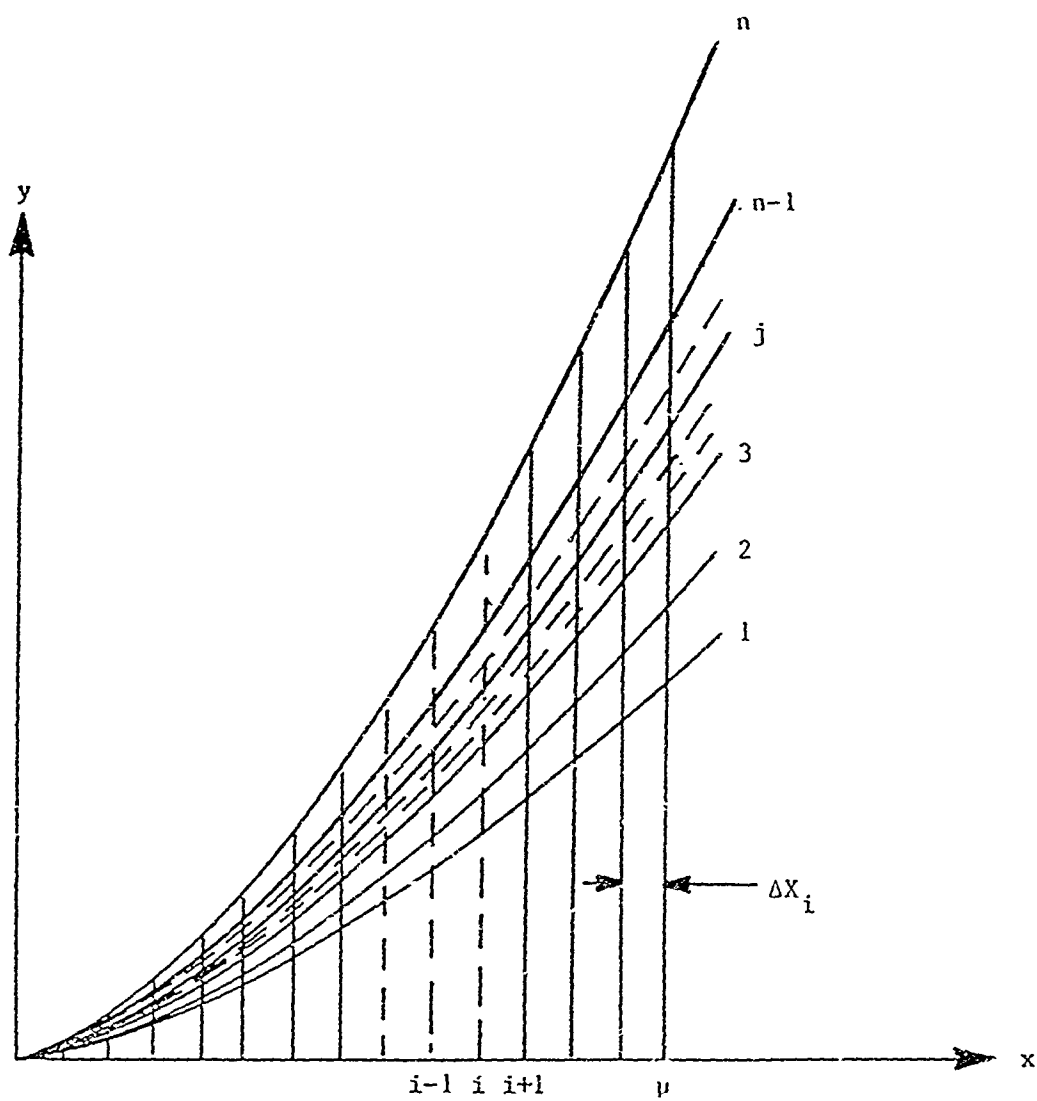


Figure 2.1. General curves relating the random variables y and x .

CHAPTER 3

APPLICATION OF THE ANALYSIS TECHNIQUE

3.1 MASS-VOLUME AND INDEX DATA

Dry density data obtained for an area located near Yuma, Arizona (Area A) are plotted versus depth in Figure 3.1. Four layers were used as an initial attempt to determine a subsurface profile based on the dry density data. The depth to layer interfaces and dry density mean and standard deviation values for each layer are in Table 3.1. The calculated F values (Equations 2.1-2.3) and values for an α of 0.05 for the F distribution ($F_{0.05}$) are also shown. The one-way analysis of variance tests between adjacent layers is conducted by comparing the calculated F value with the $F_{0.05}$ value. The results for the tests between layers 1 and 2 and between layers 3 and 4 (Table 3.1) indicate that the difference between the mean values is not statistically significant, i.e., F_{1-2} and F_{3-4} are less than their respective values of $F_{0.05}$. An attempt that uses a slightly different interface between layers 1 through 3 and combines layers 3 and 4 is summarized in Table 3.2.

In Table 3.2, the test between layers 1 and 2 does not indicate a statistically significant difference, but the test between layers 2 and 3 does indicate a statistically significant difference. Therefore, layers 1 and 2 were combined and the test repeated. The results of this analysis are shown in Table 3.3. Since the analysis of variance test between the two layers indicates a statistically significant difference, this sequence of layers is used to describe the dry density-based profile at Area A. The results of the analysis are shown graphically in Figure 3.1. The results from applying the procedure to the dry density data obtained from an area that is adjacent to Area A (designated Area B) are summarized in Table 3.4 and shown graphically in Figure 3.2.

No significant trends could be identified for water content and specific gravity versus depth. Mean and standard deviation values for water content at Area A are 3.8 and 1.6 percent, respectively; for Area B, these values are 3.3 and 1.3 percent, respectively. Mean and

standard deviation values for specific gravity of 2.68 and 0.01, respectively, are used for both areas.

The mean and standard deviation values for wet density γ , degree of saturation S , and air voids content V_a are calculated using the Rosenblueth procedure. A symmetrical distribution and no correlation is assumed. From a visual inspection of Figures 3.1 and 3.2, the assumption of a symmetrical distribution for dry density is probably adequate since an equal amount of data is approximately on either side of the mean value. Since the layering that was determined for the dry density data could not be applied to the water content and specific gravity data, it is reasonable to assume that these properties are uncorrelated; therefore, the value of ρ in equations 2.13 and 2.15 is assumed to be zero. The value of γ in terms of dry density γ_d and water content ω , and the value of S and V_a in terms of γ_d , ω , and specific gravity G_s are given by (Reference 18)

$$\gamma = \frac{\gamma_d}{1 + \omega} \quad (3.1)$$

$$S = \frac{\omega \gamma_d G_s}{G_s \gamma_d - \gamma_d} \quad (3.2)$$

$$V_a = 1 - \gamma_d \left(\frac{1}{G_s} + \omega \right) \quad (3.3)$$

Equations 3.1-3.3 can be easily incorporated into the Rosenblueth procedure. The resulting set of equations for $E[\gamma]$ and $V[\gamma]$ are

$$E[\gamma] = \frac{1}{4} [\gamma^{++} + \gamma^{+-} + \gamma^{-+} + \gamma^{--}] \quad (3.4)$$

$$V[\gamma] = \frac{1}{4} [(\gamma^{++})^2 + (\gamma^{+-})^2 + (\gamma^{-+})^2 + (\gamma^{--})^2] - E^2[\gamma] \quad (3.5)$$

The resulting set of equations for $E[S]$, $V[S]$, $E[V_a]$, and $V[V_a]$ are

$$E[S] = \frac{1}{8} [S^{+++} + S^{++-} + S^{+-+} + S^{-++} + S^{---} + S^{--+} + S^{-+-} + S^{+--}] \quad (3.6)$$

$$V[S] = \frac{1}{8} [(S^{+++})^2 + (S^{++-})^2 + (S^{+-+})^2 + (S^{-++})^2 + (S^{---})^2 + (S^{--+})^2 + (S^{-+-})^2 + (S^{+--})^2] - E^2[S] \quad (3.7)$$

$$E[V_a] = \frac{1}{8} [V_a^{+++} + V_a^{++-} + V_a^{+-+} + V_a^{-++} + V_a^{---} + V_a^{--+} + V_a^{-+-} + V_a^{+--}] \quad (3.8)$$

$$V[V_a] = \frac{1}{8} [(V_a^{+++})^2 + (V_a^{++-})^2 + (V_a^{+-+})^2 + (V_a^{-++})^2 + (V_a^{---})^2 + (V_a^{--+})^2 + (V_a^{-+-})^2 + (V_a^{+--})^2] - E^2[V_a] \quad (3.9)$$

In equations 3.4-3.9, terms with a "+" in the superscript indicate the use of the mean + 1 standard deviation ($\hat{\sigma}$) value and terms with a "-" in the superscript indicate the use of the mean - $\hat{\sigma}$ value. The procedure is illustrated in Figure 3.3 for the first layer of Area A. The mean and standard deviation values for the mass-volume relations of both areas are summarized in Tables 3.5 and 3.6.

3.2 MECHANICAL PROPERTY DATA

The mechanical property data associated with the first layer of the dry density-based profile for Area A will be used to illustrate the technique for developing probabilistic mechanical properties.

3.2.1 Grouping of the Mechanical Property Data

The results from uniaxial strain (UX), UX with lateral stress measurement (Ko), and hydrostatic compression (HC) tests conducted on specimens obtained from the upper 49 ft of Area A were grouped to generate the UX, Ko, and HC data bases. The results from these tests

conducted on specimens obtained from the upper 49 ft of Area B and whose dry density is within one standard deviation of the mean dry density determined in Section 3.1 were used to supplement the data bases. Insufficient data are available to group the results from the triaxial compression (TXC) tests with respect to depth. The available TXC data were grouped based on the confining pressure at the start of the shear phase. Pertinent information on the individual tests is summarized in Tables 3.7-3.12.

The K_o tests are separated into two groups, i.e., K_o and EXT K_o tests (Tables 3.8 and 3.9, respectively). The K_o tests were conducted in a standard TY test device, and the EXT K_o tests were conducted in an extension TX test device (Reference 19). The extension TX test device differs from the standard TX test device in that the piston is the same diameter as the test specimen. During an EXT K_o test, the axial stress can be unloaded to zero.

The results from static and dynamic tests are used in the application of the analysis technique. Static tests are conducted with times to peak stress of several minutes. Dynamic tests are conducted with times to peak stress of several milliseconds.

3.2.2 Smoothing of the Data

The mechanical property test data were smoothed using the technique described in Section 2.2.1. The smoothing process begins by determining which part of the data requires smoothing. It is suggested that a small value for n be used initially. The section can be smoothed repeatedly with the same window size until a satisfactory response is produced or until further repetitions produce no change in the "smoothed" curve. If additional smoothing is required, a larger window size must be used.

Much of the UX and higher pressure K_o and TXC test results required some smoothing. Figure 3.4 shows a comparison between raw data and smoothed data. Note that it is difficult to distinguish individual responses in the raw data (Figure 3.4a). Figure 3.4b shows the data after smoothing. It is much easier to see the trends in the data and to distinguish individual responses. The general characteristics of the data are not altered.

3.2.3 Covariance Analysis

A program used to conduct the covariance (COV) analysis was written for a Hewlett-Packard 9816 with approximately 300 kbytes of available memory after the 4.0 Basic operating system was loaded. This restricted the number of increments that could be used in the analysis. Also, the run time for the program becomes unrealistically high if a large number of increments is used. It is desirable to use as many increments as possible since the accuracy of the analysis increases with decreasing increment size. During the development of the program, it was determined that approximately 70 increments provided good results in a reasonable length of time, i.e., a few minutes of calculation time per data set depending on the number of tests.

The curves used in the COV analysis must be monctonic in the incremented axis direction. The analysis of loading, unloading, and reload-ing responses are conducted separately. When the analysis is complete, the probabilistic loading, unloading, and reloading responses are pieced back together.

The COV analysis can be applied to test data plotted in a form that is conducive to constitutive modeling, i.e., axial strain, volumetric strain, principal strain difference, axial stress, principal stress difference, and mean normal stress, or as plots of "measured data," i.e., stresses, loads, and deflections. If the COV analysis is conducted on the "measured data," the mean and standard deviation responses are converted into the conducive forms using the Rosenblueth procedure. Both methods will be applied and their results compared.

3.2.3.1 UX test results. The results of UX tests are usually plotted as axial stress versus axial strain. The slope of the curve, i.e., axial stress/axial strain, is the constrained modulus M . Axial stress is directly measured during the test and axial strain ϵ_z is calculated as

$$\epsilon_z = \frac{\Delta H}{H_0}$$

where ΔH is the measured deflection and H_0 is the original height of the test specimen. This plot is in the form that is conducive to constitutive modeling and also reflects the "measured data."

Only the dynamic UX test data will be analyzed since there is an insufficient number of static test data to conduct a meaningful statistical analysis. A composite plot of the loading dynamic UX test data used in the analysis is shown in Figure 3.5. Note that all of the data does not extend to the same stress level. To utilize as much of the data as possible, the COV analysis was conducted on the four groups indicated by the dashed horizontal lines. All of the data is used in the first group. For the remaining groups, only those tests which have peak stresses at or above the stress level indicated by the horizontal lines are used. An additional advantage to conducting the analysis of the UX data in several groups is that smaller increments are used in the lower stress region. This provides a more accurate analysis in the region in which the most curvature is occurring.

In Section 2.2.2, it was noted that the COV analysis could be conducted by incrementing along the X-axis or the Y-axis, i.e., the strain- or stress-axis. For the UX test, the stress-axis is chosen since a stress is applied to the specimen, and the resulting deflection is measured. The applied stress is an independent random variable, and the resulting deflection is a dependent random variable. Instead of using the incremental M , compliance $1/M$ is used in the COV analysis.

The groups of loading dynamic UX test data used in the COV analysis are shown in Figure 3.6. The mean and mean $\pm \hat{\sigma}$ responses are shown as thick solid and dashed lines, respectively. If the data are assumed to be normally distributed, then the probability that a test response is within $3\hat{\sigma}$ of the mean is approximately 100 percent. The mean $+ 3\hat{\sigma}$ response may be valid; however, the mean $- 3\hat{\sigma}$ response for low stresses is invalid because it leads to negative axial strains, which are not possible during a UX test. This implies that the low stress dynamic UX data are not normally distributed.

The mean and mean $\pm \hat{\sigma}$ responses from Figures 3.6a-3.6b are also plotted in Figure 3.7a. Although the number of curves decreases with increasing stress, the general shapes of the probabilistic responses do

not change. A continuous probabilistic response constructed with the individual responses in Figure 3.7a is shown in Figure 3.7b. The composite response is constructed by using the probabilistic response for group 1 as the base. The next section is drawn by shifting the probabilistic response for group 2 between axial stresses of 12 MPa and 30 MPa to line up with the lower pressure response. The process is repeated for each successive section. This method of constructing the probabilistic response is valid for three reasons: (1) by shifting the responses in this manner, the slope of the individual pieces is not altered; (2) as stress increases, the appearance of the individual responses becomes very similar (Figure 3.5); and (3) the effect of the high stress tests on the low stress probabilistic responses is included in the analysis. A more rigorous statistical analysis is, thereby, conducted in the region where the greatest change in slope is occurring.

A composite of the two sets of available unloading data for the dynamic UX tests along with the mean and mean $\pm \hat{\sigma}$ responses are shown in Figure 3.8. The test data for groups U1 and U2 are arbitrarily normalized to axial strains of 4 and 8 percent, respectively. Unloadings that begin at approximately the same stress level are grouped together to form the data set. Since the unloadings in a given group do not begin at exactly the same stress level, it is necessary to limit the starting stress for the unloadings to the lowest stress level for a group. The loops in the data are caused by the unload-reload effect generated by reflected stress waves within the test chamber. This caused the unusual probabilistic response near the end of unloading U2. It is not unusual to see an unloading "hook" in the UX compressibility response. However, it is unusual to see a response in which the strain decreases, increases, and then decreases again near the end of an unloading. For this reason, the responses calculated for set U2 of the unloading data will be used as only a guide. Probabilistic reloading responses are not provided due to insufficient data.

The constructed load-unload probabilistic dynamic UX response is shown in Figure 3.9. A problem in the construction process is where to place the unloading responses. From a visual inspection of the test data, the stiffer unloadings tend to coincide with the stiffer loadings, and softer unloadings tend to coincide with softer loadings.

The unloading responses are placed on the appropriate loading response at the starting stress level for the unloading group. For example, since the first unloading begins at a vertical stress of 29.5 MPa, the mean unloading curve is shifted to begin at 29.5 MPa on the mean loading curve. The stiffest unloading curve is shifted to start at 29.5 MPa on the stiffest loading curve, and the softest unloading curve begins at 29.5 MPa on the softest loading curve.

3.2.3.2 Ko test results. The Ko test data were analyzed by (a) conducting the COV analysis on data that is plotted in a form convenient for constitutive modeling, i.e., axial stress versus axial strain and principal stress difference (PSD) versus mean normal stress (MNS) and (b) conducting the COV analysis on plots of data that are closer to that actually measured during the Ko test. In Section 3.2.4, the results from the second analysis are transformed into the convenient forms for constitutive modeling using the Rosenblueth procedure. For standard Ko tests, the "measured data" plots are load/original area (L/A_o) versus axial strain and L/A_o versus radial stress. The EXT Ko tests are conducted in a test device that has upper and lower chambers for applying pressure (denoted here as UC and LC, respectively). The "measured data" plots are $(UC-LC)*A_p/A_o$ versus axial strain and $(UC-LC)*A_p/A_o$ versus LC. The area of the piston, A_p , is included to account for an upward stress on the piston if the specimen has a smaller diameter than the piston, and a downward stress on the specimen if the specimen has a larger diameter than the piston. For Ko tests, the terms L/A_o and $(UC-LC)*A_p/A_o$ are equivalent to PSD since radial strain is essentially zero.

The loading portions of Ko and EXT Ko test data plotted as described above are shown in Figures 3.10-3.13. The Ko test results are analyzed in four groups (Figures 3.10 and 3.11). The test results pointed out with the letter "A" are only used in group 4. These results were developed from hand-processed records and do not have the accuracy of the other Ko tests at lower stress levels. The remaining test results in group 4 and the test results in group 3 are not used in groups 1 and 2 because they lack the accuracy of the results at lower stress levels. One group of loading EXT Ko test data are analyzed (Figures 3.12 and 3.13). Many of the EXT Ko test results have "noisy" responses caused by (a) the electronics of the measurement system and

(b) adjustment of the applied stress to maintain zero radial strain. For this reason, the "noise" in the test results was not completely removed in the smoothing process.

As discussed in Section 3.2.3.1, the stress-axis is incremented when the data is plotted as stress versus strain. In general, as MNS increases the plot of PSD versus MNS (or stress path) begins to break over. If this response is assumed to be typical, more of the loading data is used if the MNS-axis is incremented. The L/Ao- and (UC-LC)*Ap/Ao-axes are incremented to provide a common axis for applying the Rosenblueth procedure.

The test data (thin solid line) and mean, $\text{mean} \pm \hat{\sigma}$, and $\text{mean} \pm 3\hat{\sigma}$ responses from the COV analysis (thick solid, thick dashed, and thin dashed lines, respectively) are presented in Figures 3.12-3.17. All of the test data are within the $\text{mean} \pm 3\hat{\sigma}$ responses. However, like the UX tests, the axes form a boundary for the test results. Since the $\text{mean} - 3\hat{\sigma}$ responses cross into the negative regions at low stress levels, the data are not normally distributed at low stresses. The probabilistic responses from the analysis of the EXT Ko test data (Figures 3.12 and 3.13) are much smoother than the data; therefore, the "noisy" plots did not significantly effect the results from the COV analysis.

Composite plots of the results from the analysis of the Ko test data are presented in Figures 3.18 and 3.19. The results from the analysis conducted on the stress versus strain plots for groups 1 and 2 are much softer than the results for groups 3 and 4. This difference is caused by (a) the data for groups 3 and 4 being stiffer than the data for groups 1 and 2 and (b) the exclusion of the data in groups 3 and 4 in the analysis of groups 1 and 2. The shapes of the respective stress versus strain responses are similar. The results from the analysis conducted on the respective stress versus stress plots are similar for all groups. The continuous responses in Figures 3.18 and 3.19 are constructed as described in Section 3.2.3.1.

The results from the analysis conducted on five sets of unloading and two sets of reloading Ko test data and two sets of unloading and one set of reloading EXT Ko test data are shown in Figures 3.20-3.27. Each set of data is normalized to an arbitrary X-axis value. The PSD-axis

was incremented in the analysis of the Ko test data plotted as PSD versus MNS (Figure 3.20) to utilize more of the data. The unloading Ko data sets U3, U4, and U5 and reloading set R2 (Figures 3.20-3.23) consisted of four or less curves; therefore, the results of the analyses will be used as only a guide.

Constructed probabilistic load-unload and load-unload-reload responses are presented in Figures 3.28 and 3.29 for Ko tests. Load-unload-reload responses from the analysis of the "measured data" plots are not presented since they are generally not used in constitutive modeling. The method outlined in Section 3.2.3.1 was used to place the Ko unloading responses on the loading responses (Figure 3.28). For clarity, the mean and mean $\pm \hat{\sigma}$ responses for Ko unloading groups U2 and U4 are plotted as thick solid and dashed lines. Different axes were incremented for the loading and unloading test data plotted as PSD versus MNS. The method used to reconstruct the load-unload PSD versus MNS responses can place the mean $\pm \hat{\sigma}$ unloadings an unequal distance from the mean unloading. The unloading responses from group U4 begin at stress levels that are higher than the peak of the loading responses. Therefore, the starting locations for the unloadings are determined by extrapolating the loading responses to the required stress level. The starting values for the Ko reloadings (Figure 3.29) are the ending values for the appropriate unloadings.

Each EXT Ko test was a complete load-unload-reload test. Therefore, the beginning values for the probabilistic unloadings and reloadings were the mean and standard deviation values for the non-incremented axis at the beginning value of the incremented axis (Figure 3.30). For example, the mean and standard deviation values for axial strain at the beginning axial stress of unloading group U1 (17.3 MPa) are 9.01 and 2.79 percent, respectively. The mean axial stress versus axial strain response for group U1 begins at an axial strain of 9.01 percent, the mean $+\hat{\sigma}$ response begins at 6.22 percent, and the mean $-\hat{\sigma}$ response begins at 11.80 percent.

As stated earlier, when the Ko and EXT Ko test data are plotted as PSD versus MNS, more of the data is used if the MNS-axis is incremented. The effect of incrementing along the MNS-axis as opposed to the PSD-axis is illustrated in Figure 3.31 for groups 1-4 of the Ko

test results. It is clear from this figure that incrementing along the MNS-axis provides essentially the same results as incrementing along the PSD-axis.

3.2.3.3 HC test results. The results from static and dynamic hydrostatic compression (HC) tests will now be analyzed. The static tests have times to peak stress of several minutes and the dynamic tests have times to peak stress of approximately 100 milliseconds. Most of the data are from the HC phases of triaxial compression tests. For partially saturated specimens, the volumetric strain is calculated using the axial and radial strains. Several methods are available for calculating the volumetric strain based on an assumed shape of the specimen during the test (Reference 20). In general, the volumetric strains during a HC test are calculated assuming deformation as a right circular cylinder ($dV/V_0(\text{cyl})$).

For HC test data, the plot that is convenient for constitutive modeling is MNS versus $dV/V_0(\text{cyl})$ where MNS is equivalent to the confining pressure. The "measured data" are plotted as confining pressure versus axial strain and confining pressure versus radial strain. As discussed in Section 3.2.3.1, the stress-axis is incremented.

The loading portions of the static and dynamic test data are plotted as described above in Figures 3.32-3.35. The static test data are analyzed in four groups (Figures 3.32 and 3.33). The data in groups three and four are stiffer than the data in the lower stress levels. However, in the upper stress regions, there is little change in curvature. Continuous responses constructed from the results of the analyses of each group should not be significantly different from the results of an analysis in which all of the data extended to the stress level of group 4. The dynamic test data are analyzed in two groups. The results from the analysis conducted on the data in the second group will have no statistical significance since there are only two curves in the group.

The test data (thin solid line) and mean, $\text{mean} \pm \hat{\sigma}$, and $\text{mean} \pm 3\hat{\sigma}$ responses from the COV analysis (thick solid, thick dashed, and thin dashed lines, respectively) of the loading portions of the HC data are presented in Figures 3.36-3.41. All of the data are within $3\hat{\sigma}$ of the mean response. Like the UX tests, the axes form a boundary

for the test results. Since the mean $- 3\hat{\sigma}$ responses cross into the negative region at low stress levels, the data are not normally distributed at low stresses.

Composite plots of the mean and mean $\pm \hat{\sigma}$ responses from the analysis of the loading static HC test data are presented in Figures 3.42 and 3.43. The probabilistic response for group 1 is softer than those for the other groups, and the probabilistic response for group 2 is slightly softer than that for groups 3 and 4. The HC data plotted in Figures 3.32 and 3.33 also indicate this order of stiffness. The continuous responses in Figures 3.42, 3.43b, and 3.43d are constructed by the method outlined in Section 3.2.3.1. From visual inspection, the responses shown in Figures 3.40, 3.41, and 3.43 indicate that the material responds isotropically to HC loading.

The data and results from the analysis of two groups of unloading and reloading static HC test data and two groups of unloading dynamic HC test data are presented in Figures 3.44-3.48. The responses are normalized to arbitrary values of strain. There are more unloading responses in group U2 of the dynamic HC tests than there are in group 2 of the loading responses. Group U2 consists of all available dynamic HC unloadings. The groups of loading dynamic HC test data included only the tests with times to peak stress of approximately 100 msec. The loading portion of the faster dynamic HC tests were very erratic, but the unloadings were well behaved.

Constructed load-unload-reload responses are shown in Figures 3.49 and 3.50. The procedure described in Section 3.2.3.2 was used to determine where the unloadings and reloadings should be placed. Although there are only two curves in group 2 of the loading dynamic HC test data, the constructed response looks reasonable (Figure 3.50). Constructed load-unload-reload responses for the plots of "measured data" are not presented since they are not generally used in constitutive modeling.

3.2.3.4 TXC test results. The results from TXC tests are plotted as PSD versus axial strain and PSD versus principal strain difference for use in constitutive models. For subsequent use in the Rosenblueth technique, the "measured data" plots are L/Ao versus axial strain and L/Ao versus radial strain. When plotted as PSD versus axial strain and

PSD versus principal strain difference, the strain-axis is incremented to utilize more of the data. From Figure 3.51, incrementing the strain-axis as opposed to the PSD-axis has little effect on the results of the COV analysis. The L/Ao-axis is incremented in the analysis of the "measured data" plots.

The data and results from the COV analysis conducted on the loading portion of the static TXC test data plotted as described above are shown in Figures 3.52-3.69 for confining pressures ranging from zero to 80.0 MPa. The test data are normalized to zero strain prior to conducting the COV analysis. With the exception of the data for confining pressures of 17.5, 20.0, and 55.0 MPa (Figures 3.55, 3.56, 3.58, 3.64, 3.65, and 3.67), there is insufficient data to conduct meaningful statistical analyses. The radial strains are plotted as negative values in Figures 3.61-3.69 because radial deflection during the shear phase of a TXC test is generally expansive. The radial strain from some of the tests are positive during shear. This response is likely caused by wrinkles in the membrane surrounding the specimen, irregularities in the specimen surface, etc. Most of the test data are within the mean $\pm 3\hat{\sigma}$ responses. The data are not normally distributed at low values of strain since the mean - $3\hat{\sigma}$ responses in Figures 3.55-3.60 and 3.64-3.69 imply negative values. Some of the individual tests had "noisy" responses that do not significantly effect the calculation of the mean and mean $\pm \hat{\sigma}$ responses.

The data and results from COV analysis of the available unloading and reloading static TXC test data are presented in Figures 3.70-3.85 for the various confining pressures. For a given confining pressure, the responses are grouped based on the strain at which the unloadings begin. The stress-axis is incremented to utilize more of the unloading and reloading data. Much less variation occurs in the unloading and reloading data than in the loading data.

The constructed probabilistic load-unload-reload responses for PSD versus axial strain and PSD versus principal strain difference plots of the TXC test data are presented in Figures 3.86-3.93. The beginning strains for the unloading and reloading responses are the average values for the respective groups of data. The unloadings and reloadings do not extend to the loading responses since the unloading (or reloading) which

starts at the lowest value of PSD (highest for reloadings) governs the starting PSD for the group. The final unloading responses start at values of strain that are larger than the end of the loading response. The loading responses must stop at the smallest ending value of strain for a given group of loading test data. The load-unload-reload responses for the "measured data" plots are not constructed since they are not used in constitutive modeling.

Results from the COV analysis in which axial strain reached 15 percent or a "peak" strength was obtained do not necessarily provide mean and mean $\pm \hat{\sigma}$ values for strength at failure. For example, the results for a confining pressure of 0.35 MPa (Figure 3.53) imply mean and mean $\pm \hat{\sigma}$ values for "peak" strength of 1.44 MPa, 1.79 MPa, and 1.34 MPa, respectively. The implied mean $+\hat{\sigma}$ and mean $-\hat{\sigma}$ values are not an equal distance from the mean. A probabilistic "peak" strength envelope based on the test data will be provided in Chapter 4.

3.2.4 Rosenblueth Procedure

In this section, the Rosenblueth equations presented in Chapter 2 (equations 2.15 through 2.18) are used to convert the results from the COV analysis conducted on plots of "measured data" (Section 3.2.3) into forms that are conducive to constitutive modeling. The mean and variance of secant slopes are used in the conversion. Since slopes are calculated, the effect of correlation coefficients on the results from the Rosenblueth procedure must be evaluated. The calculation of the correlation coefficients is discussed in Section 3.2.4.2.

3.2.4.1 Equations for the function $y(x)$. The equations for converting the probabilistic responses from the COV analysis conducted on the K_o , EXT K_o , HC, and TXC "measured" test data are presented in Figures 3.94-3.97, respectively. For K_o tests, the target plots are PSD versus MNS (stress path) and axial stress versus axial strain (Figure 3.94). The stress path is developed by simply modifying the L/A_o versus radial stress results. The mean and variance of the inverse slope are calculated (MNS/PSD). The probabilistic response is calculated by multiplying the results of the Rosenblueth procedure by L/A_o since L/A_o is equal to PSD for a K_o test. The Rosenblueth

procedure requires two combinations since there is only one dependent variable (radial stress). The axial stress versus axial strain response requires the COV analysis results for data plotted as L/Ao versus axial strain and L/Ao versus radial stress. There are four combinations since there are two dependent variables. The mean and variance of the inverse slope are calculated (axial strain/axial stress). The probabilistic values for axial strain are calculated for values of axial stress. Axial stress is calculated using the given value for L/Ao and the mean value for radial stress. The reason for using the inverse slope is the same as that described in Section 3.2.3.2 for COV analysis on data plotted as axial stress versus axial strain, i.e., strain is the dependent variable, and stress is the independent variable.

The target plots for the EXT Ko tests are the same as those for the Ko tests, and the procedures are the same (Figure 3.95). The only difference is the substitution of $(UC-LC)*Ap/Ao$ for L/Ao and LC for radial stress.

The target plot for the HC tests is MNS versus $dV/Vo(cyl)$. The Rosenblueth equation is developed in Figure 3.96. Mean normal stress is equal to the confining pressure since it is an equal all-around stress. The inverse slope $(dV/Vo(cyl) / MNS)$ is calculated since stress is the independent variable and strain is the dependent variable. The mean and variance of $dV/Vo(cyl)$ is calculated by multiplying the mean and variance of the inverse slope by the current value of confining pressure (MNS). The Rosenblueth procedure requires four combinations since there are two dependent variables (axial strain and radial strain).

The target plots for the TXC tests are PSD versus axial strain and PSD versus principal strain difference. The Rosenblueth equations are developed in Figure 3.97. A problem with the TXC tests is that PSD is calculated as load divided by the current area, where the current area is the original area multiplied by the quantity one minus the true radial strain squared. The plots of L/Ao versus radial strain are normalized to zero; therefore, the true radial strain is not incorporated in the COV analysis. The results of the COV analysis on data plotted as L/Ao versus radial strain are shifted to account for the

normalization. The shift is determined by calculating the mean and standard deviation for radial strain at the start of shear for the tests at a given confining pressure. The mean result from the COV analysis is shifted by the mean radial strain at the start of shear. The mean + $\hat{\sigma}$ and mean - $\hat{\sigma}$ results are shifted by the mean + $\hat{\sigma}$ and mean - $\hat{\sigma}$ values for radial strain at the start of shear, respectively. The inverse slope is calculated (strain/PSD) since PSD is the independent variable and strain is the dependent variable. The mean and variance for strain are calculated by multiplying the mean and variance of the slope by the mean value of PSD for the current increment. The mean value of PSD is calculated using the current value of L/A_0 and the mean true radial strain. The Rosenblueth procedure requires four combinations since there are two dependent random variables (axial strain and radial strain).

3.2.4.2 Correlation coefficients. In this report, correlation coefficients (ρ) are estimated by a linear regression analysis conducted on the two random variables. The shortcoming of this approach is that large absolute values of ρ imply that the degree of correlation between the two random variables is high, whereas small absolute values imply only the weakness of a linear trend and not necessarily a weakness in correlation. Positive values of ρ tend to imply that large values of one variable coincide with large values of the other variable and visa versa. Negative values of ρ tend to imply that large values of one variable coincide with small values of the other variable and visa versa.

From equations 2.13 and 2.15, values of ρ approaching 1 will increase the significance of the ++ and -- calculations, and values of ρ approaching -1 will increase the significance of the +- and -+ calculations. Equal weight is given to all parts of the Rosenblueth calculation when ρ is equal to zero. Depending on the function $y(x)$ and the values of the correlation coefficients, the effect of including ρ in the calculations can be significant. The effect of ρ on the mean response varies depending on the relative magnitudes of the ++, +-, -+, and -- values. The effect of ρ on the variance is predetermined by the sign of ρ and the rank of the various combinations. If the ++ and -- combinations provide the extremes, the variance will increase for

positive values of ρ and decrease for negative values of ρ . If the +- and -+ combinations provide the extremes, then the variance will decrease for positive values of ρ and increase for negative values of ρ .

Given n pairs of values, the correlation coefficient is estimated by the sample correlation coefficient r

$$r = \frac{S_{xy}}{\sqrt{S_{xx} S_{yy}}} \quad (3.10)$$

where,

$$S_{xx} = n \sum_{i=1}^n x_i^2 - \left(\sum_{i=1}^n x_i \right)^2 \quad (3.11)$$

$$S_{yy} = n \sum_{i=1}^n y_i^2 - \left(\sum_{i=1}^n y_i \right)^2 \quad (3.12)$$

$$S_{xy} = n \sum_{i=1}^n x_i y_i - \left(\sum_{i=1}^n x_i \right) \left(\sum_{i=1}^n y_i \right) \quad (3.13)$$

Correlation coefficients for the loading portion of each test type are plotted versus the incremented axis in Figures 3.98-3.103. For Ko tests (Figure 3.98), the correlation coefficients for groups 1 and 2 are between 0.5 and 1.0 to a L/Ao of 3.4 MPa; the correlation coefficients are approximately 0.75 above a L/Ao of 3.4 MPa. For groups 3 and 4 of the Ko test data, the values for ρ are initially between 0.7 and 1.0. The values of ρ decrease rapidly to 0 at an axial stress of 14 MPa. Above 14 MPa, the values for group 3 fluctuate about 0 while the values for group 4 continue to decrease to a low of -0.4 at 66 MPa. The correlation coefficients for EXT Ko tests (Figure 3.99) gradually decrease from 0.95 to 0.4 as (UC-LC)*Ap/Ao increases.

The correlation coefficients for groups 1 and 2 of the static HC test data (Figure 3.100a) decrease rapidly as confining pressure increases to 1 MPa. Above a confining pressure of 1.5 MPa, the correlation coefficients for group 1 are approximately 0.35; for group 2, the correlation coefficients are approximately 0 above 6 MPa.

The correlation coefficients for groups 3 and 4 (Figure 3.100b) change rapidly below a confining pressure of 4 MPa. For group 3, the values then decrease slowly from -0.17 to -0.45 at 32 MPa; for group 4, the correlation coefficients are approximately 0.65 above 4 MPa. The plots of confining pressure versus ρ for groups 1 and 2 of the dynamic HC tests are in Figure 3.101. The correlation coefficients for group 2 are a constant -1 since there are only two tests. For group 1, the value of ρ is approximately 0 initially; it then decreases to -0.42 as confining pressure increases to 4 MPa. Above 4 MPa the values of ρ for group 1 increase to 0.55 at 22 MPa.

Most of the correlation coefficients for the TXC tests decrease as L/A_o increases (Figures 3.102 and 3.103). At low values of L/A_o , the TXC tests at confining pressures less than 10 MPa (Figure 3.102) have correlation coefficients that alternate from large positive to large negative values. The values for ρ ultimately approach -1. Since there are only two tests for a confining pressure of 0.7 MPa, the values of ρ are either 1 or -1. The correlation coefficients for TXC tests at confining pressures greater than 10 MPa (Figure 3.103) are not as erratic at low stresses as the correlation coefficients in Figure 3.102. Except for the values of ρ for a confining pressure of 80 MPa (Figure 3.103d), the correlation coefficients in Figure 3.103 gradually decrease as L/A_o increases; the values approach -1 near peak L/A_o .

3.2.4.3 Results. The probabilistic plots obtained by applying the Rosenblueth procedure to the results from the COV analysis of the "measured data" are shown in Figures 3.104-3.120. For the K_o , EXT K_o , and HC tests (Figures 3.104-3.108), the thick lines are the results that include correlation coefficients. Correlation coefficients are not needed to calculate the stress path (Figures 3.105 and 3.106b) since there is only one variable. The inclusion of ρ had a greater effect on the variance than the mean response.

The load-unload-reload responses calculated by applying the Rosenblueth procedure, including ρ , to the "measured data" from TXC tests are shown in Figures 3.109-3.117 for the various confining pressures. The unloadings and reloadings are shifted to the corresponding mean values of axial strain and principal strain difference determined as

described in Section 3.2.3.4. As illustrated in Figures 3.118-3.120, the inclusion of ρ only affected the variance.

The probabilistic responses from applying the Rosentblueth procedure to the constructed continuous plots of "measured data" from Ko and HC tests are shown in Figures 3.121-3.123. The value of ρ for a given increment is determined by which group that section comes from. For example, if a section of the combined response comes from group 3, then the correlation coefficients for that section of the calculated response also come from group 3. Where relatively severe shifts in ρ occur at section interfaces, the inclusion of ρ results in very "jagged" responses; whereas, the omission of ρ results in smooth responses. The omission of ρ seems to provide an "average" response.

The probabilistic load-unload and load-unload-reload responses for Ko, EXT Ko, and HC tests are shown in Figures 3.124-3.128. For the Ko and HC tests, correlation coefficients are included in the calculation of the unloading and reloading responses, but are not included in the calculation of the loading responses. The starting values of axial stress for the Ko unloading and reloading responses are calculated as L/A_o at the start of the unloading or reloading plus the mean radial stress for all of the unloading or reloading curves in a given group. The starting value of axial strain for an unloading response is the value on the loading response at the calculated value of axial stress. The starting value of MNS for the unloading stress path is the intersection of the loading response and the starting L/A_o (PSD) value for the group of unloading data. For both plot types, a given reloading response begins at the end of the associated unloading response.

The starting value of axial stress for an EXT Ko unload or reload response is calculated as the value of $(UC-LC)*A_p/A_o$ plus the mean LC stress at the beginning of a given group of responses. The starting values of axial strain are the mean and mean $\pm \hat{\sigma}$ values calculated at the starting value of $(UC-LC)*A_p/A_o$ for the unnormalized unloading or reloading group. The mean and mean $\pm \hat{\sigma}$ values for MNS at the beginning of unload or reload PSD versus MNS responses are calculated as the starting value of $(UC-LC)*A_p/A_o$ divided by 3 plus the mean and mean $\pm \hat{\sigma}$ LC stress values for the appropriate set of responses.

The starting points for the HC unloading responses are the MNS at the start of the unloading set and the strain at which that value of MNS intersects the the loading responses; the reloadings begin at the end of their associated unloading response. For all test types, the stiff unloading and reloading responses are placed with the stiff loading response, and the soft unloading and reloading responses are placed with the soft loading response.

3.2.5 Comparison of the Results from the Two Analysis Techniques

The results from the COV analysis of the loading mechanical property test data plotted in forms conducive to constitutive modeling (COV technique) and the results from applying the Rosenblueth procedure to the results from the COV analysis of "measured data" (COV/Rosenblueth technique) are compared in Figures 3.129-3.141. The thick lines are the results from the COV technique, and the thin lines are the results from the COV/Rosenblueth technique. Correlation coefficients are not included in the Rosenblueth calculations.

Both techniques provide similar mean responses when applied to K_o , EXT K_o , static HC, and dynamic HC test data (Figures 3.129-3.132, respectively). The variance from the COV technique is (a) slightly less than the variance from the COV/Rosenblueth technique for K_o test data, (b) very similar to the variance from the COV/Rosenblueth technique for EXT K_o test data, (c) slightly larger than the variance from the COV/Rosenblueth technique for static HC test data, and (d) for dynamic HC test data below a MNS of about 18 MPa, smaller than the variance from the COV/Rosenblueth technique and, above 18 MPa, larger than the variance from the COV/Rosenblueth technique.

For TXC tests at confining pressures less than 10 MPa (Figures 3.133-3.135), the responses from the COV/Rosenblueth technique have softer mean responses and greater variances than those from the COV technique. For confining pressures greater than 10 MPa (Figures 3.136-3.141), the mean and mean $\pm \hat{\sigma}$ responses from both techniques are very similar. The greatest difference occurs near the PSD level where the curves begin to break over. From Section 3.2.3.4, the loading TXC test data exhibit one or more of the following phenomena: (a) the strengths continue to increase during the test such that the shear

responses are concave to the MNS axis, (b) the strength for a given test begins to decrease after achieving a peak PSD, or (c) at some level of PSD, the strength remains nearly constant with increasing strain. Since the stress axis is incremented in the COV/Rosenblueth technique, these phenomena are not incorporated into the probabilistic responses.

The unloading and reloading responses from the two techniques are very similar.

Table 3.1. First attempt at the dry density-based profile for Area A.

Layer No.	Depth ft	Mean Dry Density pcf	Dry Density Standard Deviation pcf	Number of Dry Density Points	F	F _{0.05}
1	0	114.85	5.17	260		
2	21	115.00	4.78	123	0.07	-3.84
3	39	111.09	5.00	23	12.78	-3.92
4	59	108.26	5.88	12	2.24	4.13

Table 3.2. Second attempt at the dry density-based profile for Area A.

Layer No.	Depth ft	Mean Dry Density pcf	Dry Density Standard Deviation pcf	Number of Dry Density Points	F	F _{0.05}
1	0	114.72	5.30	207		
2	17	114.71	4.90	193	0.07	-3.84
3	49	109.60	5.80	18	17.34	-3.92

Table 3.3. Third attempt at the dry density-based profile for Area A.

Layer No.	Depth ft	Mean Dry Density pcf	Dry Density Standard Deviation pcf	Number of Dry Density Points	F	F _{0.05}
	0					
1	49	114.72	5.11	400	17.09	-3.92
2		109.60	5.80	18		

Table 3.4. Dry density-based profile for Area B.

Layer No.	Depth ft	Mean Dry Density pcf	Dry Density Standard Deviation pcf	Number of Dry Density Points	F	F _{0.05}
	0					
1	12	117.72	4.79	78	30.39	-3.92
2	32	113.82	5.45	192	11.38	-3.92
3	67	115.86	4.72	119	28.59	-3.92
4		111.60	4.63	49		

Table 3.5. Summary of probabilistic mass-volume properties for Area A.

Layer No.	Depth ft	Water Content %		Dry Density pcf		Wet Density pcf		Degree of Saturation %		Air Voids Content %	
		$E(w)$	$\hat{\sigma}(w)$	$E(\gamma_d)$	$\hat{\sigma}(\gamma_d)$	$E(\gamma)$	$\hat{\sigma}(\gamma)$	$E(S)$	$\hat{\sigma}(S)$	$E(V_a)$	$\hat{\sigma}(V_a)$
1	0	3.8	1.6	114.7	5.1	119.1	5.6	22.6	9.9	24.4	4.4
2	49	3.8	1.6	109.6	5.8	113.8	6.2	19.7	8.7	27.8	4.7

Table 3.6. Summary of probabilistic mass-volume properties for Area B.

Layer No.	Depth ft	Water Content %		Dry Density pcf		Wet Density pcf		Degree of Saturation %		Air Voids Content %	
		$E(w)$	$\hat{\sigma}(w)$	$E(\gamma_d)$	$\hat{\sigma}(\gamma_d)$	$E(\gamma)$	$\hat{\sigma}(\gamma)$	$E(S)$	$\hat{\sigma}(S)$	$E(V_a)$	$\hat{\sigma}(V_a)$
1	0	3.3	1.3	117.7	4.8	121.6	5.2	21.5	9.0	23.3	4.0
2	12	3.3	1.3	113.8	5.4	117.6	5.8	19.3	8.1	25.9	4.3
3	32	3.3	1.3	115.9	4.7	119.7	5.1	20.4	8.5	24.5	3.9
4	67	3.3	1.3	111.6	4.6	115.3	4.9	18.1	7.5	27.3	3.8

Table 3.7. Summary of the results from dynamic uniaxial strain tests used in the analysis of mechanical properties for layer 1 of Area A.

Depth ft.	Depth m	Posttest Water Content %	Wet Density g/cc	Dry Density g/cc	Degree of Saturation %	Air Voids Content %	Static Prestress MPa	Peak Live Stress MPa	Axial Strain At Peak Axial Stress %
Area A									
6.02	1.84	5.46	1.982	1.879	34.3	19.6	*	69.0	19.1
6.70	2.04	5.87	1.996	1.885	37.3	18.6	*	98.3	10.8
13.40	4.09	5.76	1.987	1.879	36.2	19.1	*	40.1	17.5
14.50	4.42	5.52	1.940	1.839	32.3	21.3	*	27.3	17.3
15.72	4.79	4.22	1.980	1.900	27.5	21.1	*	30.9	12.3
25.39	7.74	4.56	1.876	1.794	24.8	24.9	*	29.8	14.4
25.80	7.37	4.83	1.946	1.856	29.2	21.8	*	44.1	15.1
26.00	7.93	4.82	1.913	1.825	27.6	23.1	*	97.7	19.9
26.90	8.20	7.25	1.848	1.723	35.0	23.2	*	38.5	17.6
27.20	8.29	7.54	1.943	1.807	41.8	19.0	*	16.2	9.7
40.35	12.30	4.92	1.858	1.771	25.7	25.2	*	94.6	21.3
40.50	12.35	6.40	1.899	1.783	34.5	21.9	*	88.7	14.8
41.90	12.77	4.76	1.839	1.755	24.2	26.1	*	98.8	22.6
47.22	14.40	3.83	1.900	1.830	22.1	24.7	*	76.0	17.6
Area B									
8.85	2.70	2.74	1.805	1.757	14.0	29.6	0.2	30.1	9.7
9.79	2.98	2.61	1.887	1.839	15.3	26.6	0.1	32.9	8.4
19.28	5.88	4.67	1.877	1.793	25.3	24.7	0.2	34.8	12.8
29.34	8.95	4.47	1.942	1.764	23.1	26.3	*	35.1	13.0
29.61	9.03	4.79	1.928	1.840	28.1	22.5	0.2	34.8	14.8
29.75	9.07	3.27	1.906	1.846	19.4	25.1	0.2	34.6	12.3
41.05	12.52	4.65	1.877	1.794	25.2	24.7	0.3	34.0	10.5

* Data not available.

Table 3.8. Summary of the results from static uniaxial strain tests with lateral stress measurements, or Ko tests, used in the analysis of mechanical properties for layer 1 of Area A.

Depth	Posttest		Wet Density g/cc	Dry Density g/cc	Degree of Saturation %	Air Voids Content %	Peak Axial Stress MPa	Axial Strain At Peak Axial Stress %	Principal Stress Difference		Mean Normal Stress At Peak Axial Stress MPa
	ft	m							Water Content %	At Peak Axial Stress MPa	
Area A											
8.60	2.62	4.55	1.969	1.883	28.8	21.2	138.9	21.0	66.4	94.9	
11.40	3.48	4.43	2.025	1.939	31.1	19.1	189.2	18.9	97.3	124.4	
11.70	3.57	3.83	1.936	1.865	23.5	23.3	91.2	16.8	41.6	63.0	
13.90	4.24	3.17	1.970	1.909	21.1	22.7	10.2	5.5	4.9	6.9	
15.00	4.57	8.63	1.670	1.537	31.1	29.4	19.4	18.5	9.0	13.4	
15.00	4.57	7.13	1.711	1.597	28.2	29.0	41.0	22.3	14.6	31.3	
15.30	4.66	3.80	1.880	1.811	21.2	25.5	21.5	12.3	11.2	14.3	
16.25	4.95	2.90	1.837	1.785	15.5	28.2	19.5	16.7	9.1	13.6	
16.30	4.97	3.83	1.939	1.867	23.6	23.2	21.1	10.0	10.7	14.3	
17.50	5.34	3.72	1.872	1.805	20.6	25.9	19.0	10.3	8.6	13.3	
18.10	5.52	3.73	1.934	1.864	22.9	23.5	20.8	13.0	10.5	13.8	
18.70	5.70	5.30	1.957	1.858	32.1	20.8	12.2	9.7	7.0	7.6	
25.09	7.65	5.59	1.790	1.695	25.8	27.3	34.5	20.3	14.9	24.6	
26.40	8.05	5.94	1.822	1.720	28.5	25.6	30.9	20.0	12.8	22.5	
30.30	9.24	5.75	1.896	1.793	31.1	22.8	10.2	13.6	4.9	6.9	
31.27	9.53	4.50	1.983	1.898	29.3	20.7	28.0	13.2	14.7	18.3	
32.60	9.94	6.11	1.949	1.837	35.7	20.2	10.9	12.3	5.5	7.2	
33.00	10.06	5.72	2.061	1.949	40.9	16.1	30.6	13.2	14.9	20.8	
35.10	10.70	3.23	1.903	1.843	19.1	25.3	10.5	10.2	5.2	7.3	
35.50	10.82	3.82	1.901	1.831	22.1	24.7	32.0	15.2	15.2	21.8	
40.50	12.35	4.46	1.873	1.793	24.2	25.1	168.9	17.4	68.6	123.2	
40.90	12.47	4.47	1.901	1.820	25.3	24.0	184.5	19.4	84.1	128.0	
41.60	12.68	4.63	1.854	1.772	24.2	25.7	130.4	20.9	39.5	104.0	
Area B											
17.80	5.43	3.80	1.851	1.783	20.3	26.7	350.0	25.3	184.0	227.0	
41.81	12.75	3.90	1.924	1.852	23.4	23.7	352.0	24.5	178.0	234.0	

Table 3.9. Summary of the results from static uniaxial strain tests with lateral stress measurements, or EXT Ko tests, used in the analysis of mechanical properties for layer 1 of Area A.

Depth	ft	m	Posttest Water Content %	Wet Density g/cc	Dry Density g/cc	Degree of Saturation %	Air Voids Content %	Peak Axial Stress MPa	Axial Strain At Peak Axial Stress %	Principal Stress		Mean Normal Stress at Peak Axial Stress MPa
										Difference At Peak Axial Stress MPa	Axial Stress MPa	
Area A												
6.30	1.92		2.84	1.920	1.867	17.5	25.0	36.2	9.7	18.1		24.2
8.80	2.68		2.00	1.877	1.840	11.7	27.7	36.2	10.6	18.0		24.3
10.10	3.08		3.14	1.618	1.569	11.9	36.5	35.4	17.6	16.7		24.3
10.20	3.11		2.81	1.608	1.564	10.6	37.2	36.8	17.7	17.0		25.6
10.20	3.11		2.29	1.719	1.681	10.3	33.4	39.1	15.8	18.1		27.0
10.48	3.20		2.44	1.841	1.797	13.3	28.6	37.0	14.7	19.9		23.8
10.50	3.20		2.60	1.802	1.756	13.2	29.9	37.2	12.1	18.5		24.9
18.75	5.72		2.55	1.903	1.856	15.4	26.0	36.3	9.2	17.2		25.0
18.80	5.73		3.58	1.938	1.871	22.2	23.5	36.6	9.8	17.9		24.7
18.80	5.73		3.22	1.849	1.791	17.4	27.4	36.4	12.1	16.9		25.3
18.98	5.79		3.23	1.913	1.853	19.4	24.9	37.3	10.8	18.8		24.8
19.14	5.84		2.69	1.920	1.870	16.6	25.2	36.9	10.5	18.9		24.4
19.15	5.84		4.57	1.817	1.738	22.6	27.2	36.8	14.3	18.3		24.6
21.44	6.54		2.47	1.998	1.950	17.7	22.4	37.9	9.0	20.1		24.6
Area B												
18.15	5.53		2.87	1.968	1.913	19.2	23.1	70.5	16.4	36.4		46.1

Table 3.10. Summary of the results from static hydrostatic compression tests used in the analysis of mechanical properties for layer 1 of Area A.

Depth		Posttest Water Content	Wet Density	Dry Density	Degree of Saturation	Air Voids Content	Confining Pressure
ft	m	%	g/cc	g/cc	%	%	MPa
Area A							
4.12	1.26	7.62	1.977	1.837	44.5	17.5	17.40
5.40	1.65	3.77	1.840	1.773	19.8	27.2	58.00
5.50	1.68	4.24	1.770	1.698	19.6	29.4	20.60
6.74	2.05	8.11	1.868	1.728	39.4	21.5	17.40
8.70	2.65	4.31	1.934	1.854	25.9	22.8	17.40
8.90	2.71	4.70	1.936	1.849	28.0	22.3	17.40
9.00	2.74	4.09	1.891	1.817	23.1	24.8	80.00
9.20	2.80	5.79	2.041	1.929	39.9	16.8	16.90
10.30	3.14	2.83	1.890	1.838	16.6	26.2	83.00
10.50	3.20	3.62	1.994	1.924	24.7	21.2	55.00
11.30	3.45	3.82	1.971	1.898	24.9	21.9	17.70
11.40	3.48	4.57	1.937	1.852	27.4	22.4	16.40
13.80	4.21	4.69	1.965	1.877	29.4	21.2	62.10
14.03	4.28	7.01	1.716	1.604	28.0	28.9	17.30
14.24	4.34	3.36	1.890	1.829	19.3	25.6	17.20
14.30	4.36	5.73	2.067	1.955	41.4	15.9	17.50
15.30	4.66	3.44	1.871	1.809	19.1	26.3	100.20
15.90	4.85	4.49	2.050	1.962	32.9	18.0	56.50
16.80	5.12	3.97	1.937	1.863	24.3	23.1	17.90
17.90	5.46	4.30	1.951	1.871	26.6	22.2	17.50
18.80	5.73	3.48	1.927	1.862	21.2	24.0	60.50
18.90	5.76	3.81	1.903	1.833	22.1	24.6	22.10
19.20	5.85	4.77	1.816	1.733	23.4	27.1	17.70
20.20	6.16	3.88	2.026	1.950	27.8	19.7	56.50
20.25	6.17	5.90	1.958	1.849	35.2	20.1	21.60
21.30	6.49	5.06	1.954	1.860	30.8	21.2	17.90
26.80	8.17	3.98	1.937	1.863	24.3	23.1	84.90
31.00	9.45	4.16	1.882	1.807	23.1	25.1	21.00
32.20	9.82	4.61	2.043	1.953	33.2	18.1	105.10
35.40	10.79	4.33	1.909	1.830	25.0	23.8	24.20
Area B							
10.00	3.05	4.80	1.977	1.886	30.6	20.6	173.00
26.35	8.03	3.55	1.909	1.844	21.0	24.7	20.80

Table 3.11. Summary of the results from dynamic hydrostatic compression tests used in the analysis of mechanical properties for layer 1 of Area A.

Depth	Posttest		Wet Density g/cc	Dry Density g/cc	Degree of Saturation %	Air Voids Content %	Confining Pressure MPa
	ft	m					
Area A							
12.68	3.87	4.09	1.850	1.777	21.6	26.4	50.10
13.93	4.25	0.34	1.903	1.897	2.2	28.6	23.80
15.46	4.71	0.81	1.971	1.955	5.9	25.5	24.30
25.09	7.65	5.23	1.911	1.876	29.5	22.7	46.50
26.30	8.02	2.88	1.980	1.925	19.7	22.6	40.00
40.56	12.37	1.22	1.961	1.937	8.5	25.3	25.20
40.95	12.48	4.35	1.910	1.830	25.1	23.7	24.50
41.06	12.52	1.01	1.842	1.824	5.8	30.1	25.00
41.24	12.57	0.68	1.999	1.985	5.2	24.6	52.40
45.30	13.81	3.16	1.824	1.768	16.4	28.4	34.20
46.46	14.16	2.96	1.869	1.815	16.7	26.9	23.10
Area B							
18.06	5.51	3.66	1.923	1.855	22.1	24.0	40.00

Table 3.12. Summary of the results from static triaxial compression tests used in the analysis of mechanical properties for layer 1 of Area A.

Depth		Mass-Volume Data					Confining Pressure MPa	"Peak" Strength		
		Posttest	Wet Density g/cc	Dry Density g/cc	Degree of Saturation %	Air Voids Content %		Principal Stress Difference MPa	Mean Normal Stress MPa	Axial Strain %
		Water Content %								
ft	m	%								
Area A										
10.90	3.32	3.65	1.973	1.904	24.0	22.0	0.7	2.4	1.5	5.3
10.10	3.08	2.52	1.873	1.827	14.5	27.2	0.7	2.2	1.4	10.9
45.40	13.84	4.66	1.947	1.860	28.3	21.9	1.7	5.1	3.5	7.7
45.85	13.98	2.82	1.927	1.874	17.6	24.8	1.7	5.1	3.4	15.0
55.05	16.78	9.77	1.922	1.751	49.3	17.6	1.7	3.3	2.8	15.0
130.60	39.82	4.66	1.807	1.727	22.6	27.5	1.7	4.4	3.2	15.0
14.10	4.30	3.11	2.108	2.044	26.8	17.4	3.4	8.8	6.3	9.4
12.80	3.90	3.80	1.946	1.875	23.7	22.9	3.4	9.3	6.6	12.3
41.40	12.62	5.21	1.870	1.777	27.5	24.4	3.6	8.1	6.4	15.0
11.40	3.48	4.57	1.937	1.852	27.4	22.4	16.4	41.1	30.5	14.9
9.20	2.80	5.79	2.041	1.929	39.9	10.8	16.9	36.2	28.9	13.4
14.24	4.34	3.36	1.890	1.829	19.3	25.6	17.2	41.4	31.2	15.0
14.03	4.28	7.01	1.716	1.604	28.0	28.9	17.3	37.4	29.9	15.0
8.70	2.65	4.31	1.934	1.854	25.9	22.8	17.4	40.7	30.6	15.0
14.30	4.36	5.73	2.067	1.955	41.4	15.9	17.5	38.1	30.2	13.4
17.90	5.46	4.30	1.951	1.871	26.6	22.2	17.5	43.0	31.3	14.1
11.30	3.45	3.82	1.971	1.898	24.9	21.9	17.7	41.8	31.3	15.0
19.20	5.85	4.77	1.816	1.733	23.4	27.1	17.7	38.8	30.0	15.0
16.80	5.12	3.97	1.937	1.863	24.3	23.1	17.9	43.3	32.0	15.0
21.30	6.49	5.06	1.954	1.860	30.8	21.2	17.9	37.1	29.2	15.0
5.50	1.68	4.24	1.770	1.698	19.6	29.4	20.6	44.3	35.6	15.0
100.40	30.61	3.58	1.811	1.748	18.0	28.5	20.8	43.8	35.5	14.0
100.30	30.58	3.38	1.882	1.820	19.2	25.9	20.9	45.1	35.8	15.0
31.00	9.45	4.16	1.882	1.807	23.1	25.1	21.0	46.0	36.0	15.0
140.40	42.80	4.49	2.029	1.942	31.7	18.8	21.6	---	---	---
20.25	6.17	5.90	1.958	1.849	35.2	20.1	21.6	42.8	36.5	15.0
18.90	5.76	3.81	1.903	1.833	22.1	24.6	22.1	51.2	39.5	15.0
35.40	10.79	4.33	1.909	1.830	25.0	23.8	24.2	---	---	---
110.30	33.63	5.34	1.757	1.668	23.6	28.9	27.2	47.4	46.2	15.0
15.50	4.73	6.13	1.604	1.511	21.2	34.3	40.0	---	---	---
50.50	15.40	5.64	1.874	1.774	29.6	23.8	42.3	69.0	69.7	15.0
60.40	18.41	4.22	1.656	1.589	16.5	34.0	46.6	87.5	76.0	13.3
66.60	20.30	3.48	1.893	1.829	20.1	25.4	51.9	120.6	96.0	15.0
10.50	3.20	3.62	1.994	1.924	24.7	21.2	55.0	114.8	93.8	14.0
140.35	42.79	4.57	1.751	1.674	20.4	29.9	55.4	97.9	88.4	14.0
60.45	18.43	3.36	1.726	1.670	14.9	32.1	55.6	107.5	91.6	15.0
140.20	42.74	3.97	1.804	1.735	19.5	28.4	56.0	107.1	91.8	15.0
140.35	42.79	5.70	1.724	1.631	23.8	29.8	56.0	89.2	85.7	15.0
5.20	1.59	4.65	1.835	1.753	23.6	26.4	56.2	111.8	96.3	15.0
20.20	6.16	3.88	2.026	1.950	27.8	19.7	56.5	---	---	---
15.90	4.85	4.49	2.050	1.962	32.9	18.0	56.5	94.2	88.0	14.2
82.20	25.06	3.98	1.788	1.720	19.1	29.0	57.2	101.2	90.5	15.0
5.40	1.65	3.77	1.840	1.773	19.8	27.2	58.0	124.4	108.4	15.0
18.80	5.73	3.48	1.927	1.862	21.2	24.0	60.5	---	---	---
13.60	4.21	4.69	1.965	1.877	29.4	21.2	62.1	---	---	---
9.00	2.74	4.09	1.891	1.817	23.1	24.8	80.0	---	---	---
50.30	15.34	3.84	1.975	1.902	25.2	21.7	81.5	180.6	147.8	15.0
10.30	3.14	2.83	1.890	1.838	16.6	26.2	83.0	178.7	145.0	15.0
26.80	8.17	3.98	1.937	1.863	24.3	23.1	84.9	163.2	144.0	15.0
Area B										
3.37	1.03	5.98	2.028	1.914	40.0	17.2	0.00	0.12	0.04	2.0
13.60	4.15	7.14	1.928	1.800	39.1	20.0	0.00	0.22	0.07	2.9
35.95	10.96	4.35	1.937	1.856	26.3	22.7	0.00	0.16	0.05	1.5
5.65	1.72	4.87	1.770	1.879	20.6	20.8	0.10	0.76	0.36	2.5
5.75	1.75	5.20	1.975	1.877	32.6	20.2	0.10	0.69	0.33	3.5
36.13	11.02	4.86	2.083	1.986	37.3	15.2	0.10	0.76	0.36	2.0
3.87	1.18	4.64	1.993	1.905	30.5	20.1	0.21	0.85	0.49	5.0
15.25	4.65	4.92	1.964	1.872	30.5	20.9	0.21	0.90	0.51	5.6
36.12	11.01	4.43	2.071	1.983	33.8	17.2	0.35	1.38	0.66	2.2
35.63	10.86	5.94	2.003	1.891	36.1	18.2	0.35	1.87	0.97	2.3
6.25	1.91	4.08	1.940	1.864	25.0	22.8	0.35	1.49	0.84	3.4
5.15	1.57	3.63	1.905	1.838	21.2	24.7	0.35	1.35	0.80	8.1
26.35	8.03	3.55	1.909	1.844	21.0	24.7	20.8	47.4	37.0	15.0

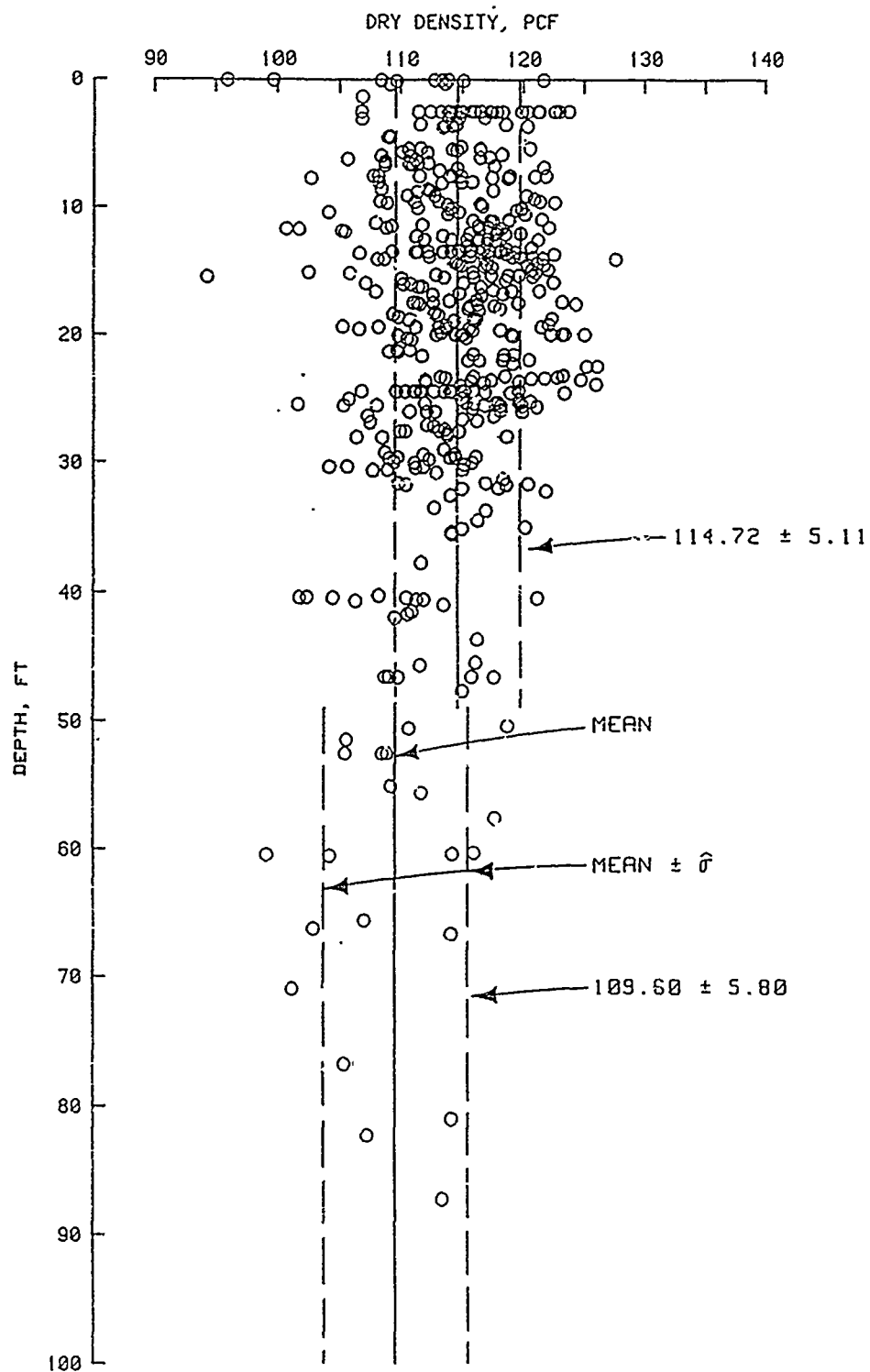


Figure 3.1. Summary of dry density data from Area A.

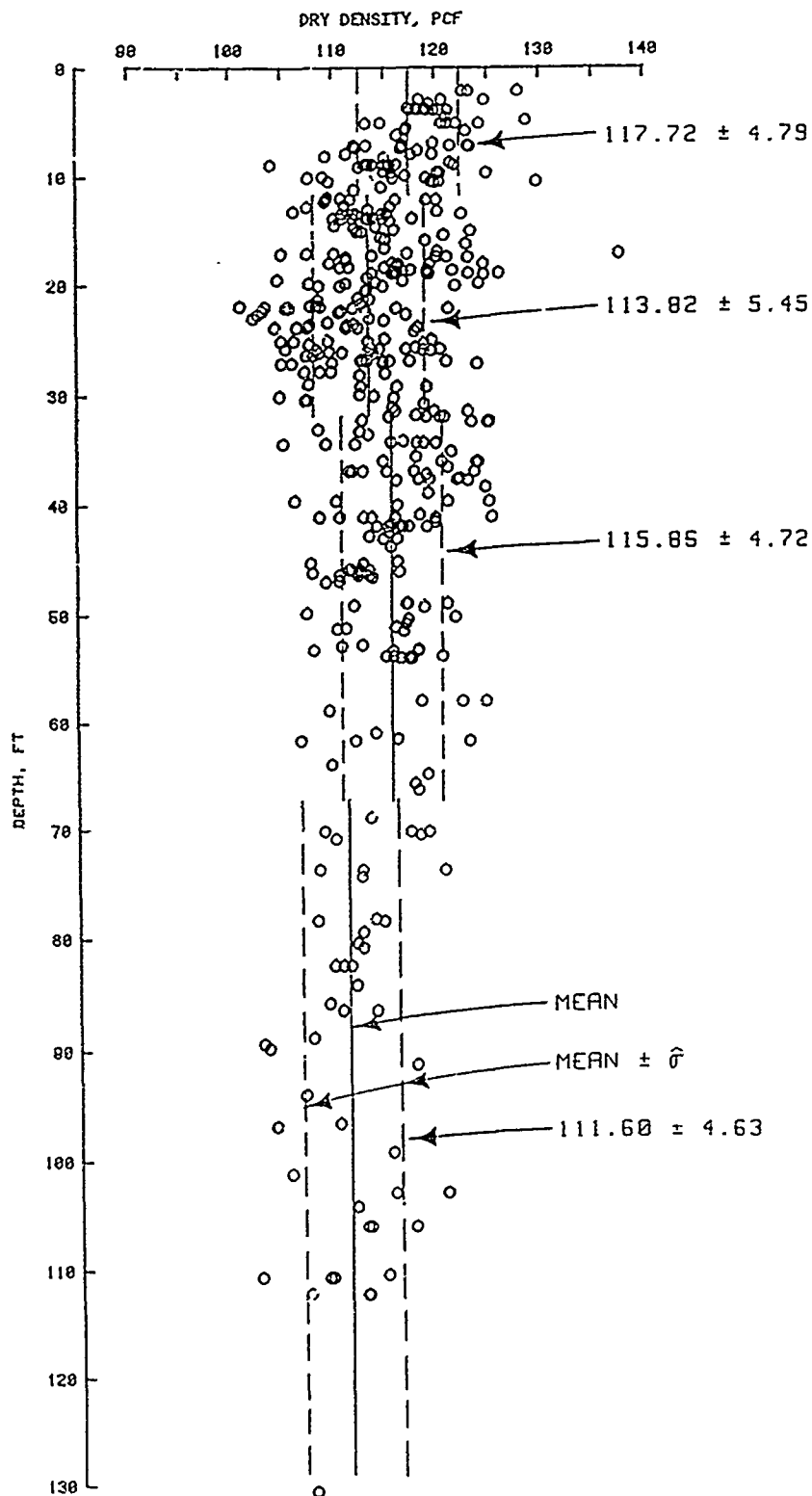


Figure 3.2. Summary of dry density data from Area B.

$$E(\gamma_d) = 114.72 \text{ pcf} , \quad \hat{\sigma}(\gamma_d) = 5.11 \text{ pcf}$$

$$E(w) = 3.81\% , \quad \hat{\sigma}(w) = 1.56\%$$

$$E(G_s) = 2.68 , \quad \hat{\sigma}(G_s) = 0.01$$

$$\gamma = \gamma_d(1 + w) , \quad V_a = 1 - \frac{\gamma_d}{\gamma_w} \left(\frac{1}{G_s} + w \right) , \quad S = \frac{w\gamma_d G_s}{\gamma_w G_s - \gamma_d}$$

$$E[\gamma] = \frac{1}{4} [\gamma^{++} + \gamma^{+-} + \gamma^{-+} + \gamma^{--}]$$

$$V[\gamma] = \frac{1}{4} [(\gamma^{++})^2 + (\gamma^{+-})^2 + (\gamma^{-+})^2 + (\gamma^{--})^2] - (E[\gamma])^2$$

$$E[V_a] = \frac{1}{8} [V_a^{+++} + V_a^{++-} + V_a^{+-+} + V_a^{+--} + V_a^{---} + V_a^{--+} - V_a^{-+-} + V_a^{-++}]$$

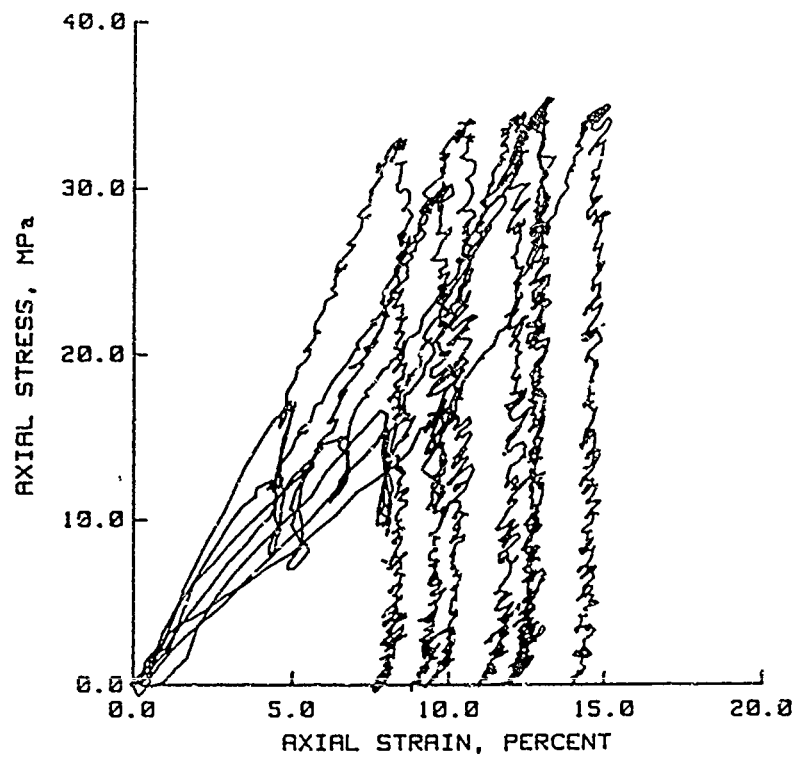
$$V[V_a] = \frac{1}{8} [(V_a^{+++})^2 + (V_a^{++-})^2 + (V_a^{+-+})^2 + (V_a^{+--})^2 + (V_a^{---})^2 + (V_a^{--+})^2 + (V_a^{-+-})^2 + (V_a^{-++})^2] - (E[V_a])^2$$

$$E[S] = \frac{1}{8} [S^{+++} + S^{++-} + S^{+-+} + S^{+--} + S^{---} + S^{--+} + S^{-+-} + S^{-++}]$$

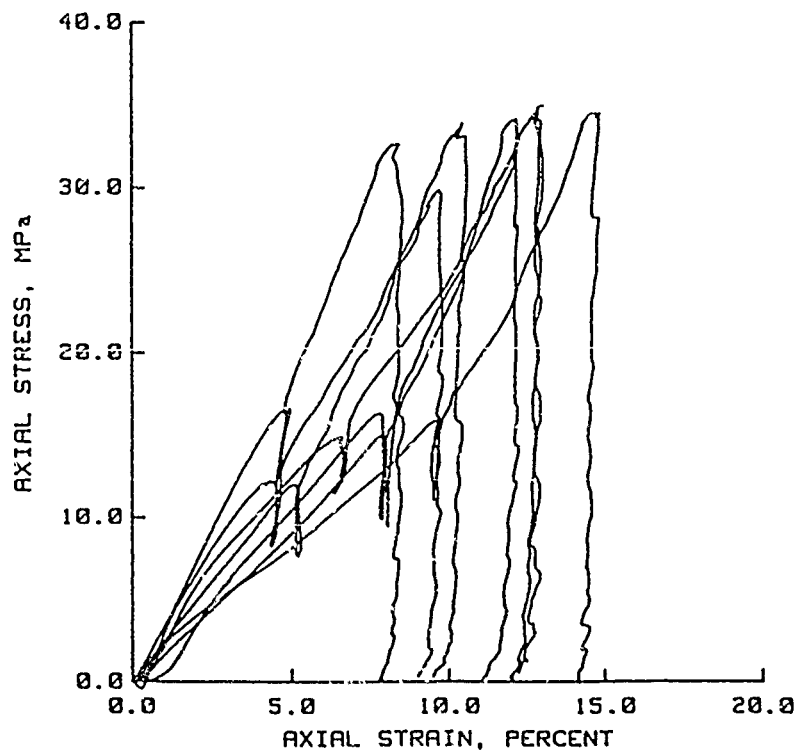
$$V[S] = \frac{1}{8} [(S^{+++})^2 + (S^{++-})^2 + (S^{+-+})^2 + (S^{+--})^2 + (S^{---})^2 + (S^{--+})^2 + (S^{-+-})^2 + (S^{-++})^2] - (E[S])^2$$

	<u>γ, pcf</u>		<u>V_a, %</u>	<u>S, %</u>
++	126.26	+++	18.30	36.04
+-	122.53	++-	17.76	36.73
-+	115.50	+--	24.29	15.10
--	112.08	---	23.76	15.39
		---	30.26	11.55
		--+	30.75	11.39
		-+-	24.78	27.57
		+-+	25.27	27.18
E	119.09		24.40	22.62
$\hat{\sigma}$	5.65		4.41	9.88

Figure 3.3. Rosenblueth procedure for calculating probabilistic values for γ , S , and V_a from probabilistic values of γ_d , w , and G_s .



a. Unsmoothed data.



b. Smoothed data.

Figure 3.4. Effect of applying the smoothing technique to noisy laboratory test responses.

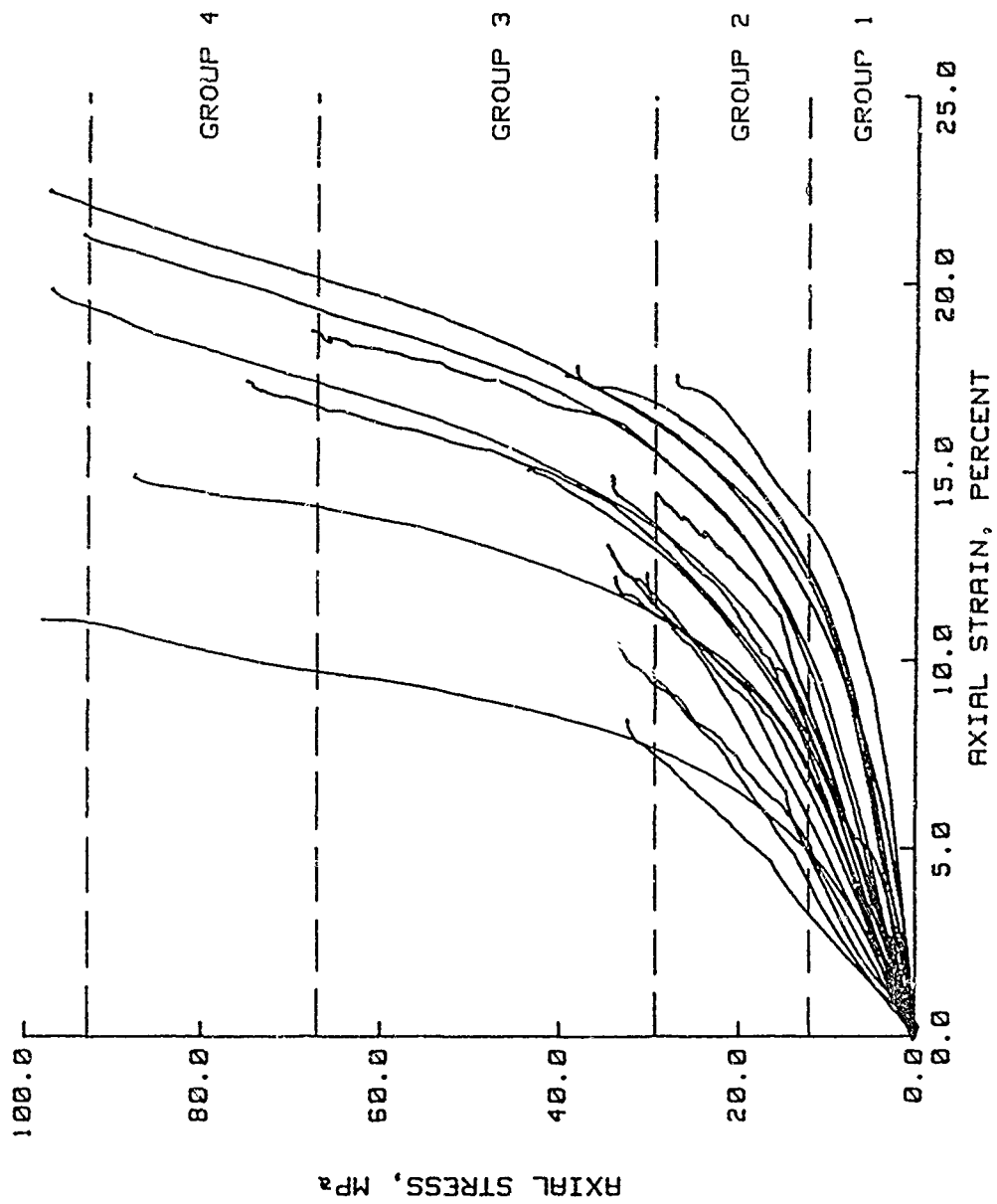
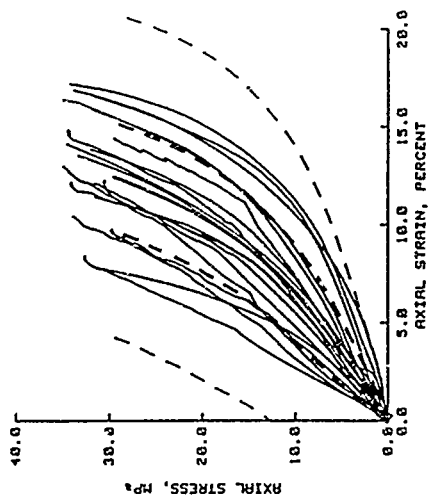
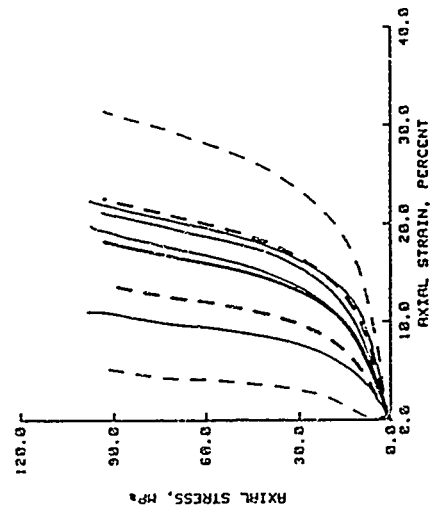


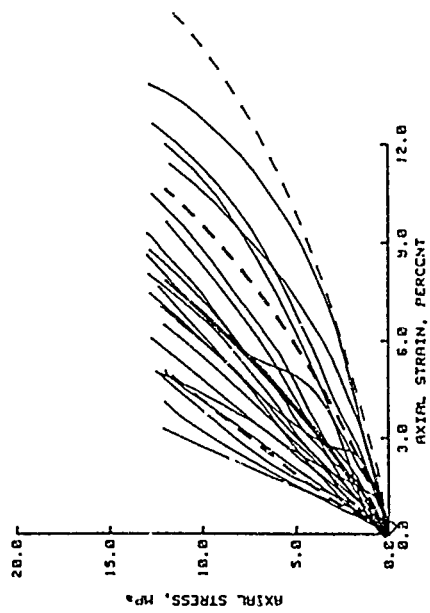
Figure 3.5. Loading dynamic UX test data.



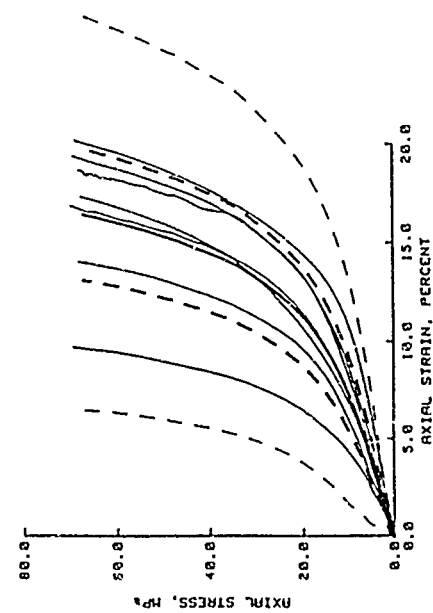
b. Group 2.



d. Group 4.



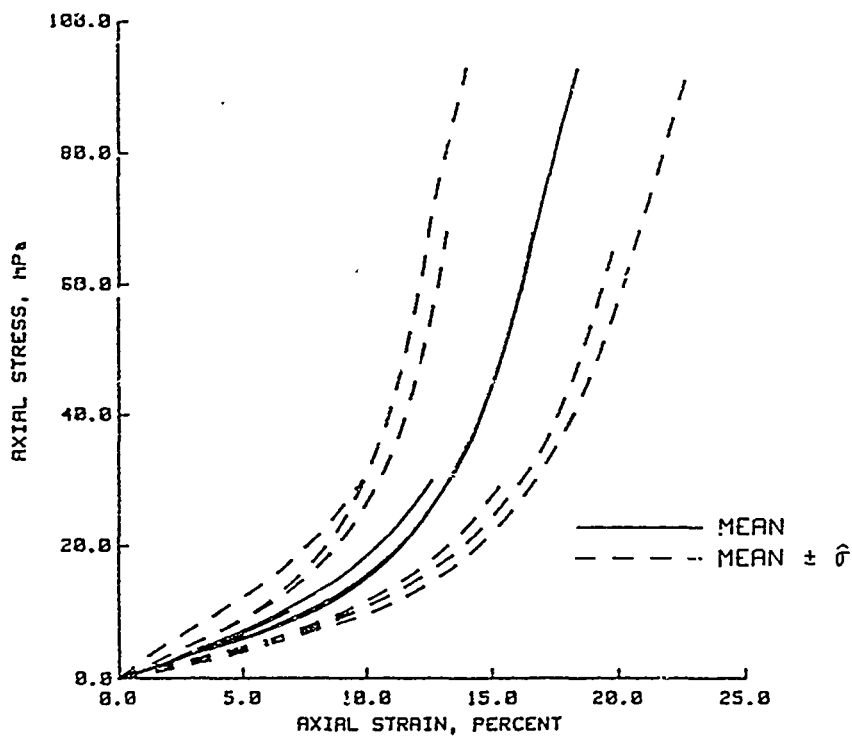
a. Group 1.



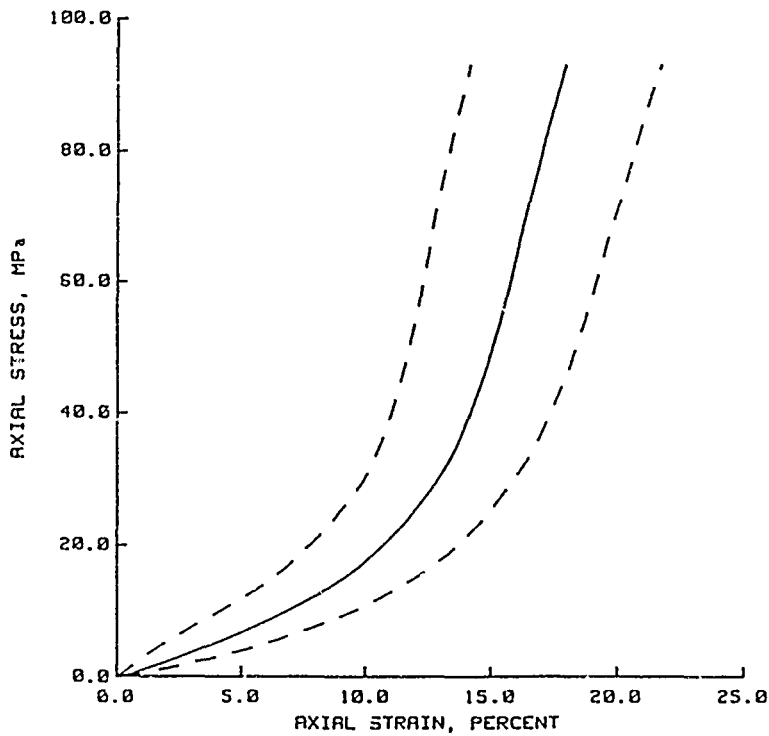
c. Group 3.

TEST DATA
 ——— MEAN
 - - - MEAN $\pm \hat{\sigma}$
 - - - MEAN $\pm 3\hat{\sigma}$

Figure 3.6. Results from applying COV analysis to loading dynamic UX test data.



a. Composite of COV analysis results.



b. Constructed continuous response.

Figure 3.7. Composite and constructed continuous plots of the results from COV analysis of loading dynamic UX test data.

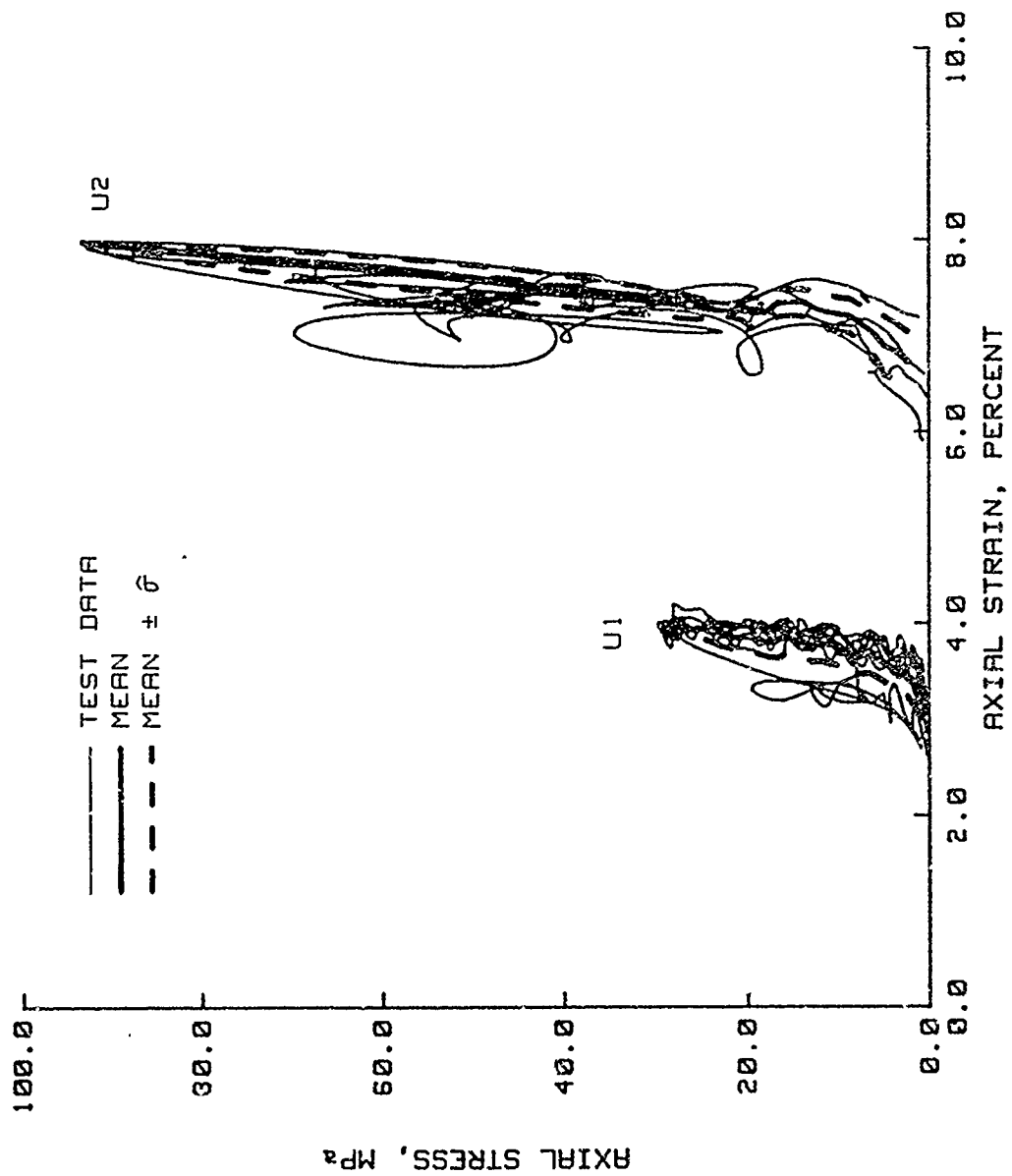


Figure 3.8. Results from the COV analysis of unloading dynamic UX test data.

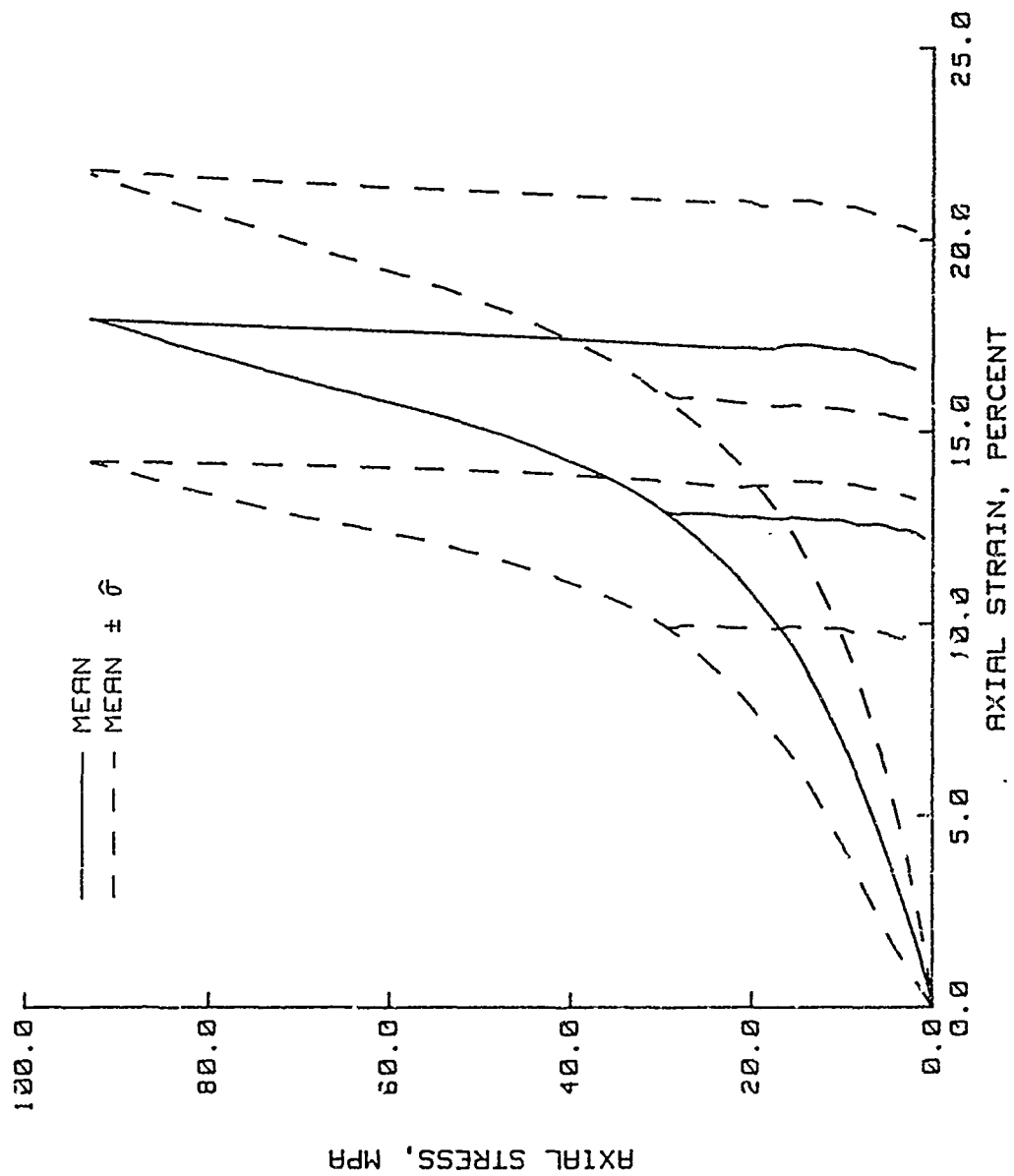
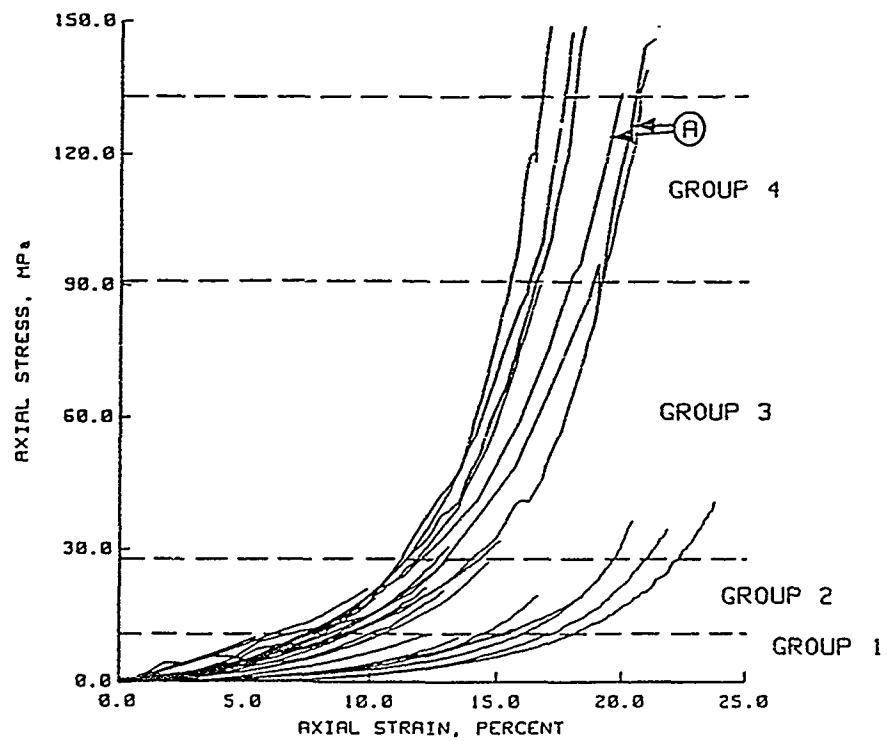
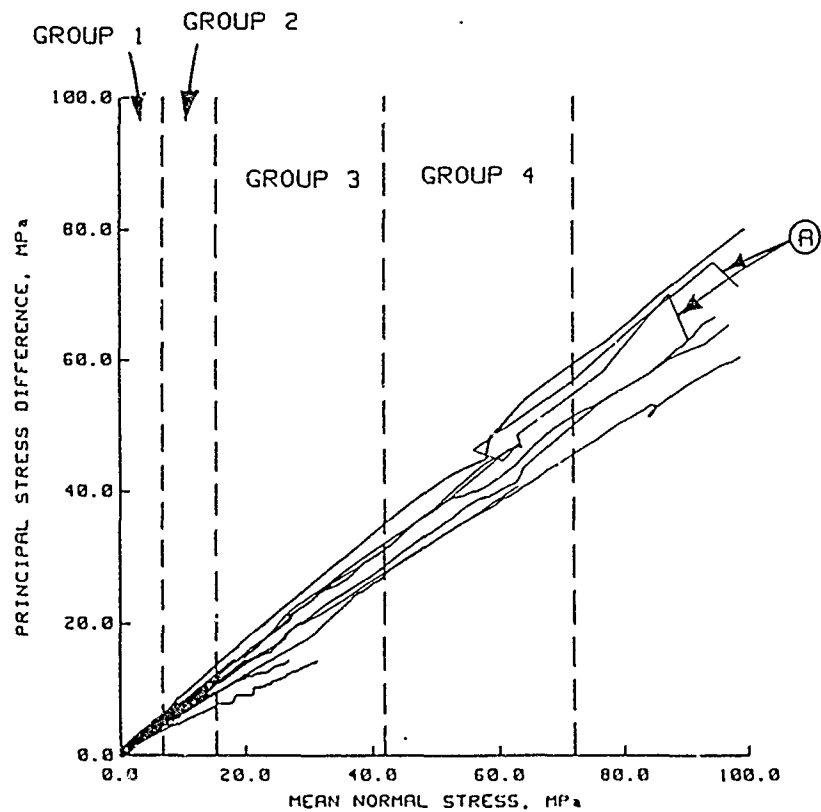


Figure 3 9. Load-unload responses constructed from the results of the COV analysis of dynamic UX test data.

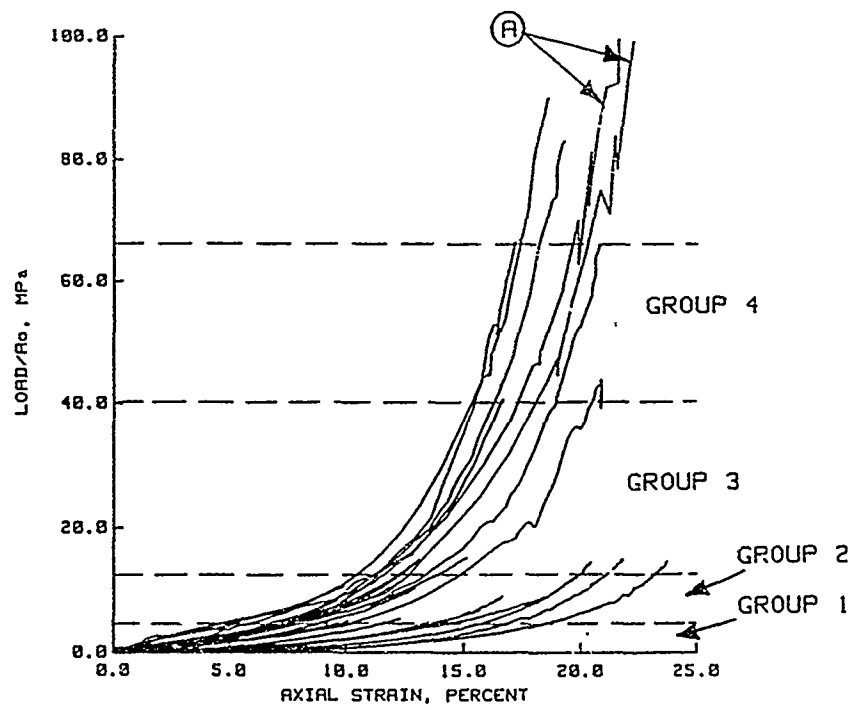


a. Axial stress versus axial strain.

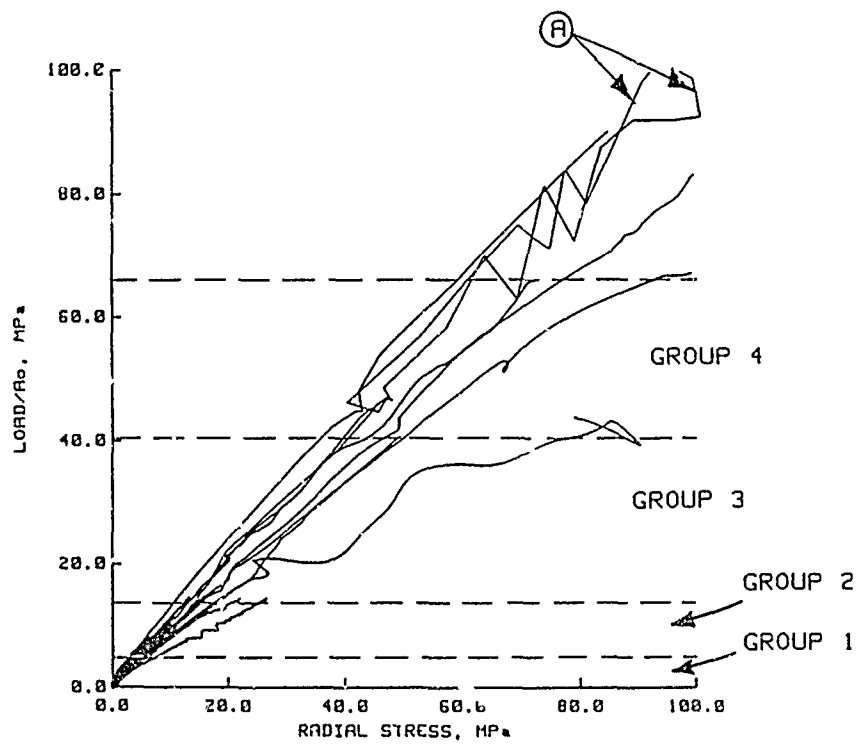


b. Principal stress difference versus mean normal stress.

Figure 3.10. Loading K_0 test data plotted in forms that are conducive to constitutive modeling.

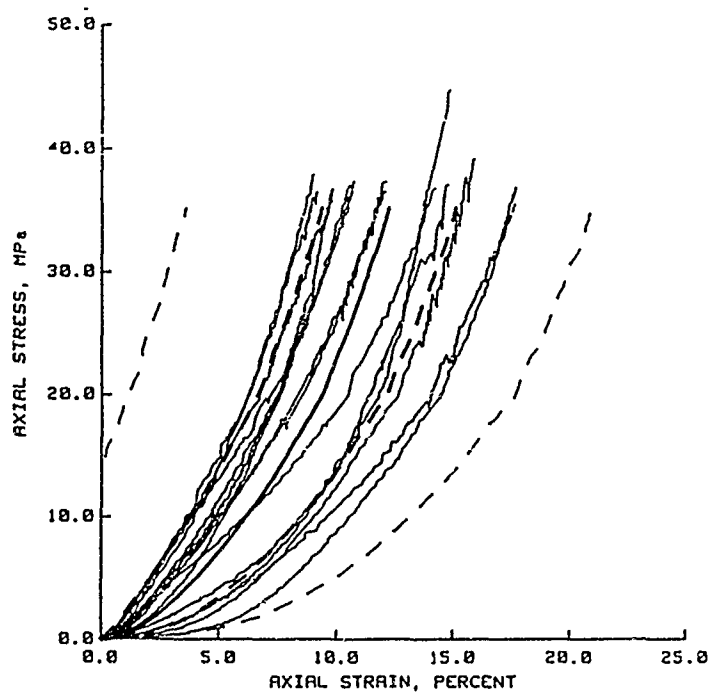


a. L/A_o versus axial strain.

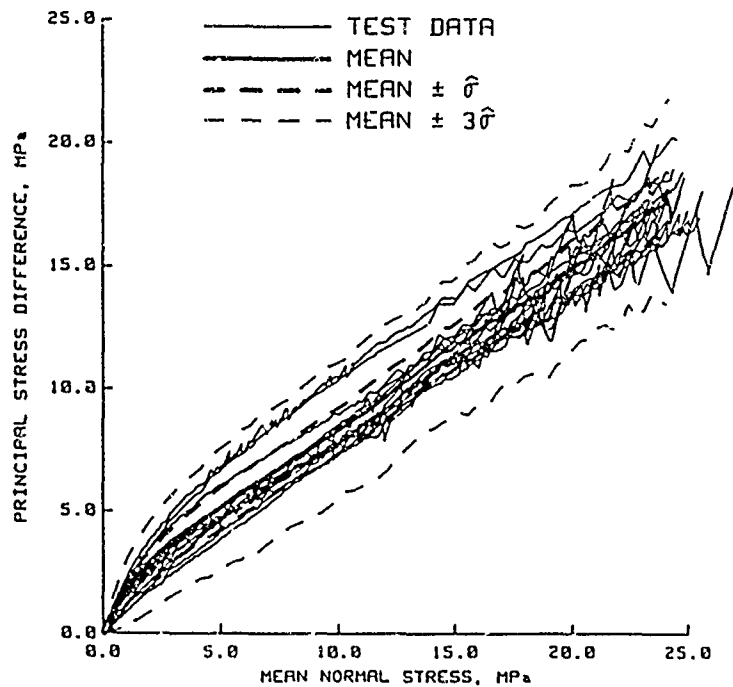


b. L/A_o versus radial stress.

Figure 3.11. "Measured data" plots of the loading portion of K_o test data.

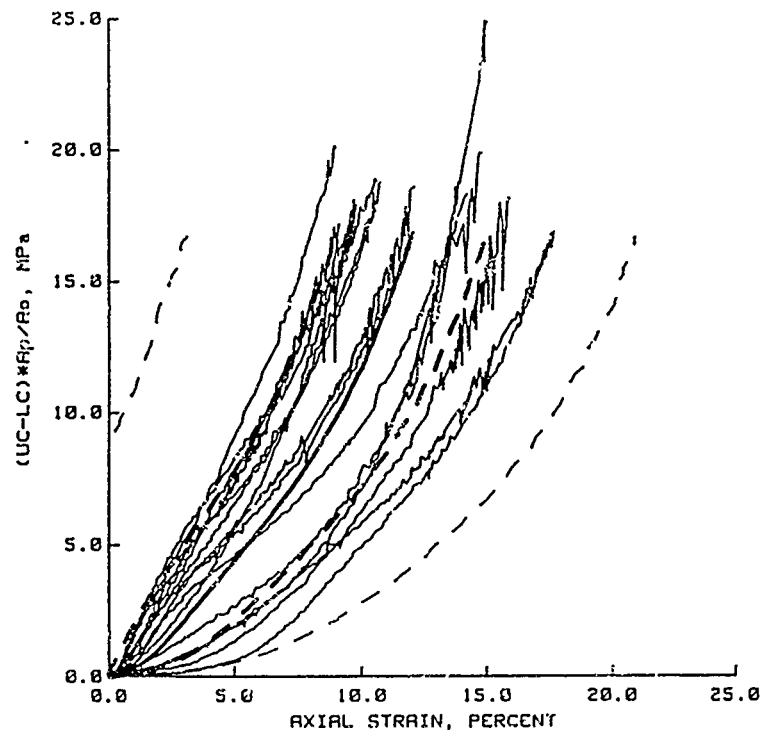


a. Axial stress versus axial strain.

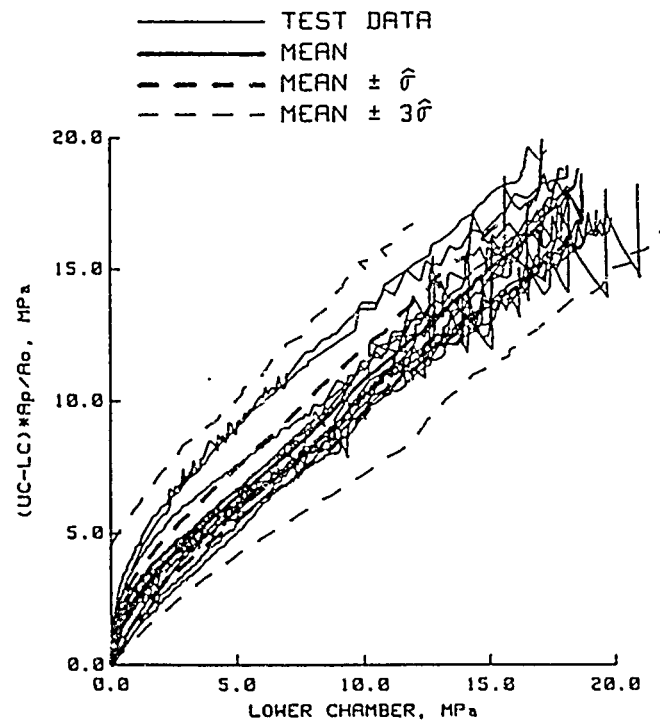


b. PSD versus MNS.

Figure 3.12. Results from the COV analysis of the loading portion of EXT K_0 test data plotted in forms that are conducive to constitutive modeling.



a. $(UC-LC) \cdot A_p/A_o$ versus axial strain.



b. $(UC-LC) \cdot A_p/A_o$ versus LC.

Figure 3.13. Results from the COV analysis of "measured data" plots of the loading portion of the results from EXT K_0 tests.

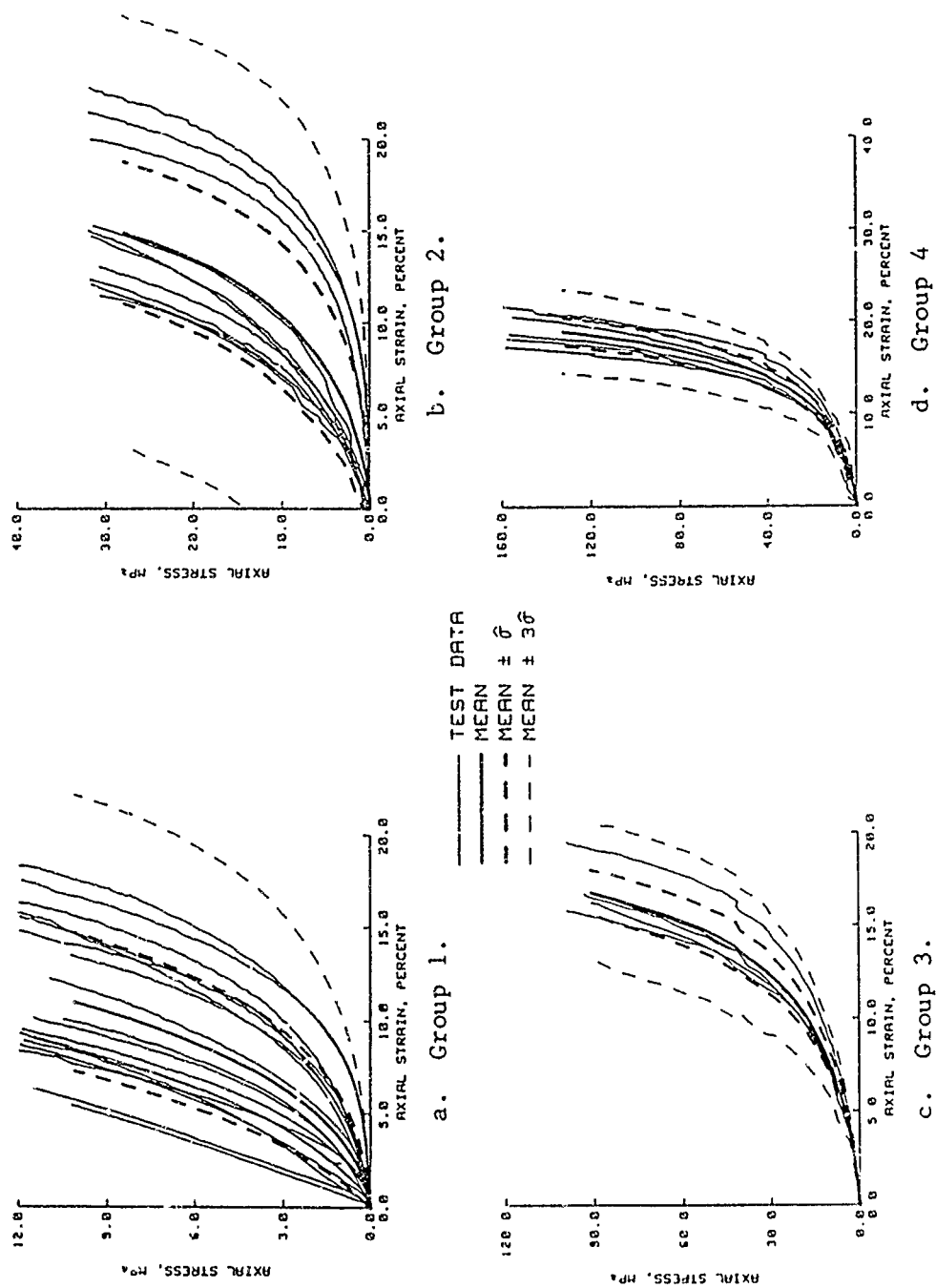
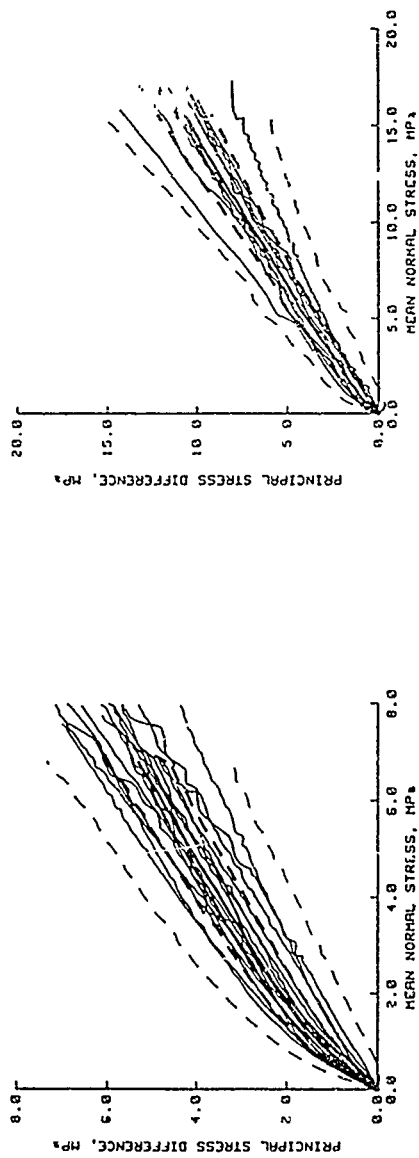
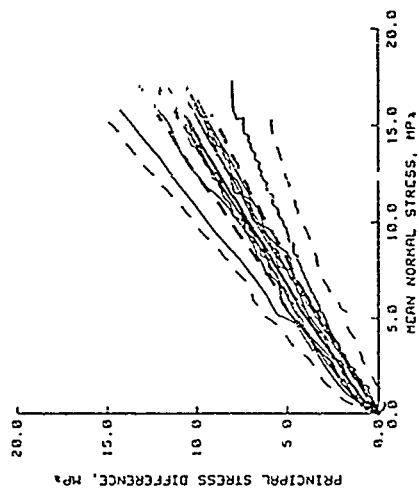


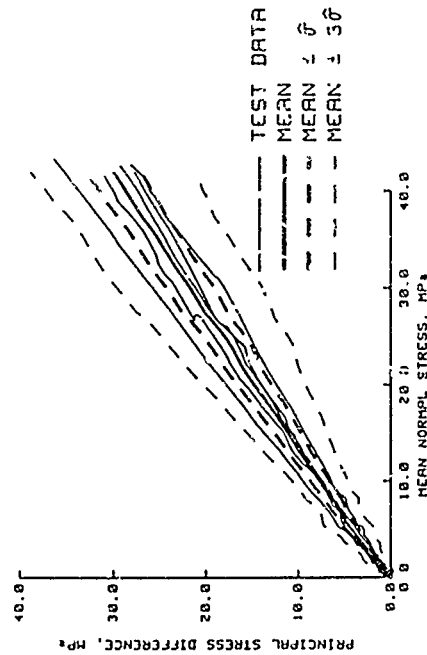
Figure 3.14. Results from the COV analysis of the loading portion of axial stress versus axial strain K_0 test data.



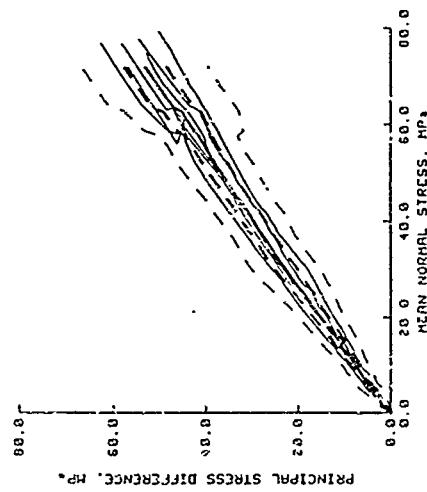
a. Group 1.



b. Group 2.



c. Group 3.



d. Group 4.

Figure 3.15. Results from the COV analysis of the loading portion of PSD versus MNS K_0 test data.

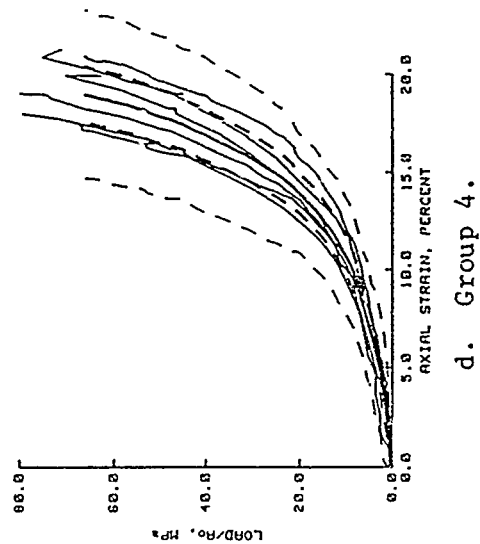
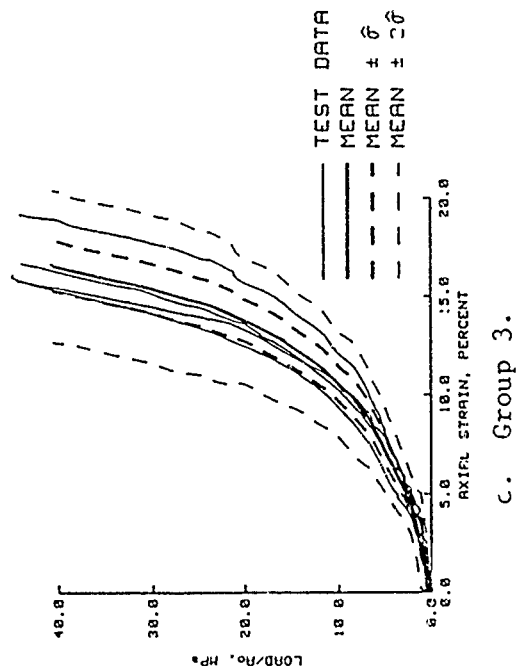
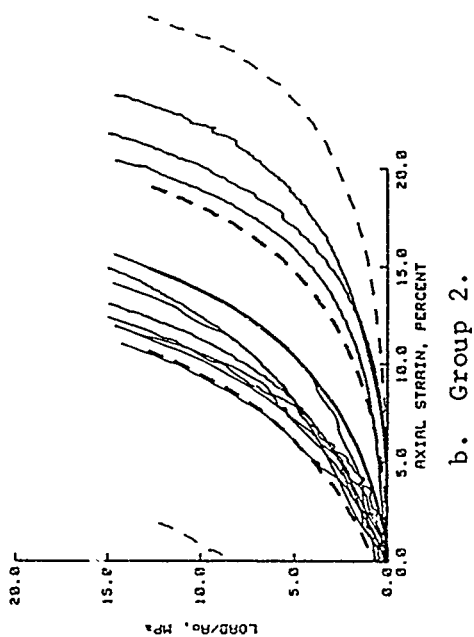
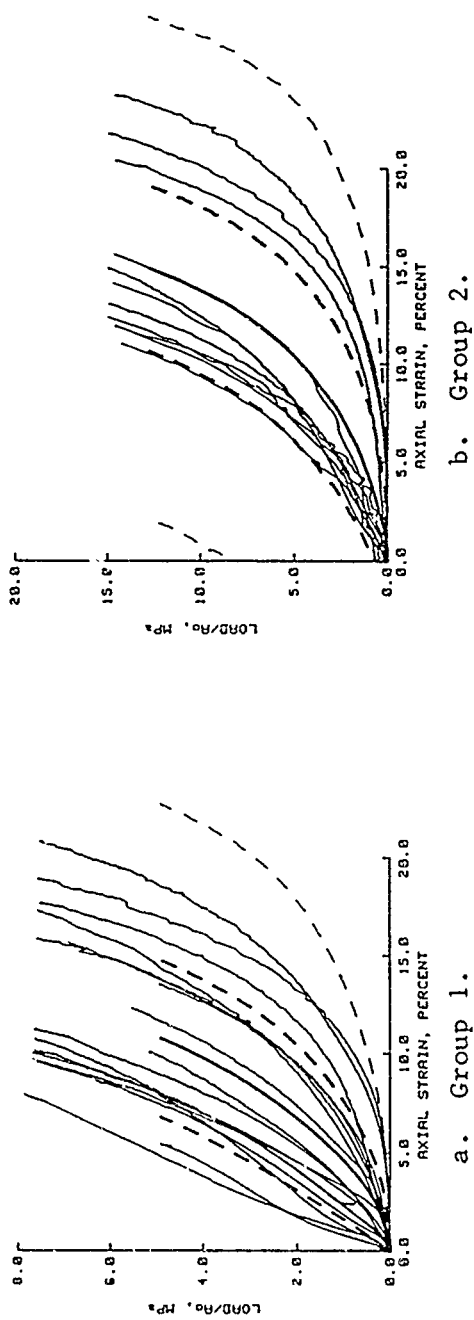


Figure 3.16. Results from the COV analysis of the loading portion of L/A_0 versus axial strain K_0 test data.

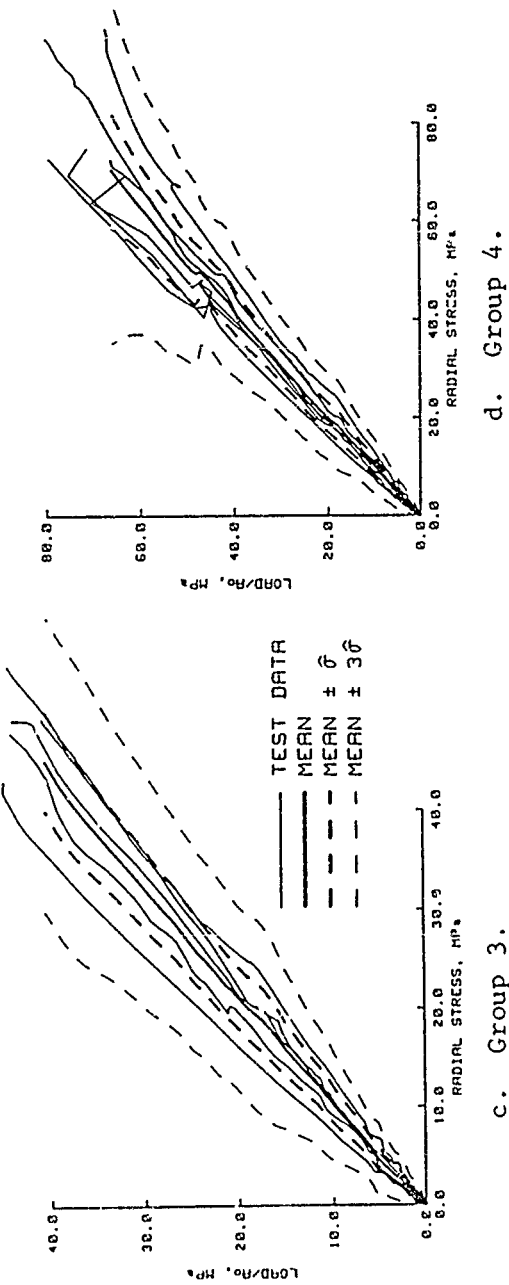
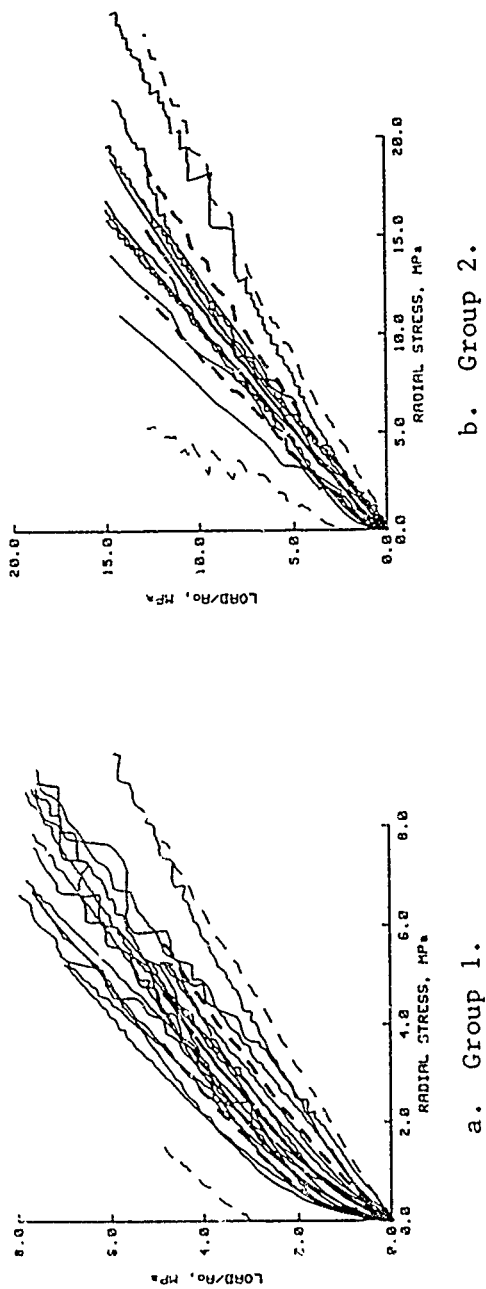
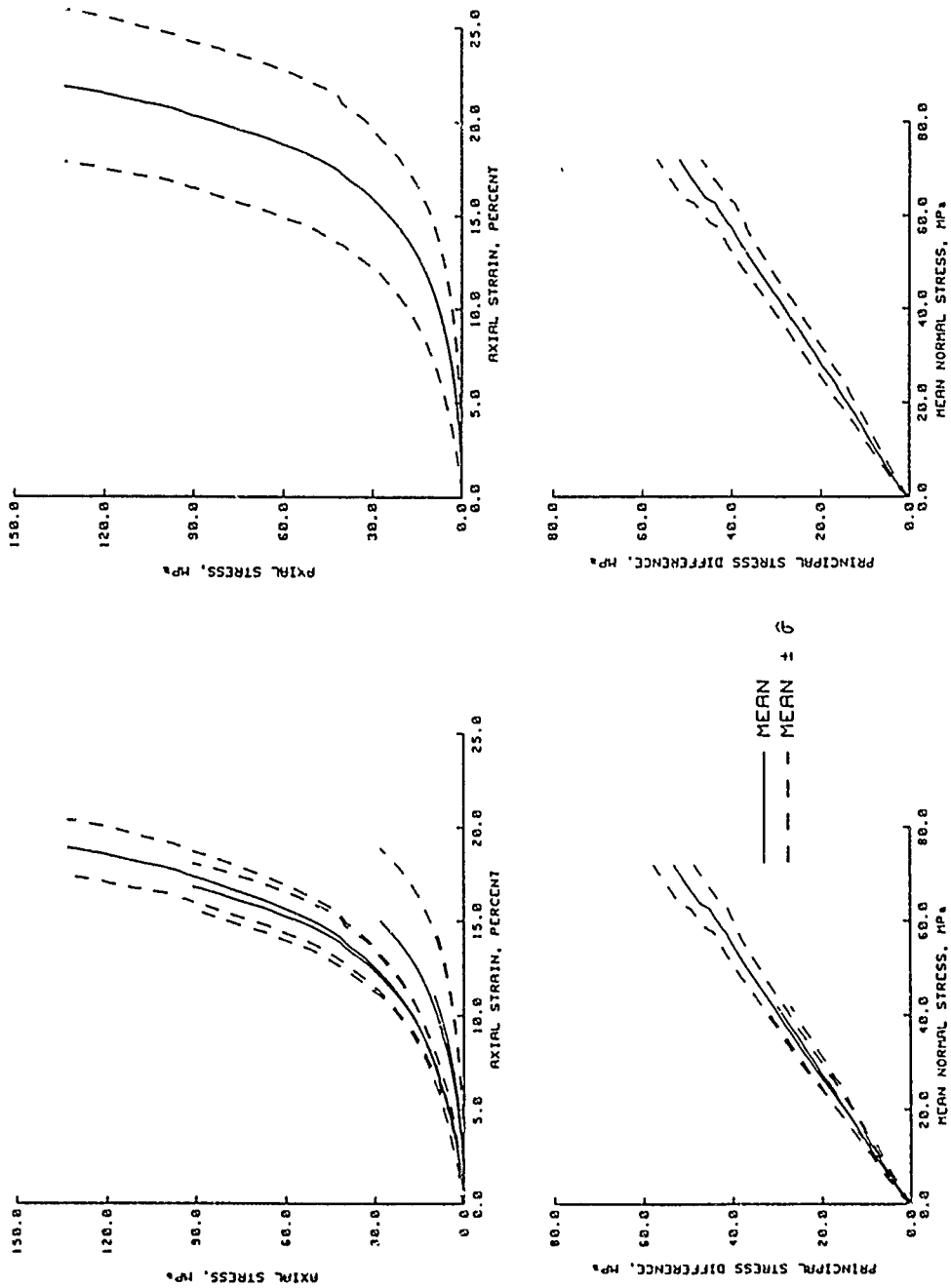


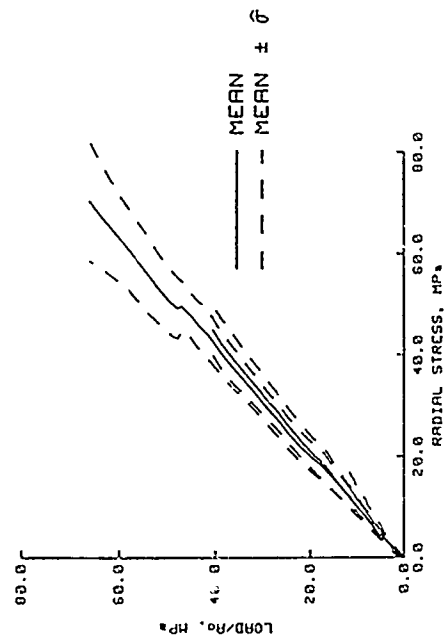
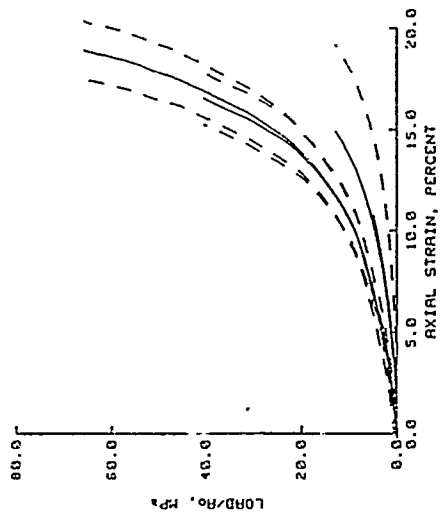
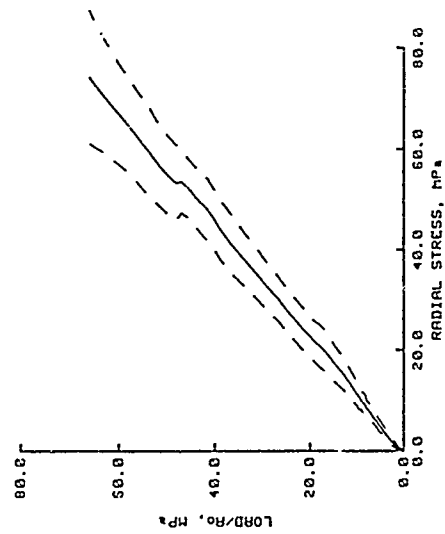
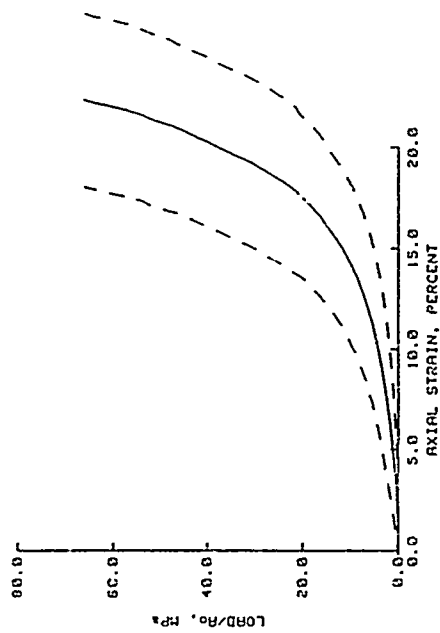
Figure 3.17. Results from the COV analysis of the loading portion of L/A_0 versus radial stress K_0 test data.



a. Composite plots.

b. Constructed continuous plots.

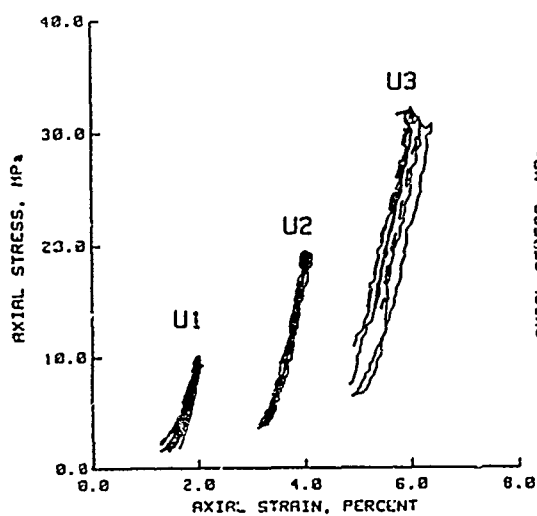
Figure 3.18. Composite and constructed continuous results from the COV analysis of the loading portion of K_0 test data plotted in forms that are conducive to constitutive modeling.



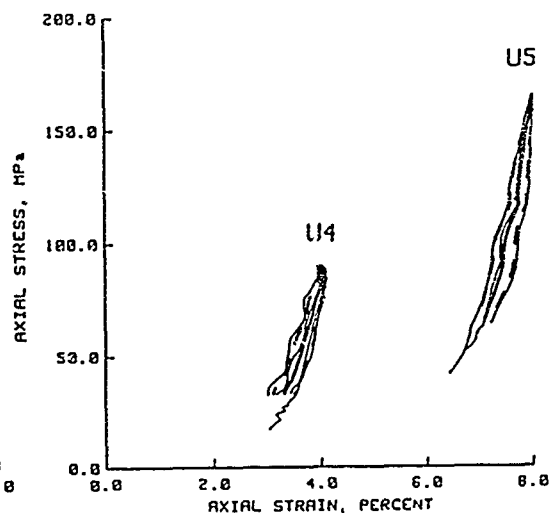
a. Composite plots.

b. Constructed continuous plots.

Figure 3.19. Composite and constructed continuous results from the COV analysis of the loading portion of "measured" K_0 test data.

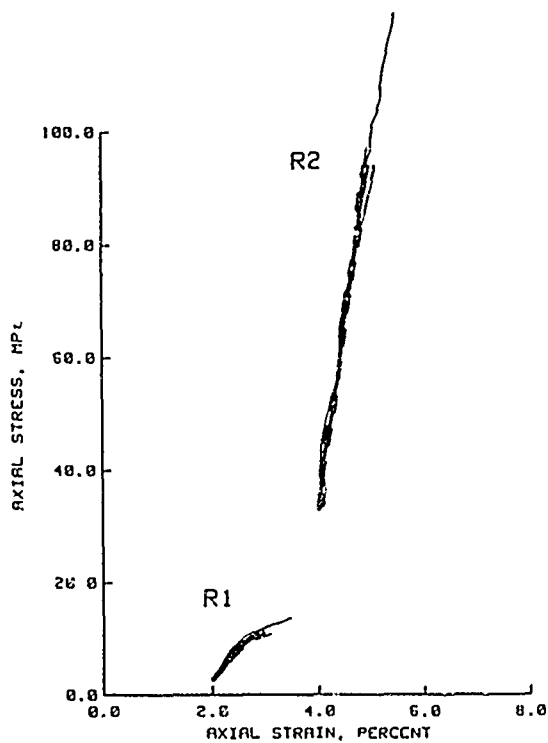


a. Unloading groups U1, U2, and U3.



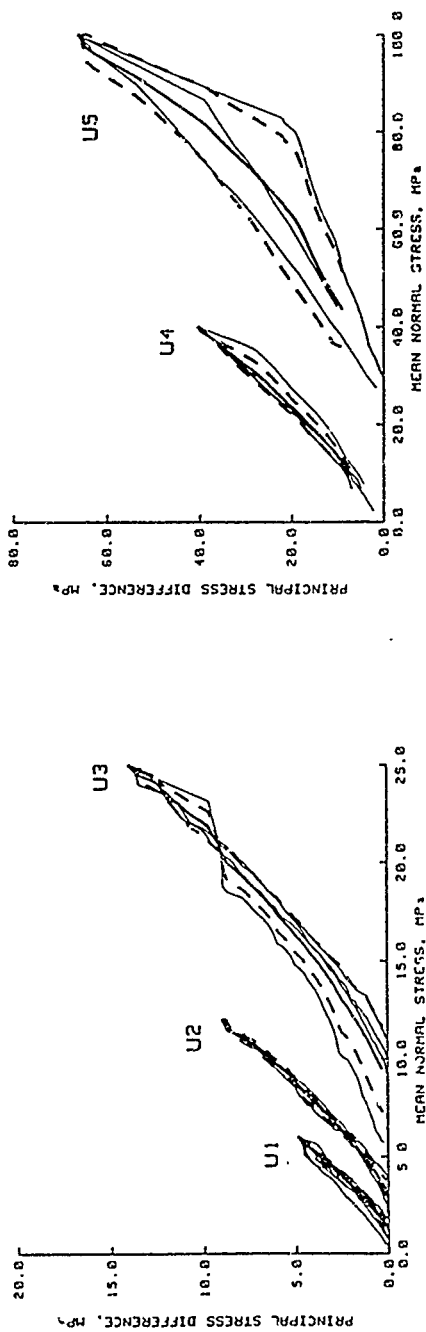
b. Unloading groups U4 and U5.

——— TEST DATA
 ——— MEAN
 - - - MEAN $\pm \hat{\sigma}$



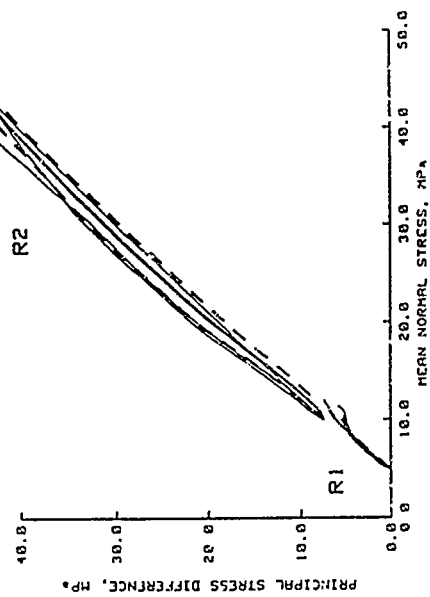
c. Reloading groups R1 and R2.

Figure 3.20. Results from the COV analysis of the unloading and reloading portions of axial stress versus axial strain K_0 test data.



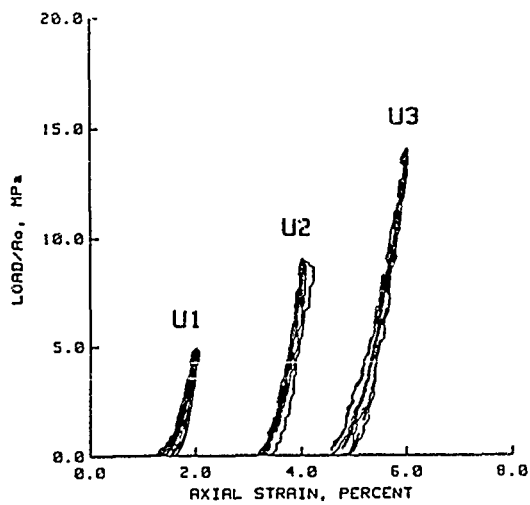
a. Unloading groups U1, U2, and U3.

b. Unloading groups U4 and U5.

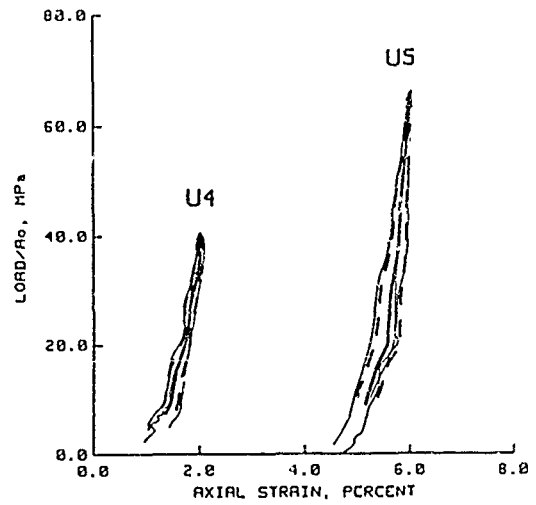


c. Reloading groups R1 and R2.

Figure 3.21. Results from the COV analysis of the unloading and reloading portions of PSD versus MNS K_0 test data.

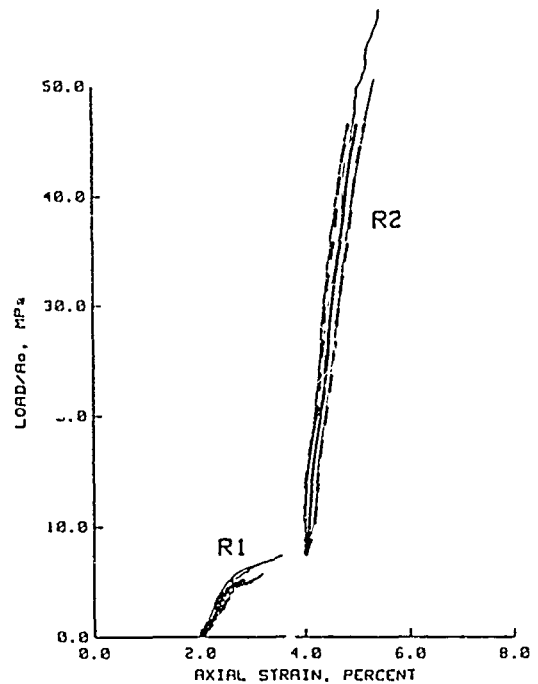


a. Unloading groups U1, U2, and U3.



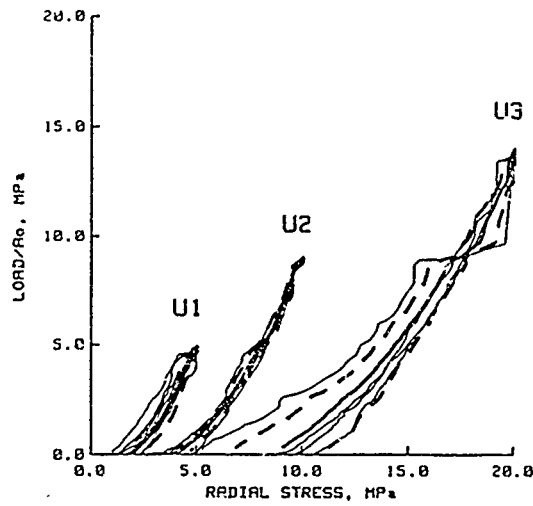
b. Unloading groups U4 and U5.

——— TEST DATA
 ——— MEAN
 - - - MEAN $\pm \hat{\sigma}$

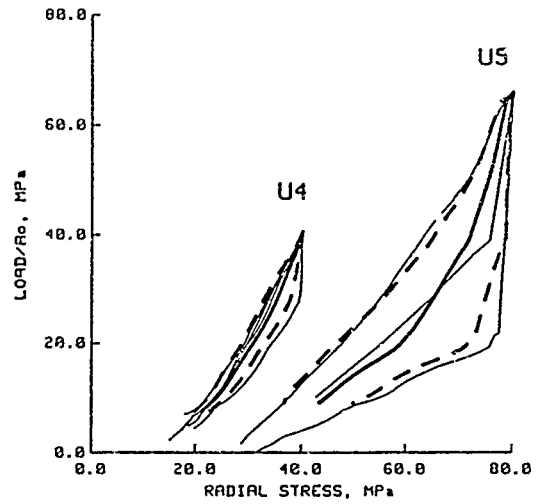


c. Reloading groups R1 and R2.

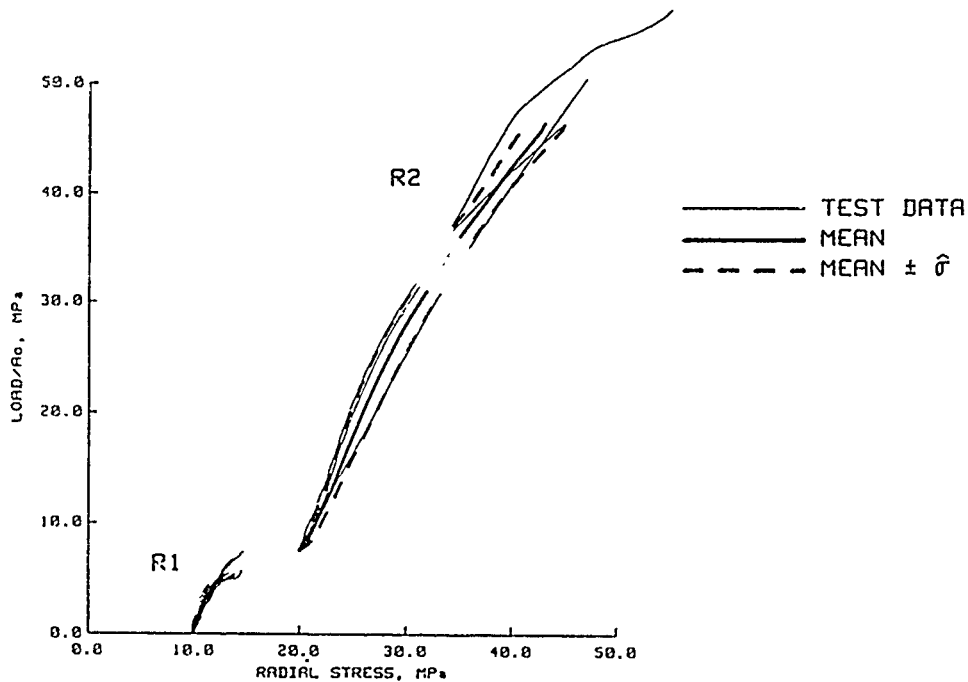
Figure 3.22. Results from the COV analysis of the unloading and reloading portions of L/A_0 versus axial strain K_0 test data.



a. Unloading groups U1, U2, and U3.

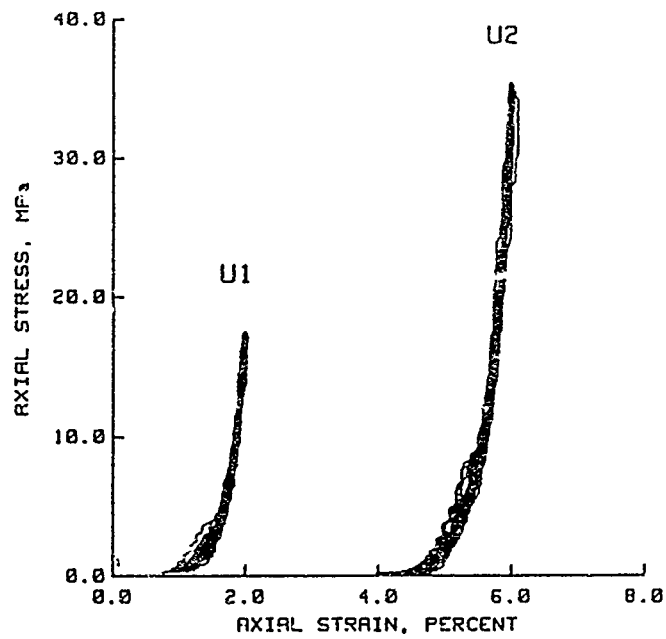


b. Unloading groups U4 and U5.

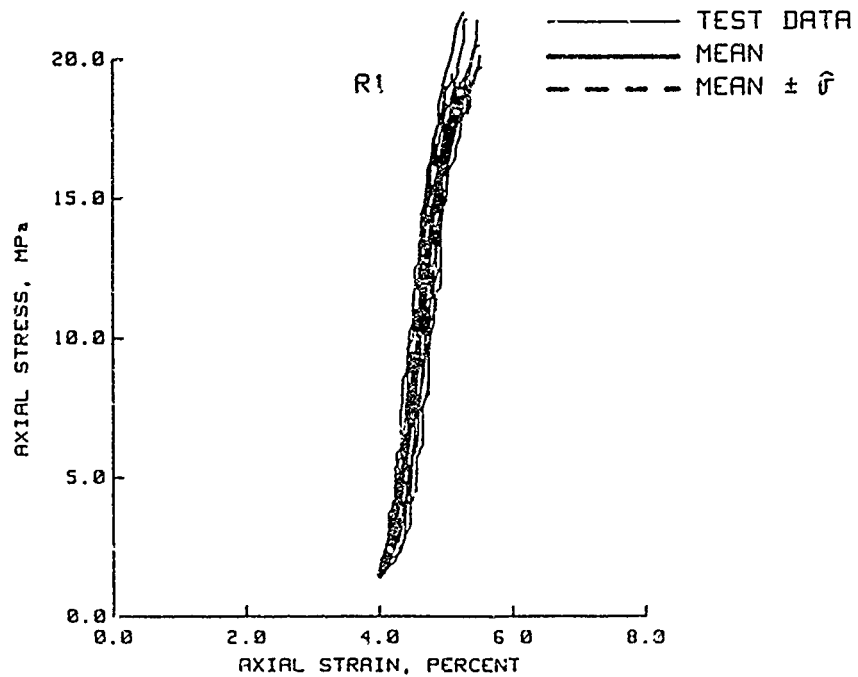


c. Reloading groups R1 and R2.

Figure 3.23. Results from the COV analysis of the unloading and reloading portions of L/A_0 versus radial stress K_0 test data.

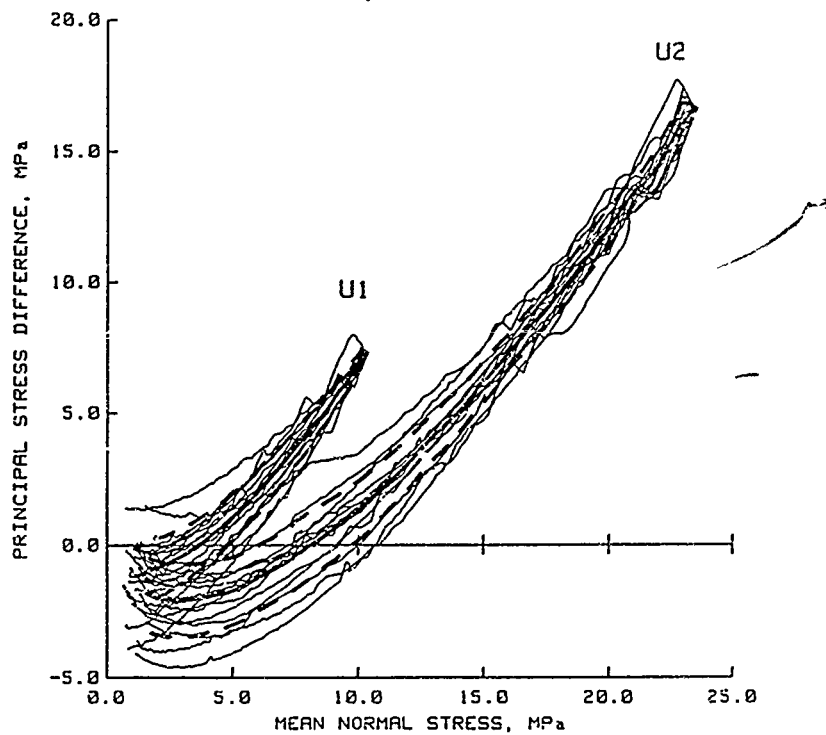


a. Unloading groups U1 and U2.

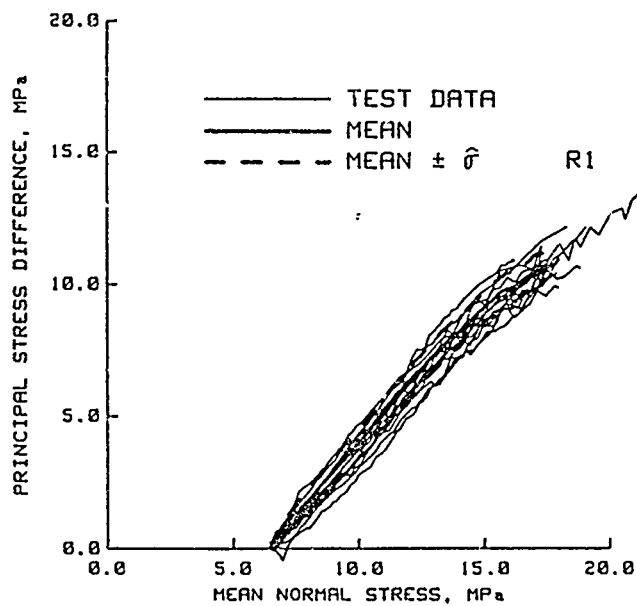


b. Reloading group R1.

Figure 3.24. Results from the COV analysis of the unloading and reloading portions of axial stress versus axial strain EXT K_0 test data.

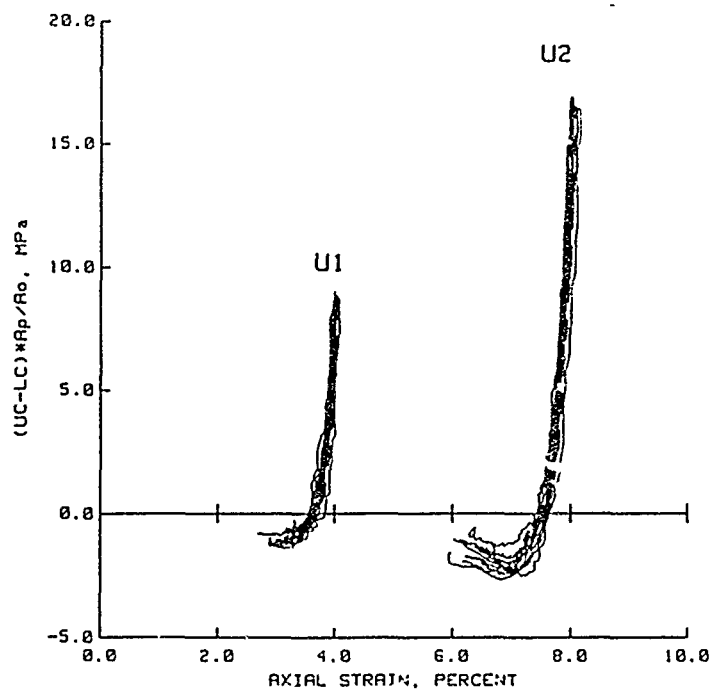


a. Unloading groups U1 and U2.

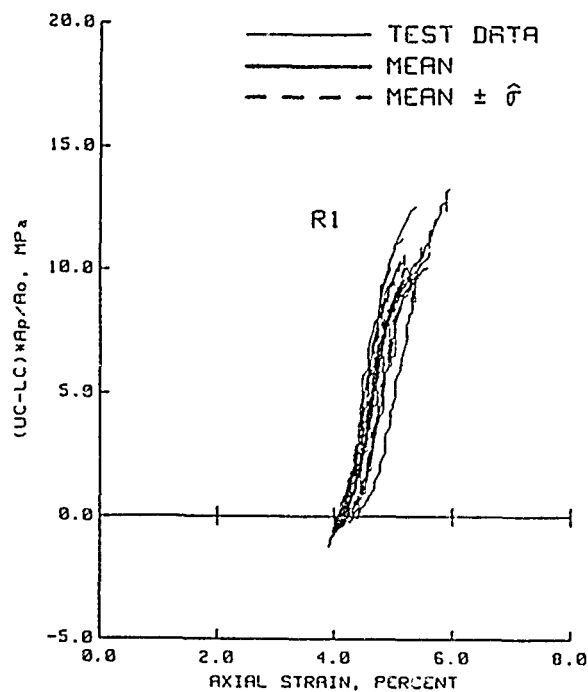


b. Reloading group R1.

Figure 3.25. Results from the COV analysis of the unloading and reloading portions of the PSD versus MNS EXT K_0 test data.

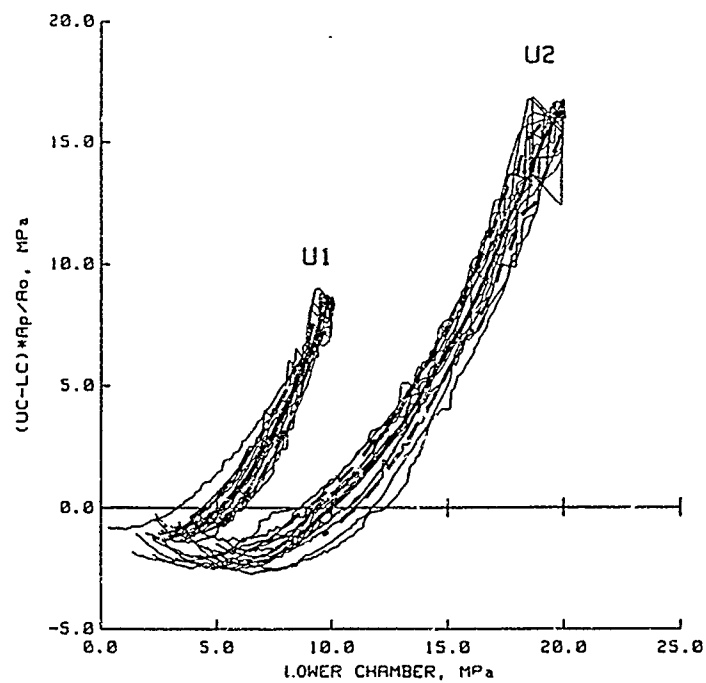


a. Unloading groups U1 and U2.

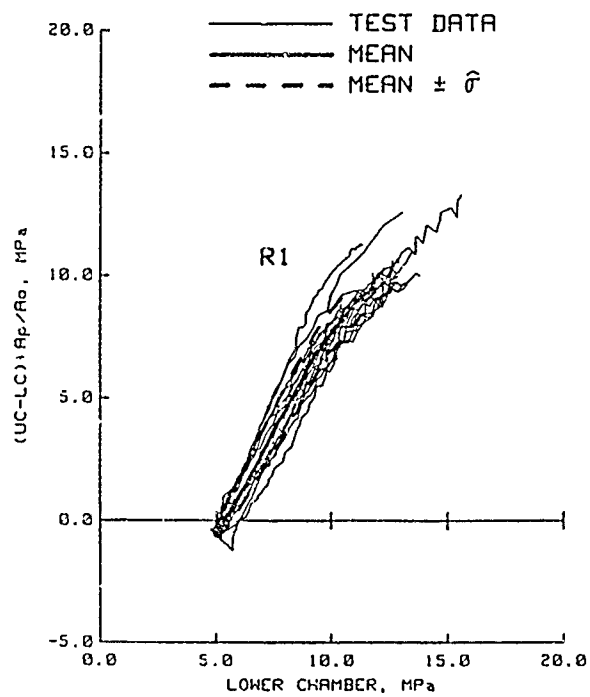


b. Reloading group R1.

Figure 3.26. Results from the COV analysis of the unloading and reloading portions of $(UC-LC) * A_p / A_o$ versus axial strain EXT K_o test data.



a. Unloading groups U1 and U2.



b. Reloading group R1.

Figure 3.27. Results from the COV analysis of the unloading and reloading portions of $(UC-LC) * A_p / A_o$ versus LC EXT K_o test data.

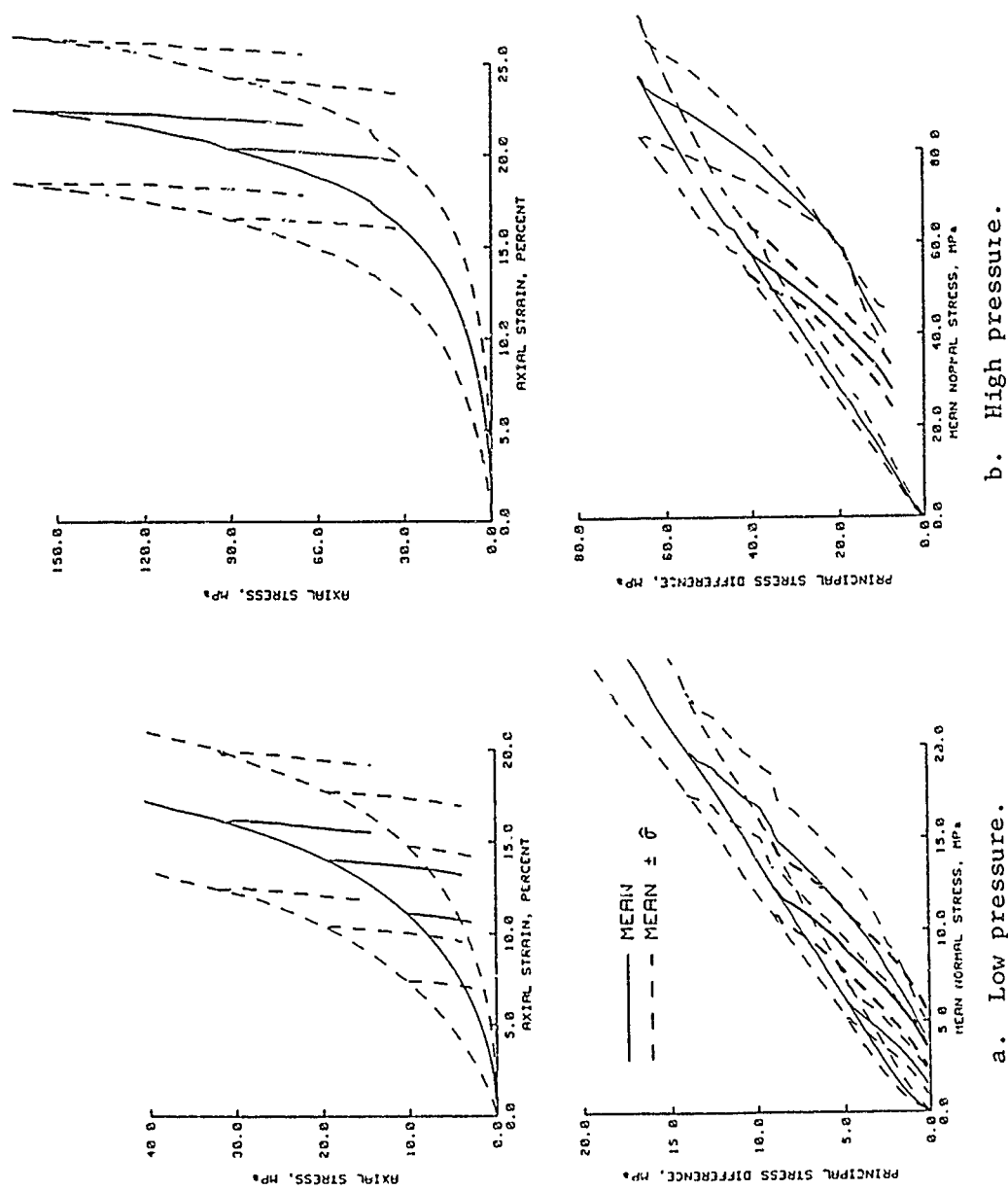
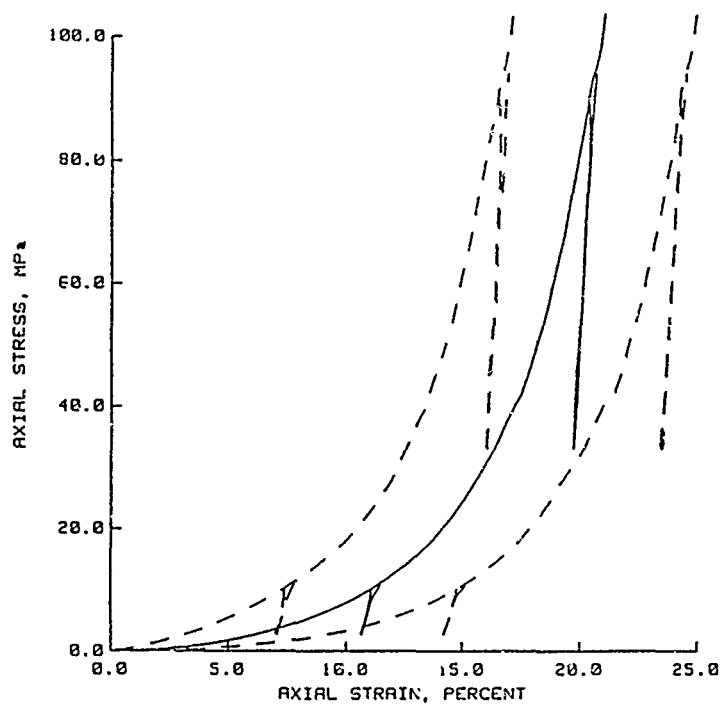
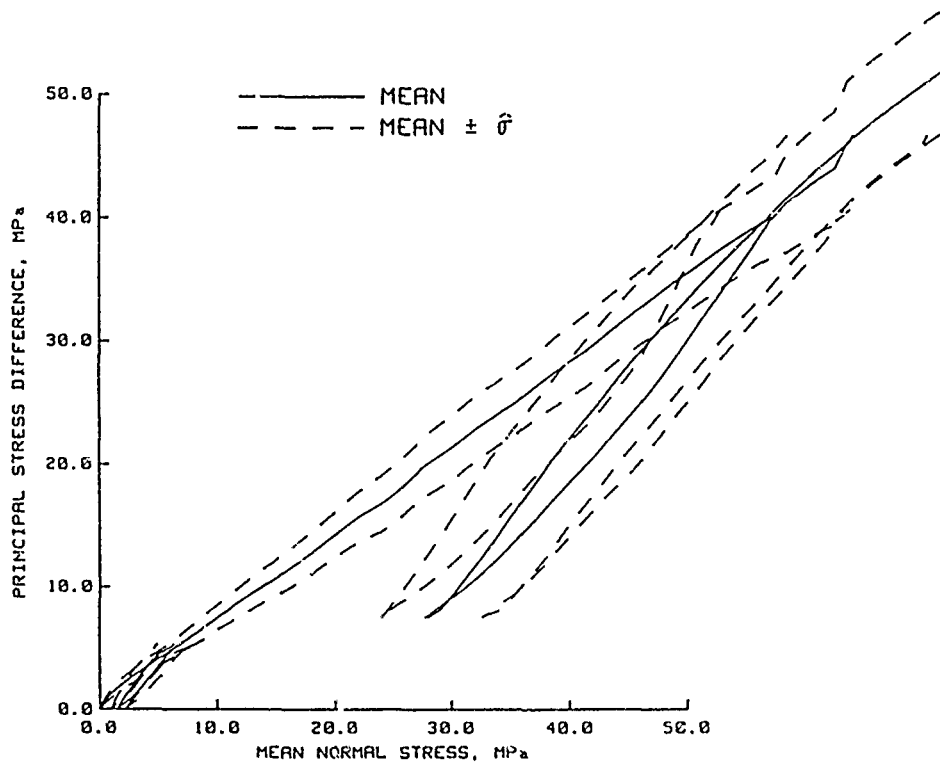


Figure 3.28. Load-unload responses constructed from the results of the COV analysis of K_0 test data plotted in forms that are conducive to constitutive modeling.

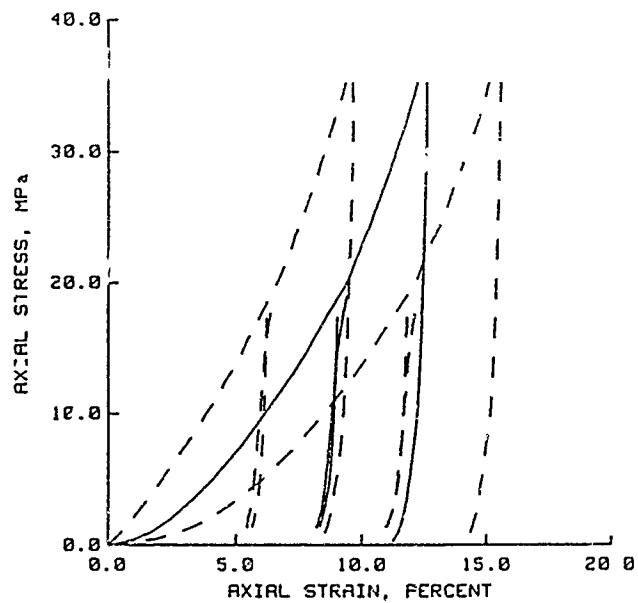


a. Axial stress versus axial strain.

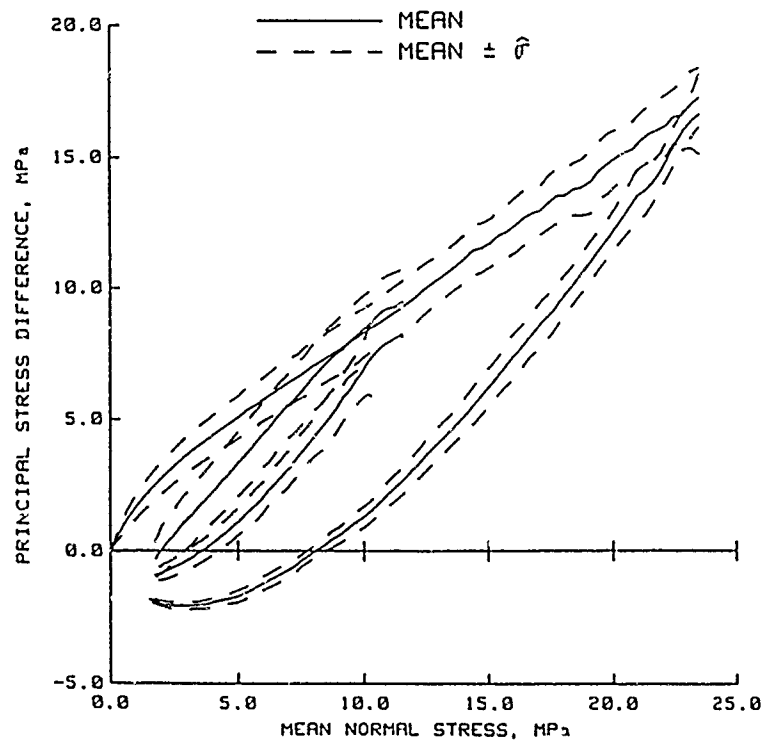


b. PSD versus NMS.

Figure 3.29. Load-unload-reload responses constructed from the results of the COV analysis of K_0 test data plotted in forms that are conducive to constitutive modeling.

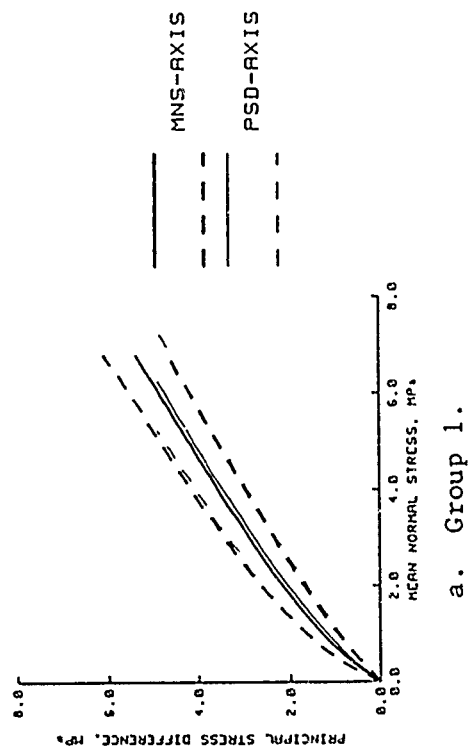


a. Axial stress versus axial strain.

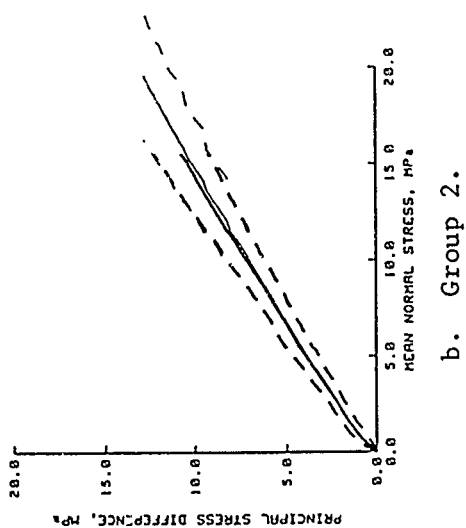


b. PSD versus MNS.

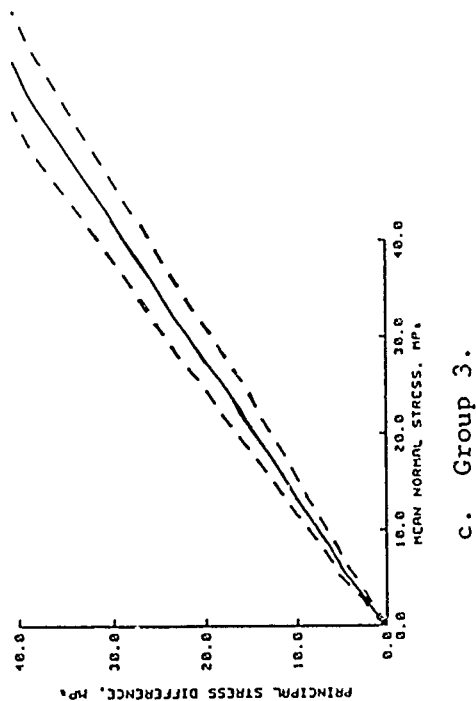
Figure 3.30. Load-unload-reload responses constructed from the results of the COV analysis of EXT K_0 test data plotted in forms that are conducive to constitutive modeling.



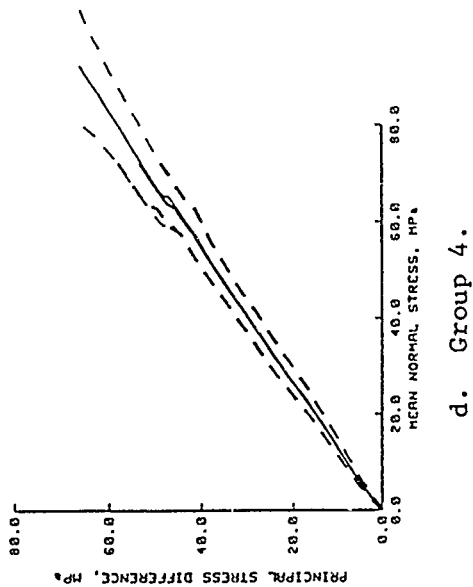
a. Group 1.



b. Group 2.



c. Group 3.



d. Group 4.

Figure 3.31. Effect of incrementing the MNS-axis as opposed to the PSD-axis in the COV analysis of K_o test data.

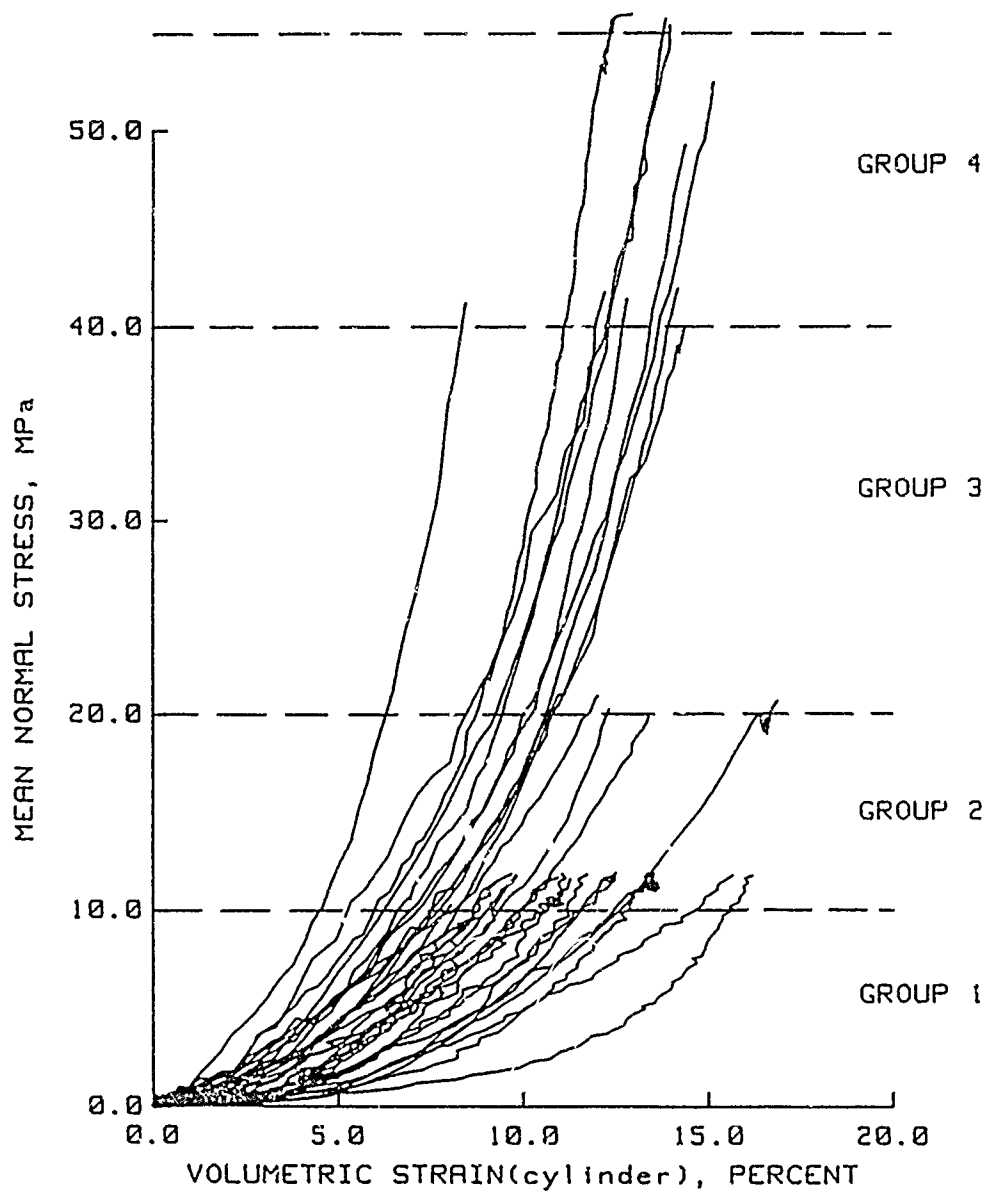
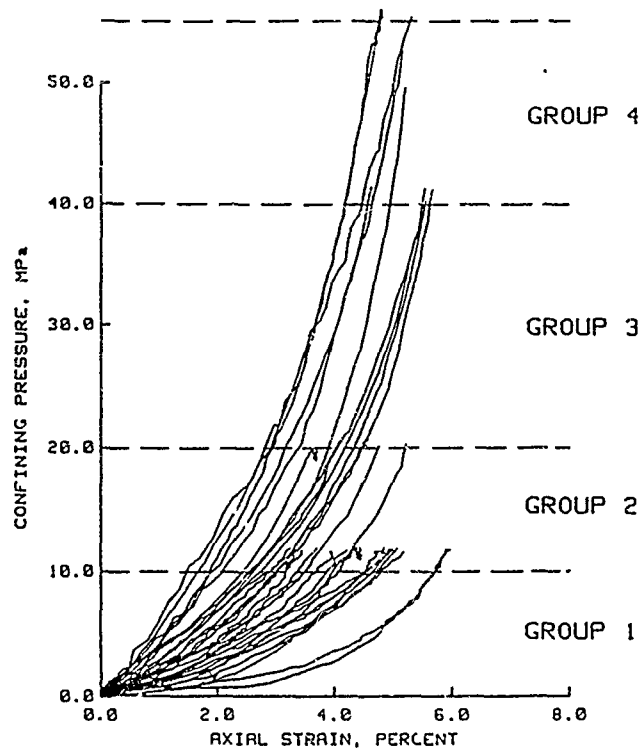
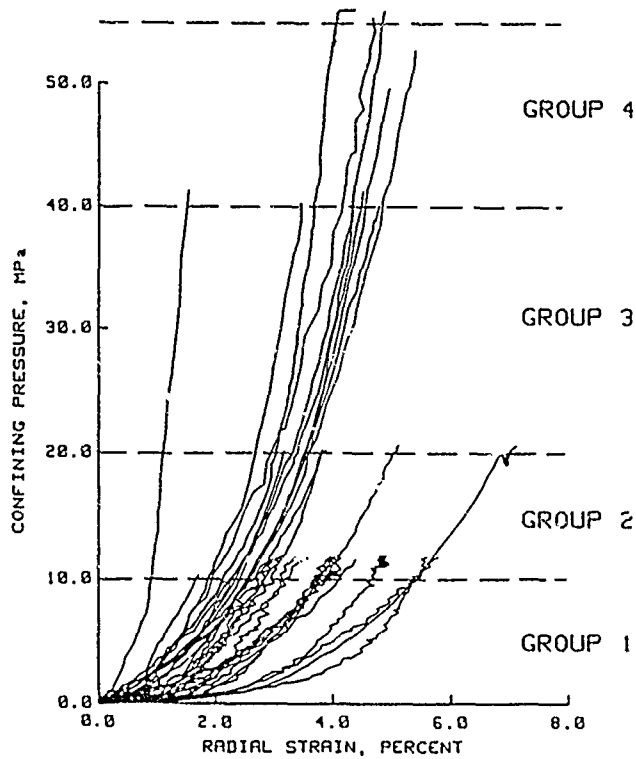


Figure 3.32. Loading static HC test data plotted in a form that is conducive to constitutive modeling.



a. Confining pressure versus axial strain.



b. Confining pressure versus radial strain.

Figure 3.33. "Measured data" plots of the loading portion of static HC test data.

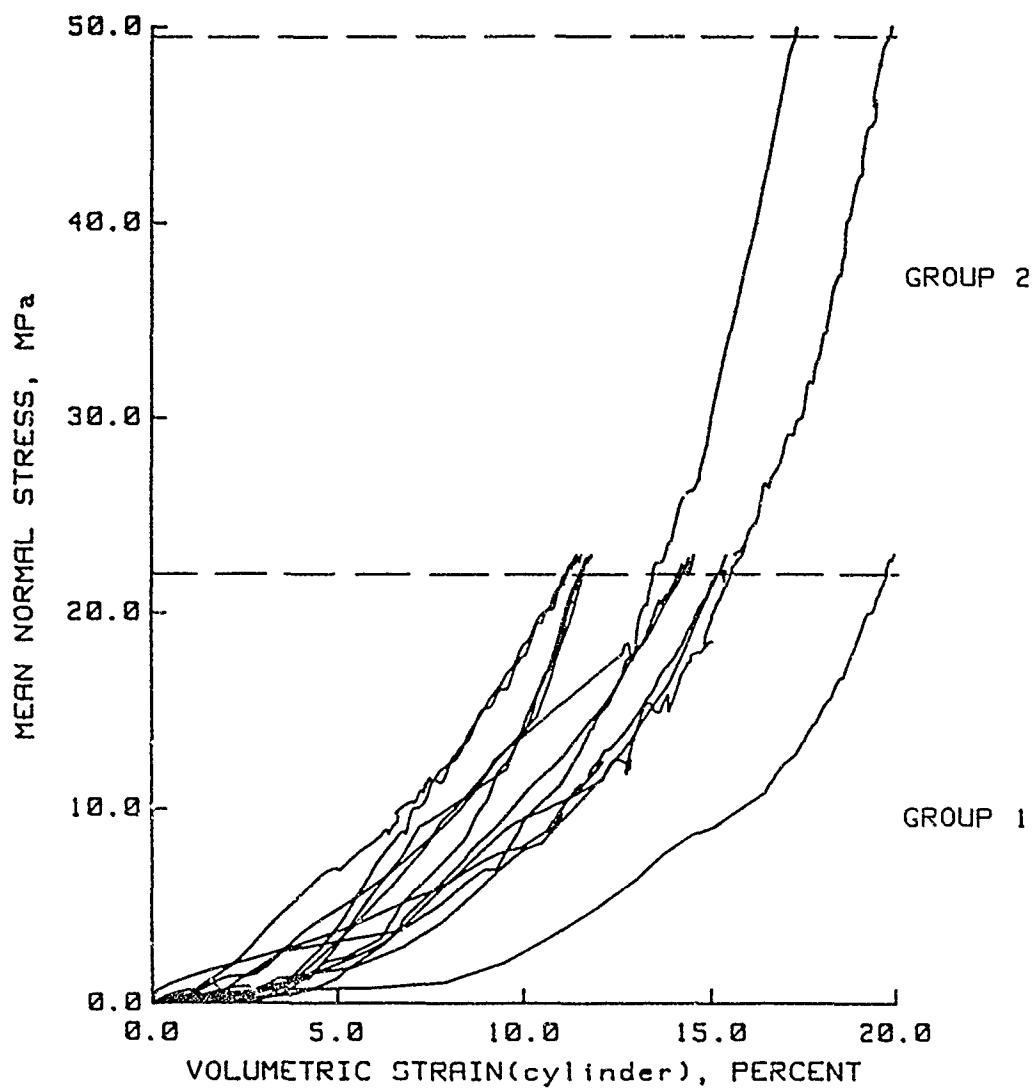
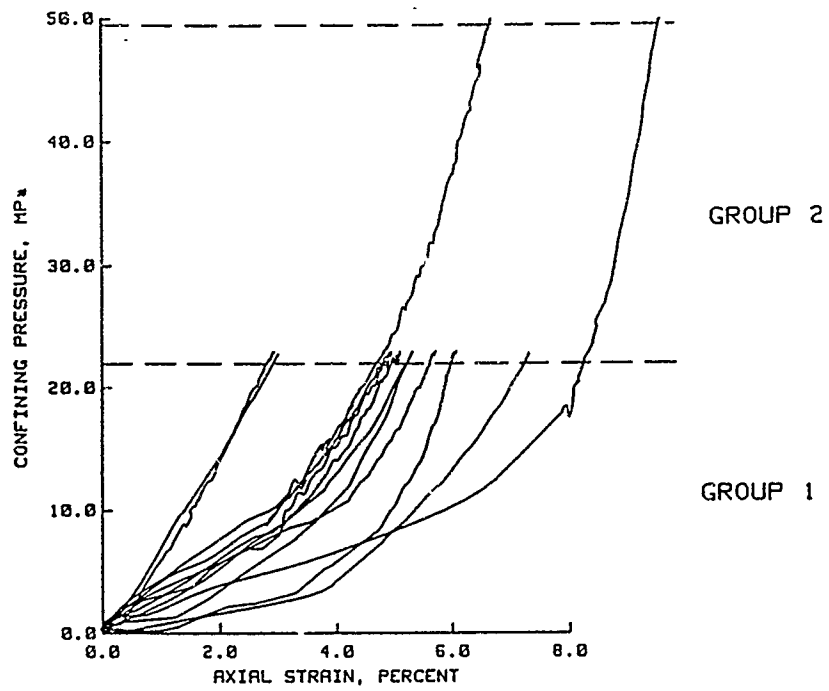
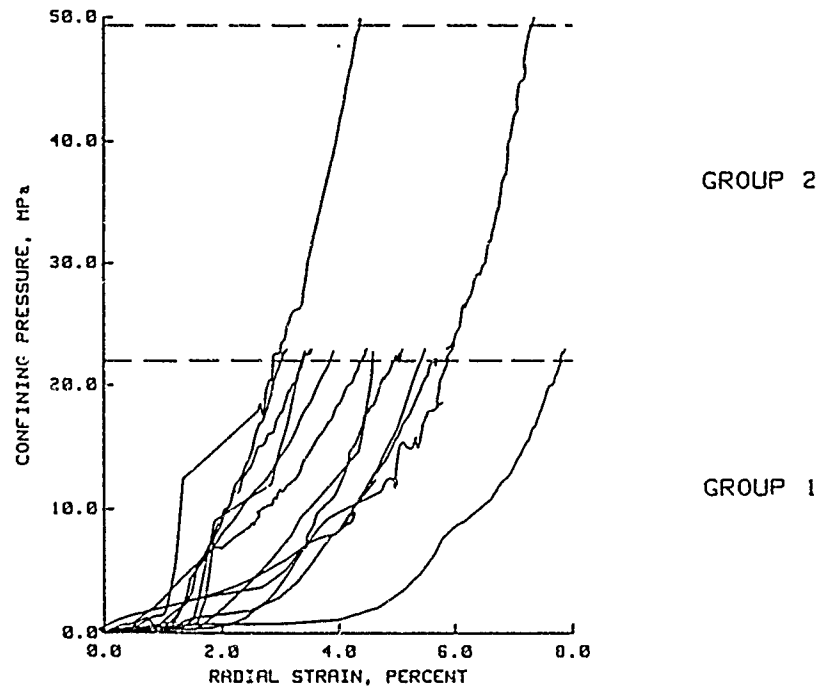


Figure 3.34. Loading dynamic HC test data plotted in a form that is conducive to constitutive modeling.

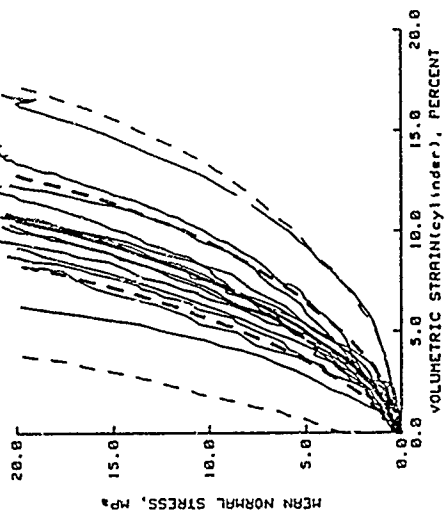


a. Confining pressure versus axial strain.



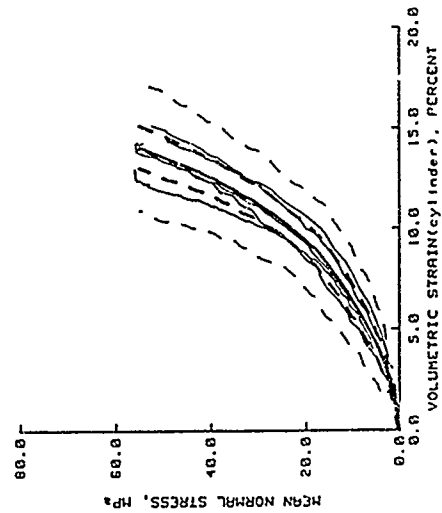
b. Confining pressure versus radial strain.

Figure 3.35. "Measured data" plots of the loading portion of dynamic HC test data.



a. Group 1.

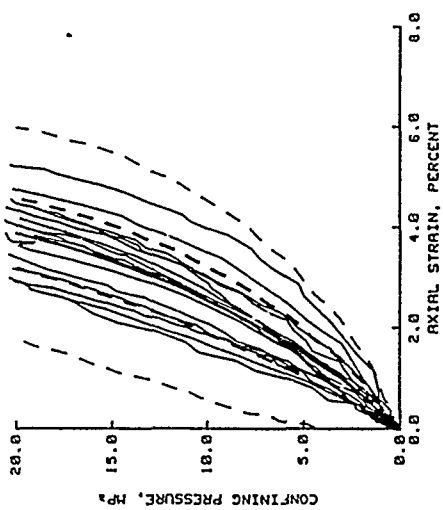
b. Group 2.



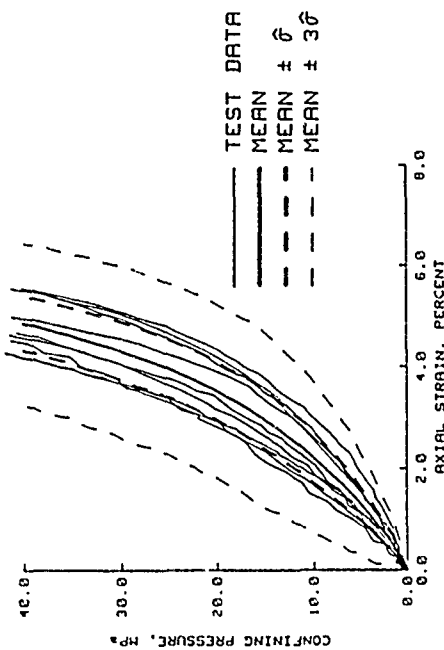
c. Group 3.

d. Group 4.

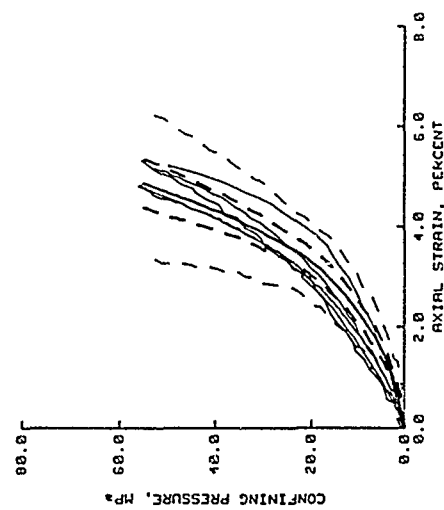
Figure 3.36. Results from the COV analysis of the loading portion of static HC test data plotted in a form that is conducive to constitutive modeling.



a. Group 1.



b. Group 2.



c. Group 3.

d. Group 4.

Figure 3.37. Results from the COV analysis of the loading portion of confining pressure versus axial strain static HC test data.

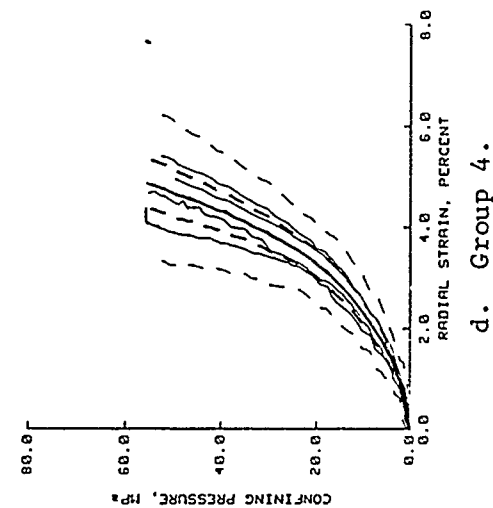
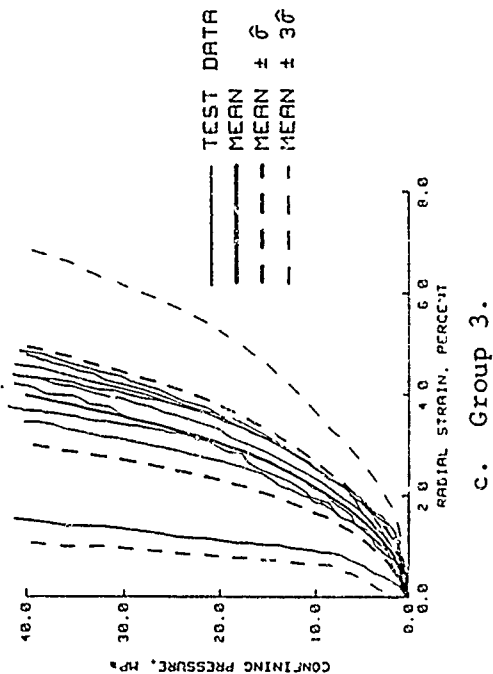
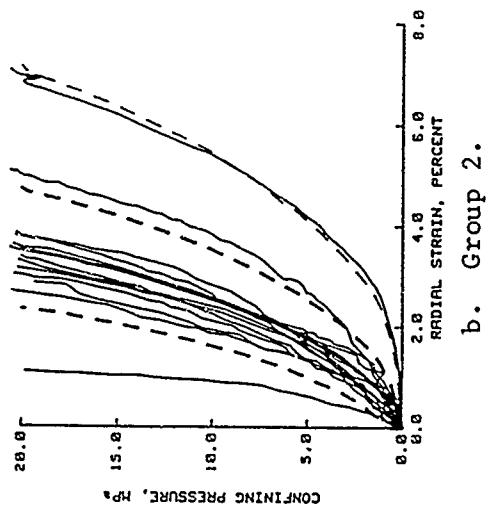
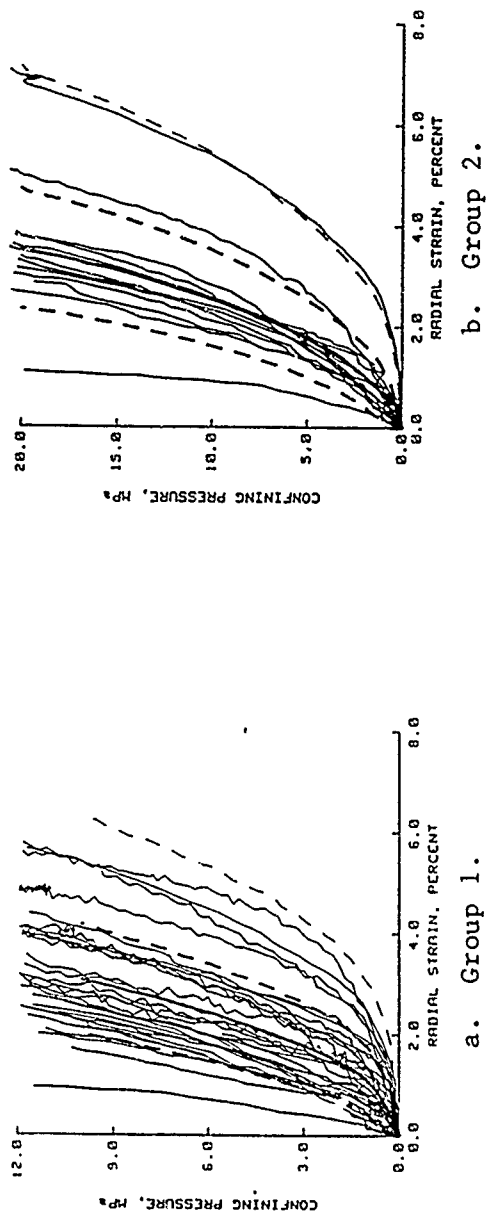
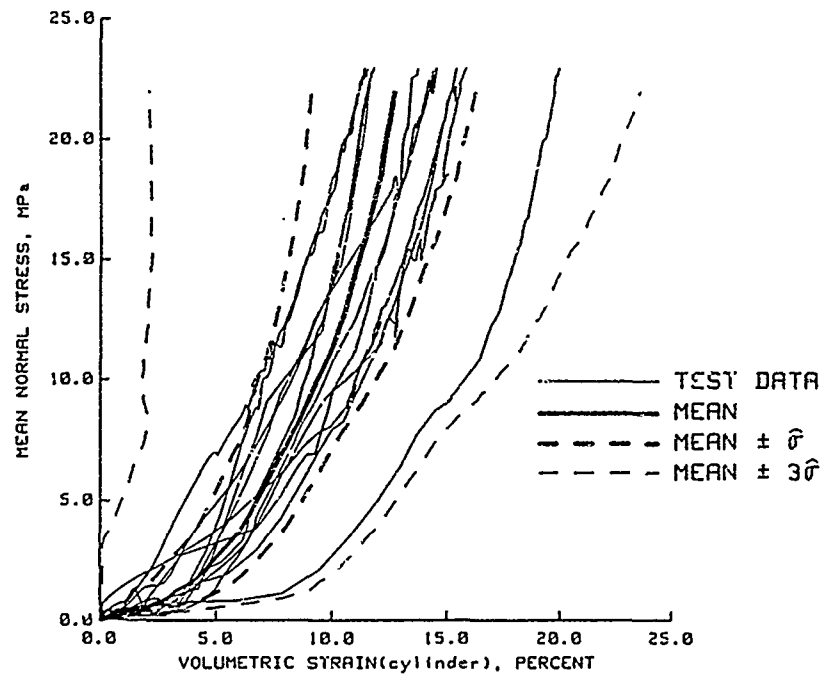
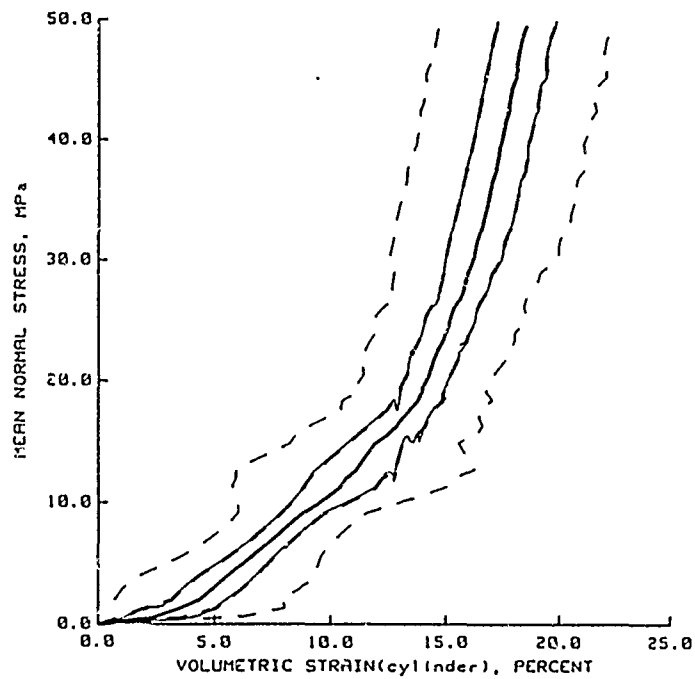


Figure 3.38. Results from the COV analysis of the loading portion of confining pressure versus radial strain static HC test data.

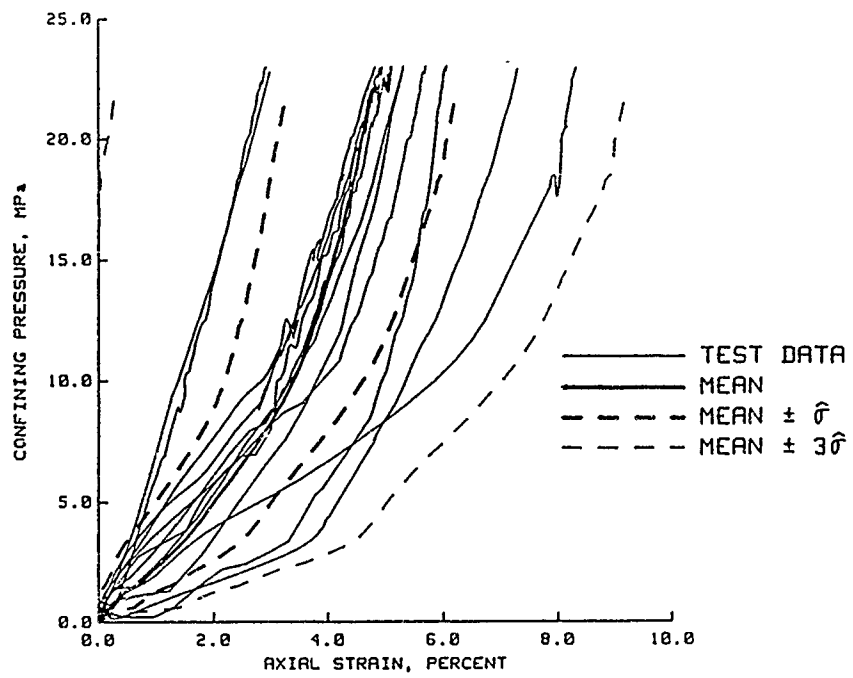


a. Group 1.

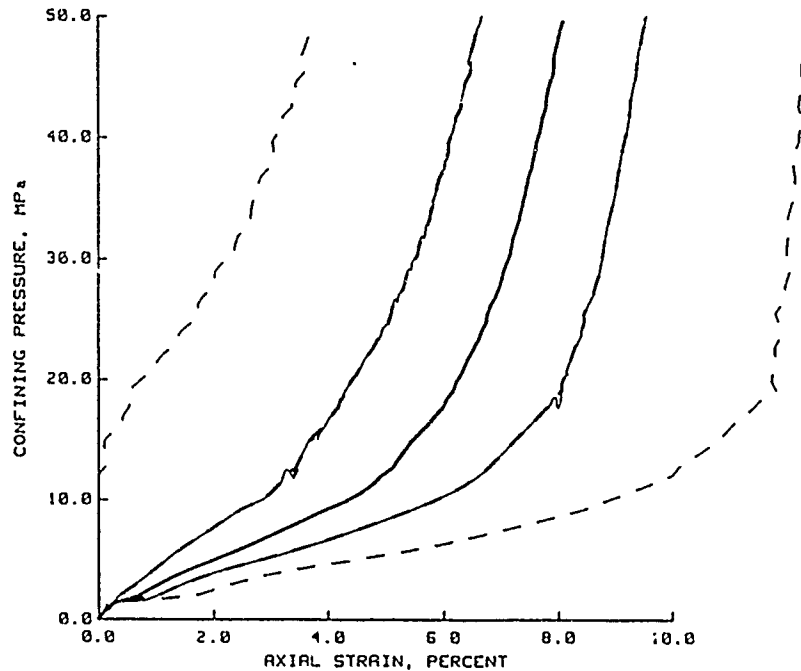


b. Group 2.

Figure 3.39. Results from the COV analysis of the loading portion of dynamic HC test data plotted in a form that is conducive to constitutive modeling.

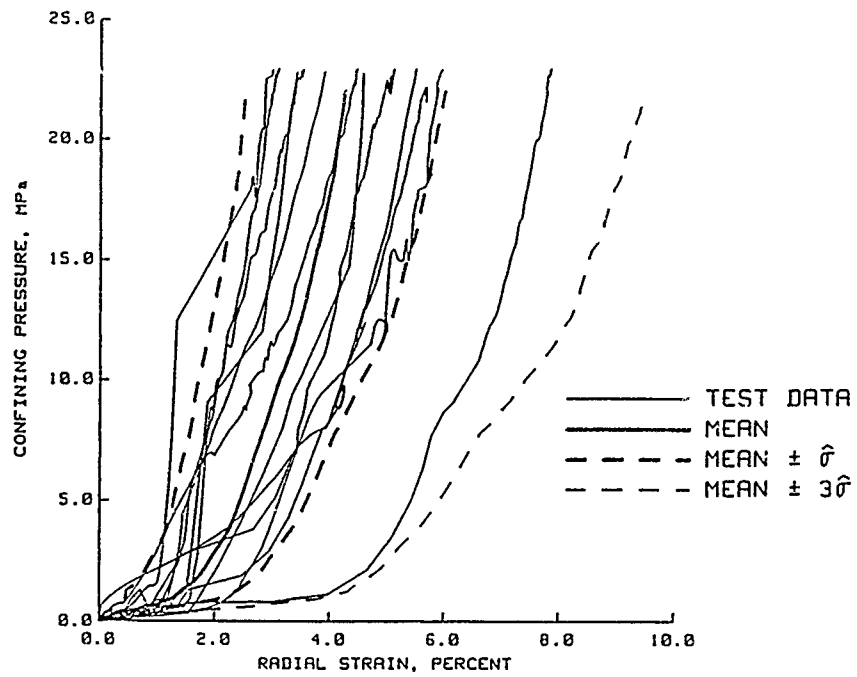


a. Group 1.

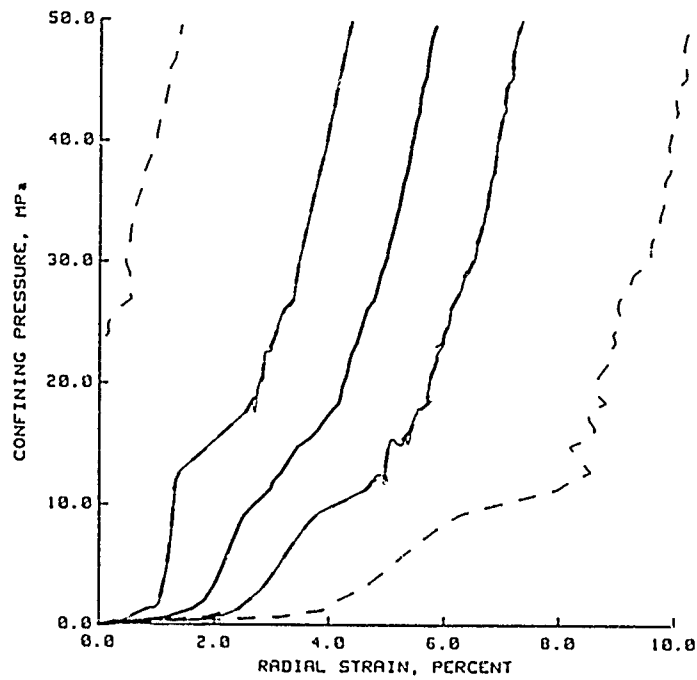


b. Group 2.

Figure 3.40. Results from the COV analysis of the loading portion of confining pressure versus axial strain dynamic HC test data.

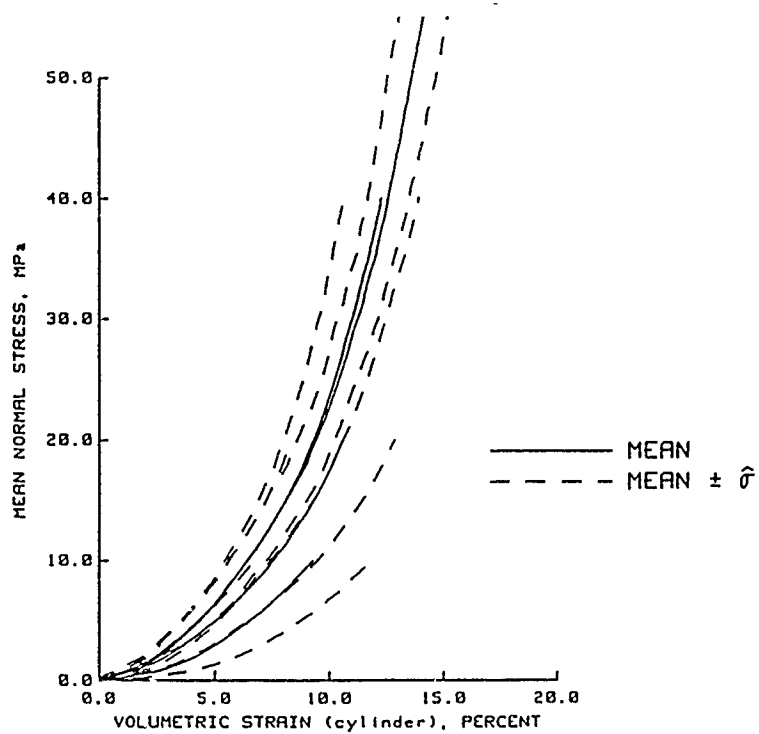


a. Group 1.

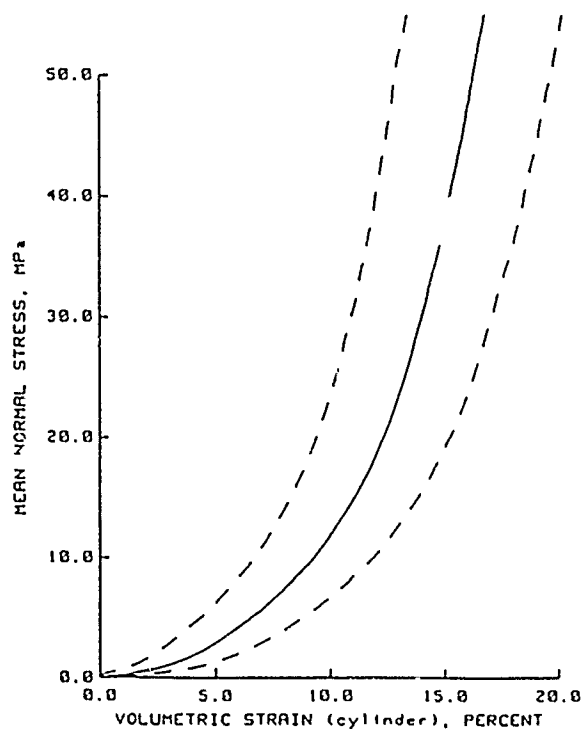


b. Group 2.

Figure 3.41. Results from the COV analysis of the loading portion of confining pressure versus radial strain dynamic HC test data.

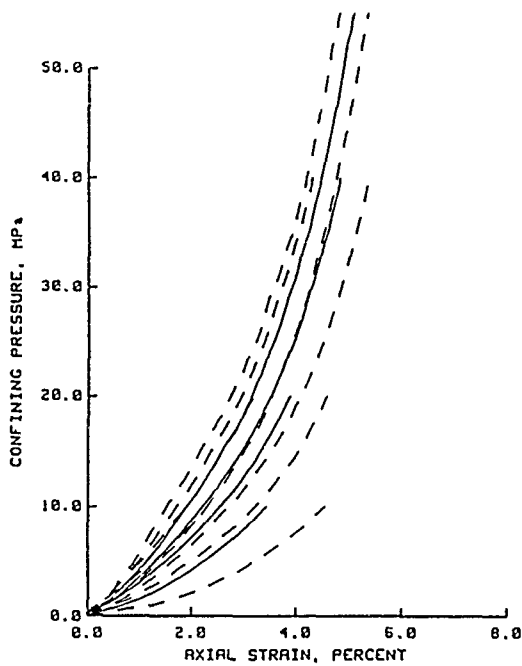


a. Composite plot.

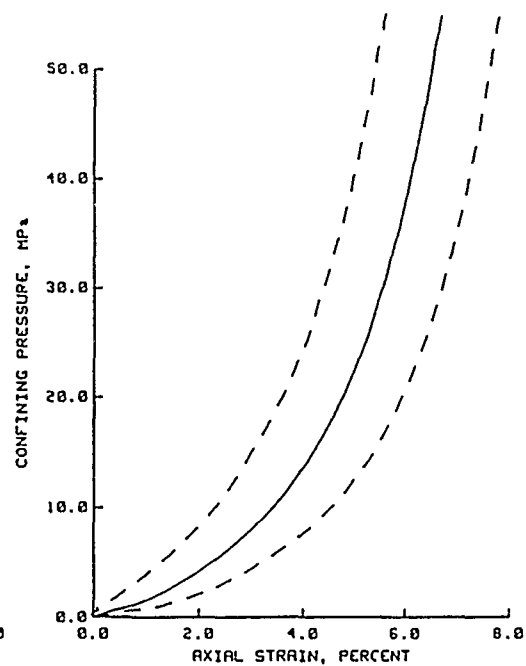


b. Constructed continuous plot.

Figure 3.42. Composite and constructed continuous results from the COV analysis of the loading portion of static HC test data plotted in a form that is conducive to constitutive modeling.

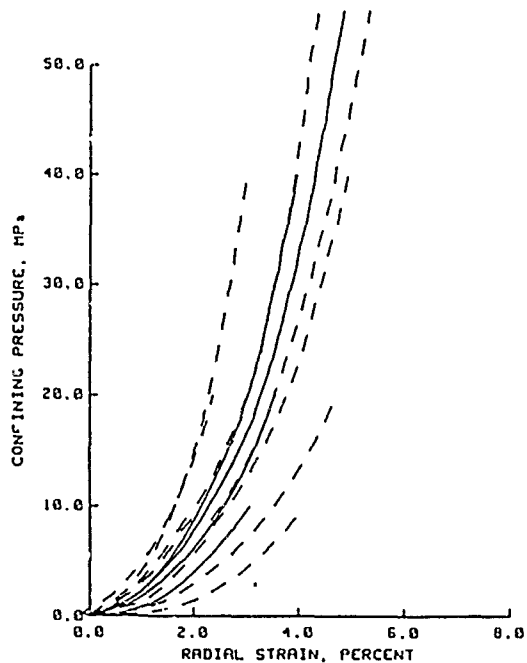


a. Composite plot of confining pressure versus axial strain.

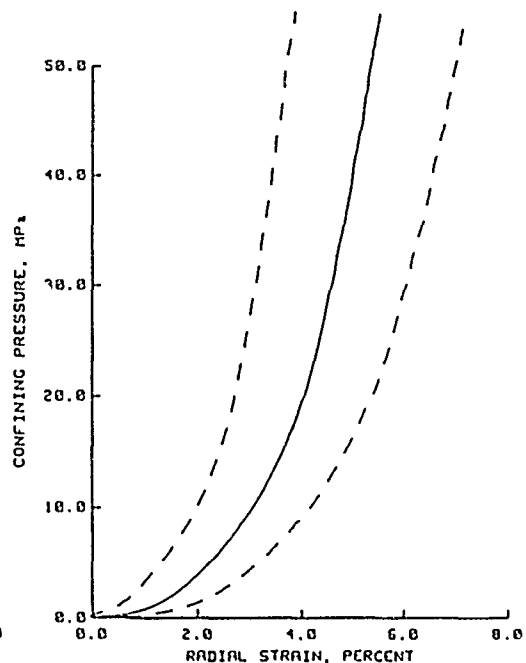


b. Constructed continuous plot of confining pressure versus axial strain.

— MEAN
 - - - MEAN $\pm \sigma$

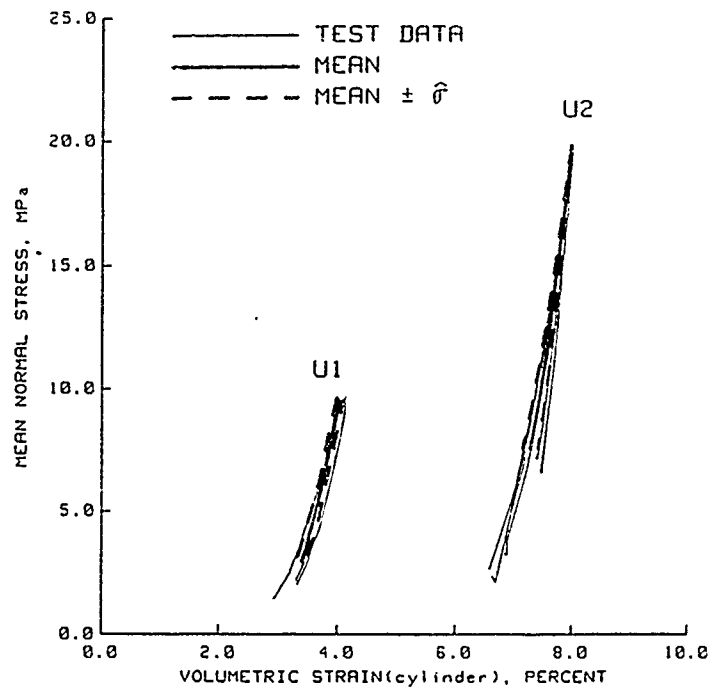


c. Composite plot of confining pressure versus radial strain.

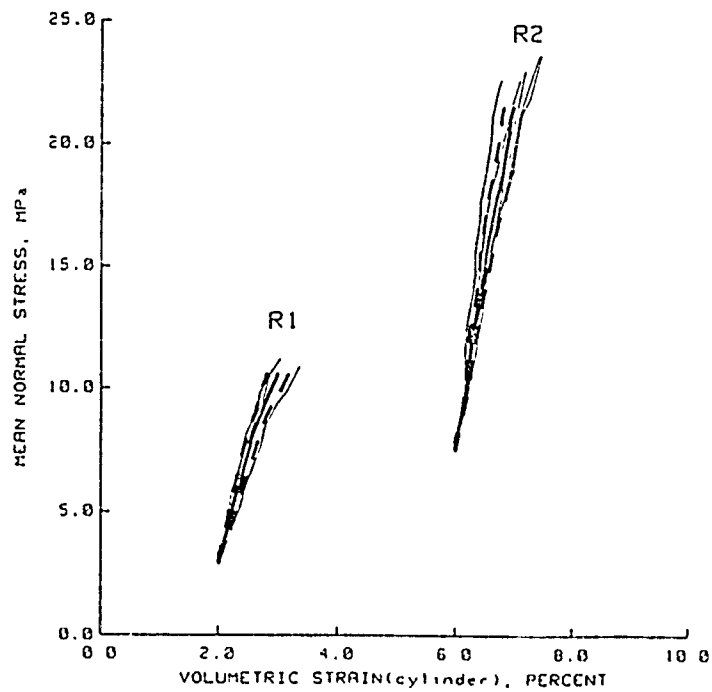


d. Constructed continuous plot of confining pressure versus radial strain.

Figure 3.43. Composite and constructed continuous results from the COV analysis of "measured" static HC test data.

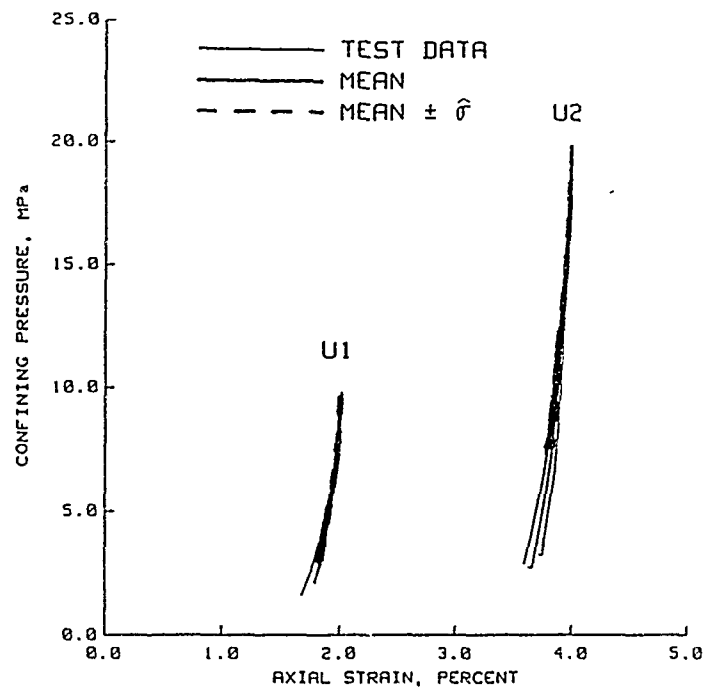


a. Unloading groups U1 and U2.

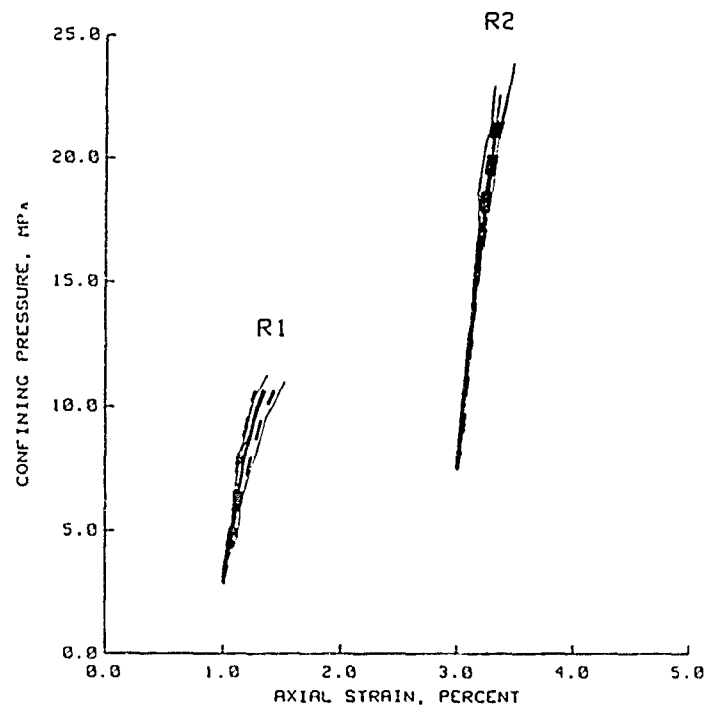


b. Reloading groups R1 and R2.

Figure 3.44. Results from the COV analysis of the unloading and reloading portions of static HC test data plotted in a form that is conducive to constitutive modeling.

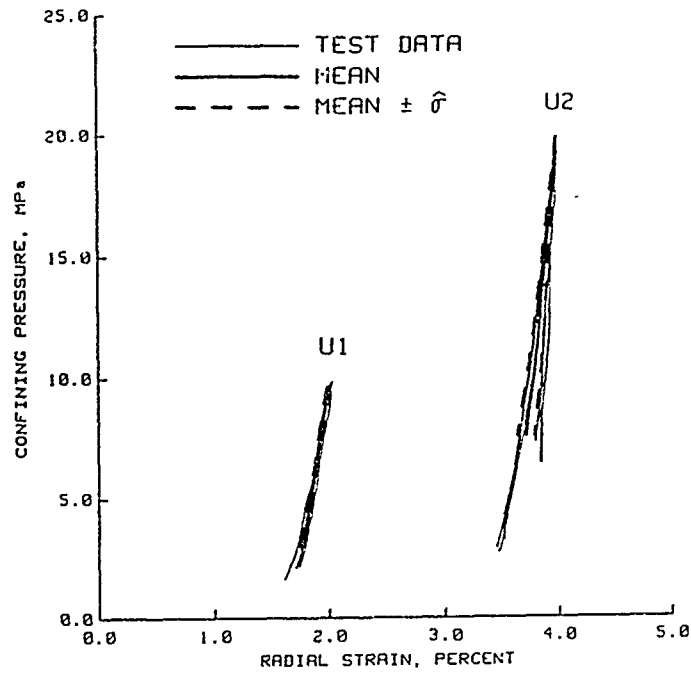


a. Unloading groups U1 and U2.

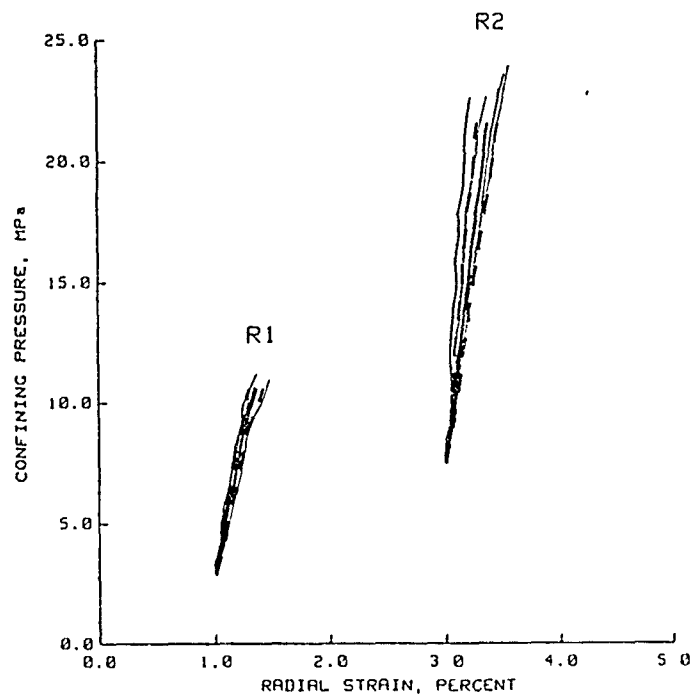


b. Reloading groups R1 and R2.

Figure 3.45. Results from the COV analysis of the unloading and reloading portions of confining pressure versus axial strain static HC test data.



a. Unloading groups U1 and U2.



b. Reloading Groups R1 and R2.

Figure 3.46. Results from the COV analysis of the unloading and reloading portions of confining pressure versus radial strain static HC test data.

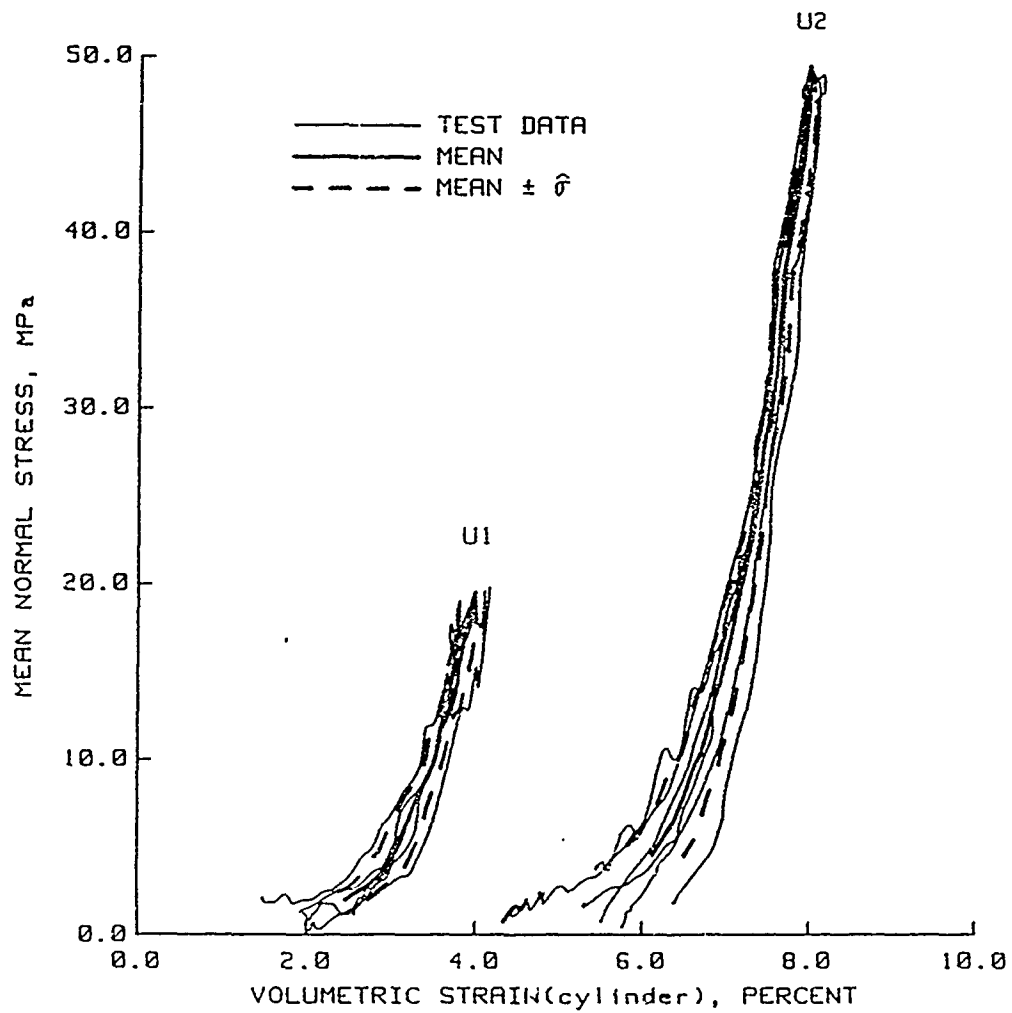
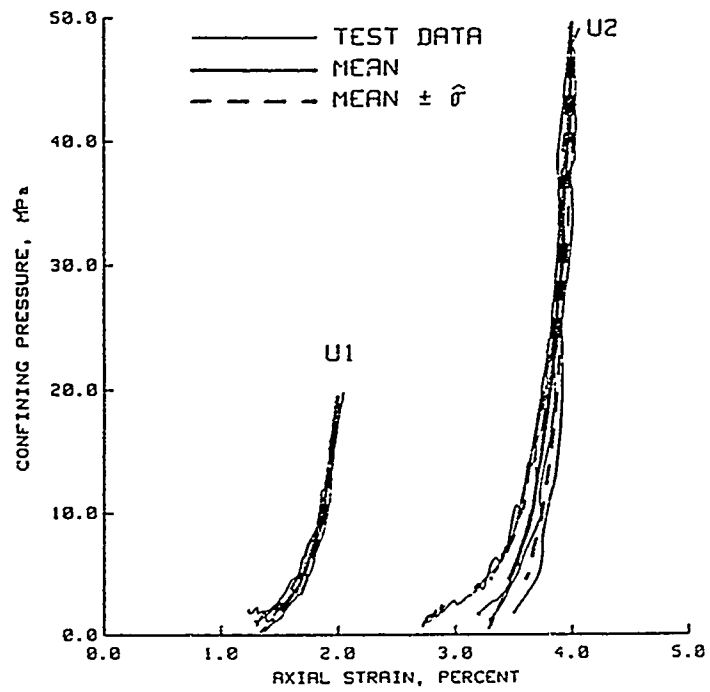
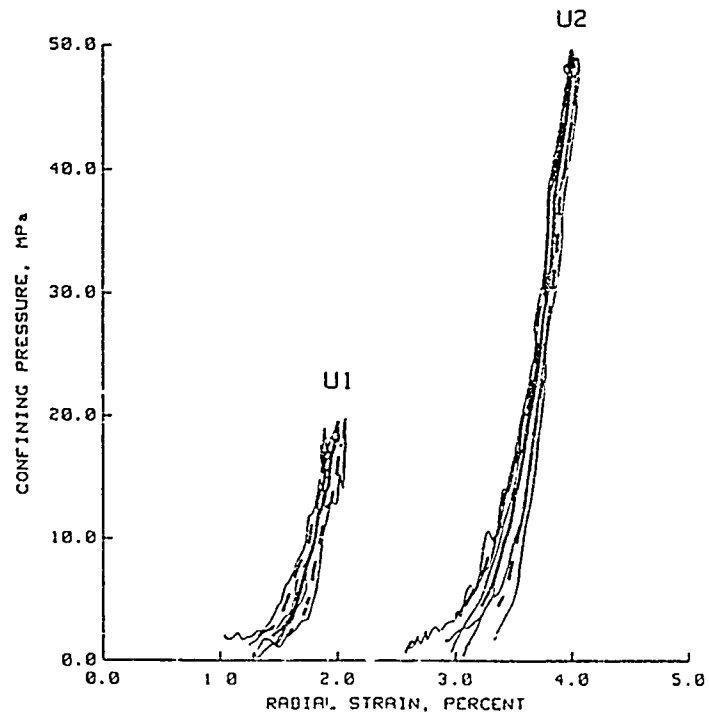


Figure 3.47. Results from the COV analysis of the unloading portion of dynamic HC test data plotted in a form that is conducive to constitutive modeling.



a. Confining pressure versus axial strain.



b. Confining pressure versus radial strain.

Figure 3.48. Results from the COV analysis of the unloading portions of "measured" dynamic HC test data.

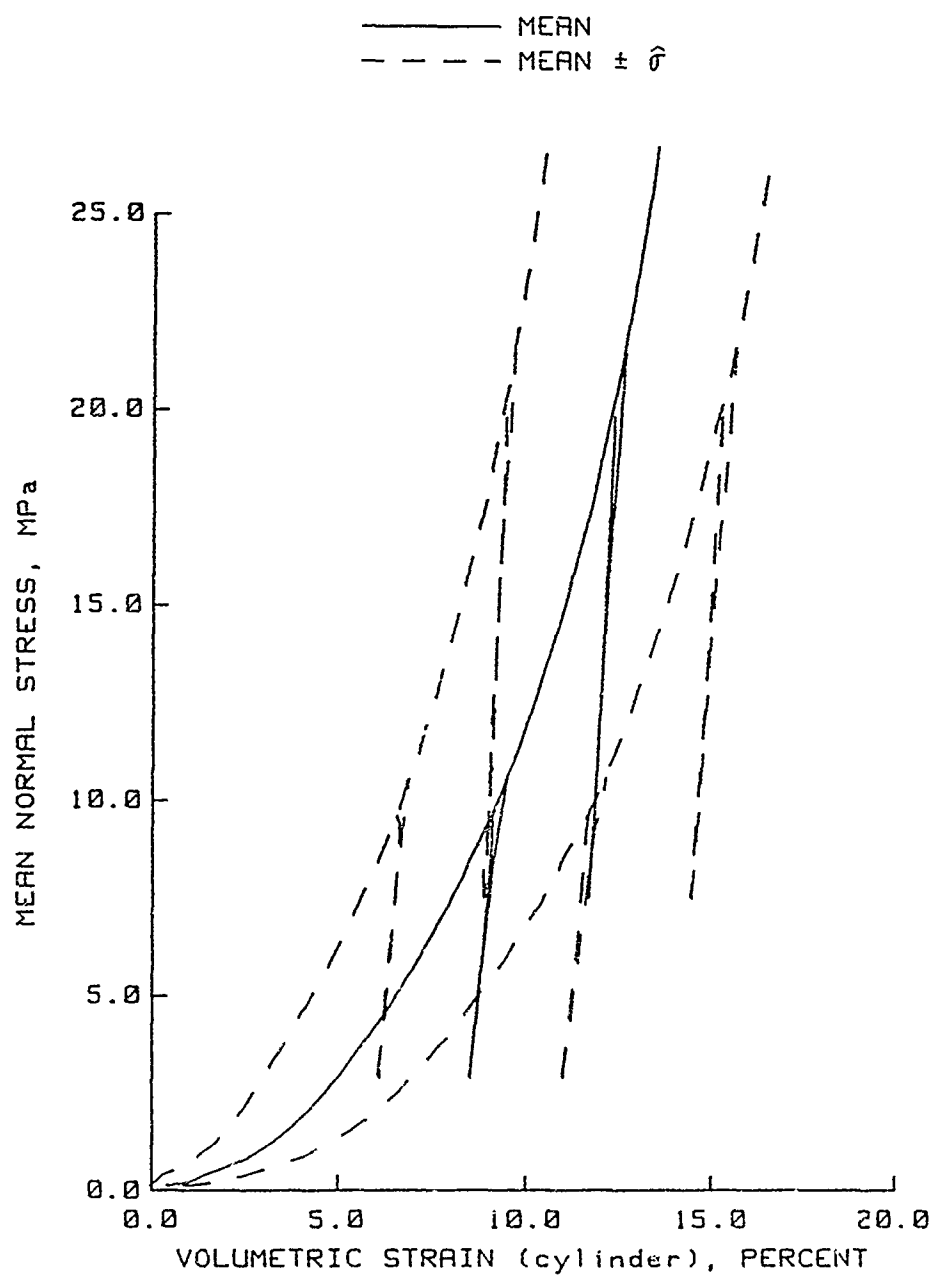


Figure 3.49. Load-unload-reload responses constructed from the results of the COV analysis of static HC test data plotted in a form that is conducive to constitutive modeling.

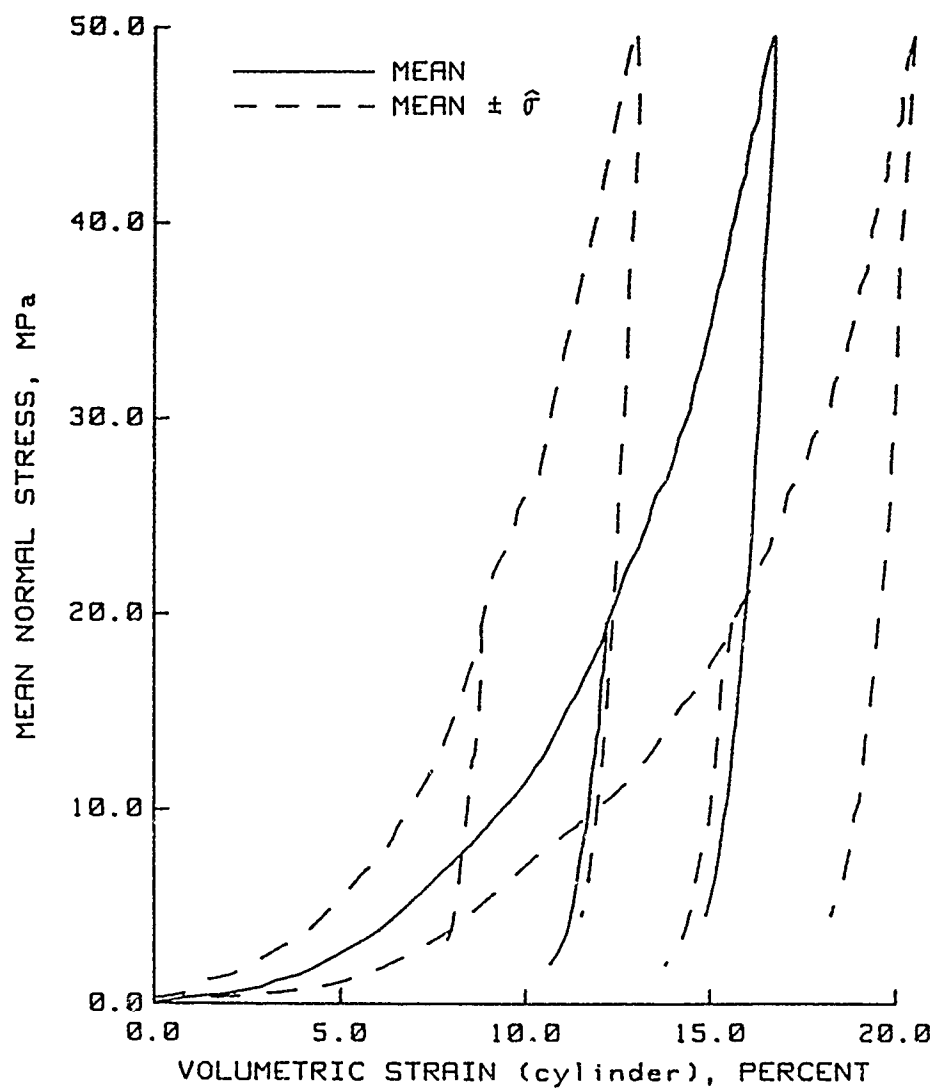


Figure 3.50. Load-unload responses constructed from the results of the COV analysis of dynamic HC test data plotted in a form that is conducive to constitutive modeling.

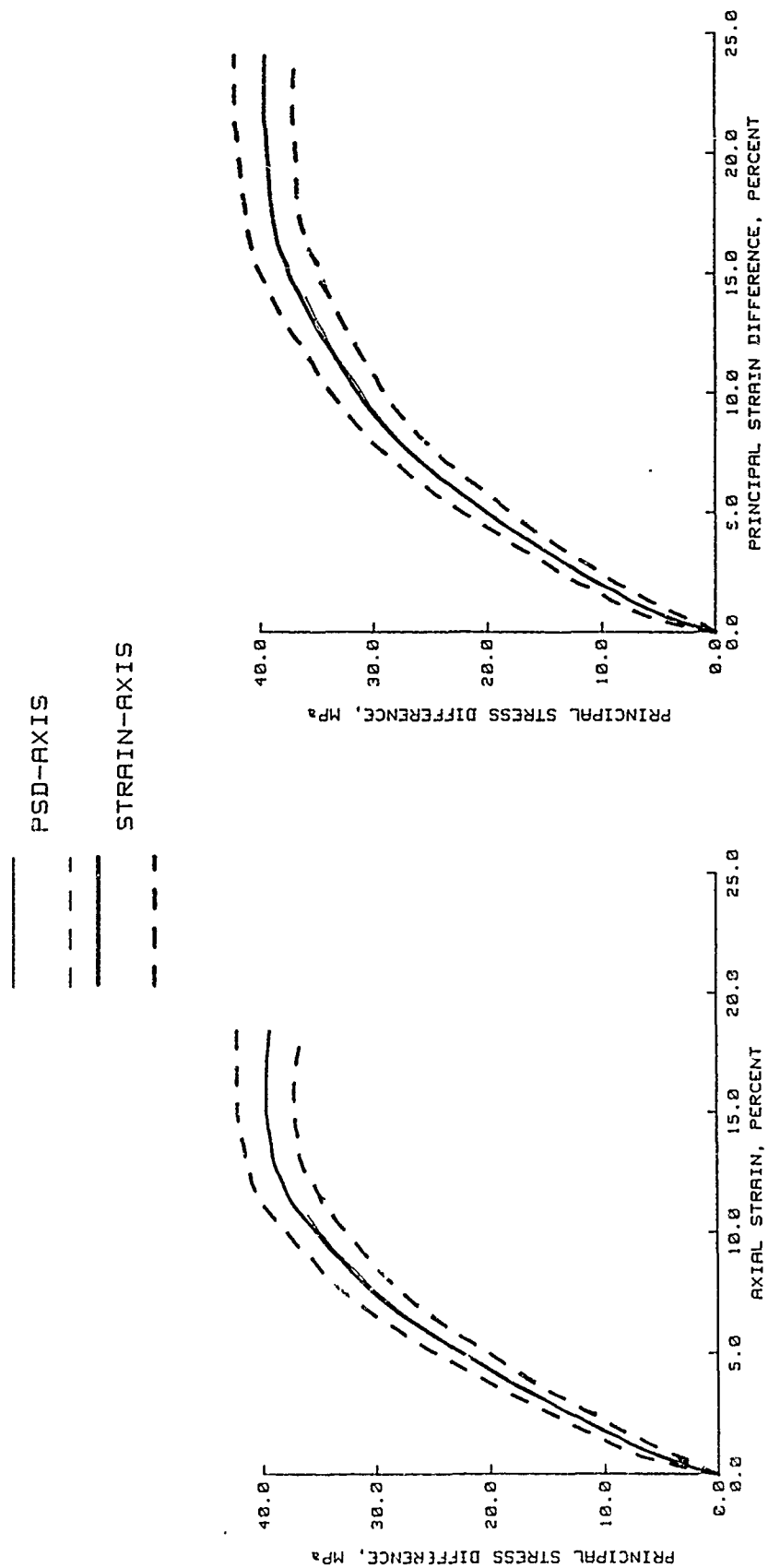


Figure 3.51. Effect of incrementing the PSD-axis as opposed to the strain-axis in the COV analysis of TXC test data plotted in forms that are conducive to constitutive modeling.

— TEST DATA
 — MEAN
 - - - MEAN $\pm \hat{\sigma}$

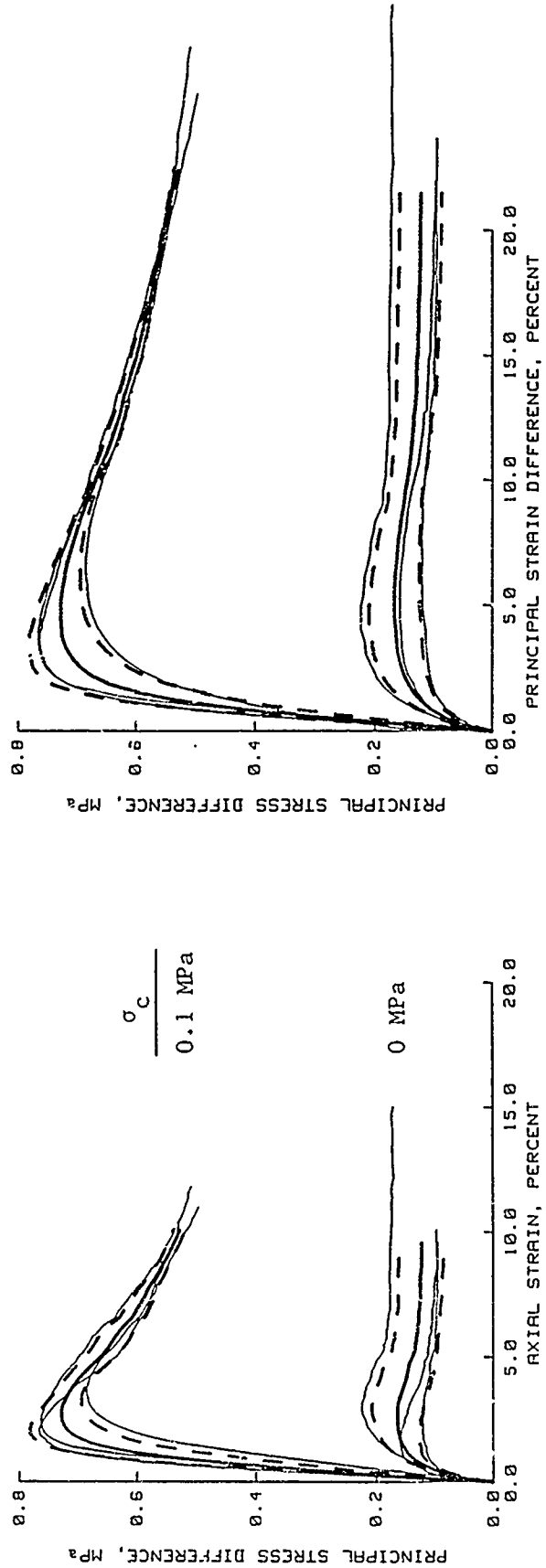


Figure 3.52. Results from the COV analysis of the loading portion of TXC test data plotted in forms that are conducive to constitutive modeling for $\sigma_c = 0$ and 0.1 MPa.

——— TEST DATA
 ——— MEAN
 - - - MEAN $\pm \sigma$

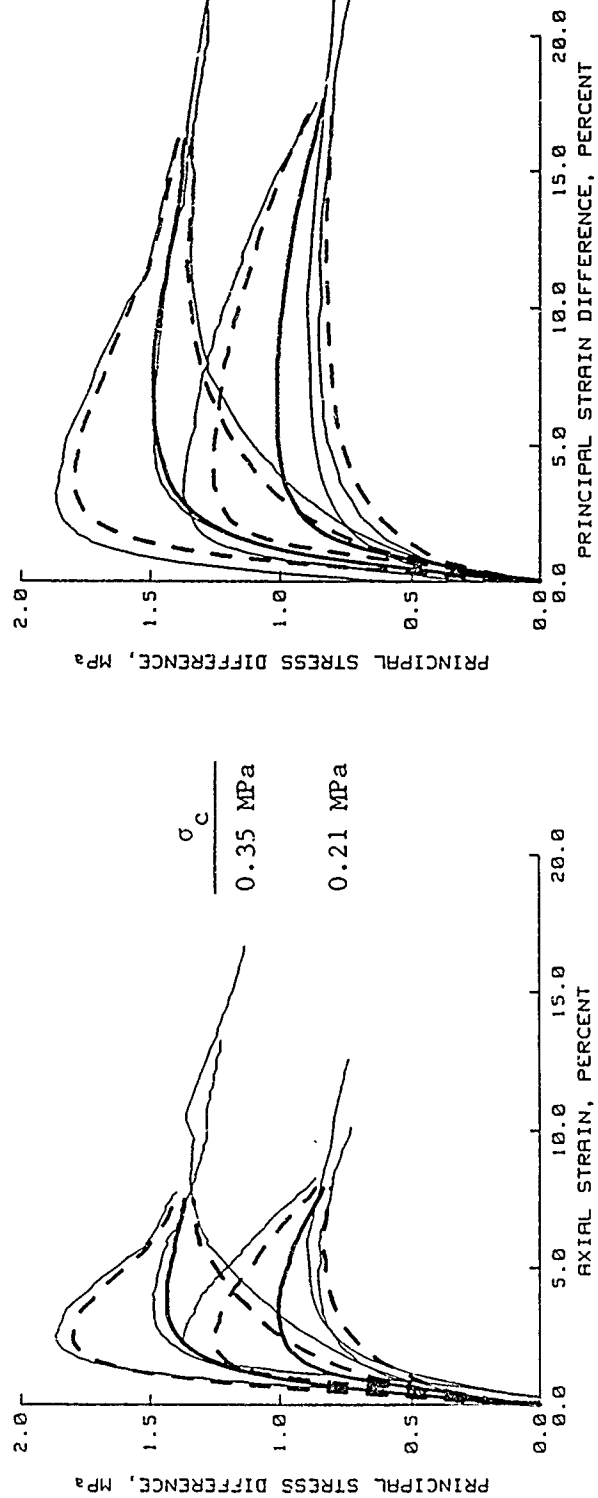


Figure 3.53. Results from the COV analysis of the loading portion of TXC test data plotted in forms that are conducive to constitutive modeling for $\sigma_c = 0.21$ and 0.35 MPa.

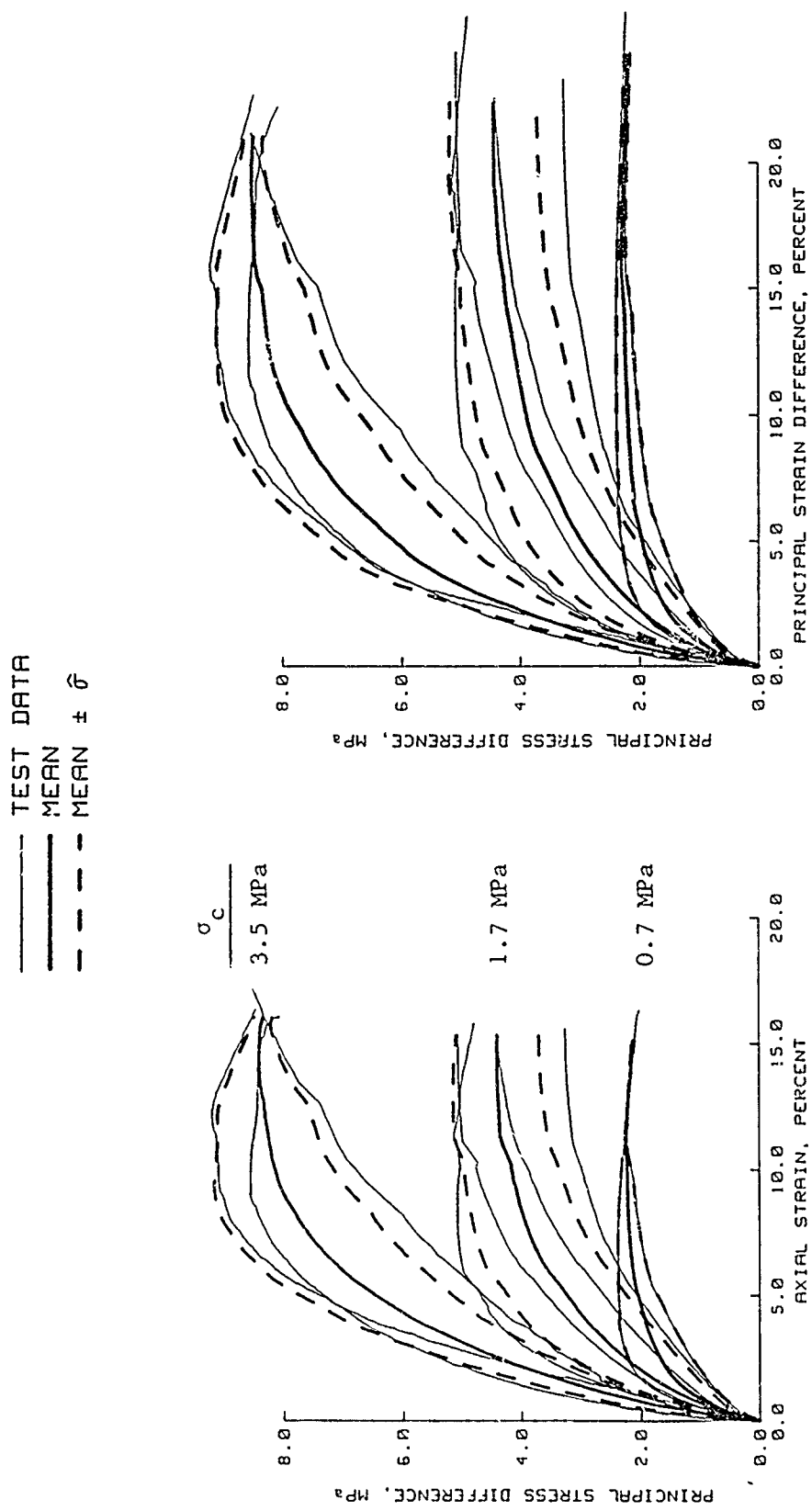


Figure 3.54. Results from the COV analysis of the loading portion of TXC test data plotted in forms that are conducive to constitutive modeling for $\sigma_c = 0.7$, 1.7, and 3.5 MPa.

TEST DATA
 ——— MEAN
 ——— MEAN $\pm \hat{\sigma}$
 - - - MEAN $\pm 3\hat{\sigma}$

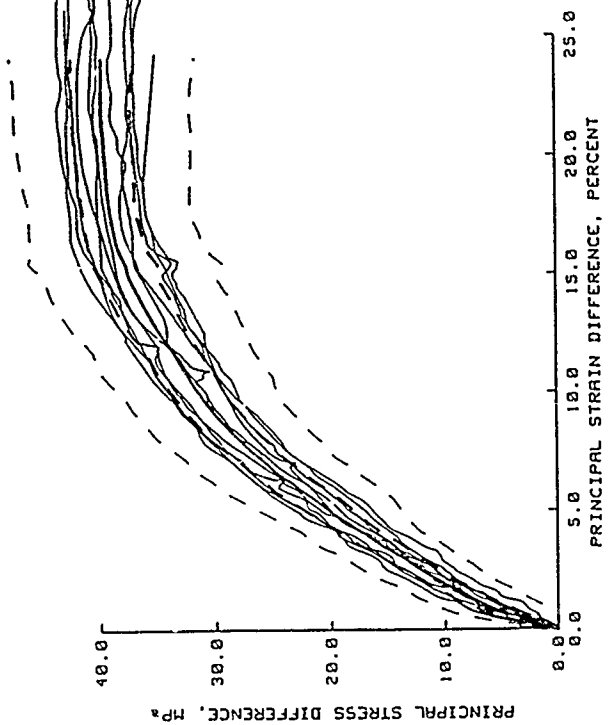
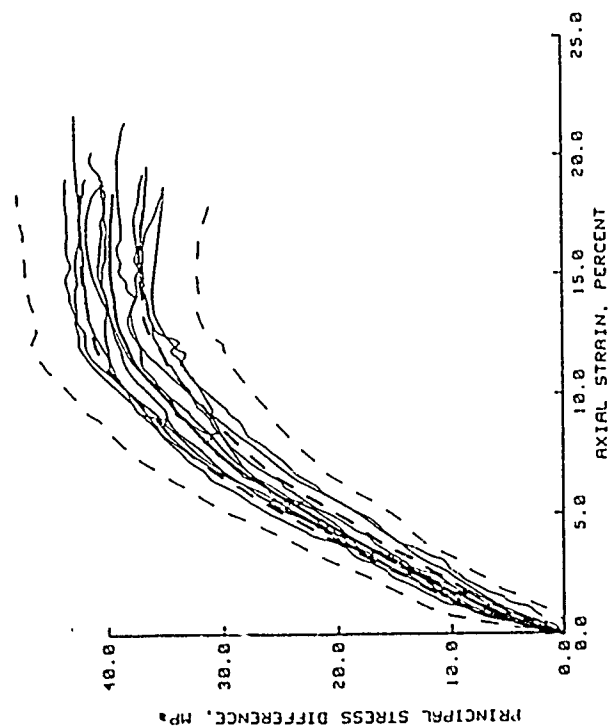


Figure 3.55. Results from the COV analysis of the loading portion of TXC test data plotted in forms that are conducive to constitutive modeling for $\sigma_c = 17.5$ MPa.

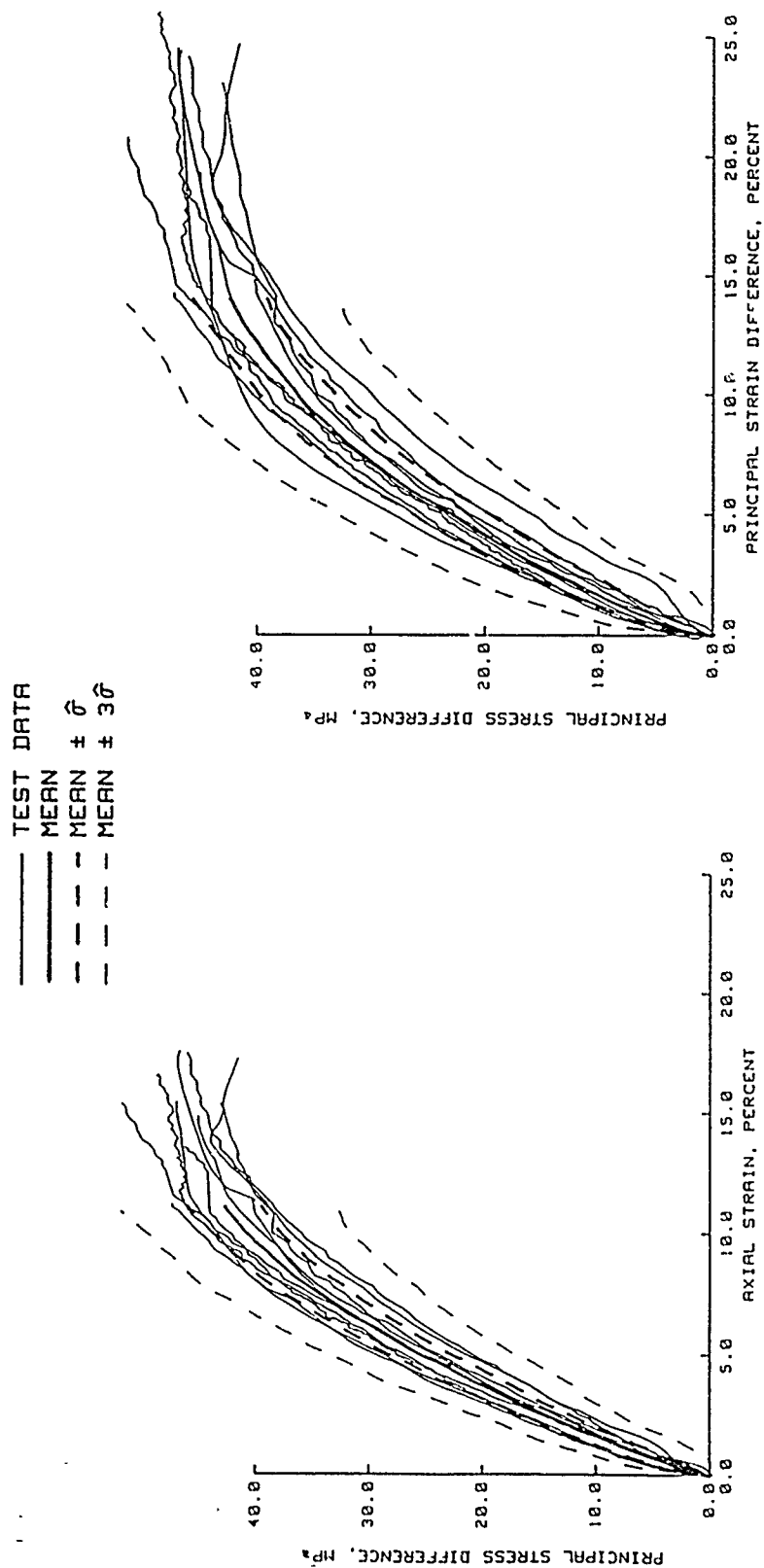


Figure 3.56. Results from the COV analysis of the loading portion of TXC test data plotted in forms that are conducive to constitutive modeling for $\sigma_c = 20.0$ MPa.

TEST DATA
 ——— MEAN
 - - - MEAN $\pm \hat{\sigma}$
 - - - MEAN $\pm 3\hat{\sigma}$

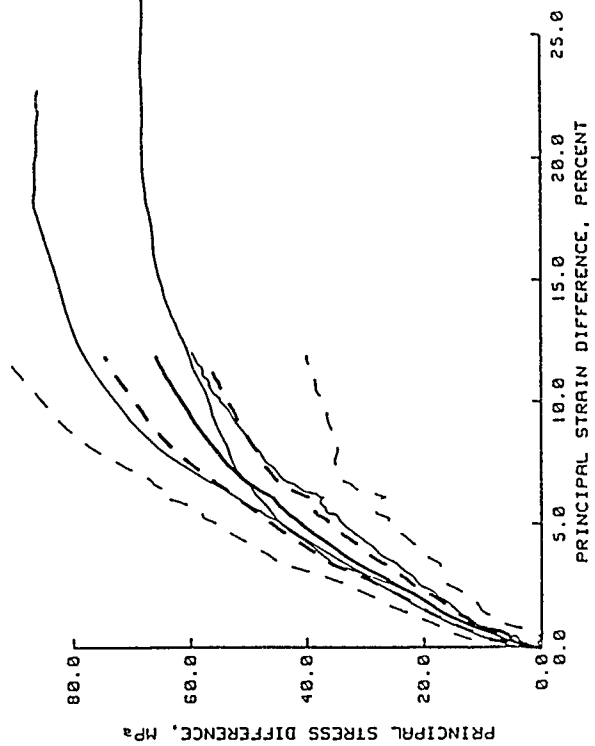
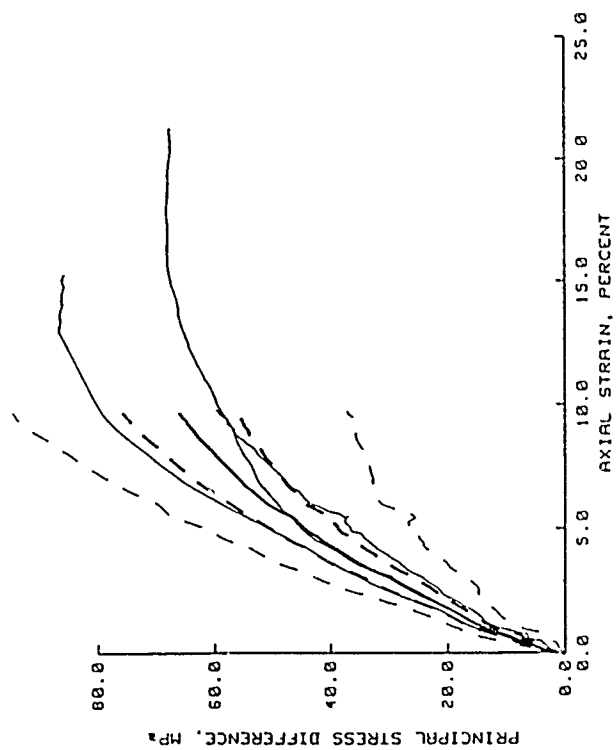


Figure 3.57. Results from the COV analysis of the loading portion of TXC test data plotted in forms that are conducive to constitutive modeling for $\sigma_c = 40.0$ MPa.

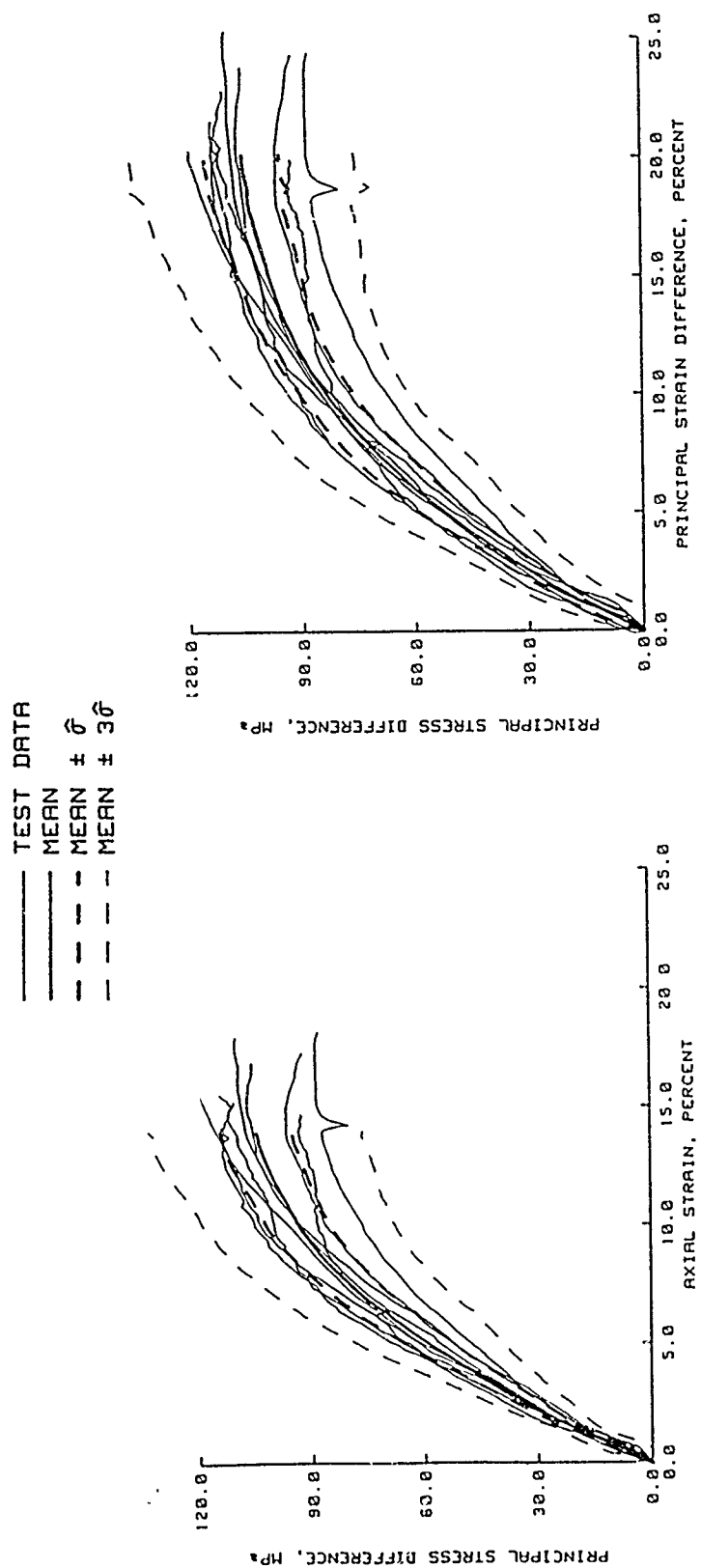


Figure 3.58. Results from the COV analysis of the loading portion of TXC test data plotted in forms that are conducive to constitutive modeling for $\sigma_c = 55.0$ MPa.

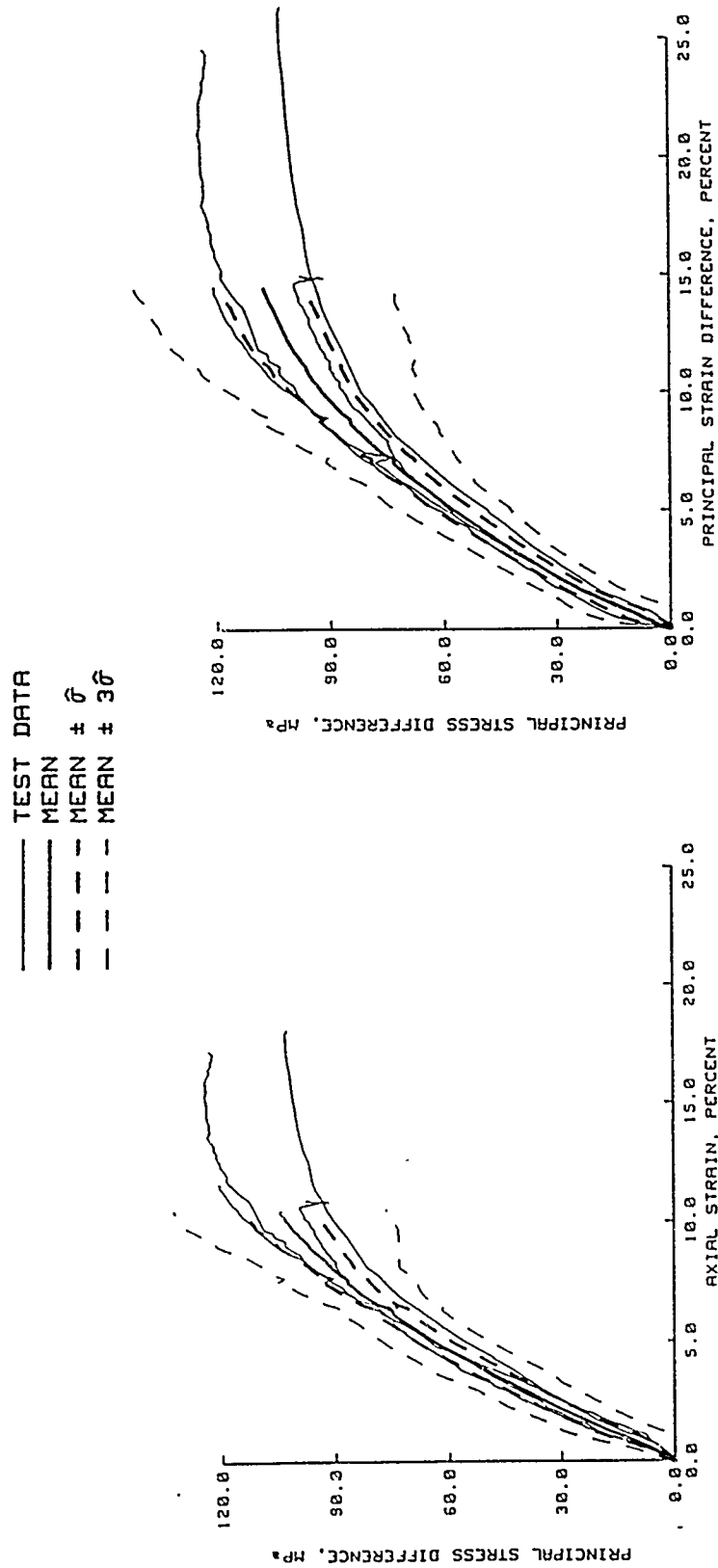


Figure 3.59. Results from the COV analysis of the loading portion of TXC test data plotted in forms that are conducive to constitutive modeling for $\sigma_c = 60.0$ MPa.

TEST DATA
 ——— MEAN
 - - - MEAN $\pm \sigma$
 - - - MEAN $\pm 3\sigma$

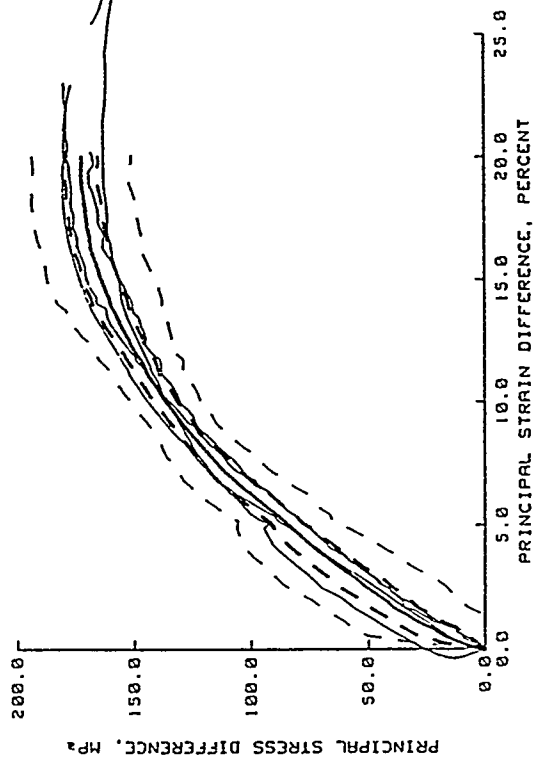
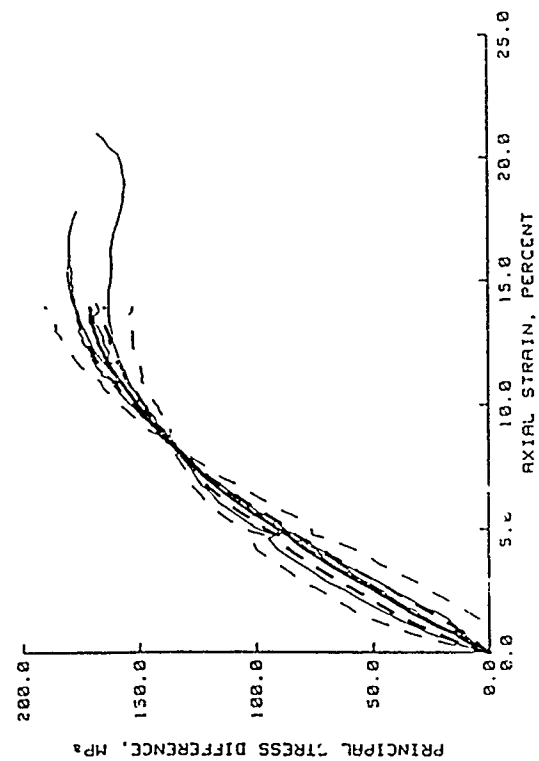


Figure 3.60. Results from the COV analysis of the loading portion of TXC test data plotted in forms that are conducive to constitutive modeling for $\sigma_c = 80.0$ MPa.

TEST DATA
 ——— MEAN
 - - - MEAN $\pm \hat{\sigma}$

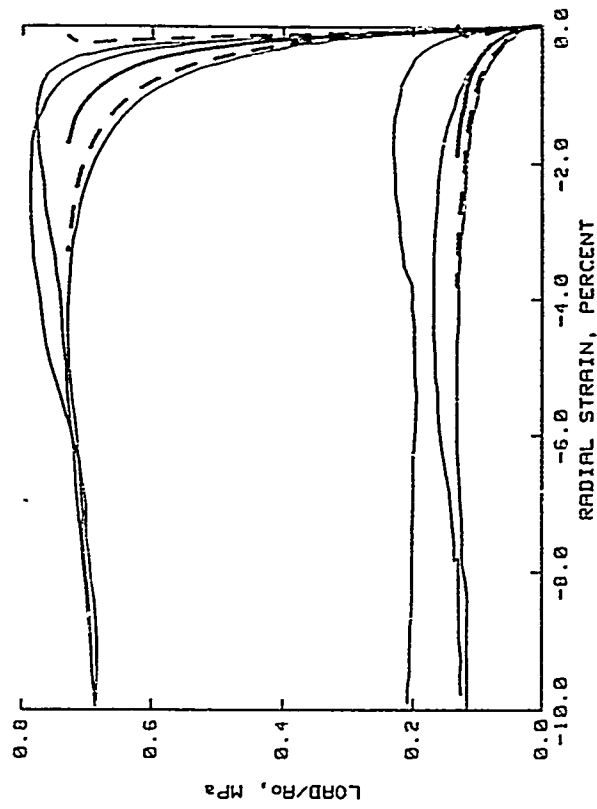
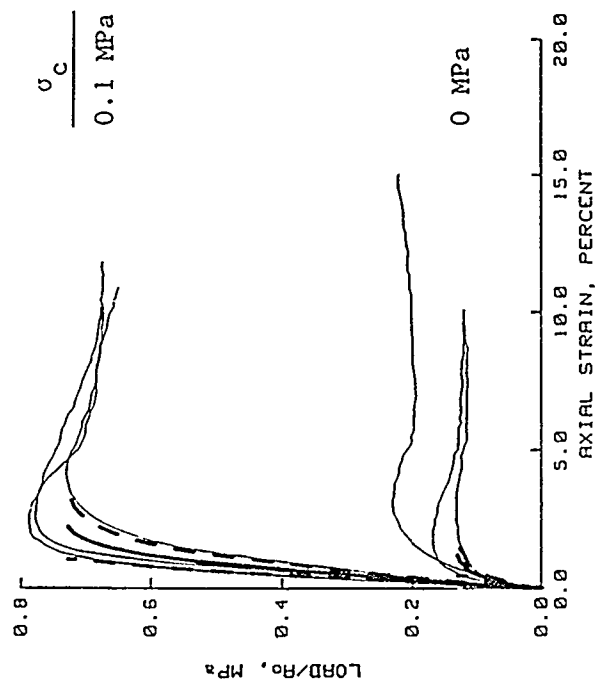


Figure 3.61. Results from the COV analysis of "measured data" plots of the loading portion of TXC test data for $\sigma_c = 0$ and 0.1 MPa.

TEST DATA
 ——— MEAN
 - - - MEAN $\pm \hat{\sigma}$

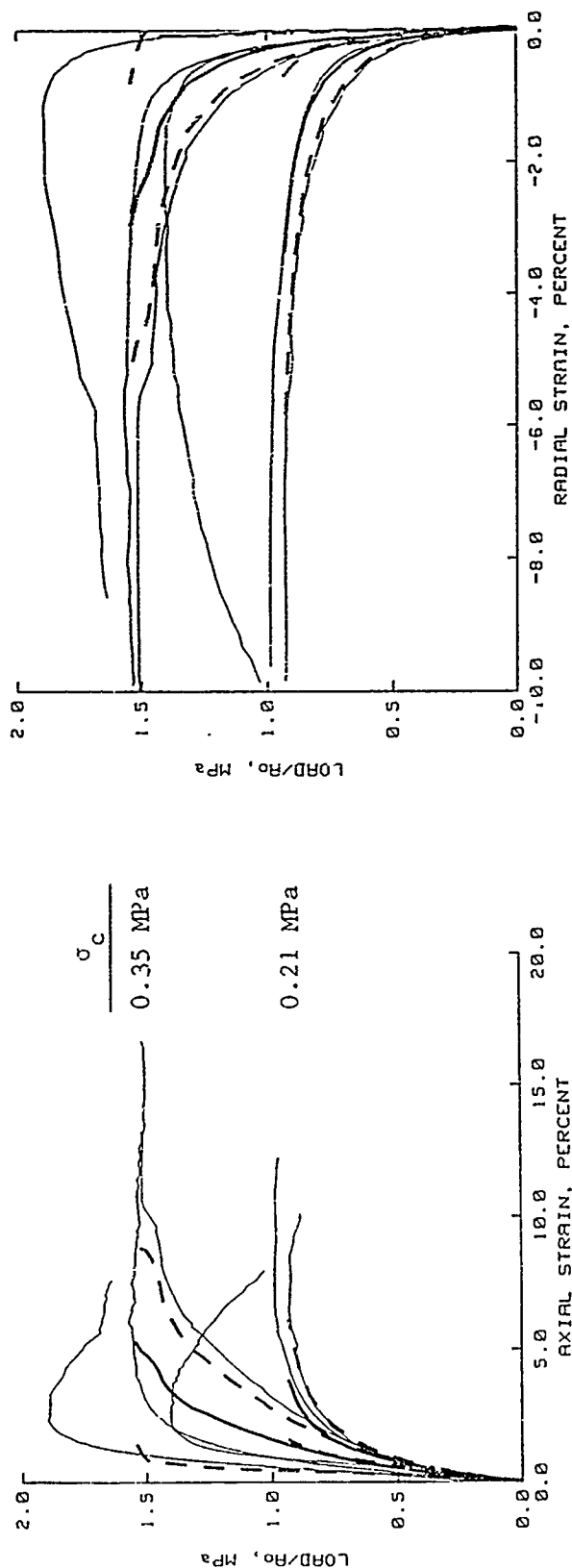


Figure 3.62. Results from the COV analysis of "measured data" plots of the loading portion of TXC test data for $\sigma_c = 0.21$ and 0.35 MPa.

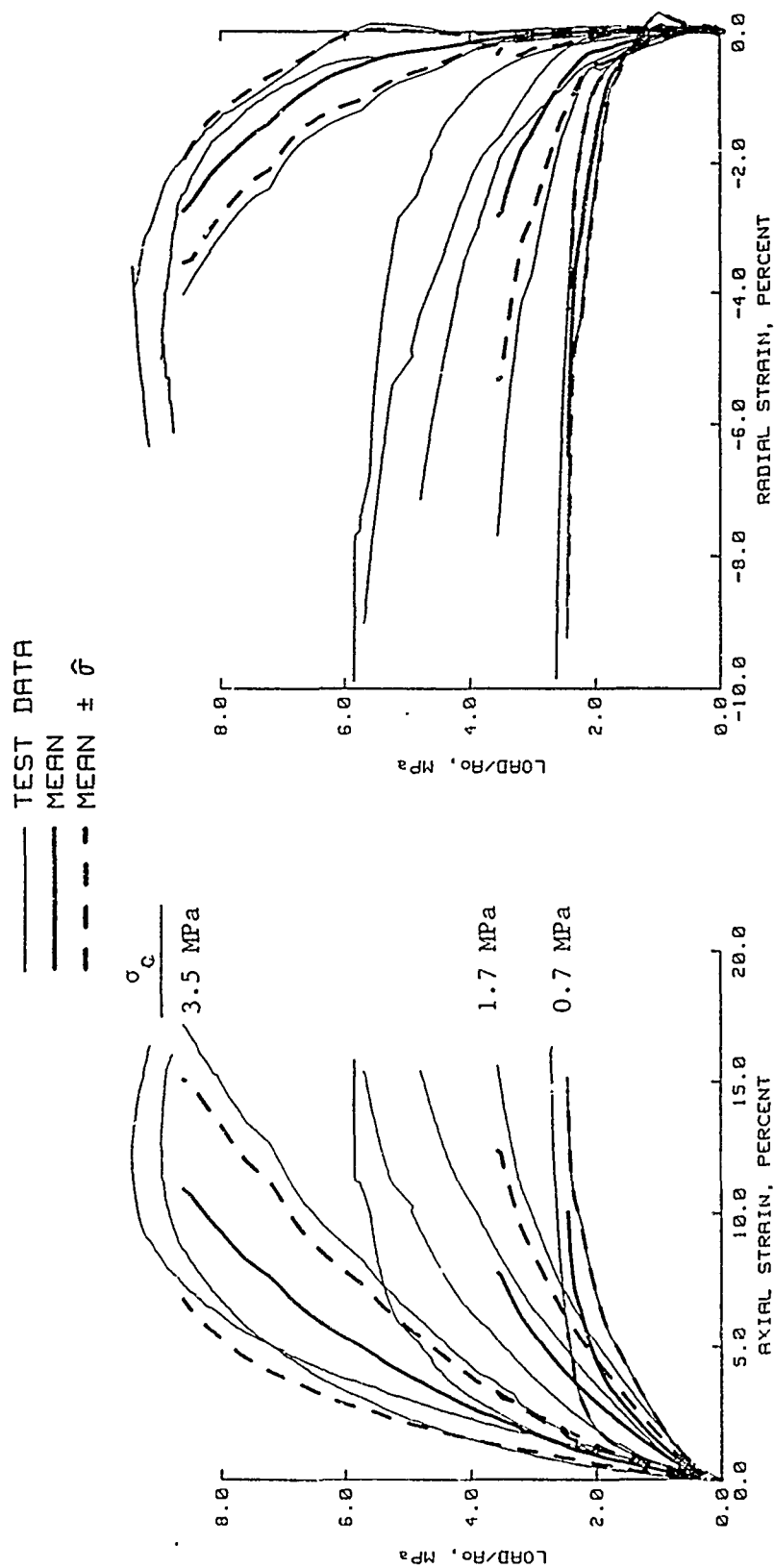


Figure 3.63. Results from the COV analysis of "measured data" plots of the loading portion of TXC test data for $\sigma_c = 0.7$, 1.7, and 3.5 MPa.

TEST DATA
 ——— MEAN
 - - - MEAN $\pm \sigma$
 - - - MEAN $\pm 3\sigma$

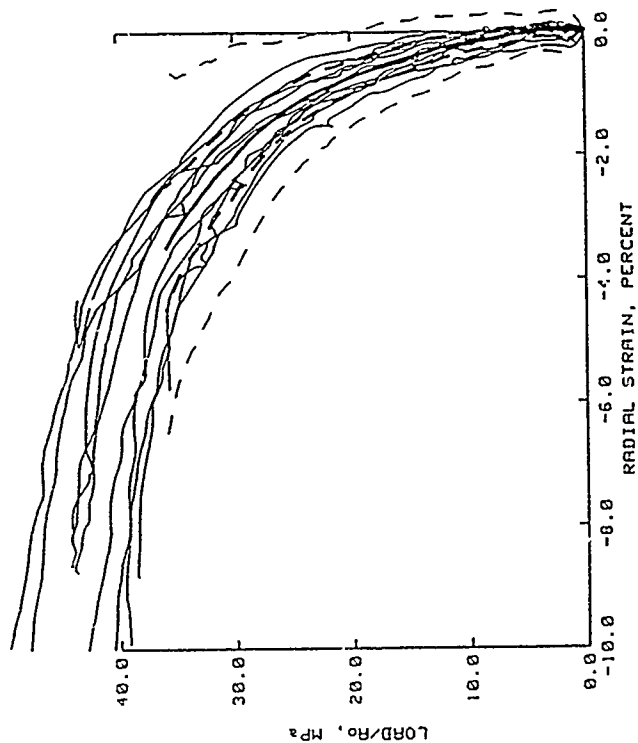
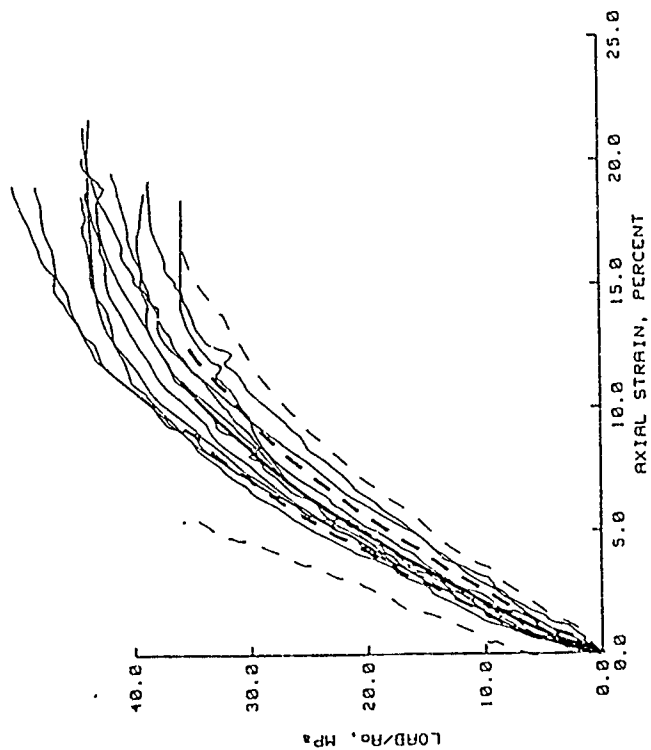


Figure 3.64. Results from the COV analysis of "measured data" plots of the loading portion of TXC test data for $\sigma_c = 17.5$ MPa.

TEST DATA
 ——— MEAN
 - - - MEAN $\pm \hat{\sigma}$
 - - - MEAN $\pm 3\hat{\sigma}$

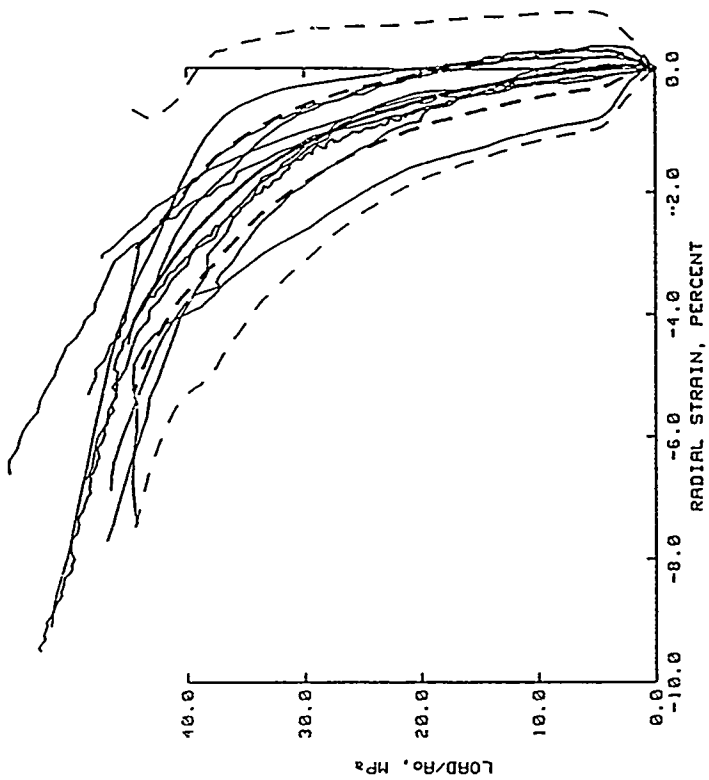
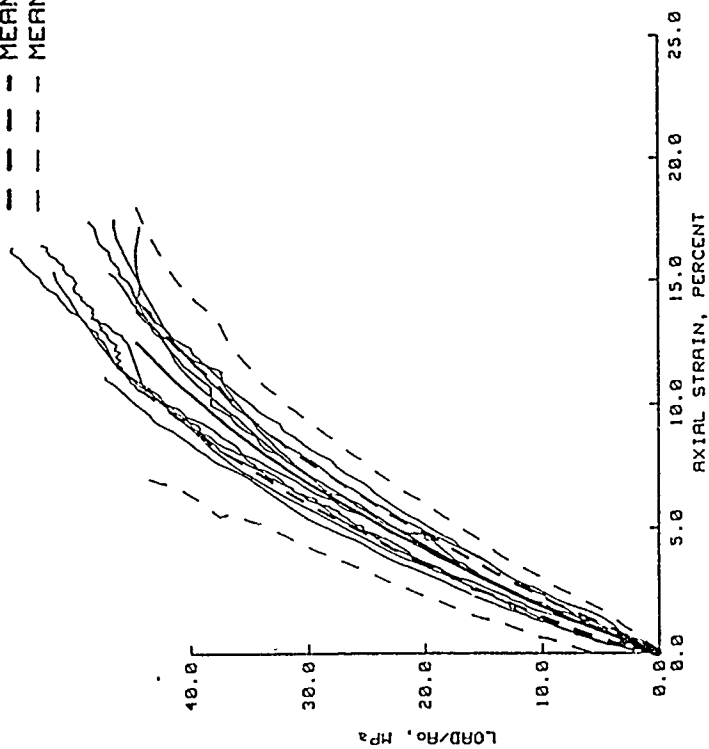


Figure 3.65. Results from the COV analysis of "measured data" plots of the loading portion of TXC test data for $\sigma_c = 20.0$ MPa.

TEST DATA
 ——— MEAN
 - - - MEAN $\pm \sigma$
 - - - MEAN $\pm 3\sigma$

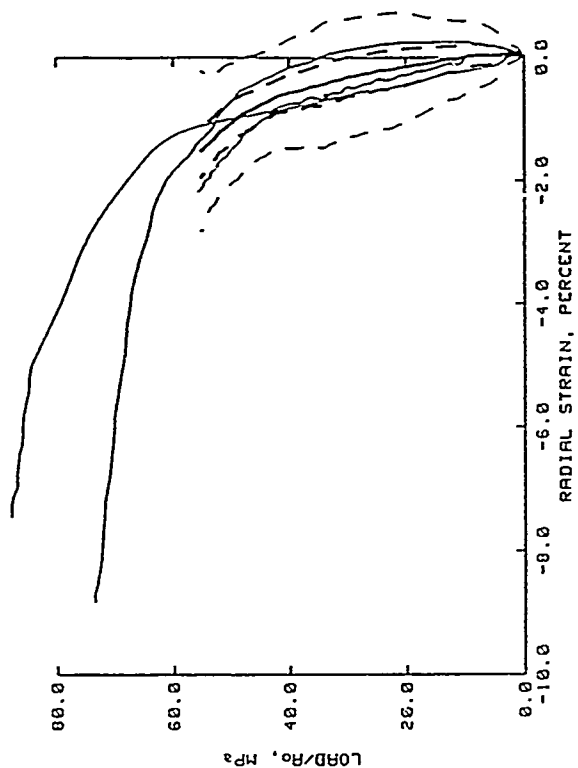
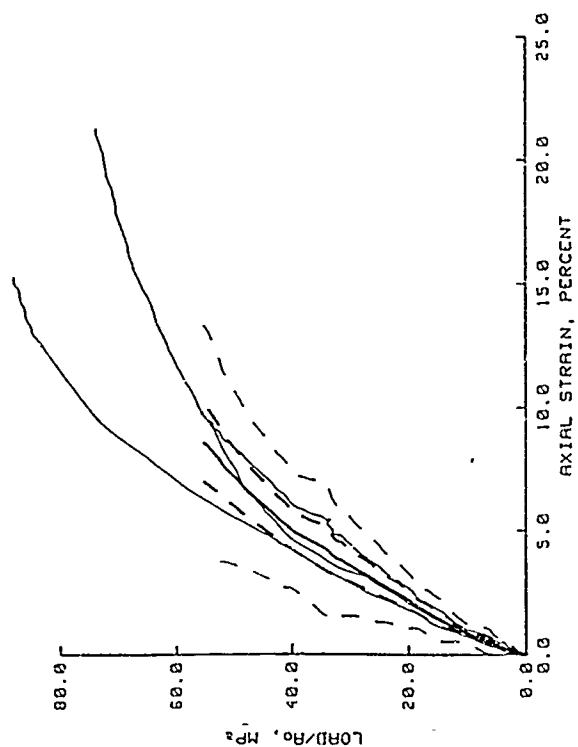


Figure 3.66. Results from the COV analysis of "measured data" plots of the loading portion of TXC test data for $\sigma_c = 40.0$ MPa.

TEST DATA
 ——— MEAN
 - - - MEAN $\pm \sigma$
 - - - MEAN $\pm 3\sigma$

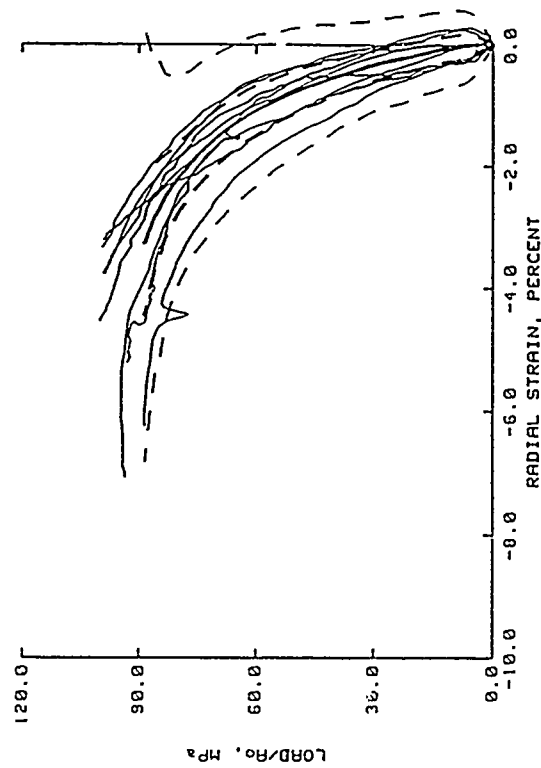
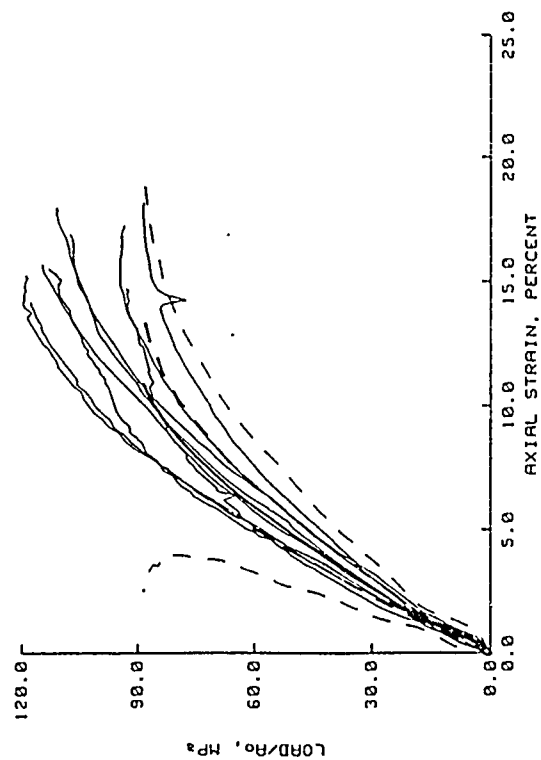


Figure 3.67. Results from the COV analysis of "measured data" plots of the loading portion of TXC test data for $\sigma_c = 55.0$ MPa.

TEST DATA
 ——— MEAN
 - - - MEAN $\pm \sigma$
 - - - MEAN $\pm 3\sigma$

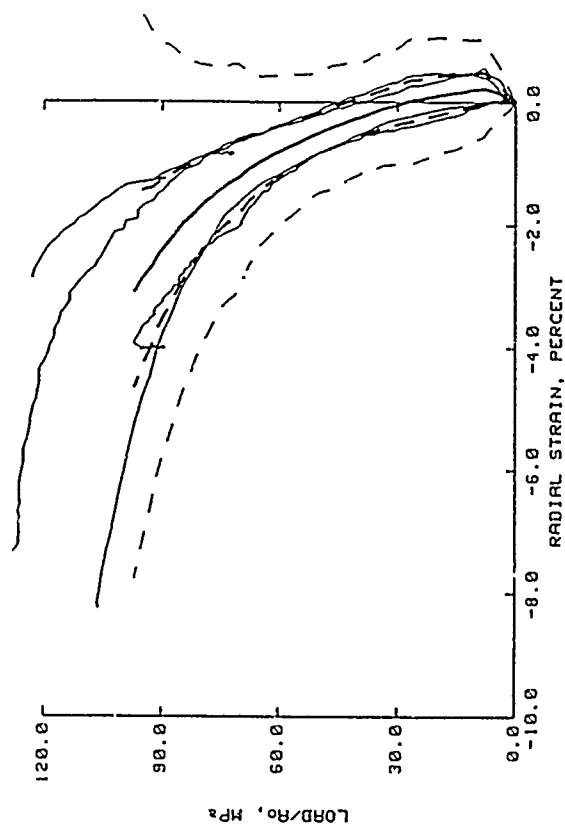
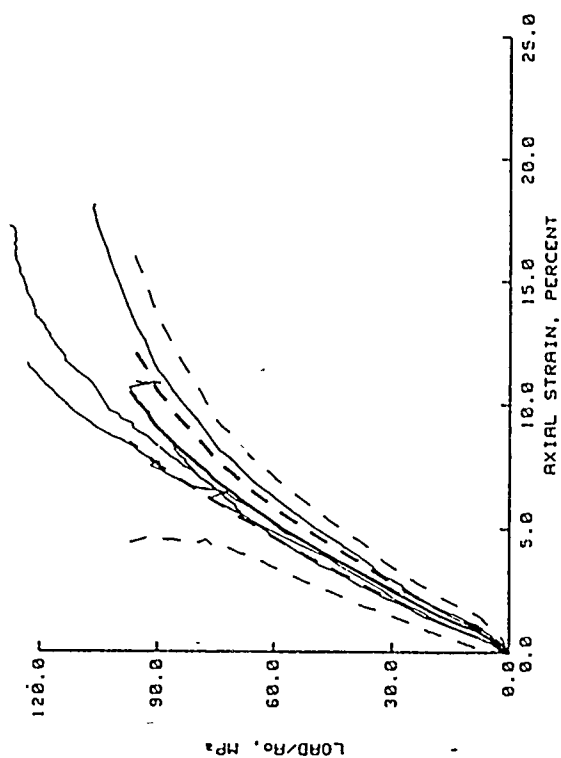


Figure 3.68. Results from the COV analysis of "measured data" plots of the loading portion of TXC test data for $\sigma_c = 60.0$ MPa.

— TEST DATA
 — MEAN
 - - - MEAN $\pm \sigma$
 - - - MEAN $\pm 3\sigma$

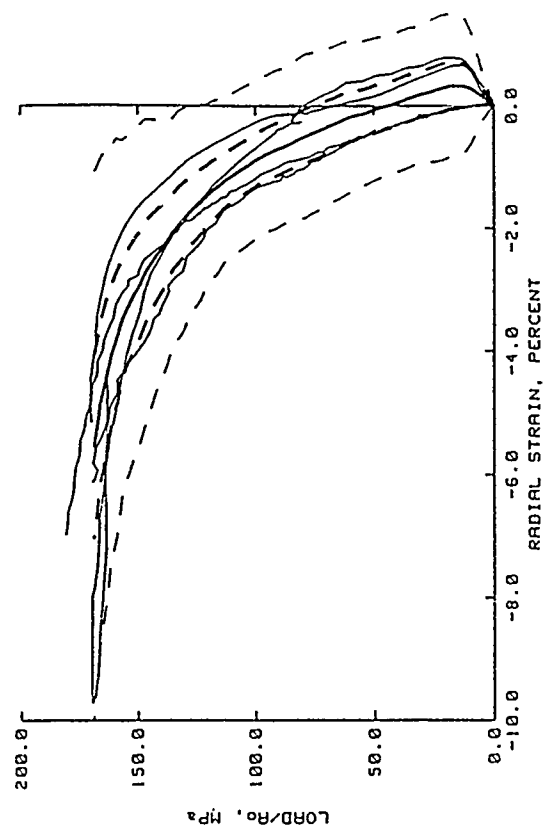
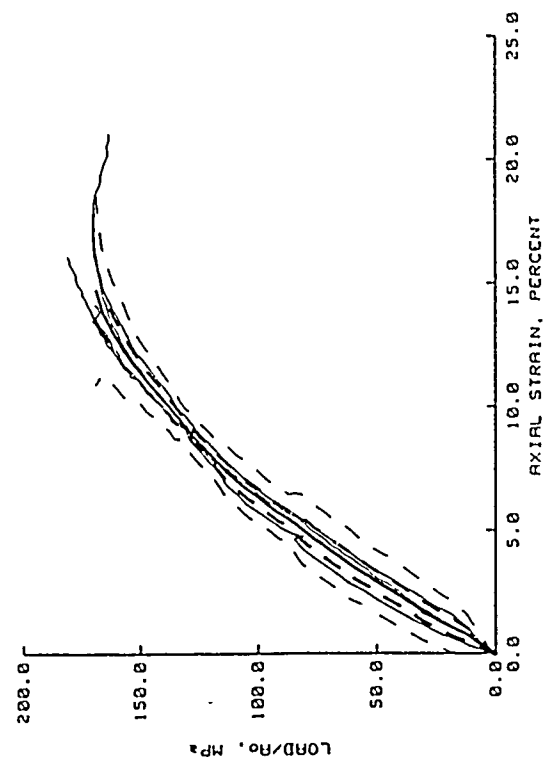


Figure 3.69. Results from the COV analysis of "measured data" plots of the loading portion of TXC test data for $\sigma_c = 80.0$ MPa.

TEST DATA
 ——— MEAN
 - - - MEAN $\pm \sigma$

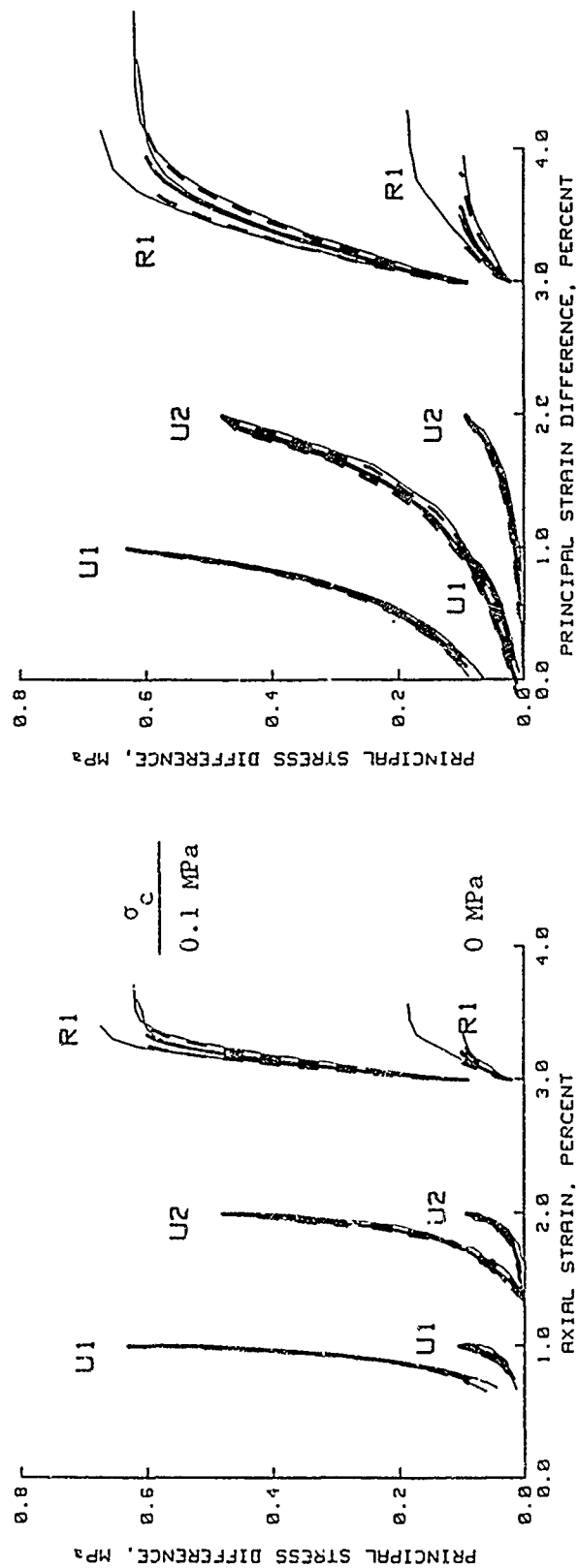


Figure 3.70. Results from the COV analysis of the unloading and reloading portions of TXC test data plotted in forms that are conducive to constitutive modeling for $\sigma_c = 0$ and 0.1 MPa.

TEST DATA
 ——— MEAN
 - - - MEAN $\pm \hat{\sigma}$

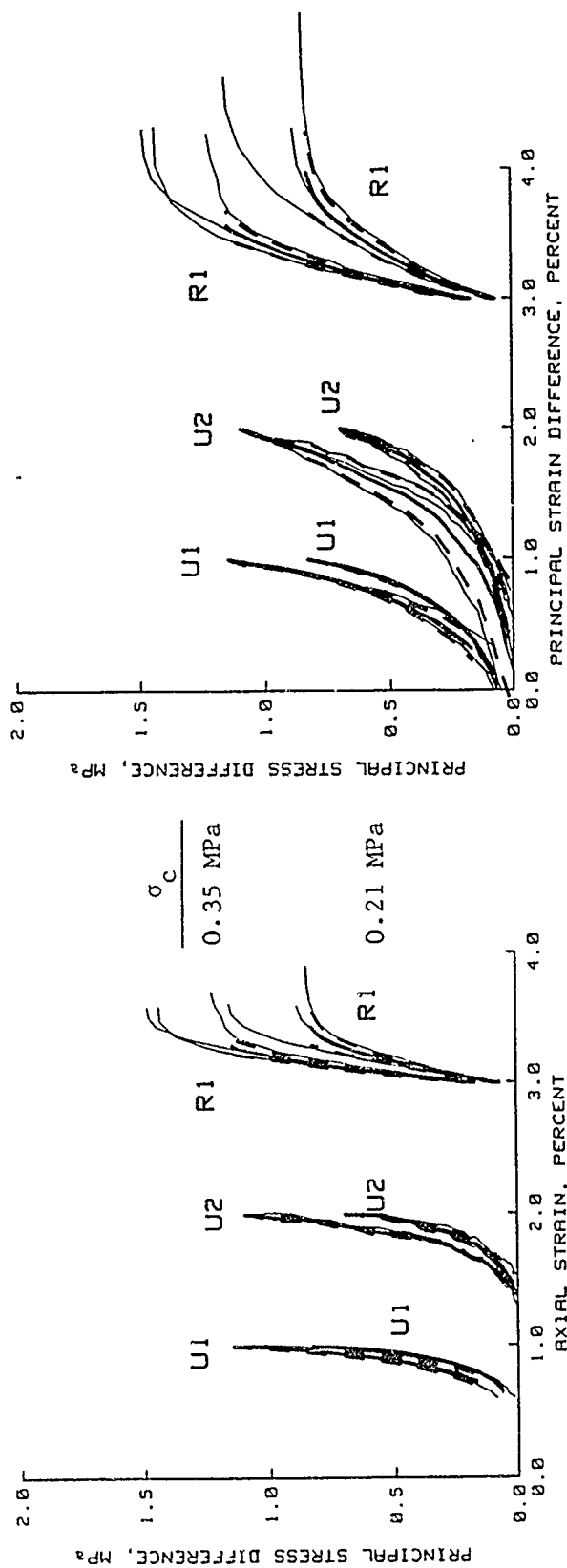


Figure 3.71. Results from the COV analysis of the unloading and reloading portions of TXC test data plotted in forms that are conducive to constitutive modeling for $\sigma_c = 0.21$ and 0.35 MPa.

TEST DATA
 ——— MEAN
 - - - MEAN $\pm \hat{\sigma}$

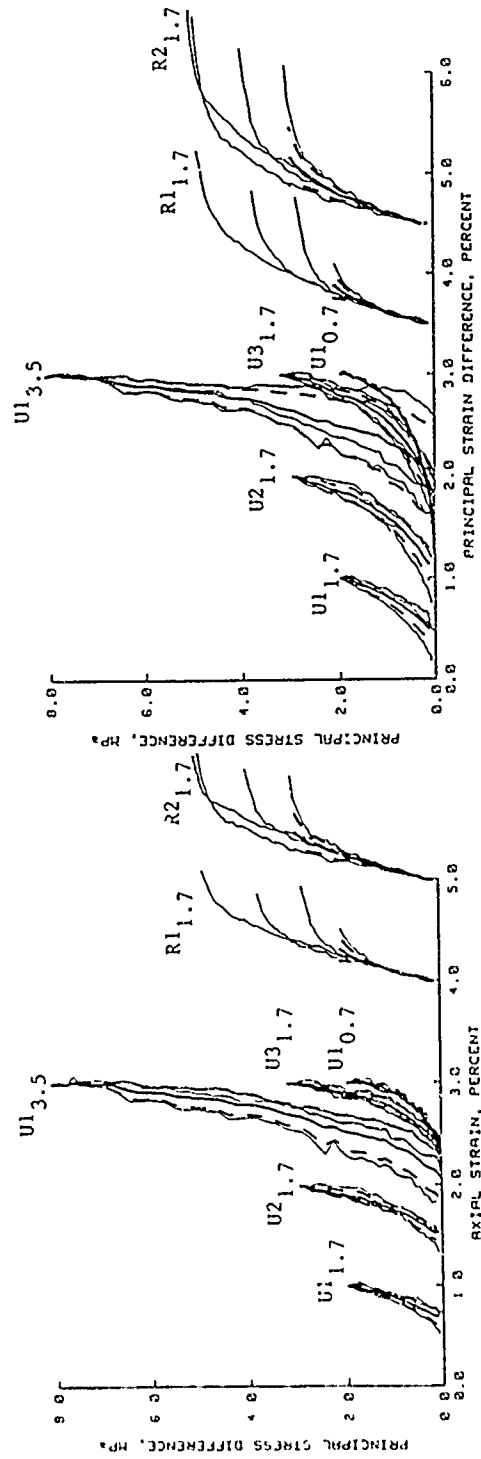


Figure 3.72. Results from the COV analysis of the unloading and reloading portions of TXC test data plotted in forms that are conducive to constitutive modeling for $\sigma_c = 0.7, 1.7$, and 3.5 MPa.

——— TEST DATA
 ——— MEAN
 - - - MEAN $\pm \sigma$

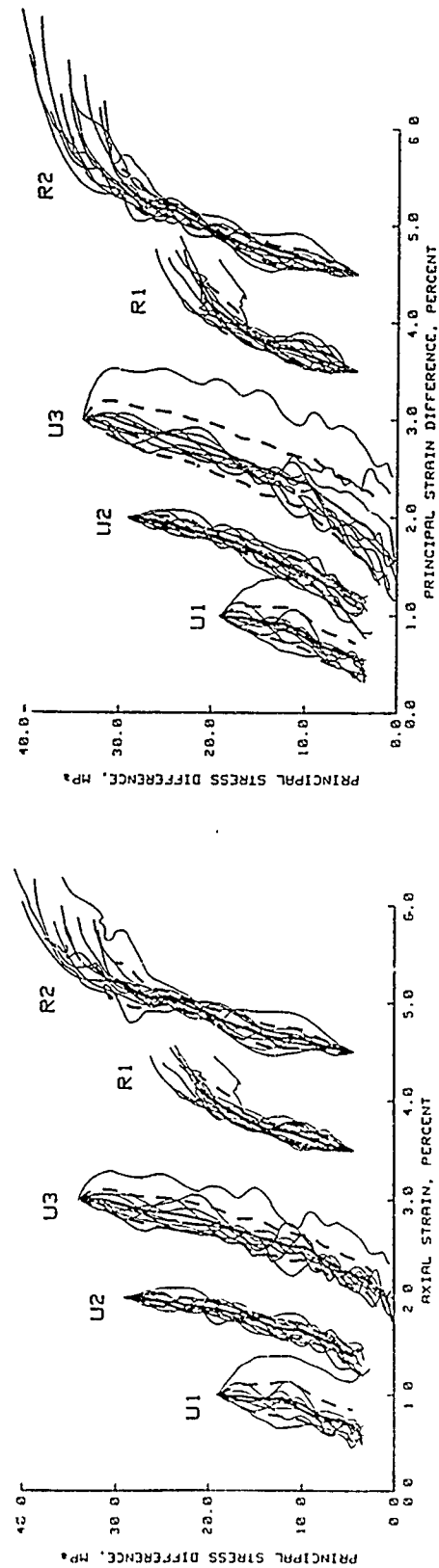


Figure 3.73. Results from the COV analysis of the unloading and reloading portions of the TXC test data plotted in forms that are conducive to constitutive modeling for $\sigma_c = 17.5$ MPa.

— TEST DATA
 — MEAN
 - - - MEAN $\pm \hat{\sigma}$

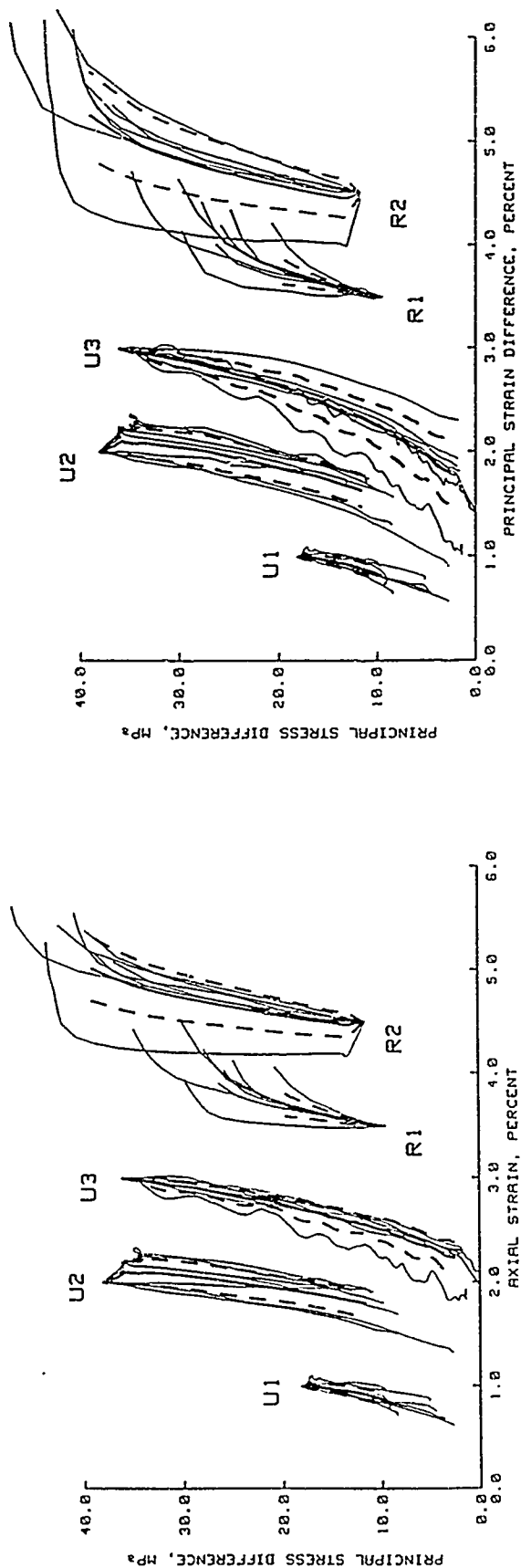


Figure 3.74. Results from the COV analysis of the unloading and reloading portions of TXC test data plotted in forms that are conducive to constitutive modeling for $\sigma_c = 20.0$ MPa.

— TEST DATA
 — MEAN
 - - - MEAN $\pm \hat{\sigma}$

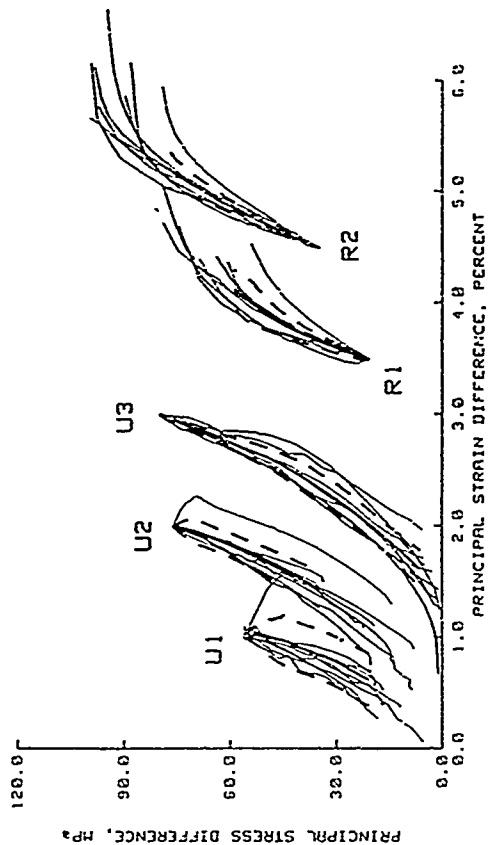
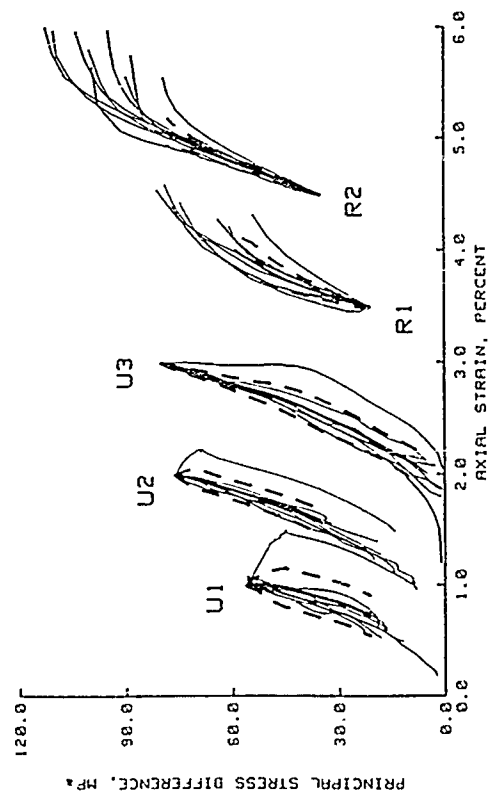


Figure 3.75. Results from the COV analysis of the unloading and reloading portions of TXC test data plotted in forms that are conducive to constitutive modeling for $\sigma_c = 55.0$ MPa.

——— TEST DATA
 ——— MEAN
 - - - MEAN $\pm \sigma$

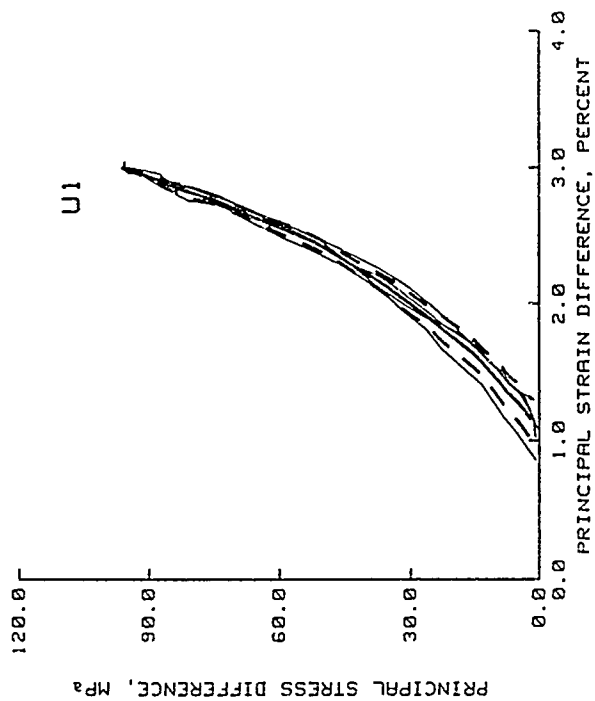
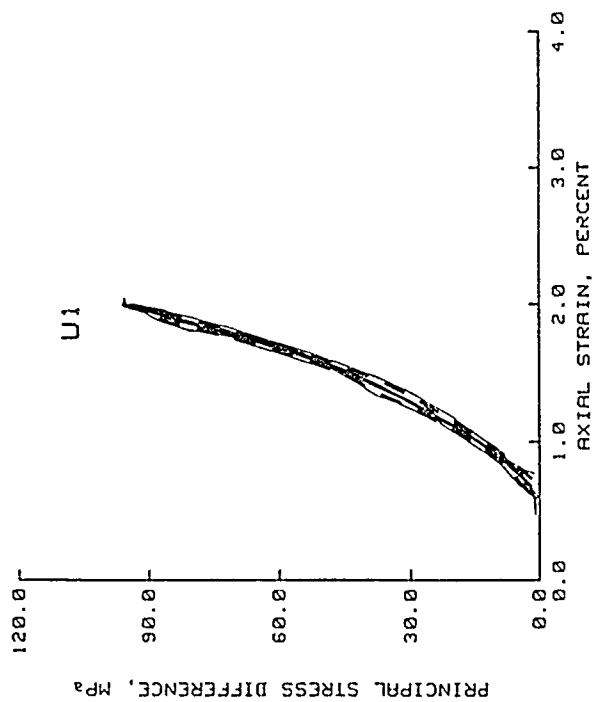


Figure 3.76. Results from the COV analysis of the unloading portion of TXC test data plotted in forms that are conducive to constitutive modeling for $\sigma_c = 60.0$ MPa.

TEST DATA
 ——— MEAN
 - - - MEAN $\pm \hat{\sigma}$

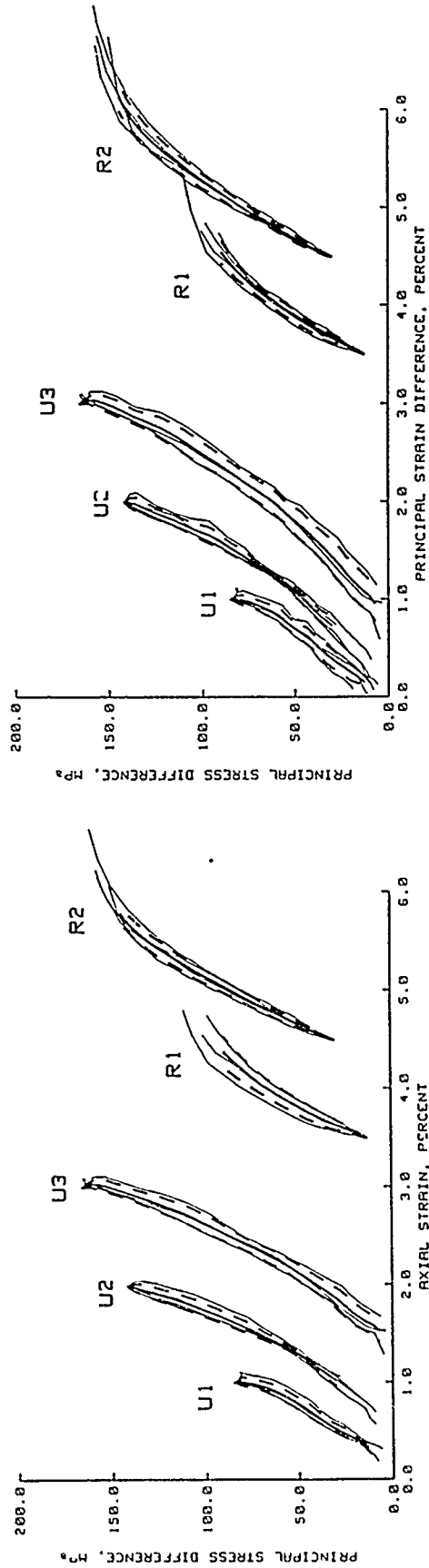


Figure 3.77. Results from the COV analysis of the unloading and reloading portions of TXC test data plotted in forms that are conducive to constitutive modeling for $\sigma_c = 80.0$ MPa

— TEST DATA
 — MEAN
 - - - MEAN $\pm \hat{\sigma}$

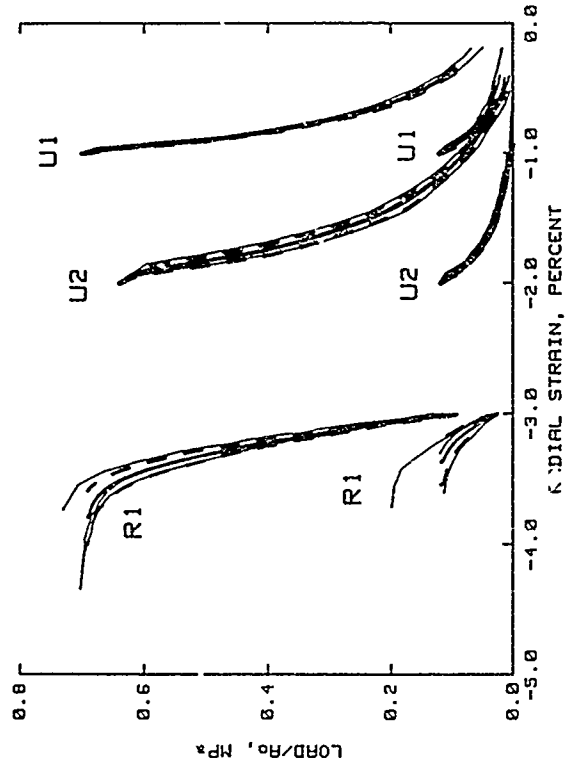
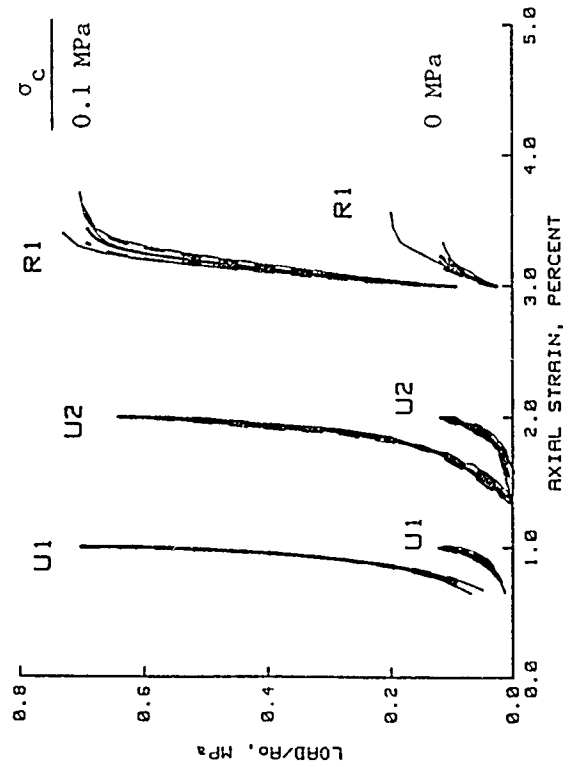


Figure 3.78. Results from the COV analysis of the unloading and reloading portions of "measured" TXC test data for $\sigma_c = 0$ and 0.1 MPa.

— TEST DATA
 — MEAN
 - - - MEAN $\pm \hat{\sigma}$

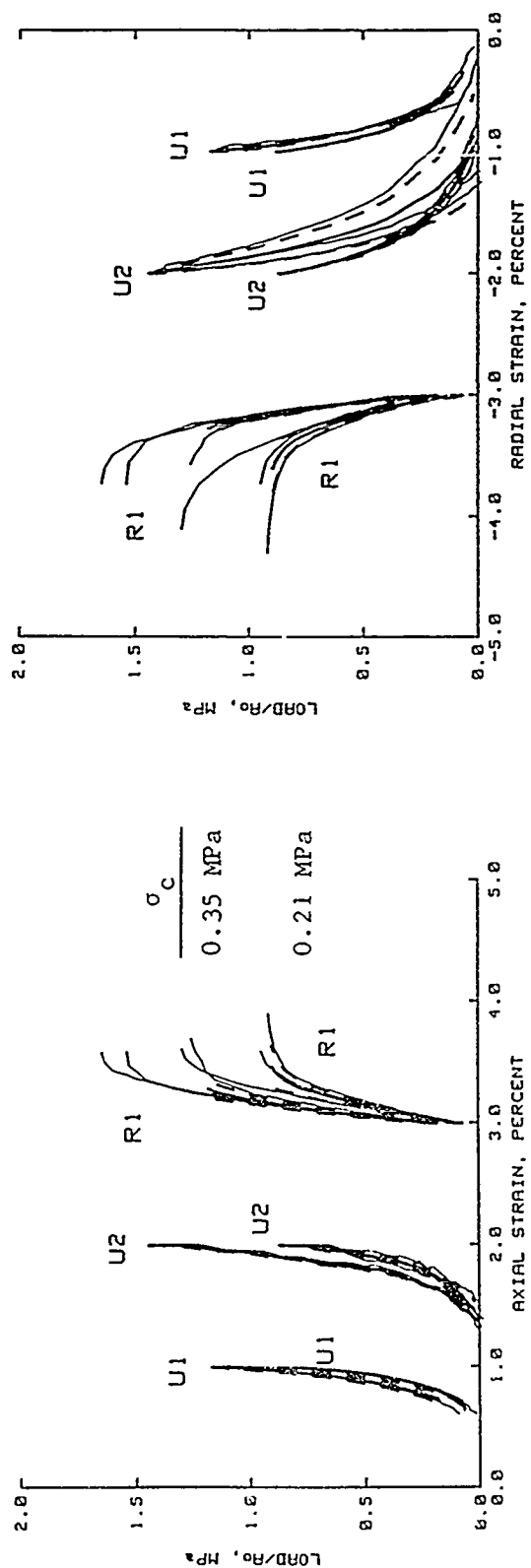


Figure 3.79. Results from the COV analysis of the unloading and reloading portions of "measured" TXC test data for $\sigma_c = 0.21$ and 0.35 MPa.

TEST DATA
 — MEAN
 - - - MEAN $\pm \sigma$

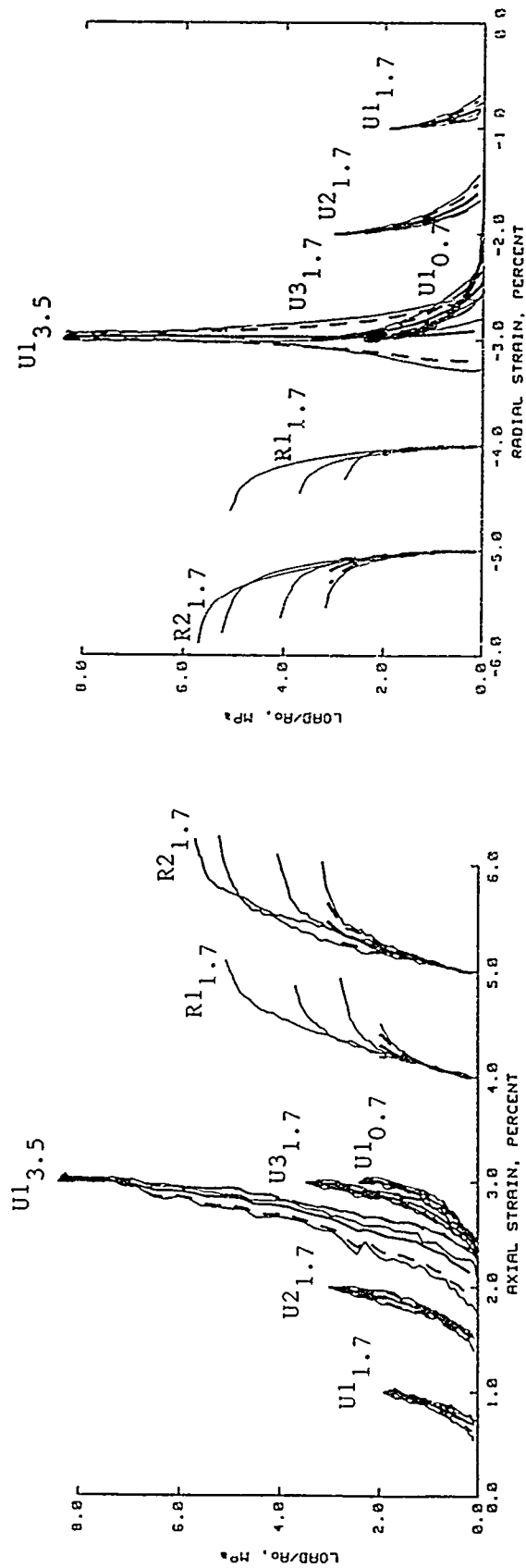


Figure 3.80. Results from the COV analysis of the unloading and reloading portions of "measured" TXC test data for $\sigma_c = 0.7, 1.7, \text{ and } 3.5 \text{ MPa}$.

TEST DATA
 ——— MEAN
 - - - MEAN $\pm \hat{\sigma}$

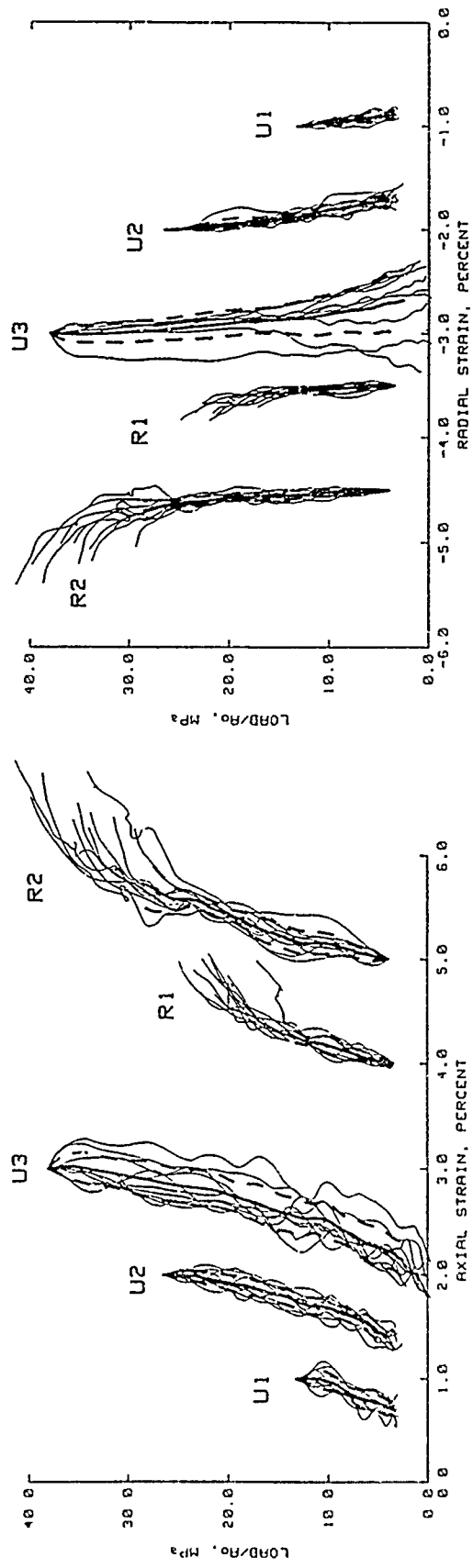


Figure 3.81. Results from the COV analysis of the unloading and reloading portions of "measured" TXC test data for $\sigma_c = 17.5$ MPa.

TEST DATA
 ——— MEAN
 - - - MEAN $\pm \sigma$

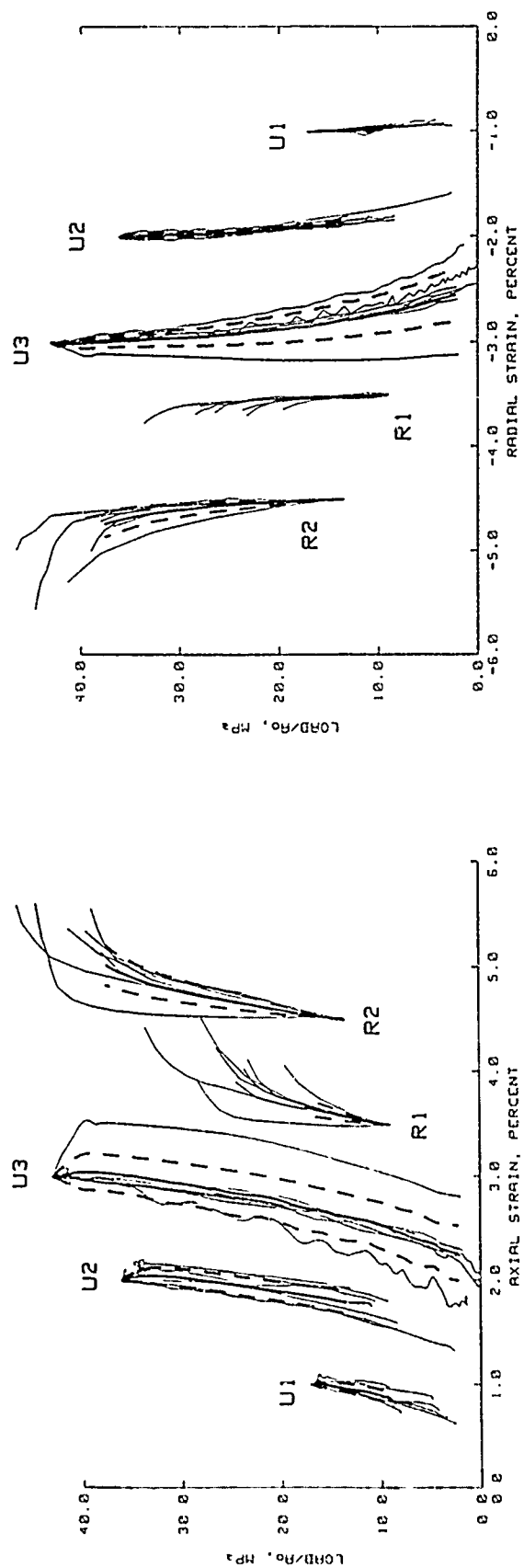


Figure 3.82. Results from the COV analysis of the unloading and reloading portions of "measured" TXC test data for $\sigma_c = 20.0$ MPa.

— TEST DATA
 — MEAN
 - - - MEAN $\pm \hat{\sigma}$

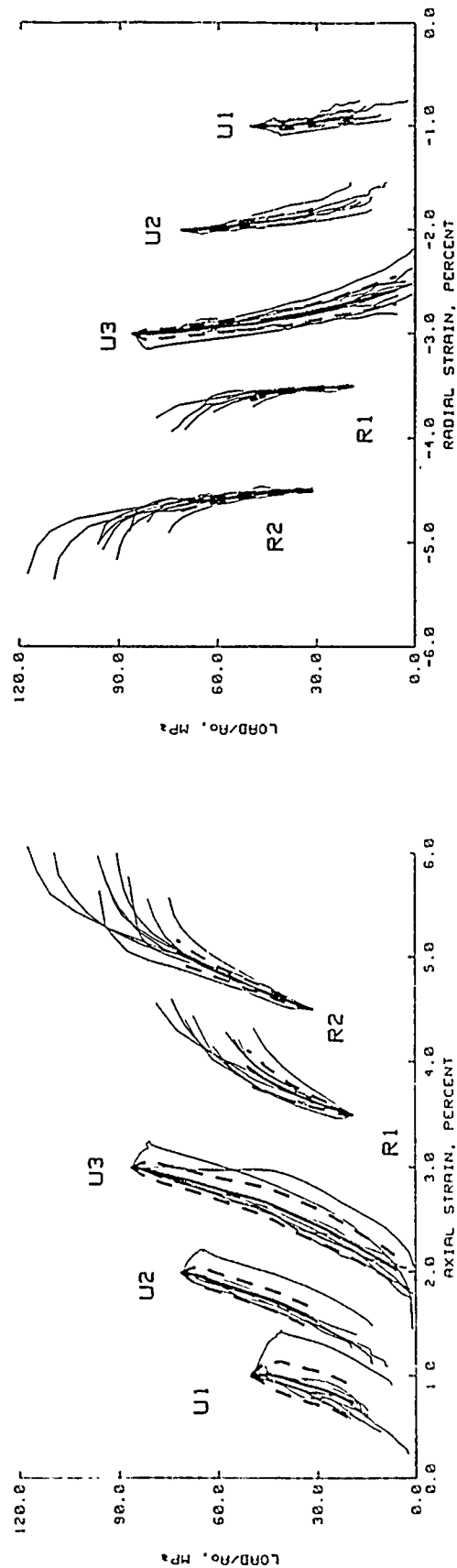


Figure 3.83. Results from the COV analysis of the unloading and reloading portions of "measured" TXC test data for $\sigma_c = 55.0$ MPa.

TEST DATA
 ——— MEAN
 - - - MEAN $\pm \sigma$

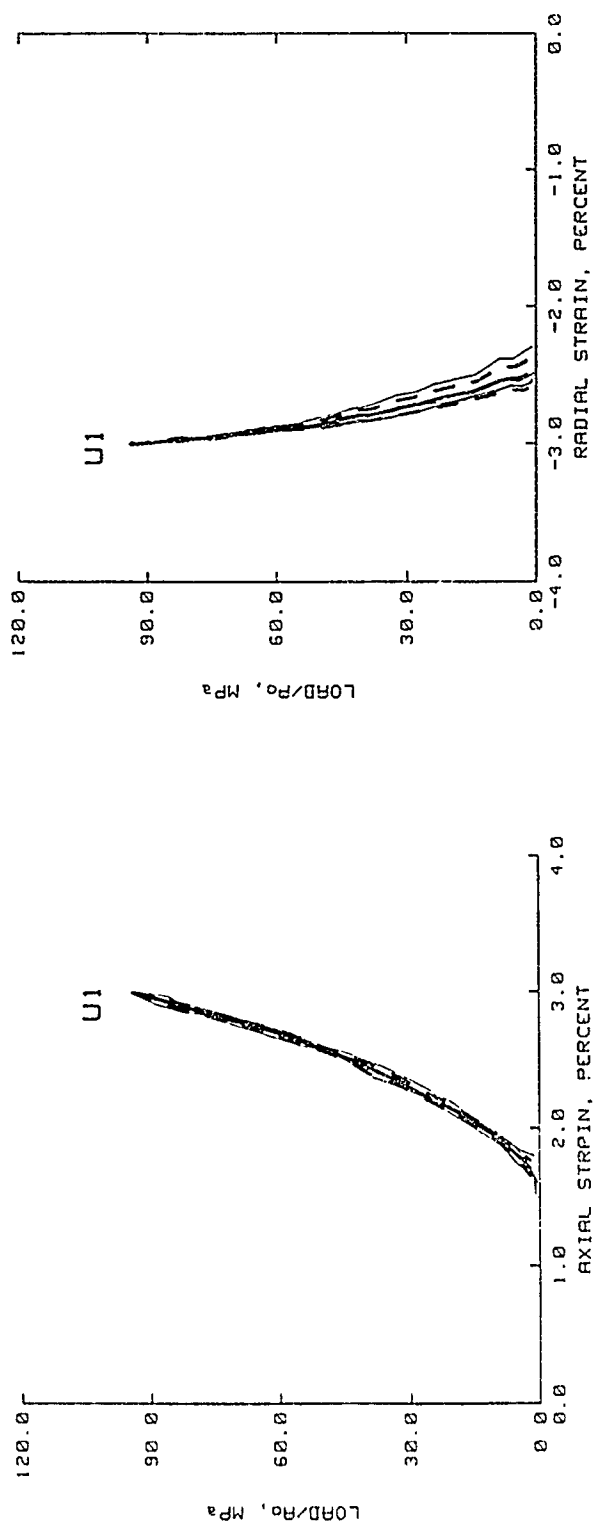


Figure 3.84. Results from the COV analysis of the unloading portion of "measured" TXC test data for $\sigma_c = 60.0$ MPa.

TEST DATA
 — MEAN
 - - - MEAN $\pm \hat{\sigma}$

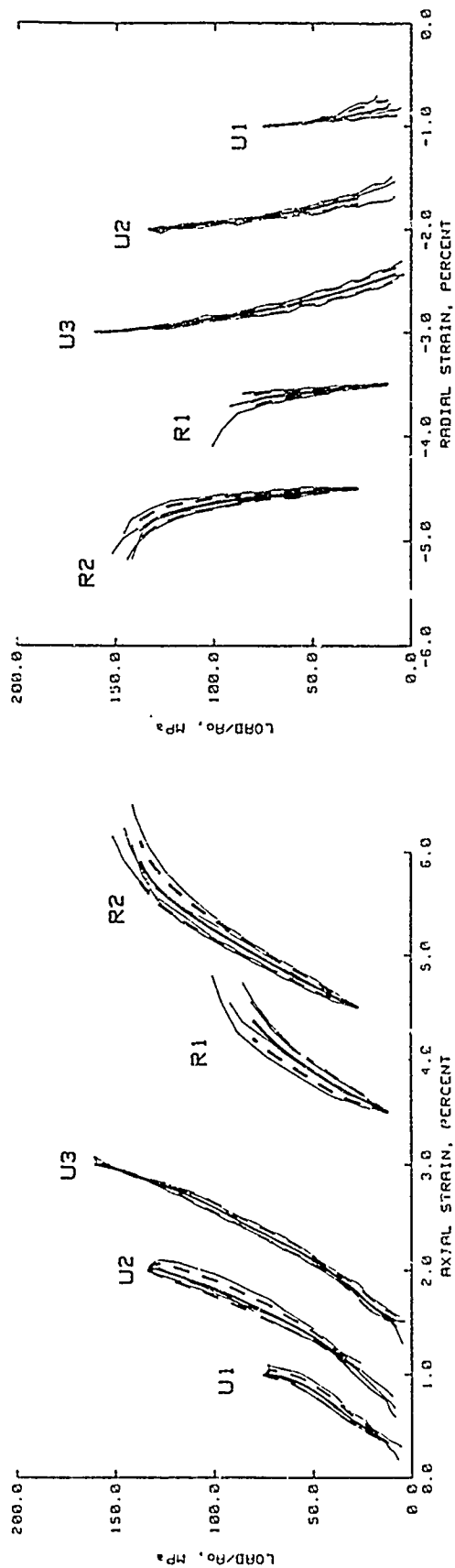


Figure 3.85. Results from the COV analysis of the unloading and reloading portions of "measured" TXC test data for $\sigma_c = 80.0$ MPa.

——— MEAN
 - - - MEAN $\pm \hat{\sigma}$

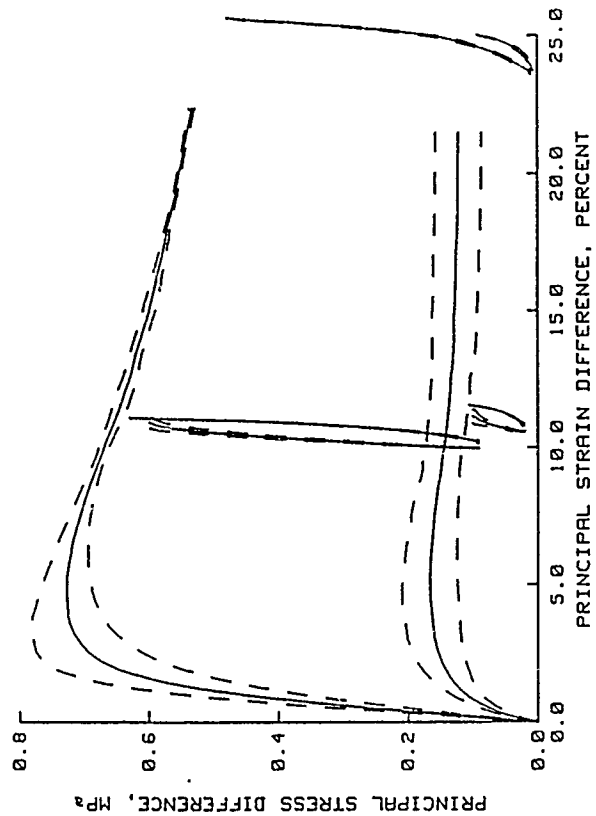
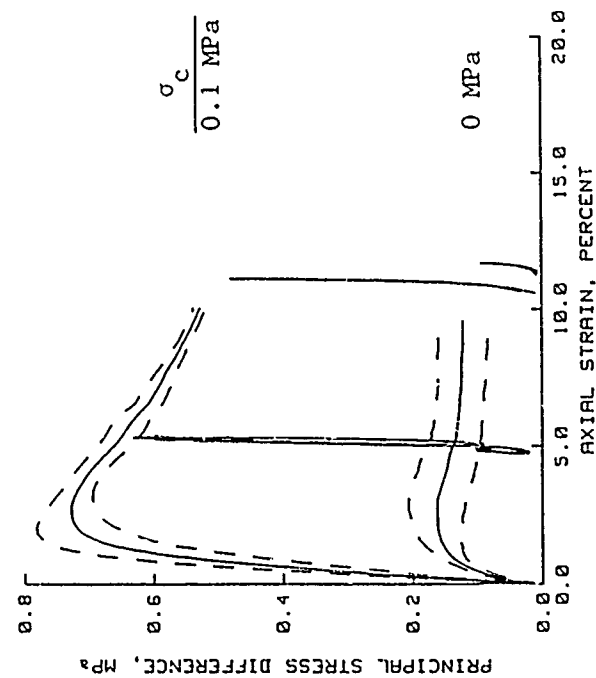


Figure 3.86. Load-unload-reload responses constructed from the results of COV analysis of TXC test data plotted in forms that are conducive to constitutive modeling for $\sigma_c = 0$ and 0.1 MPa.

——— MEAN
 - - - MEAN $\pm \hat{\sigma}$

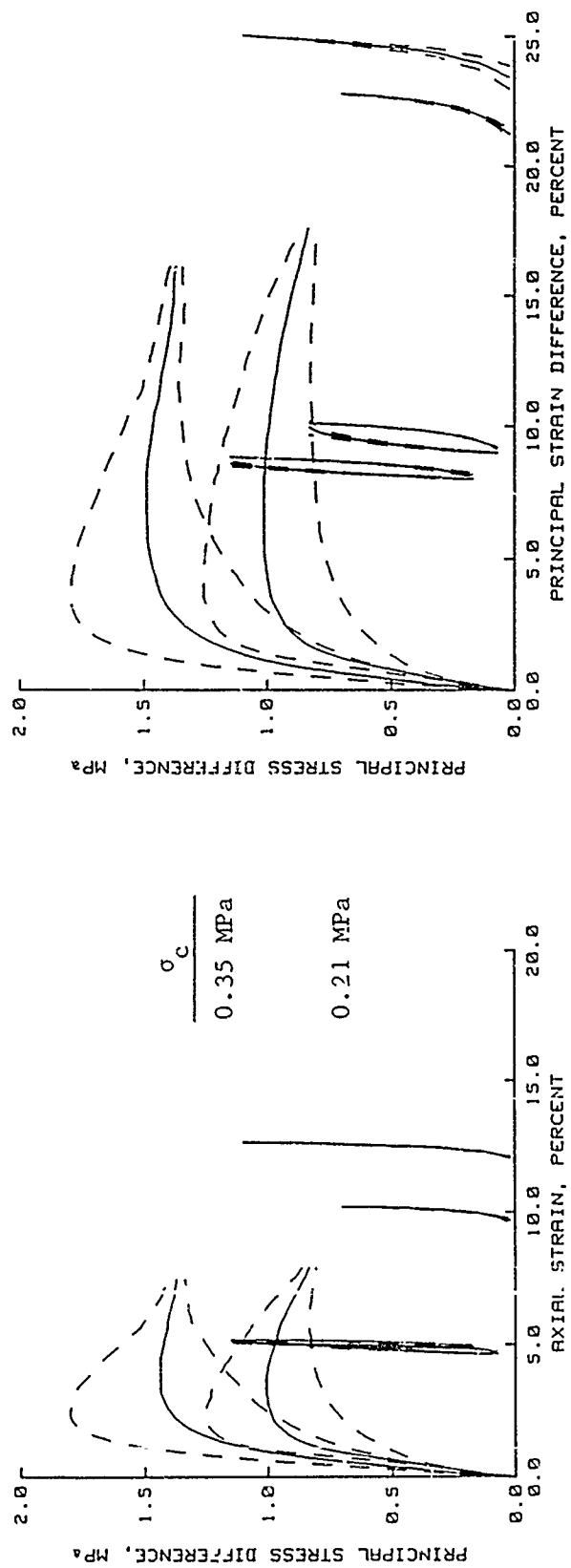


Figure 3.87. Load-unload-reload responses constructed from the results of COV analysis of TXC test data plotted in forms that are conducive to constitutive modeling for $\sigma_c = 0.21$ and 0.35 MPa.

— MEAN
 - - - MEAN $\pm \hat{\sigma}$

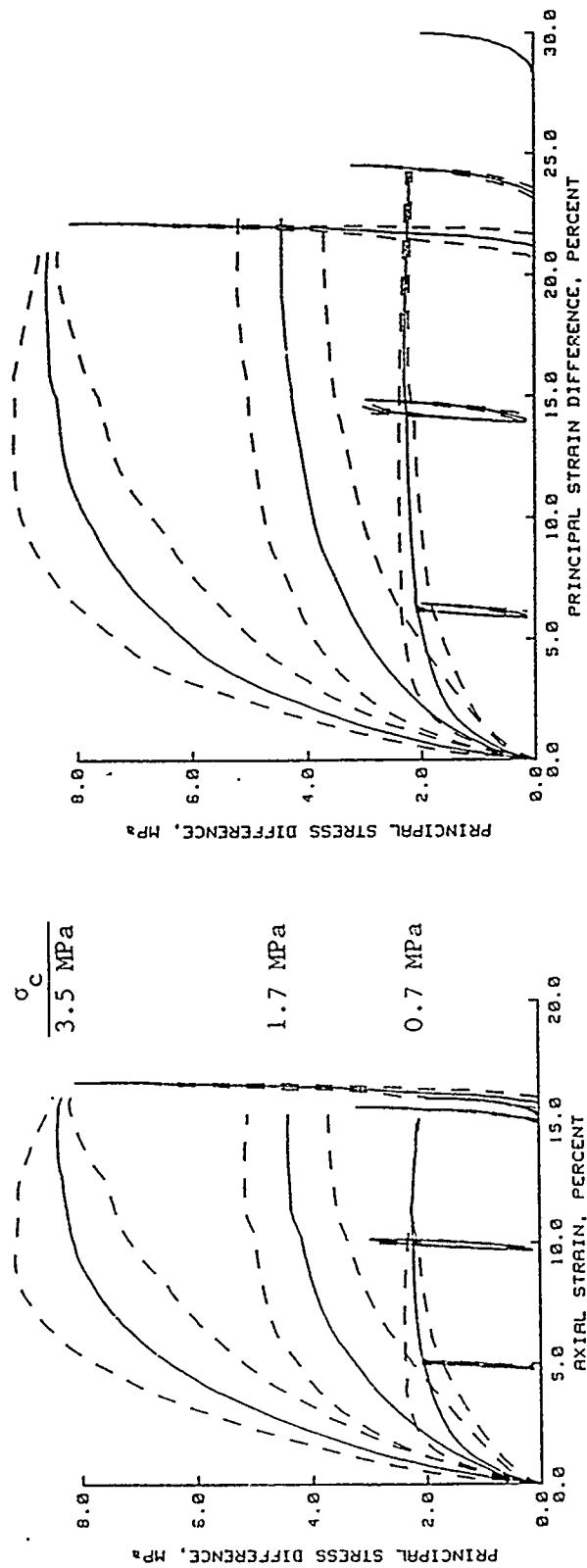


Figure 3.88. Load-unload-reload responses constructed from the results of COV analysis of TXC test data plotted in forms that are conducive to constitutive modeling for $\sigma_c = 0.7$, 1.7, and 3.5 MPa.

— MEAN
 - - - MEAN $\pm \hat{\sigma}$

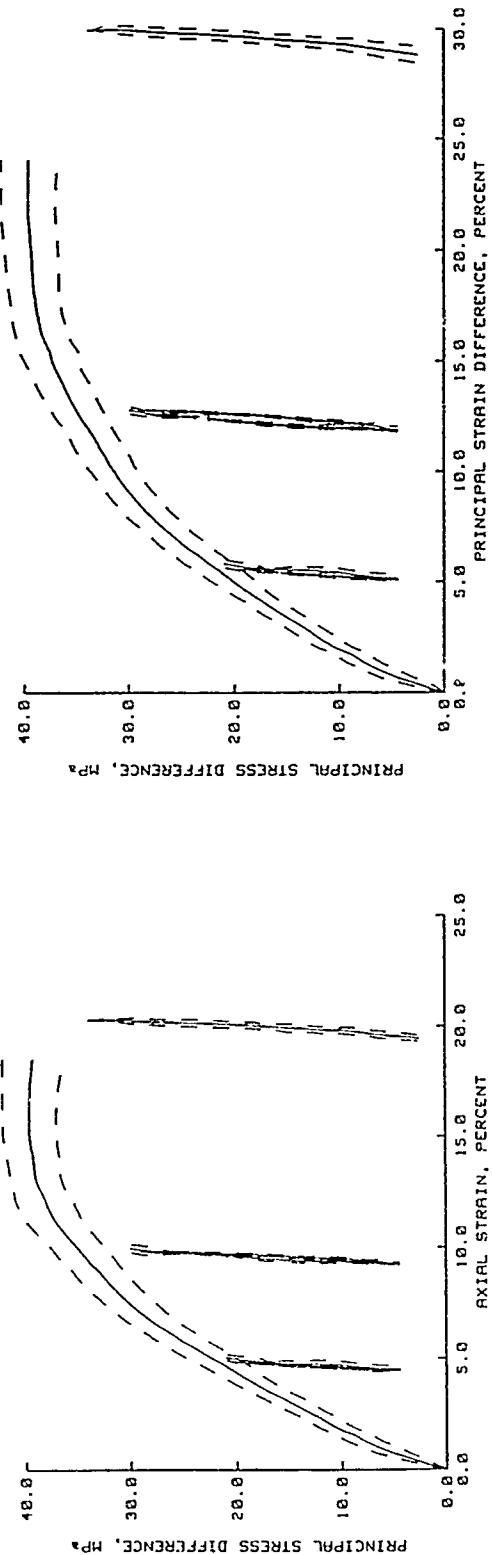


Figure 3.89. Load-unload-reload responses constructed from the results of COV analysis of TXC test data plotted in forms that are conducive to constitutive modeling for $\sigma_c = 17.5$ MPa.

——— MEAN
 - - - MEAN $\pm \sigma$

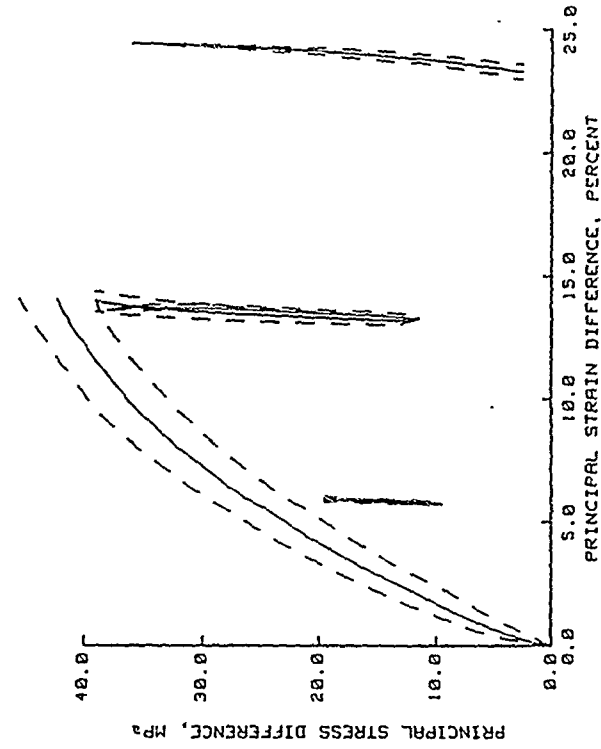
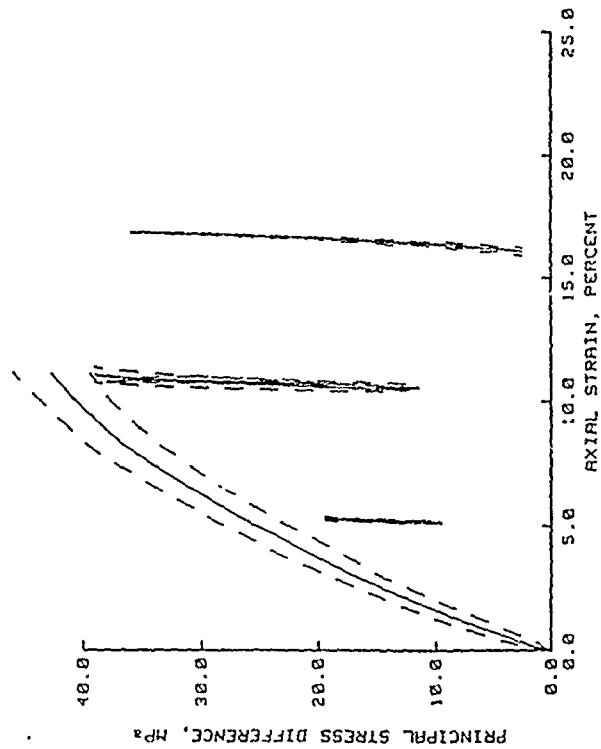


Figure 3.90. Load-unload-reload responses constructed from the results of COV analysis of TXC test data plotted in forms that are conducive to constitutive modeling for $\sigma_c = 20.0$ MPa.

——— MEAN
 - - - MEAN $\pm \sigma$

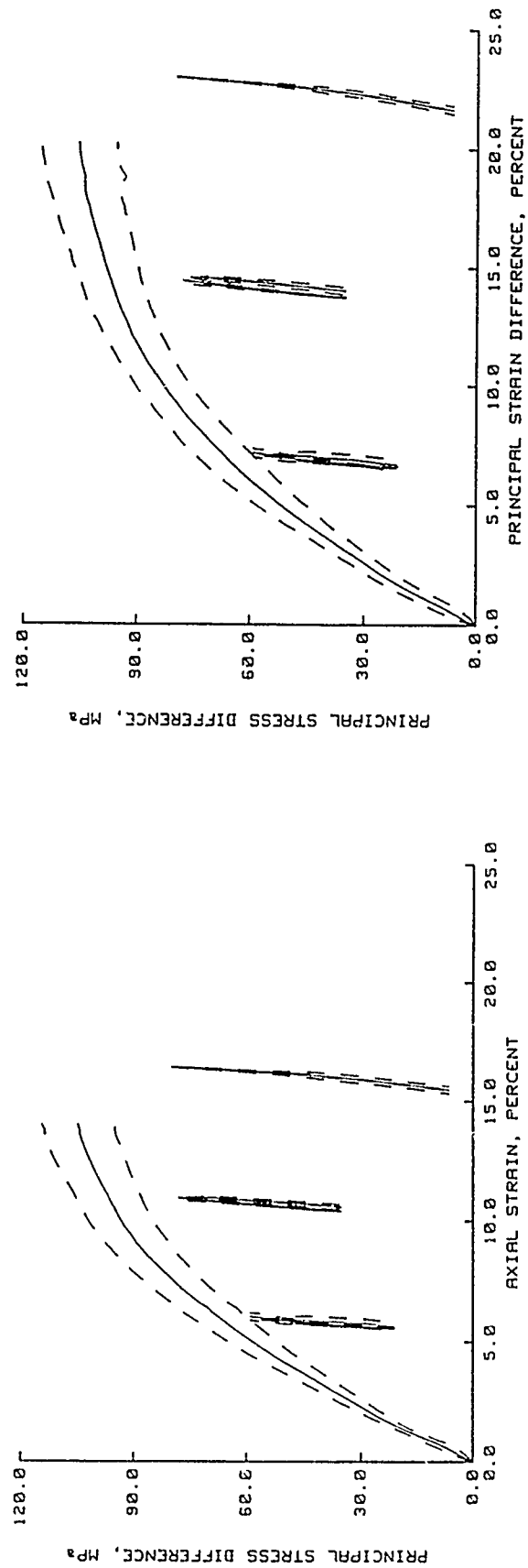


Figure 3.91. Load-unload-reload responses constructed from the results of COV analysis of TXC test data plotted in forms that are conducive to constitutive modeling for $\sigma_c = 55.0$ MPa.

— MEAN
 - - - MEAN $\pm \hat{\sigma}$

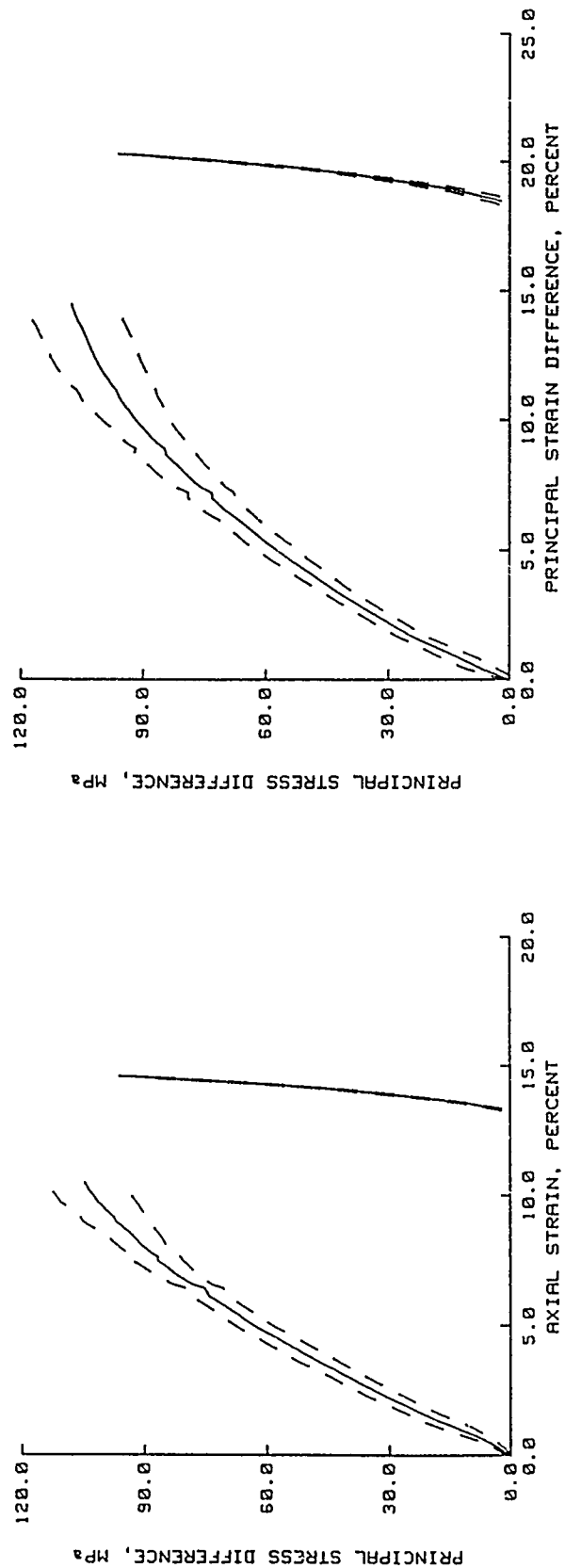


Figure 3.92. Load-unload responses constructed from the results of COV analysis of TXC test data plotted in forms that are conducive to constitutive modeling for $\sigma_c = 60.0$ MPa.

— MEAN
 - - - MEAN $\pm \sigma$

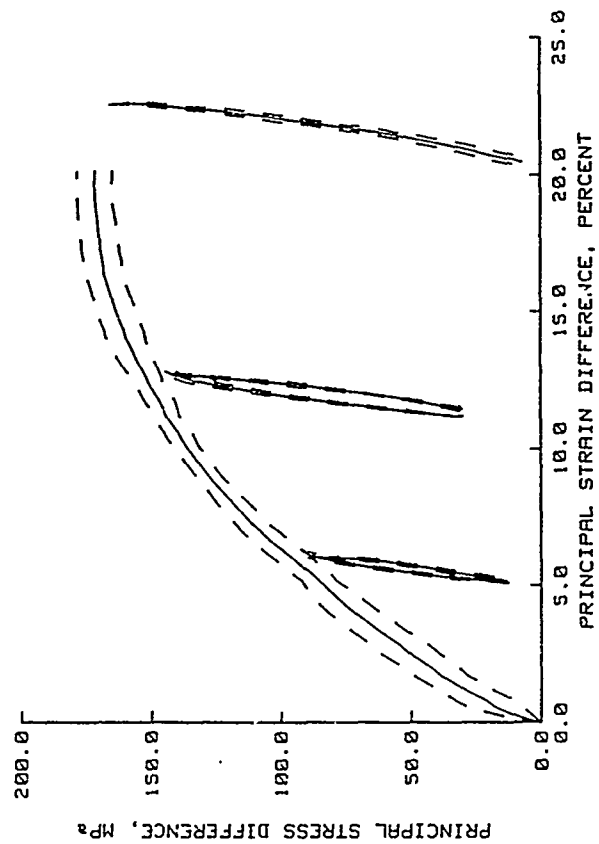
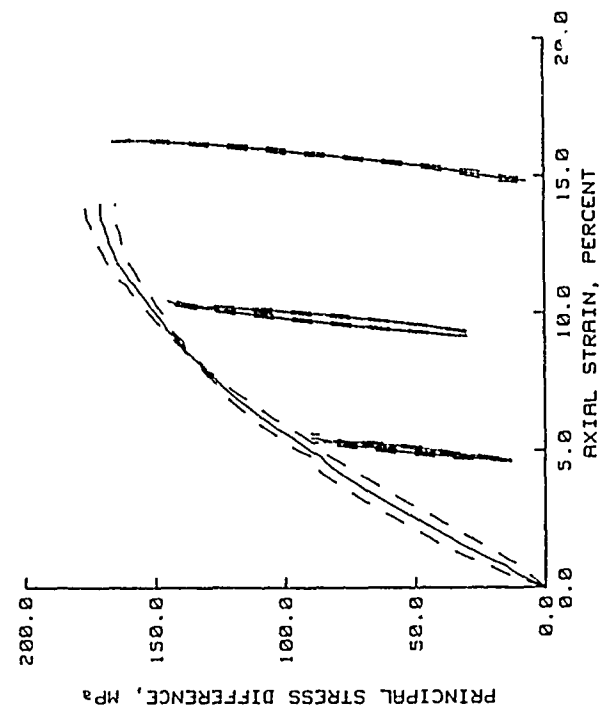
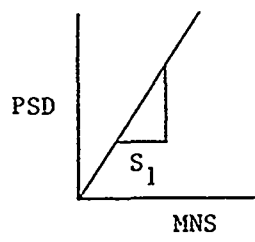


Figure 3.93. Load-unload-reload responses constructed from the results of COV analysis of TXC test data plotted in forms that are conducive to constitutive modeling for $\sigma_c = 80.0$ MPa.

PSD = L/Ao since $\epsilon_r = 0$



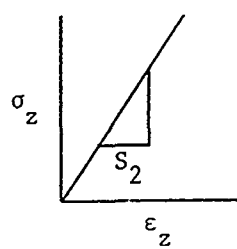
$$S_1 = \frac{MNS}{PSD}$$

$$MNS = \frac{L/Ao}{3} + \sigma_r \quad \sigma_r = \text{radial stress}$$

$$S_1 = \frac{\frac{L/Ao}{3} + \sigma_r}{L/Ao}$$

$$S_1 = \frac{L/Ao + 3\sigma_r}{3L/Ao}$$

One Variable
for Given L/Ao : σ_r



$$S_2 = \frac{\epsilon_z}{\sigma_z} \quad \sigma_z = L/Ao + \sigma_r \quad \begin{array}{l} \sigma_z = \text{Axial Stress} \\ \epsilon_z = \text{Axial Strain} \end{array}$$

$$S_2 = \frac{\epsilon_z}{L/Ao + \sigma_r}$$

Two Variables
for Given L/Ao : ϵ_z and σ_r

$$E[S_1] = \frac{1}{2} [S_1^+ + S_1^-]$$

$$V[S_1] = \left(\frac{S_1^+ - S_1^-}{2} \right)^2$$

$$E[S_2] = \frac{1}{4} [(S_2^{++})(1+\rho) + (S_2^{+-})(1-\rho) + (S_2^{-+})(1-\rho) + (S_2^{--})(1+\rho)]$$

$$V[S_2] = \frac{1}{4} [(S_2^{++})^2(1-\rho) + (S_2^{+-})^2(1-\rho) + (S_2^{-+})^2(1-\rho) + (S_2^{--})^2(1+\rho)]$$

$$- (E[S_1])^2$$

Figure 3.94. Rosenblueth equations for converting the results from the COV analysis of "measured" K_0 test data into forms that are conducive to constitutive modeling.

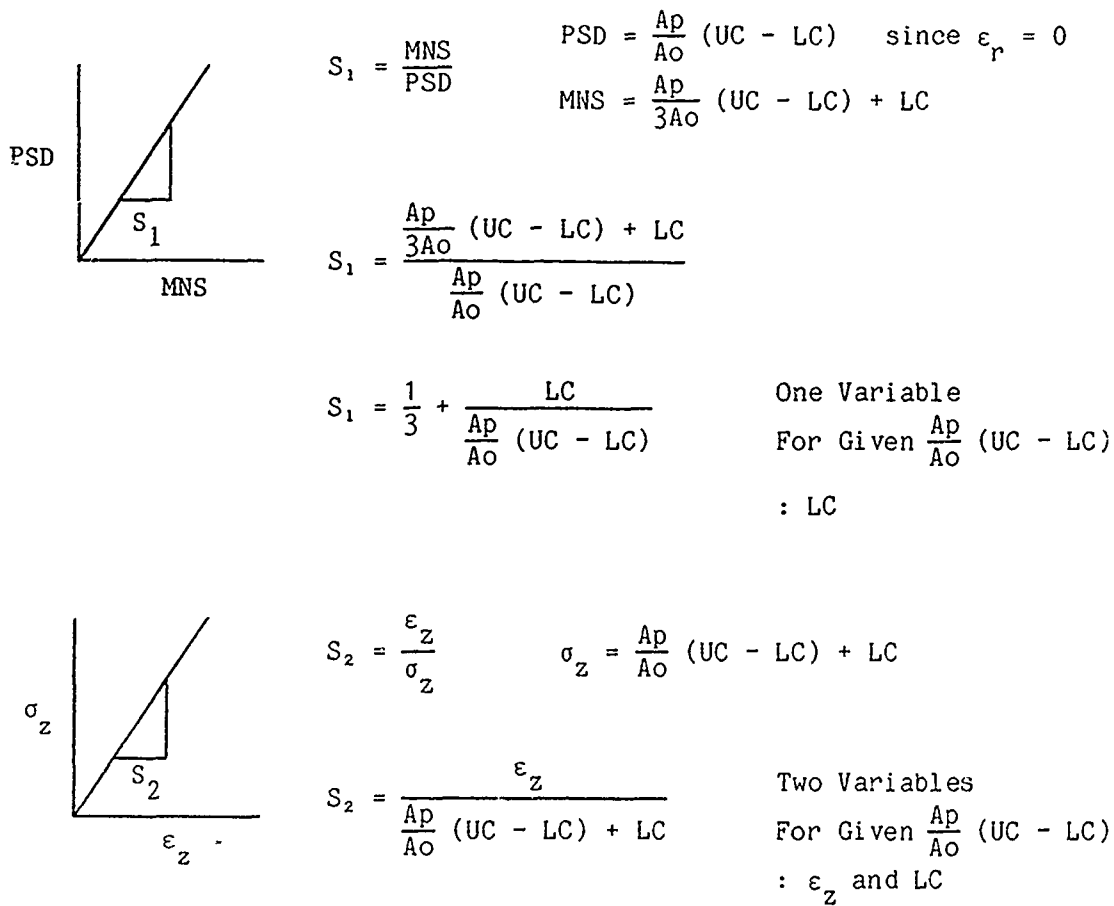
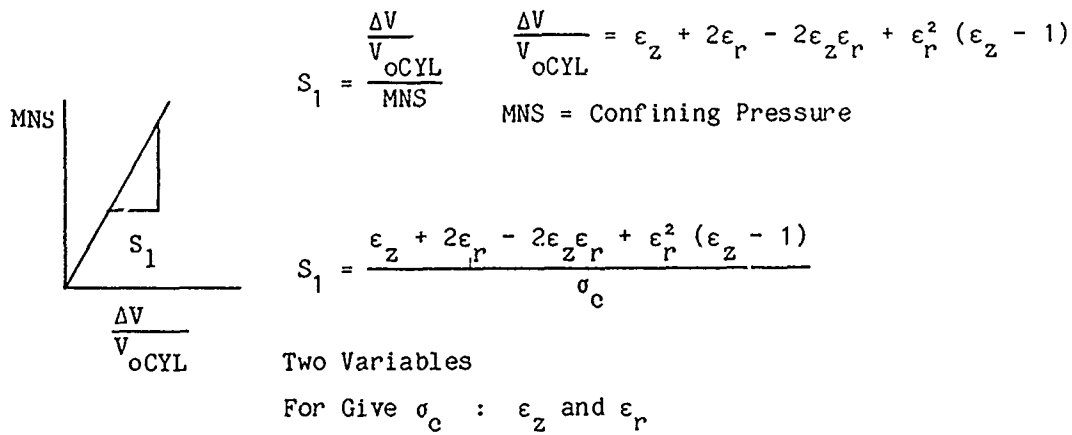


Figure 3.95. Rosenblueth equations for converting the results from the COV analysis of "measured" EXT K_0 test data into forms that are conducive to constitutive modeling.

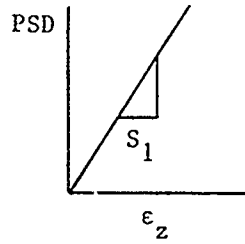


$$E[S_1] = \frac{1}{4}[(S_1^{++})(1+\rho) + (S_1^{+-})(1-\rho) + (S_1^{-+})(1-\rho) + (S_1^{--})(1+\rho)]$$

$$V[S_1] = \frac{1}{4}[(S_1^{++})^2(1+\rho) + (S_1^{+-})^2(1-\rho) + (S_1^{-+})^2(1-\rho) + (S_1^{--})^2(1+\rho)]$$

$$- (E[S_1])^2$$

Figure 3.96. Rosenblueth equations for converting the results from the COV analysis of "measured" HC test data into a form that is conducive to constitutive modeling.



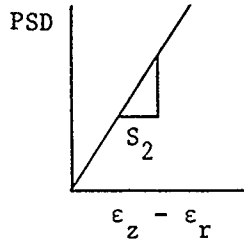
$$S_1 = \frac{\epsilon_z}{\text{PSD}} \quad \text{PSD} = \frac{L/A_0}{(1 - \epsilon_{r_T})^2}$$

where ϵ_{r_T} is the true radial strain

$$S_1 = \frac{\epsilon_z (1 - \epsilon_{r_T})^2}{L/A_0}$$

Two Variables

for Given L/A_0 : ϵ_z and ϵ_r



$$S_2 = \frac{\epsilon_z - \epsilon_r}{\text{PSD}}$$

$$S_2 = \frac{(\epsilon_z - \epsilon_{r_T})(1 - \epsilon_{r_T})^2}{L/A_0}$$

Two Variables

for Given L/A_0 : ϵ_z and ϵ_r

ϵ_{r_T} is $\epsilon_r + (\bar{\epsilon}_r, \bar{\epsilon}_r + \hat{\sigma}_{\epsilon_r}, \bar{\epsilon}_r - \hat{\sigma}_{\epsilon_r})$

where

$$\bar{\epsilon}_r = \frac{E \epsilon_r \text{ start of shear}}{N}$$

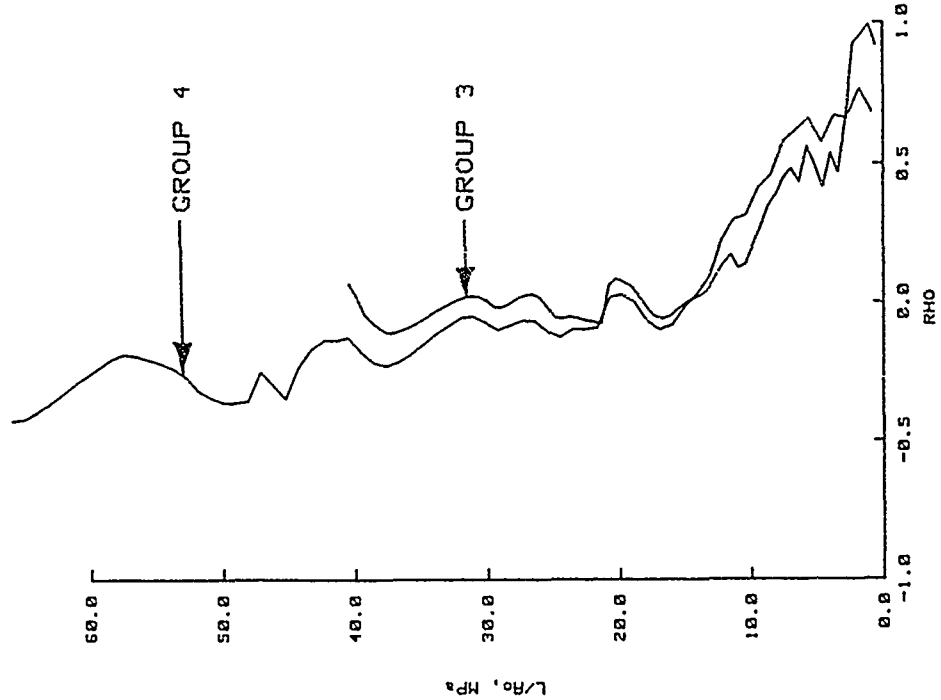
$$\hat{\sigma}_{\epsilon_r} = \frac{E(\epsilon_r \text{ start of shear} - \bar{\epsilon}_r)^2}{N - 1}$$

$$E[S] = \frac{1}{4}[(S^{++})(1+\rho) + (S^{+-})(1-\rho) + (S^{-+})(1-\rho) + (S^{--})(1+\rho)]$$

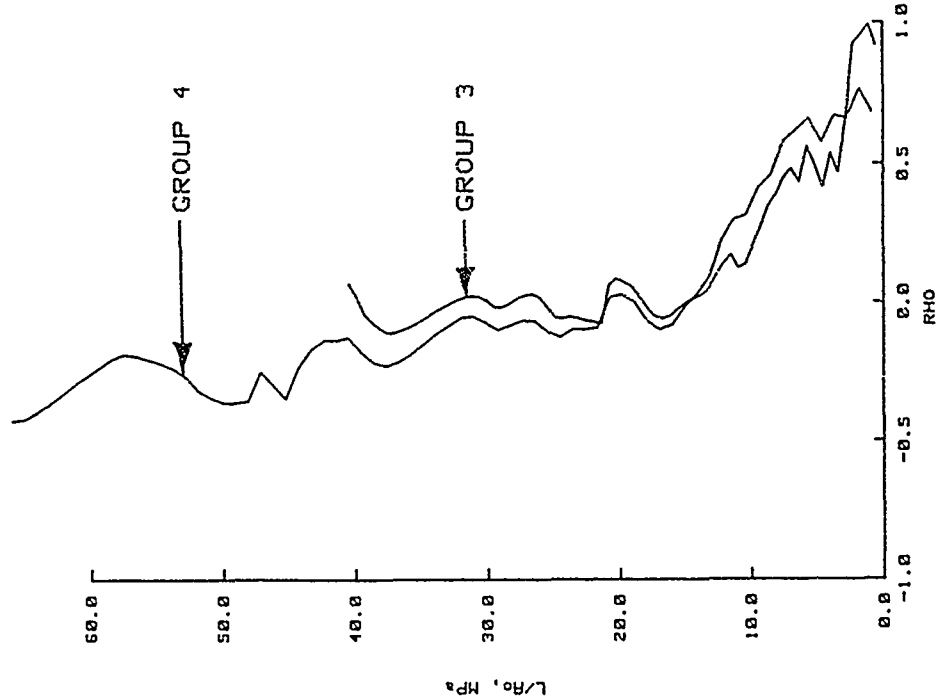
$$V[S] = \frac{1}{4}[(S^{++})^2(1-\rho) + (S^{+-})^2(1-\rho) + (S^{-+})^2(1-\rho) + (S^{--})^2(1+\rho)]$$

$$- (E[S])^2$$

Figure 3.97. Rosenblueth equations for converting the results from the COV analysis of "measured" TXC test data into forms that are conducive to constitutive modeling.



a. Groups 1 and 2.



b. Groups 3 and 4.

Figure 3.98. Correlation coefficients for loading K_o test data.

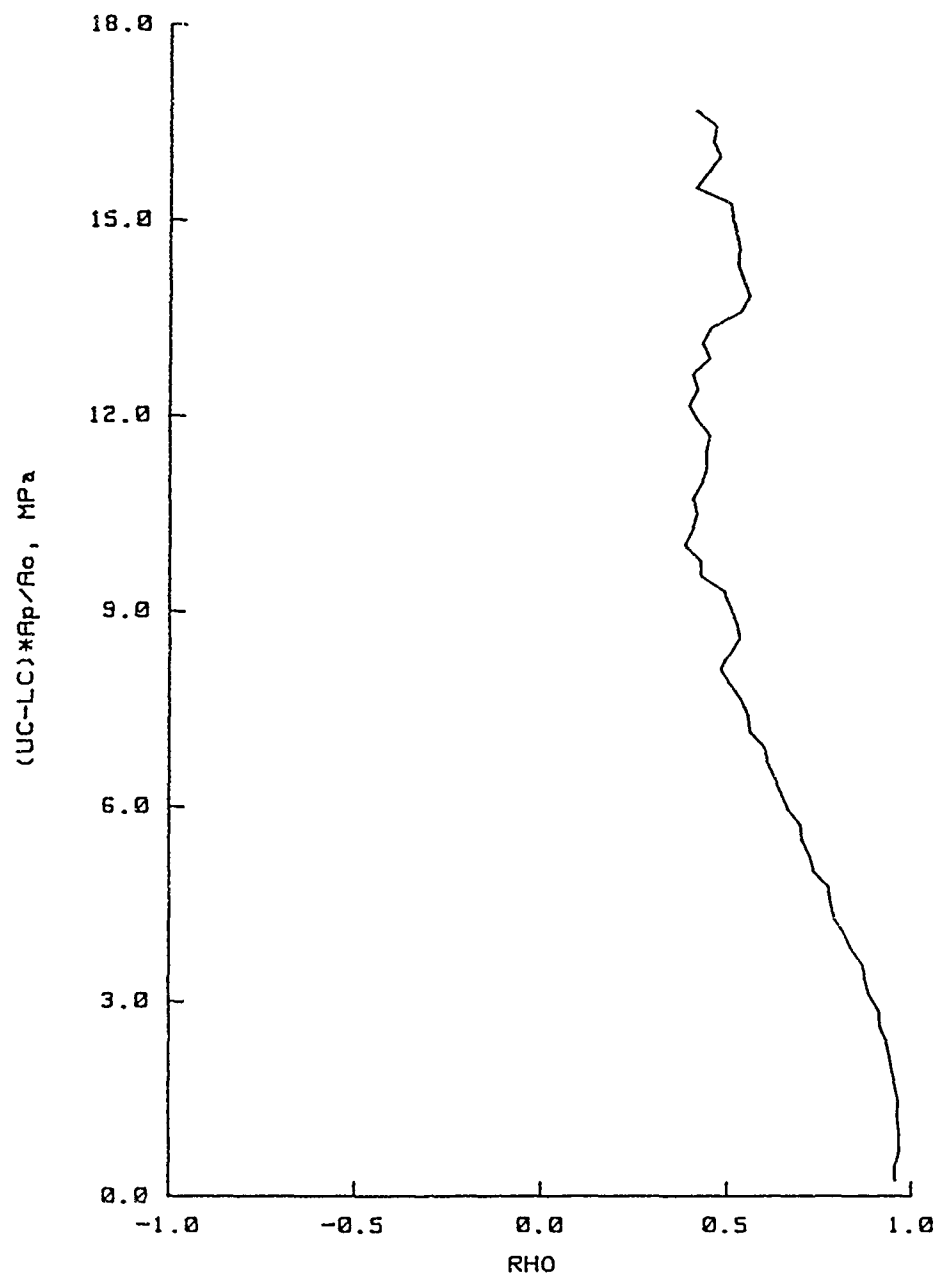


Figure 3.99. Correlation coefficients for loading EXT K_0 test data.

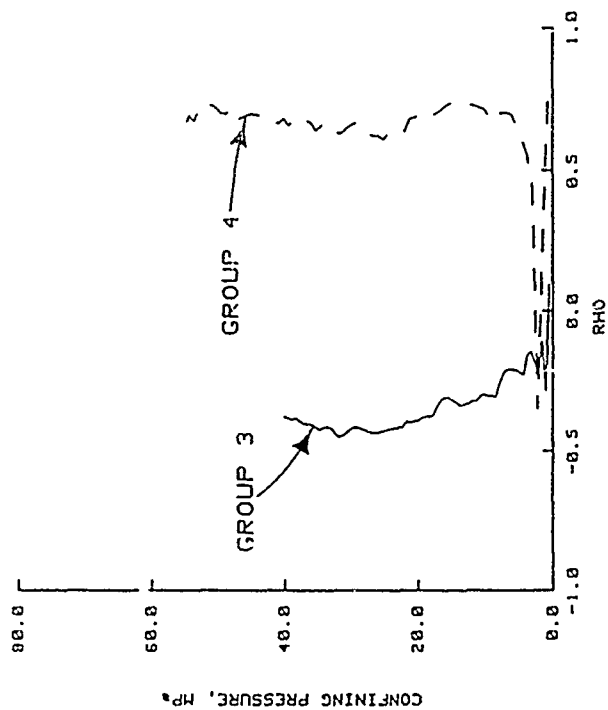
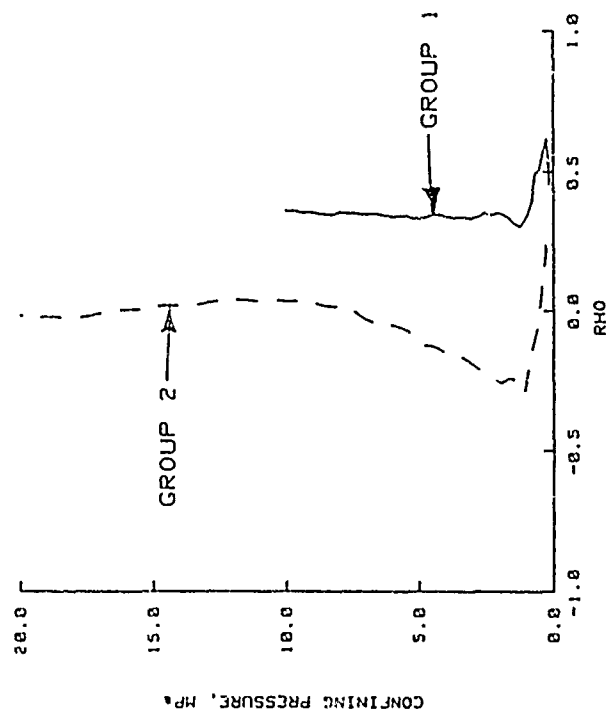


Figure 3.100. Correlation coefficients for loading static HC test data.

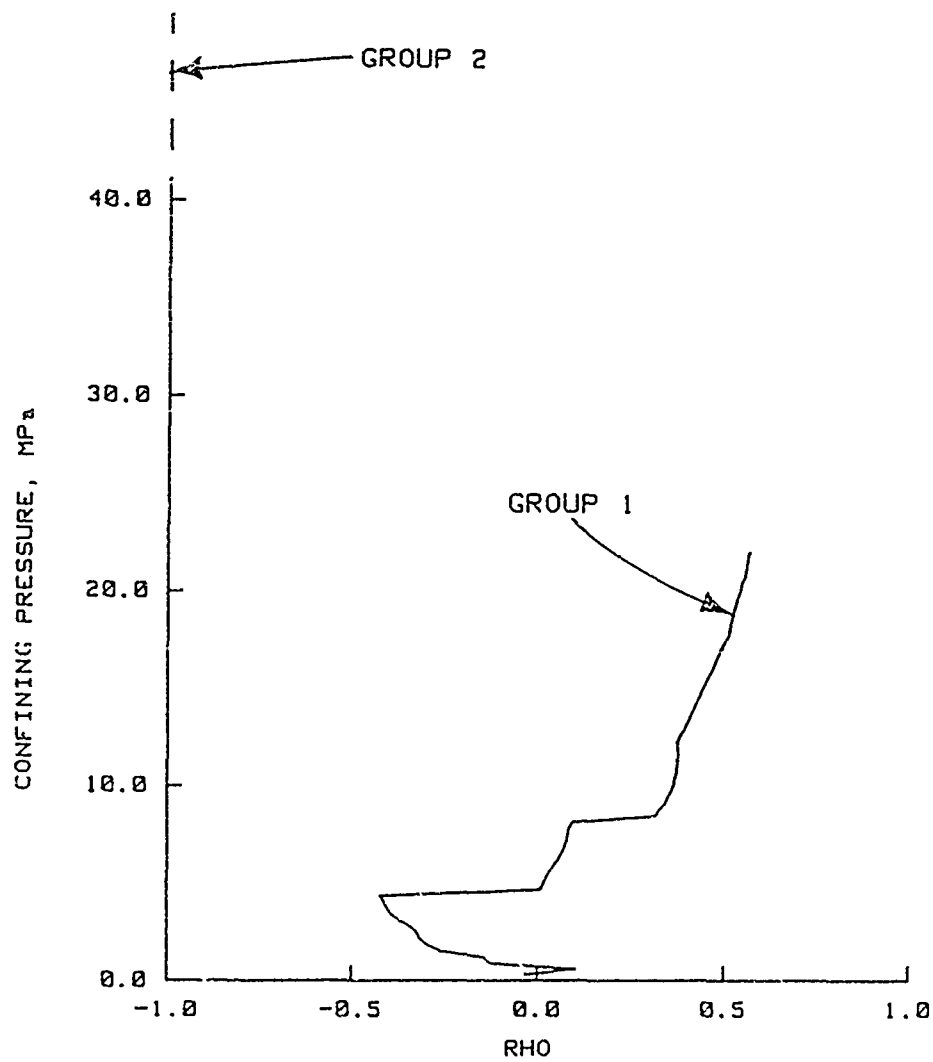


Figure 3.101. Correlation coefficients for loading dynamic HC test data.

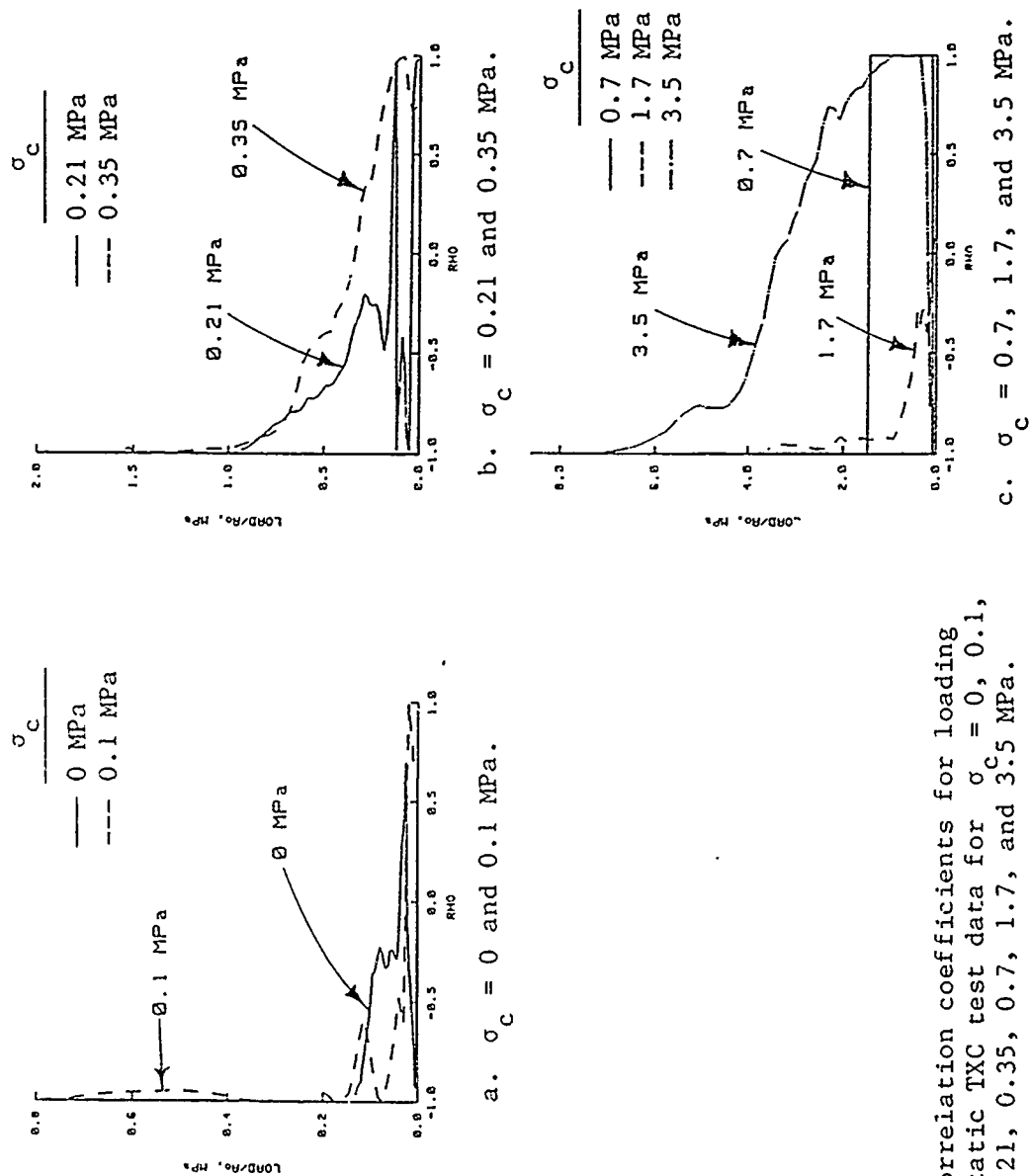
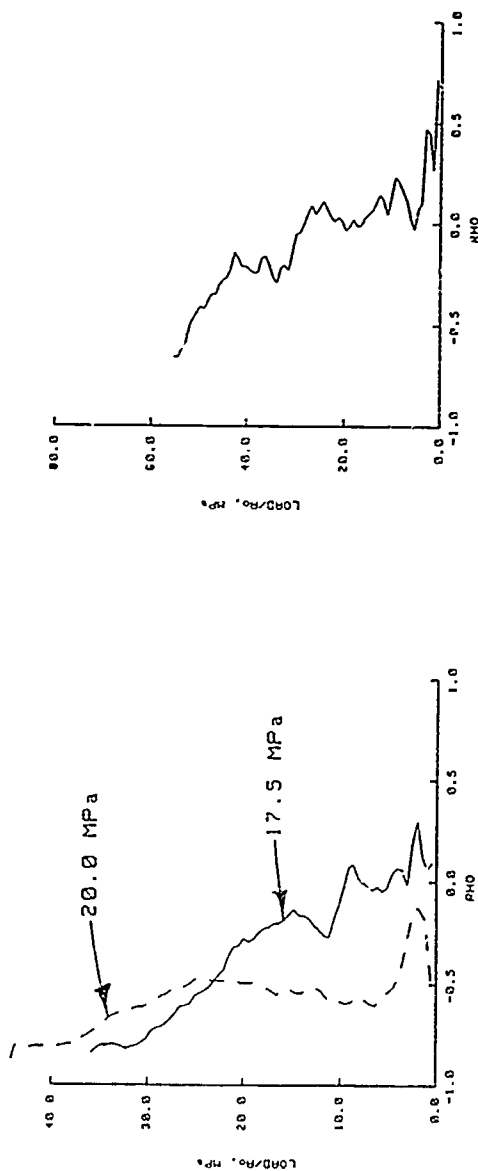
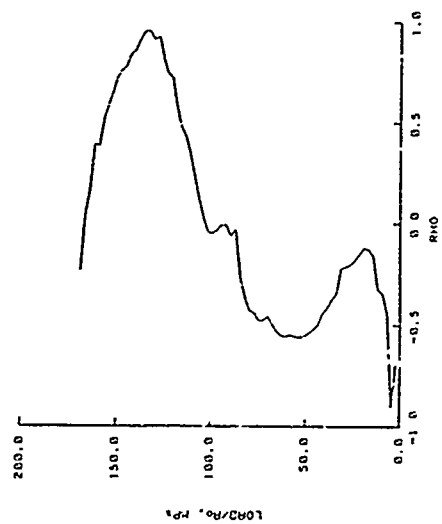


Figure 3.102. Correlation coefficients for loading static TXC test data for $\sigma_c = 0, 0.1, 0.21, 0.35, 0.7, 1.7, \text{ and } 3.5 \text{ MPa}$.



b. $\sigma_c = 40.0$ MPa.



d. $\sigma_c = 80.0$ MPa

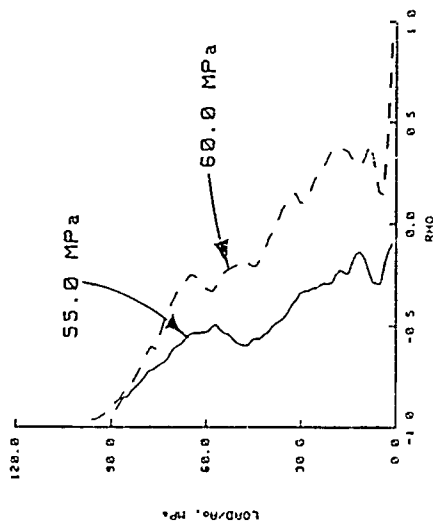


Figure 3.103. Correlation coefficients for loading static TXC test data for $\sigma_c = 17.5, 20.0, 40.0, 55.0, 60.0$, and 80.0 MPa.

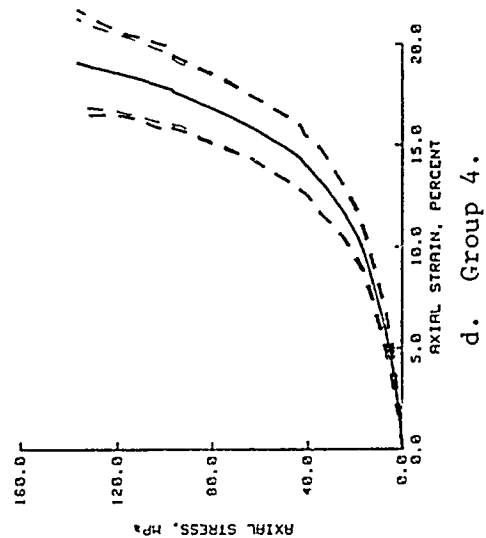
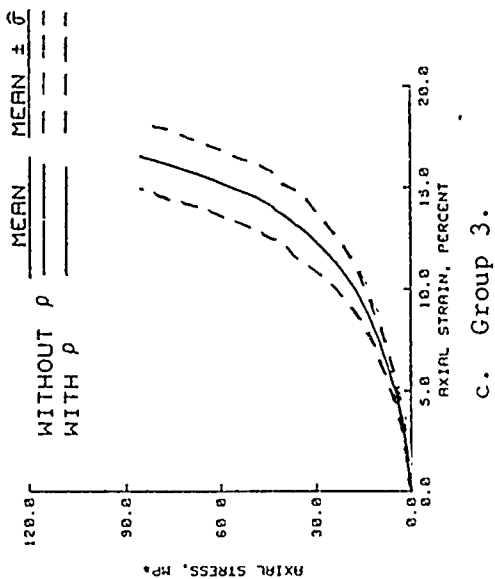
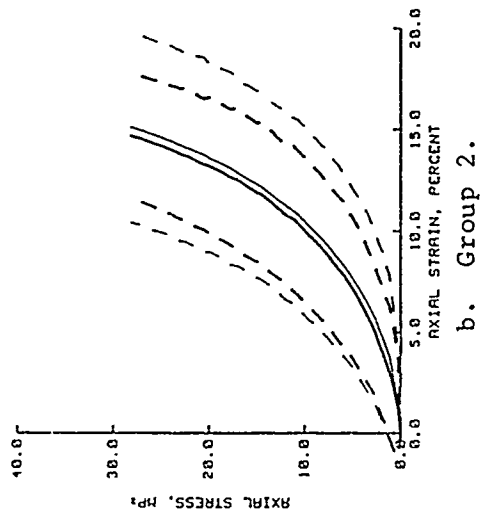
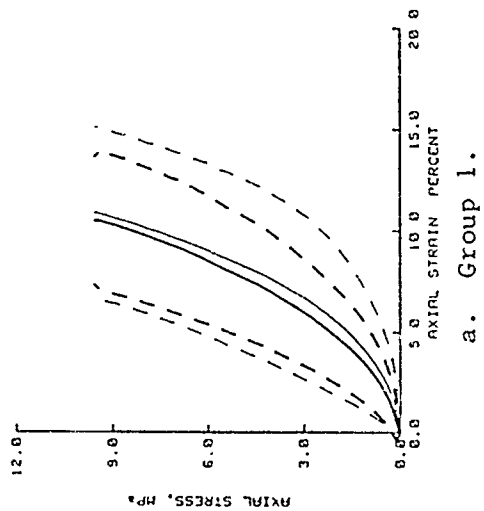
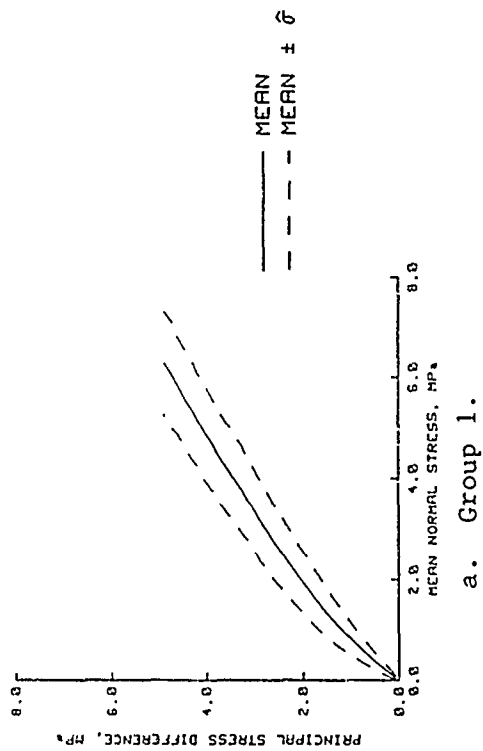
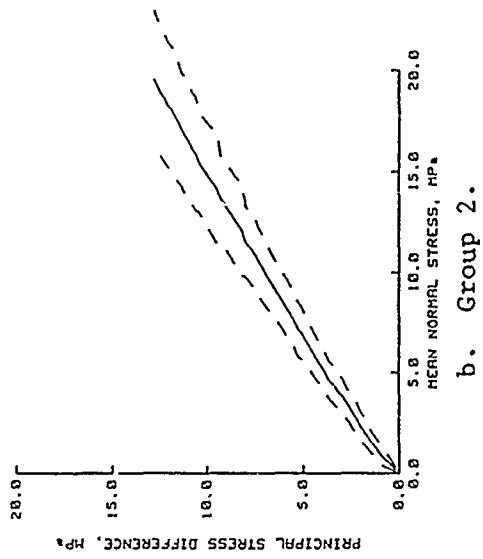


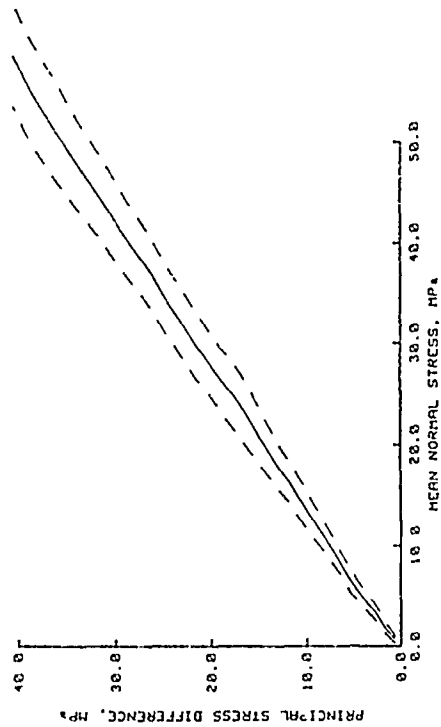
Figure 3.104. Results from applying the Rosenblueth procedure to the results from the COV analysis of "measured" K_0 test data.



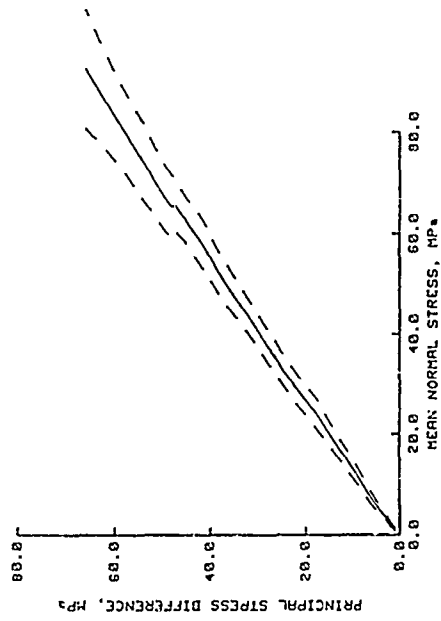
a. Group 1.



b. Group 2.



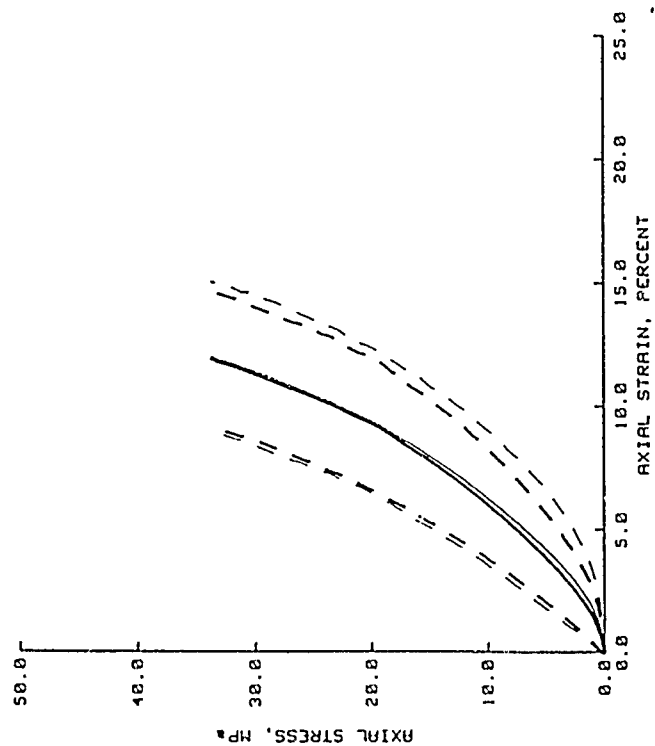
c. Group 3.



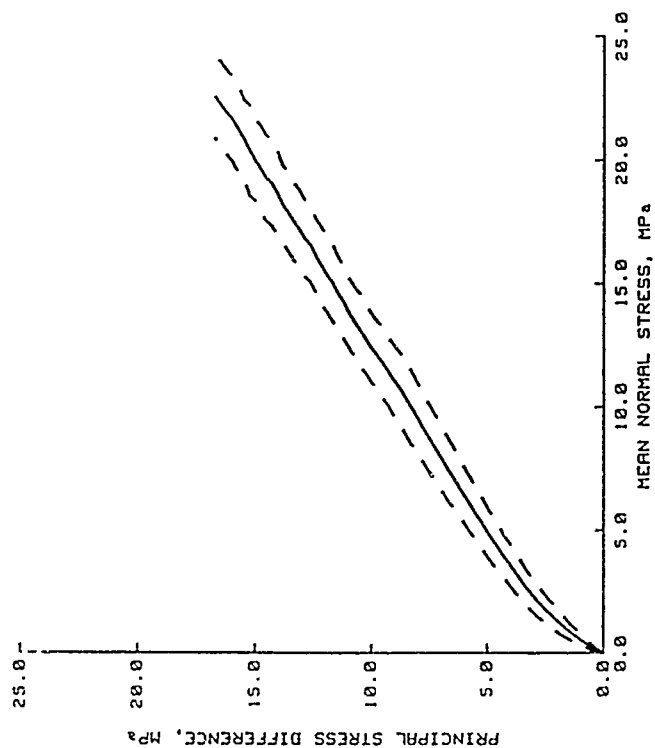
d. Group 4.

Figure 3.105. Stress paths obtained from applying the Rosenbluth procedure to the results from the COV analysis of "measured" K_0 test data.

	MEAN	MEAN $\pm \hat{\sigma}$
WITHOUT ρ	---	---
WITH ρ	---	---



a. Axial stress versus axial strain.



b. PSD versus MNS.

Figure 3.106. Results from applying the Rosenblueth procedure to the results from the COV analysis of "measured" EXT K_0 test data.

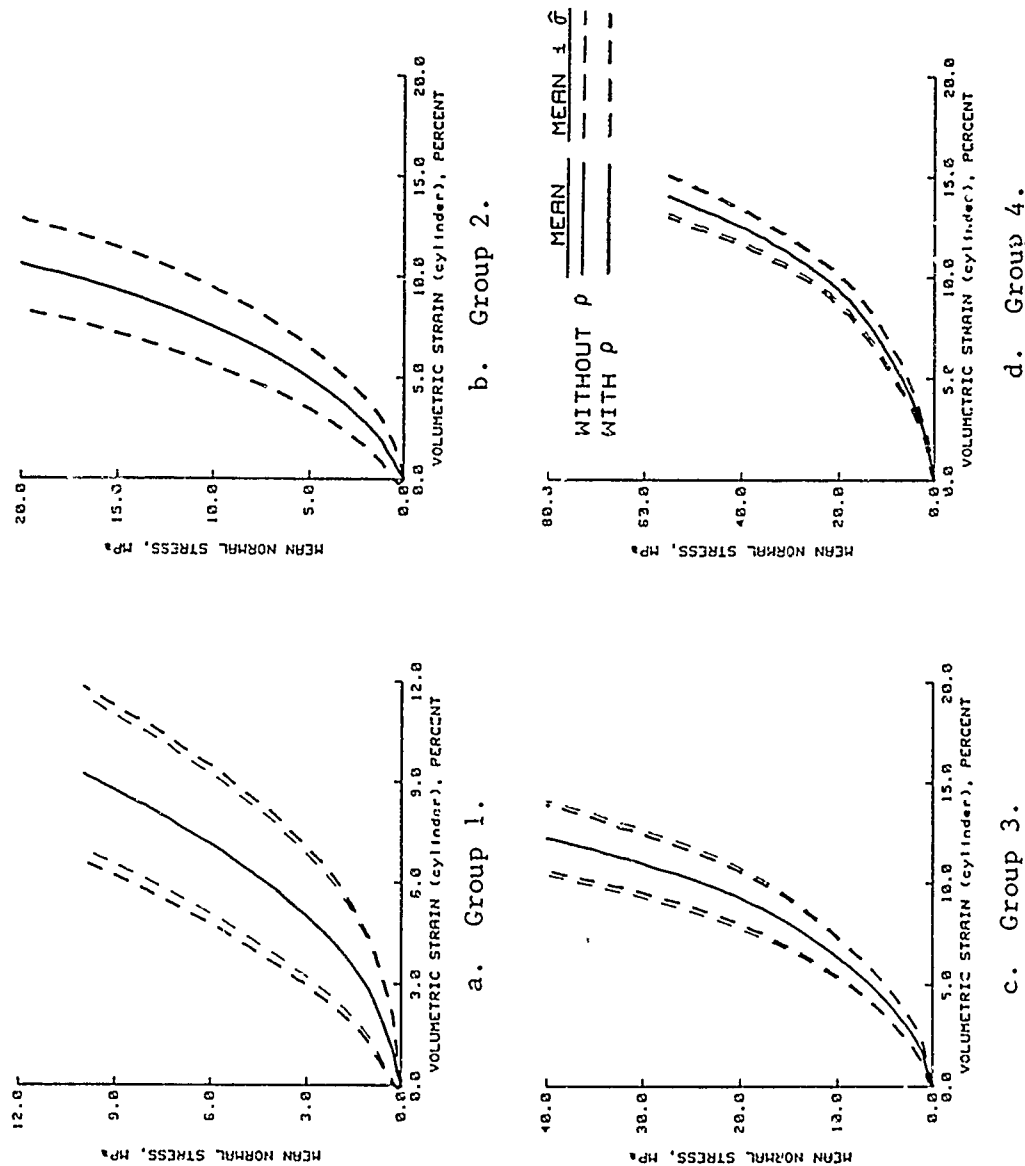


Figure 3.107. Results from applying the Rosenblueth procedure to the results from the COV analysis of "measured" static HC test data.

	MEAN	MEAN $\pm \sigma$
WITHOUT ρ	---	---
WITH ρ	---	---

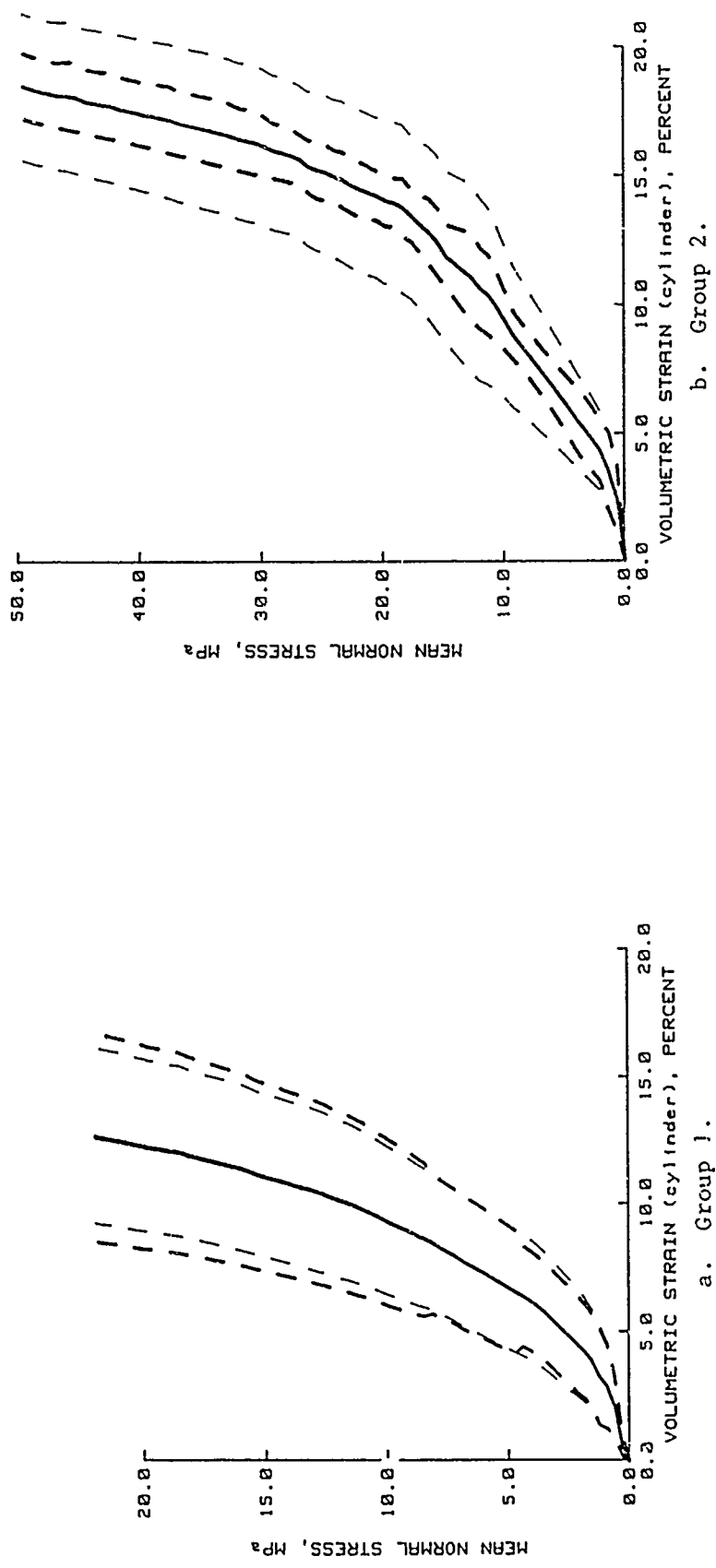


Figure 3.108. Results from applying the Rosenblueth procedure to the results from the COV analysis of "measured" dynamic HC test data.

— MEAN
 - - - MEAN $\pm \hat{\sigma}$

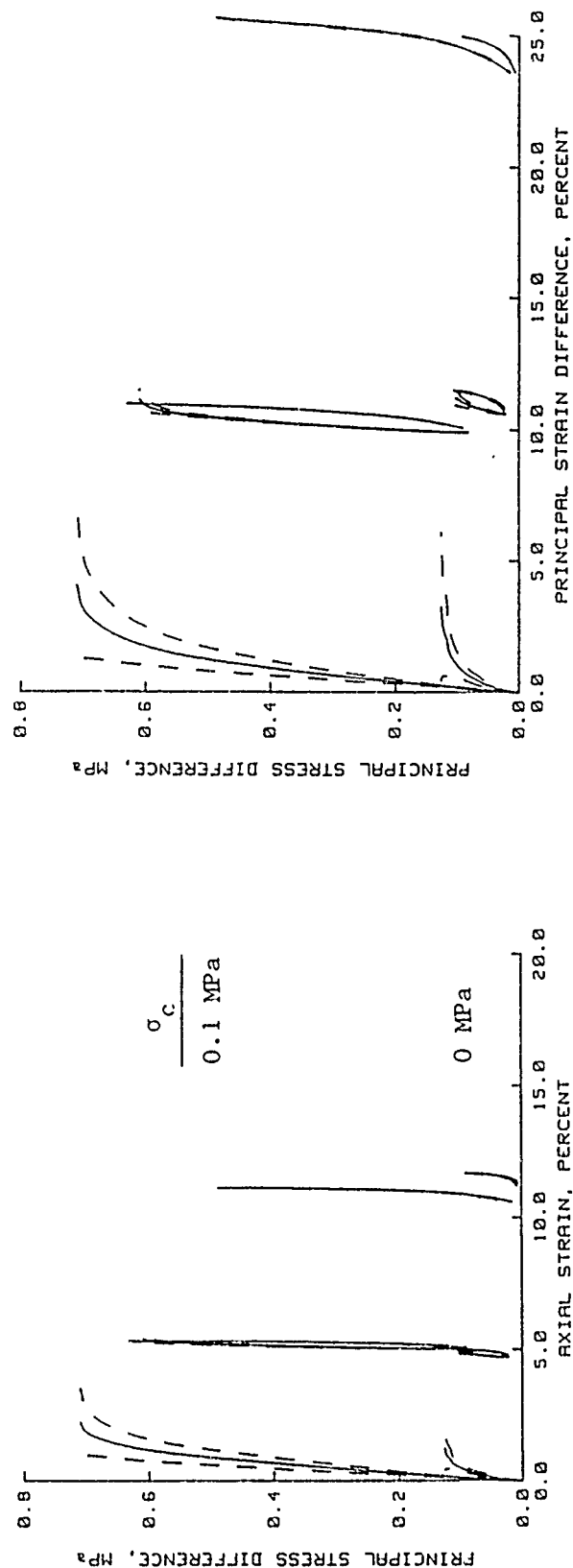


Figure 3.109. Results from applying the Rosenblueth procedure to the results from the COV analysis of "measured" TXC test data for $\sigma_c = 0$ and 0.1 MPa.

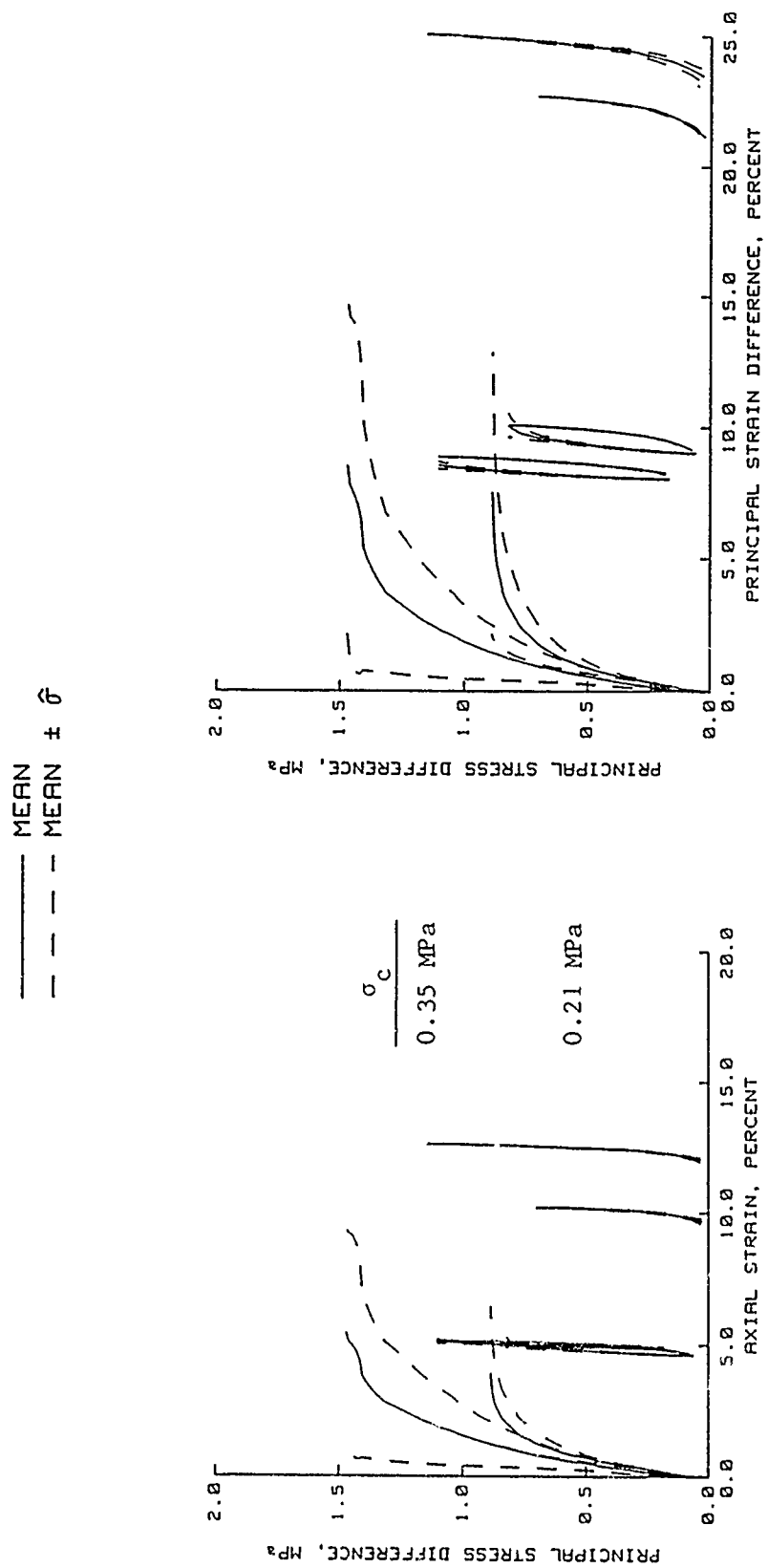


Figure 3.110. Results from applying the Rosenblueth procedure to the results from the COV analysis of "measured" TXC test data for $\sigma_c = 0.21$ and 0.35 MPa.

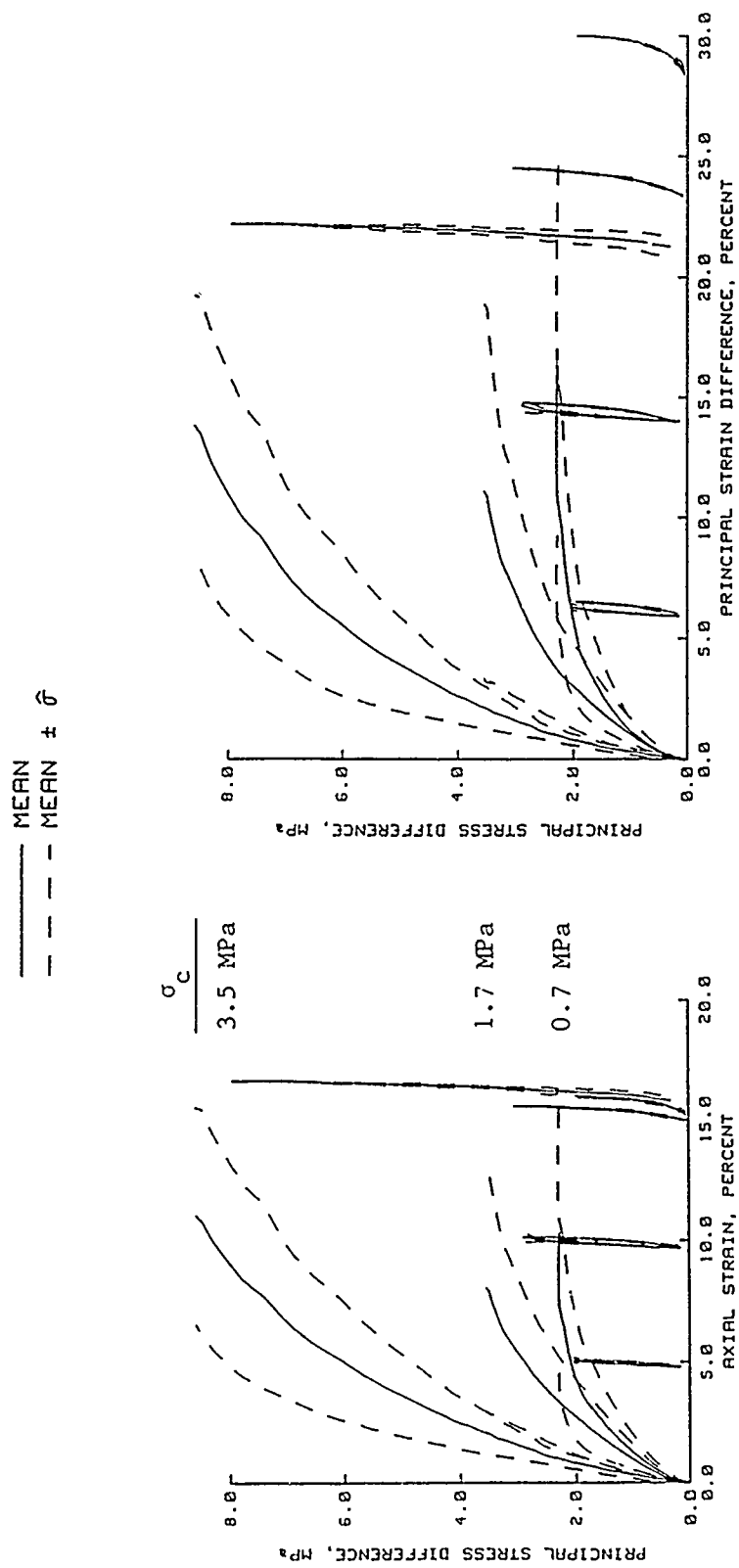


Figure 3.111. Results from applying the Rosenbluth procedure to the results from the COV analysis of "measured" TXC test data for $\sigma_c = 0.7, 1.7, \text{ and } 3.5 \text{ MPa}$.

——— MEAN
 - - - MEAN $\pm \sigma$

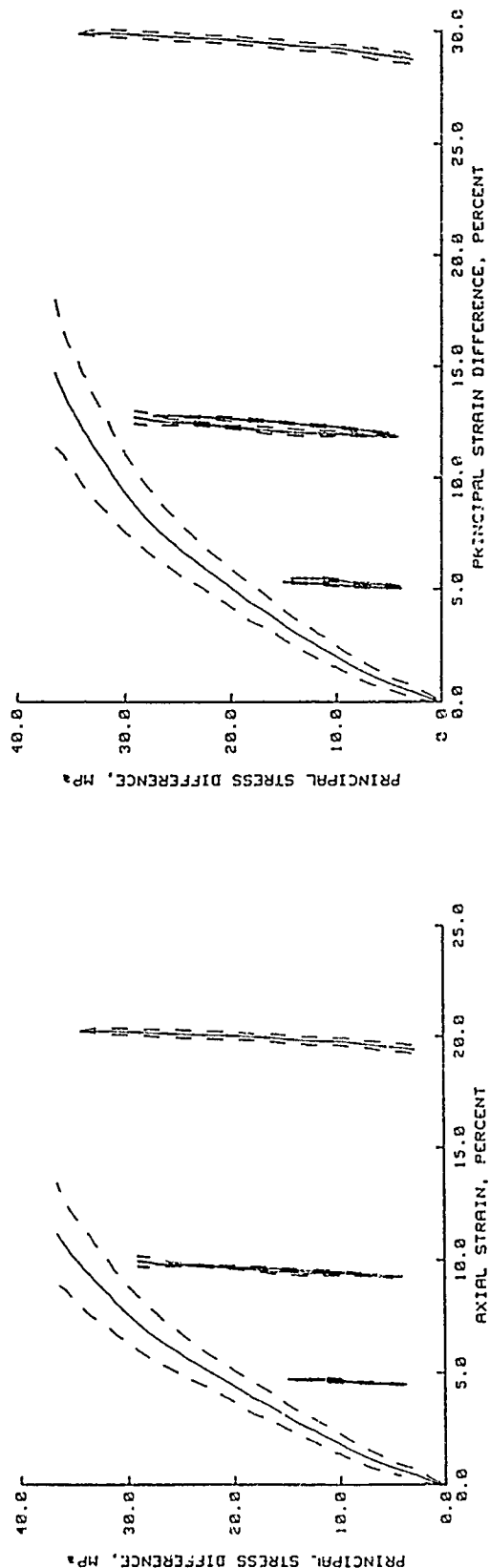


Figure 3.112. Results from applying the Rosenblueth procedure to the results from the COV analysis of "measured" TXC test data for $\sigma_c = 17.5$ MPa.

——— MEAN
 - - - MEAN $\pm \sigma$

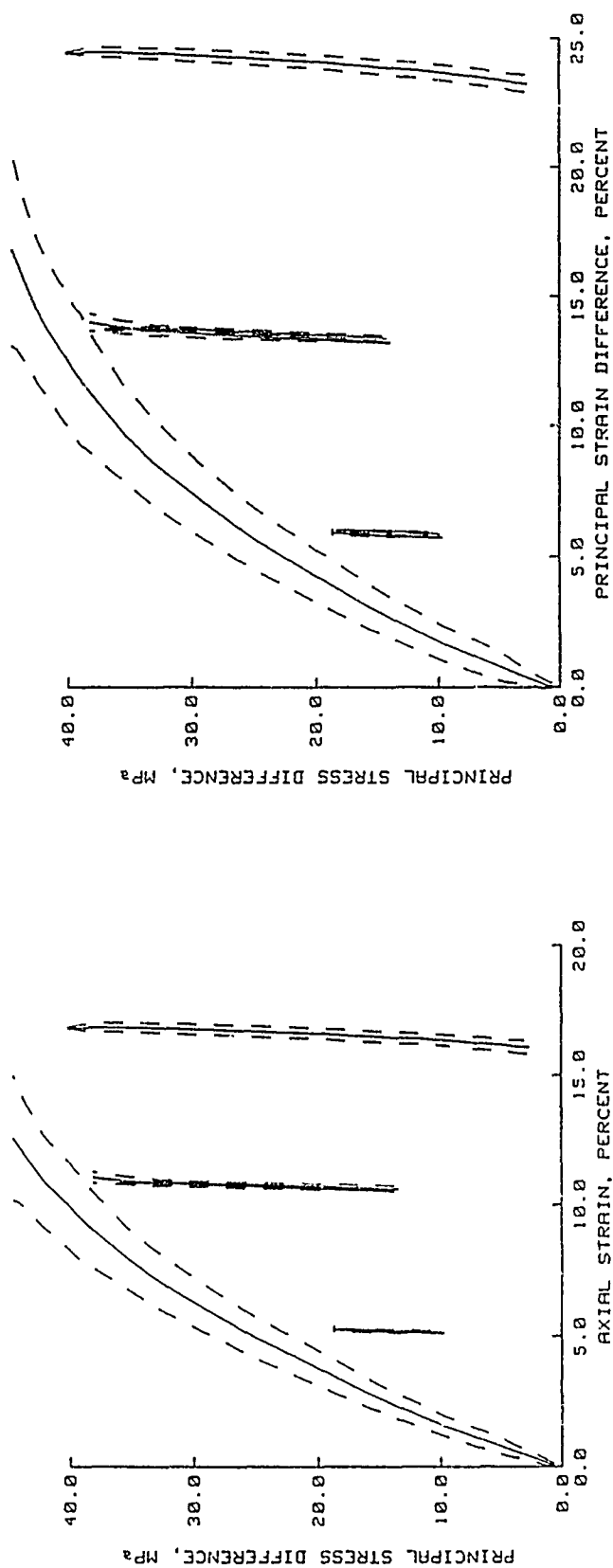


Figure 3.113. Results from applying the Rosenblueth procedure to the results from the COV analysis of "measured" TXC test data for $\sigma_c = 20.0$ MPa.

——— MEAN
 - - - MEAN $\pm \hat{\sigma}$

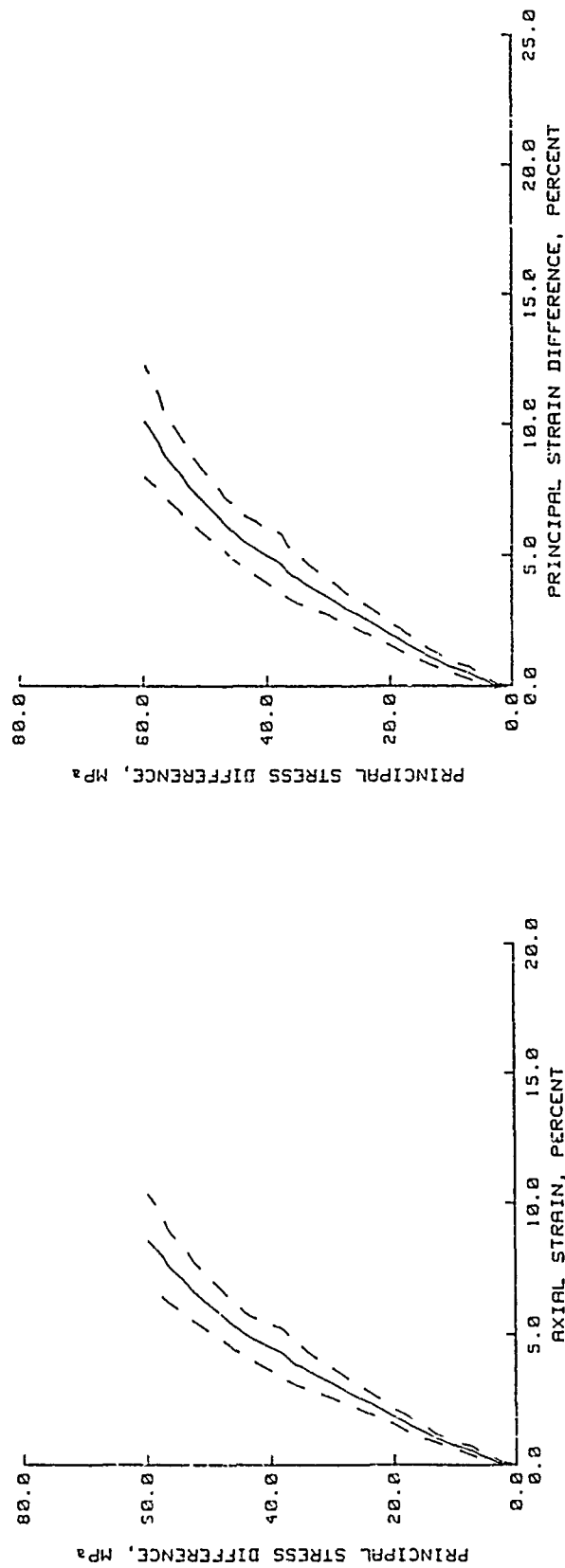


Figure 3.114. Results from applying the Rosenblueth procedure to the results from the COV analysis of "measured" TXC test data for $\sigma_c = 40.0$ MPa.

— MEAN
 - - - MEAN $\pm \hat{\sigma}$

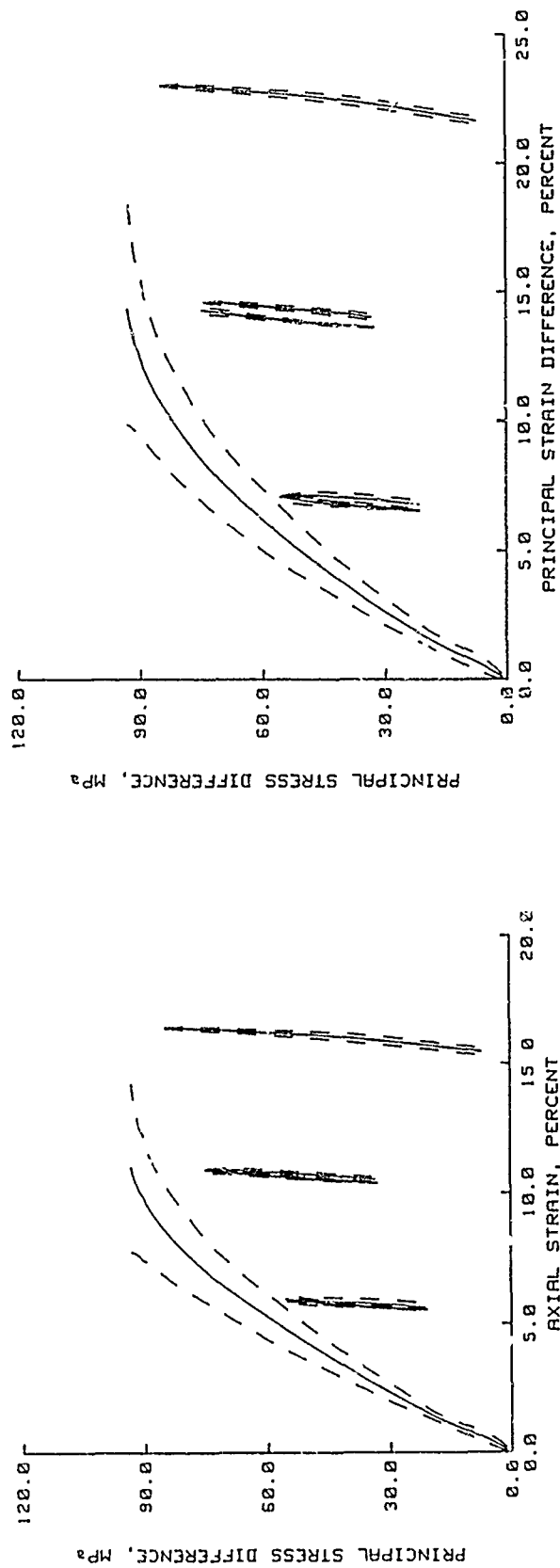


Figure 3.115. Results from applying the Rosenbluth procedure to the results from the COV analysis of "measured" TXC test data for $\sigma_c = 55.0$ MPa.

——— MEAN
 --- MEAN $\pm \hat{\sigma}$

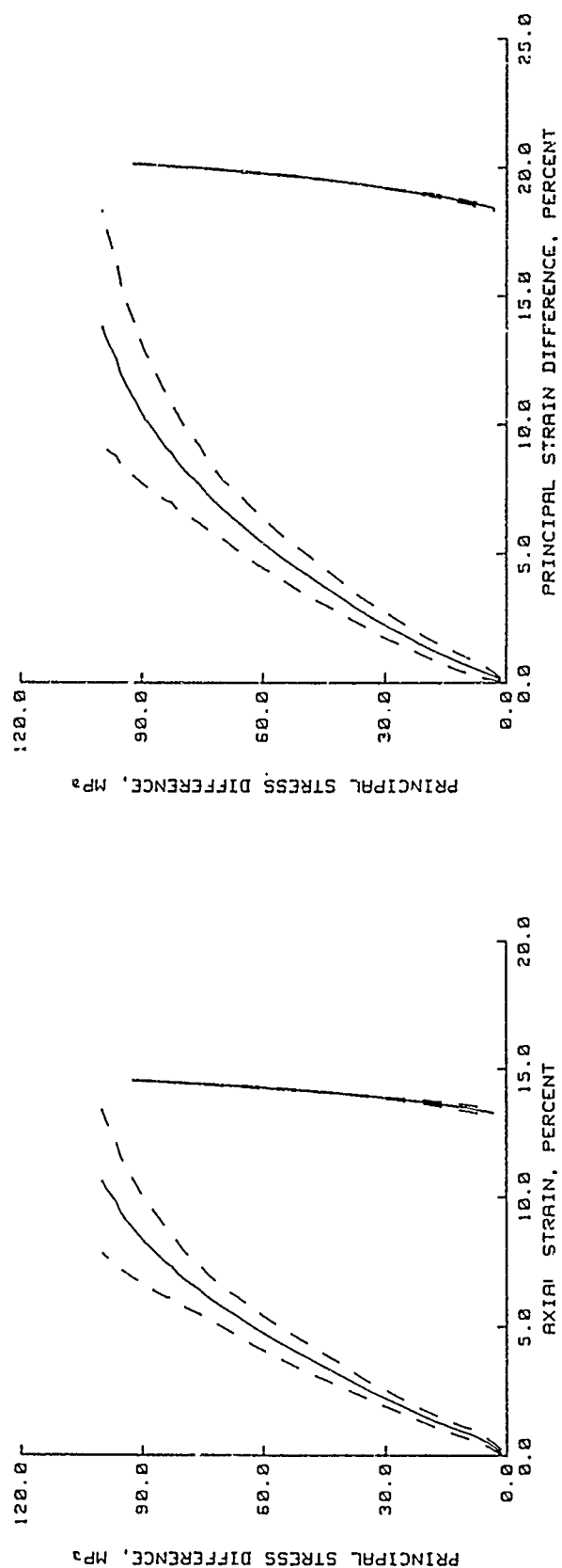


Figure 3.116. Results from applying the Rosenblueth procedure to the results from the COV analysis of "measured" TXC test data for $\sigma_c = 60.0$ MPa.

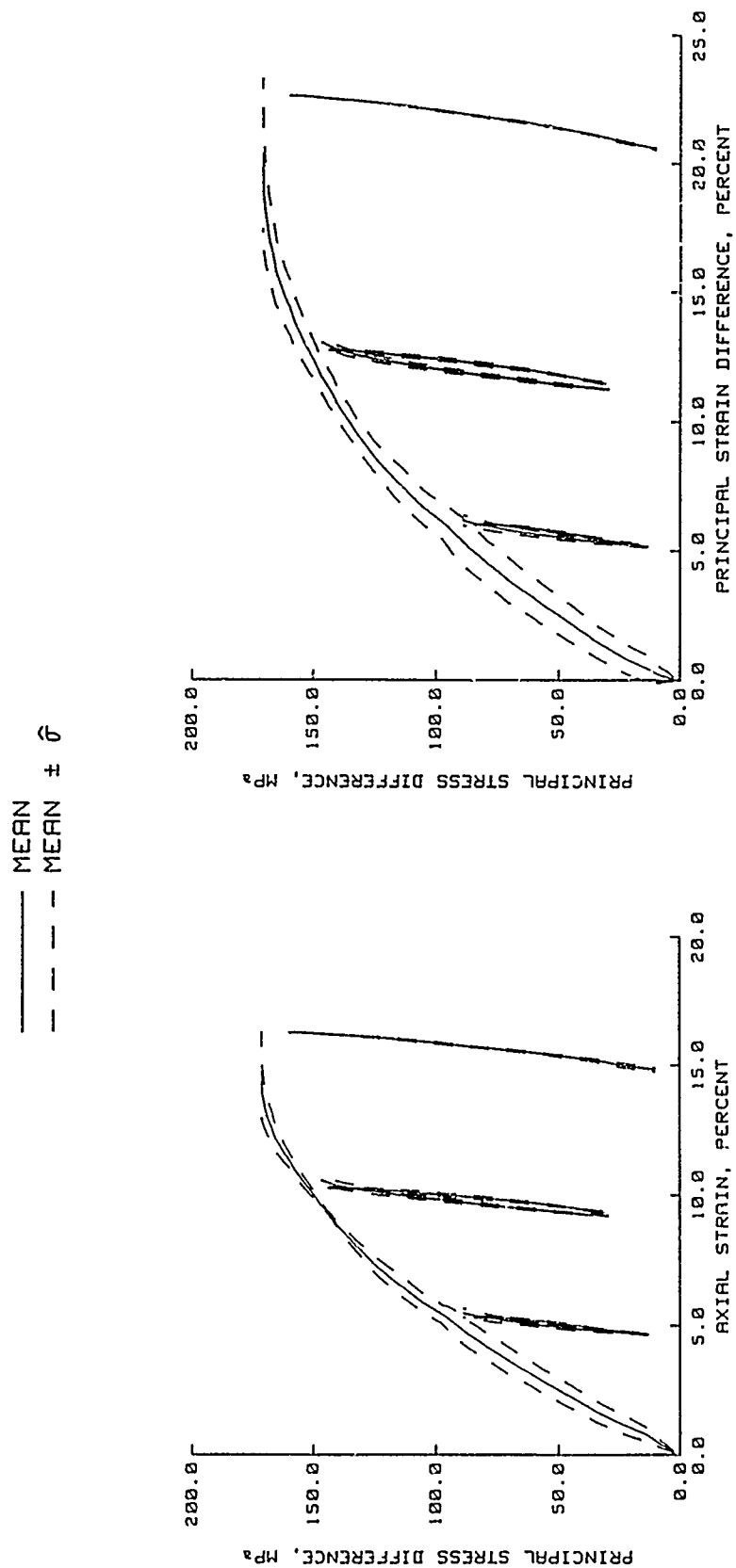


Figure 3.117. Results from applying the Rosenblueth procedure to the results from the COV analysis of "measured" TXC test data for $\sigma_c = 80.0$ MPa.

MEAN		MEAN $\pm \bar{\sigma}$
WITHOUT ρ	---	---
WITH ρ	---	---

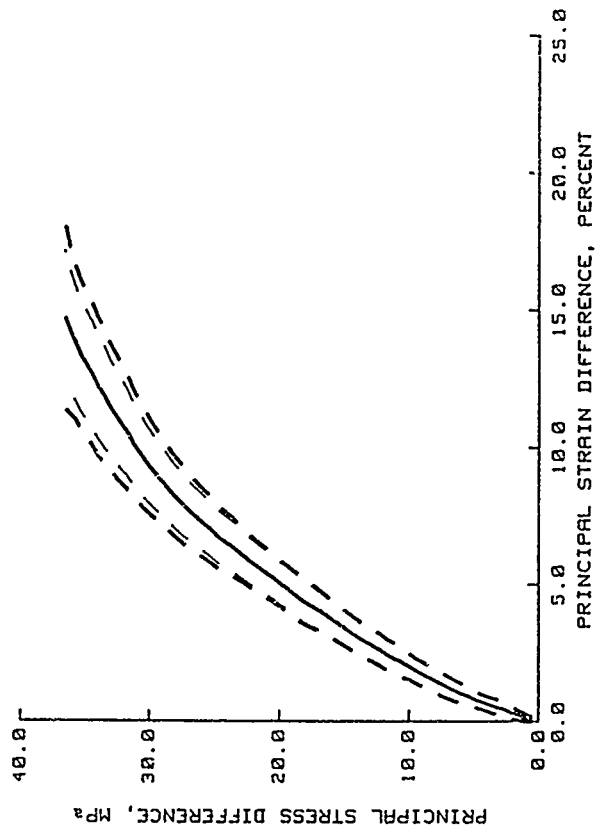
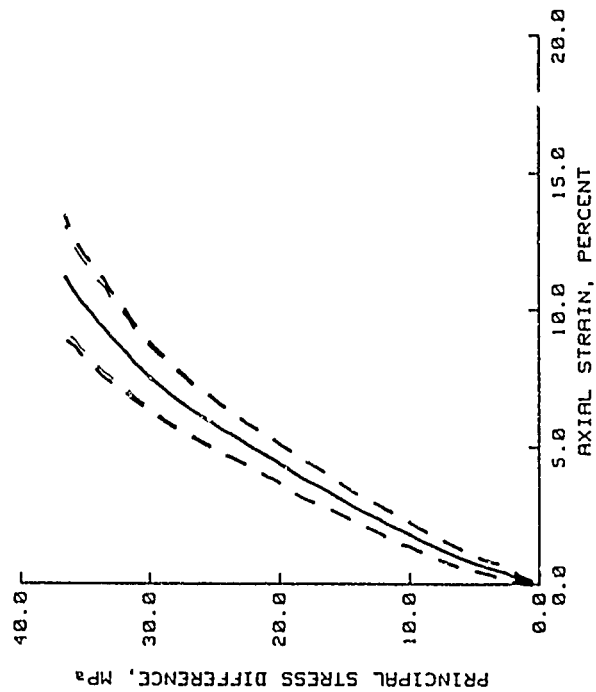


Figure 3.118. Effect of including ρ in the Rosenbluth procedure for TXC test data at $\sigma_c = 17.5$ MPa.

	MEAN	MEAN $\pm \hat{\sigma}$
WITHOUT ρ	---	---
WITH ρ	---	---

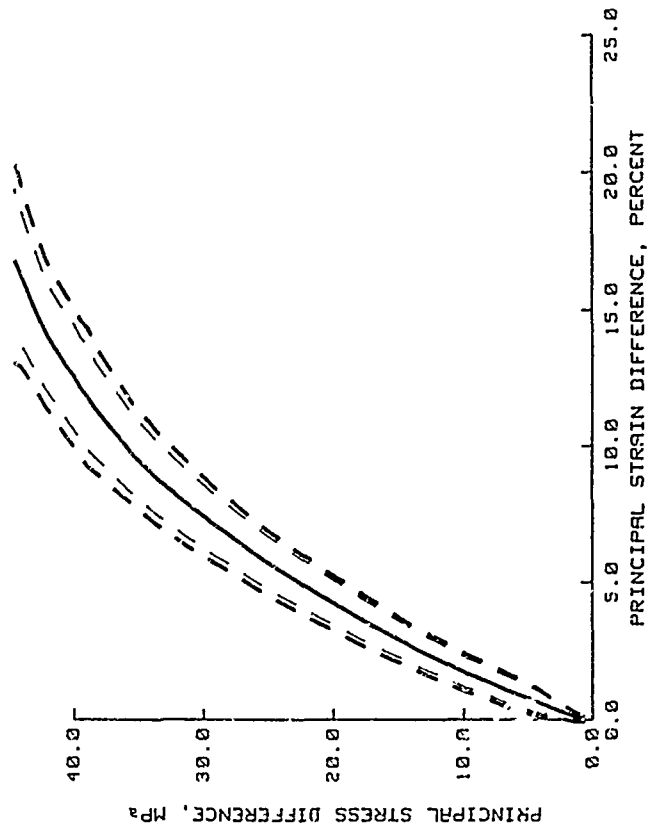
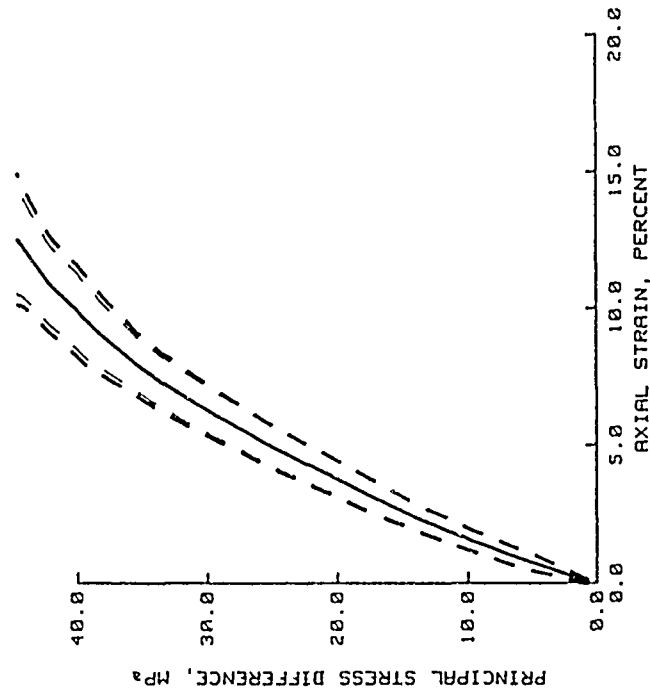


Figure 3.119. Effect of including ρ in the Rosenblueth procedure for TXC test data at $\sigma_c = 20.0$ MPa.

	MEAN	MEAN $\pm \hat{\sigma}$
WITHOUT ρ	---	---
WITH ρ	---	---

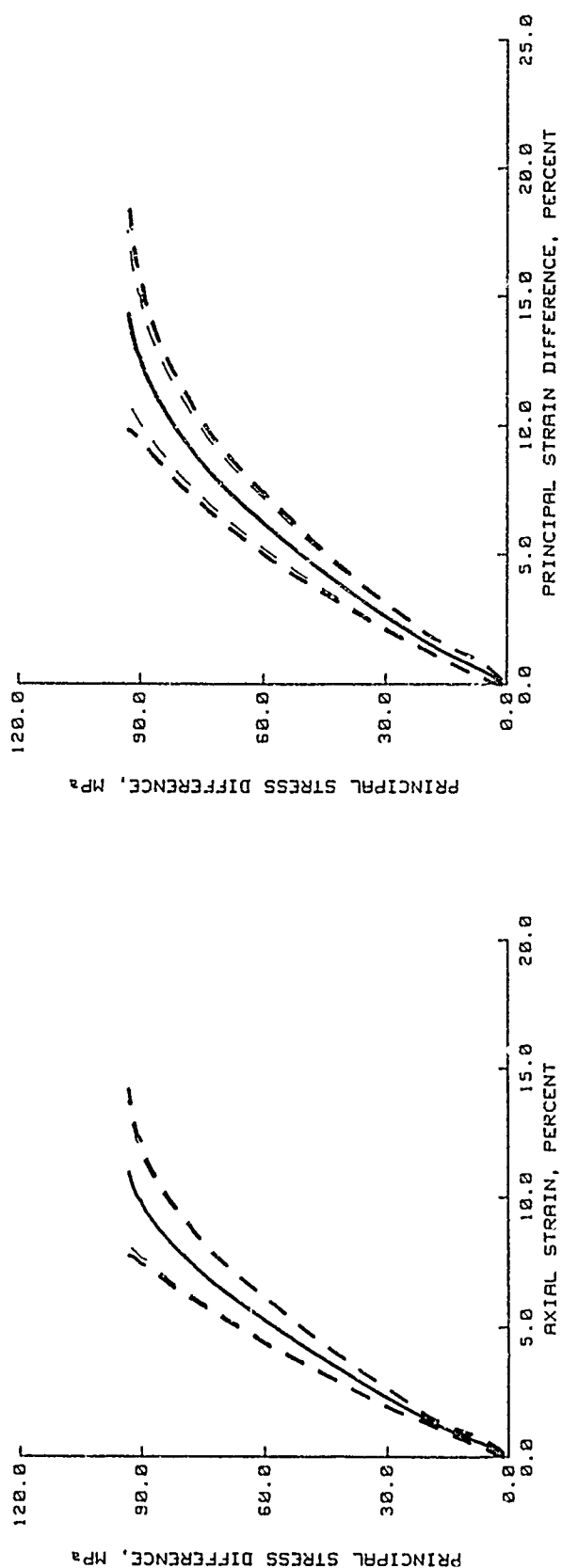
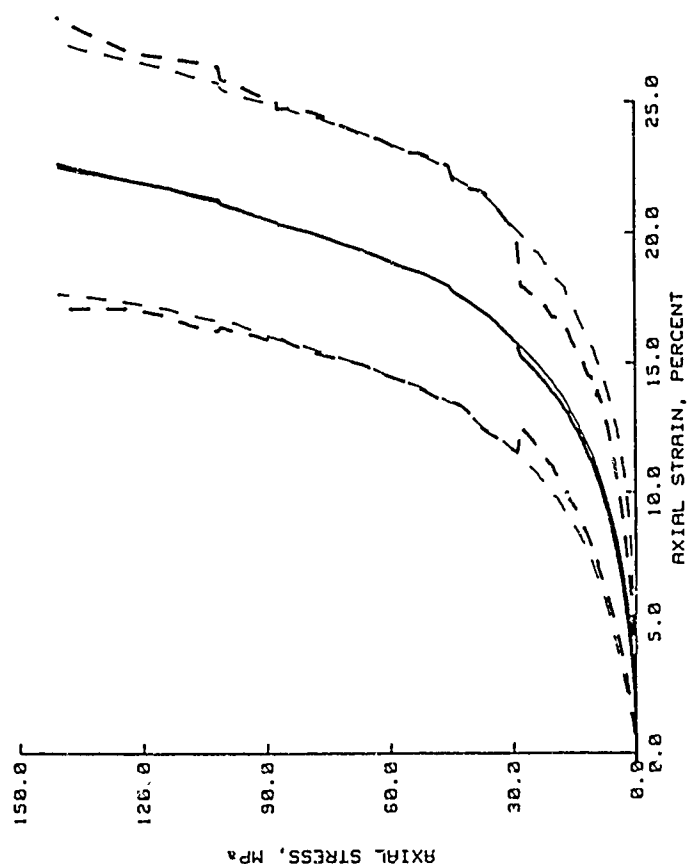
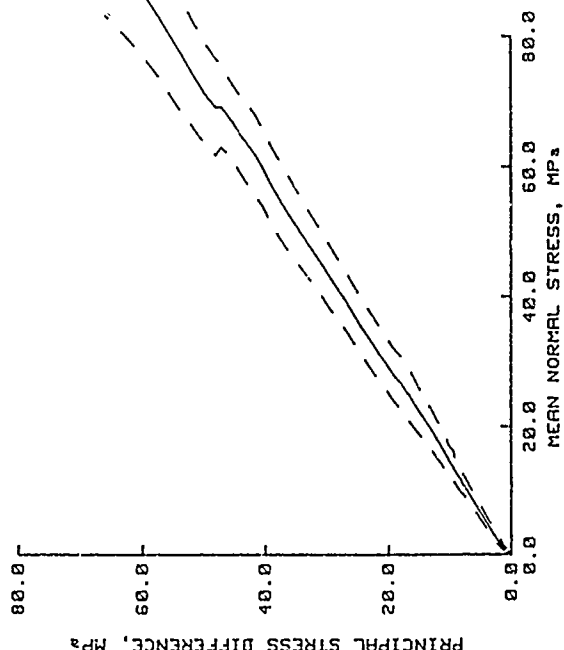


Figure 3.120. Effect of including ρ in the Rosenblueth procedure for TXC test data at $\sigma_c = 55.0$ MPa.

	MEAN	MEAN $\pm \hat{\sigma}$
WITHOUT ρ	---	---
WITH ρ	---	---



a. Axial stress versus axial strain.



b. PSD versus MNS.

Figure 3.121. Results from applying the Rosenblueth procedure to constructed continuous results from the COV analysis of "measured" K_0 test data.

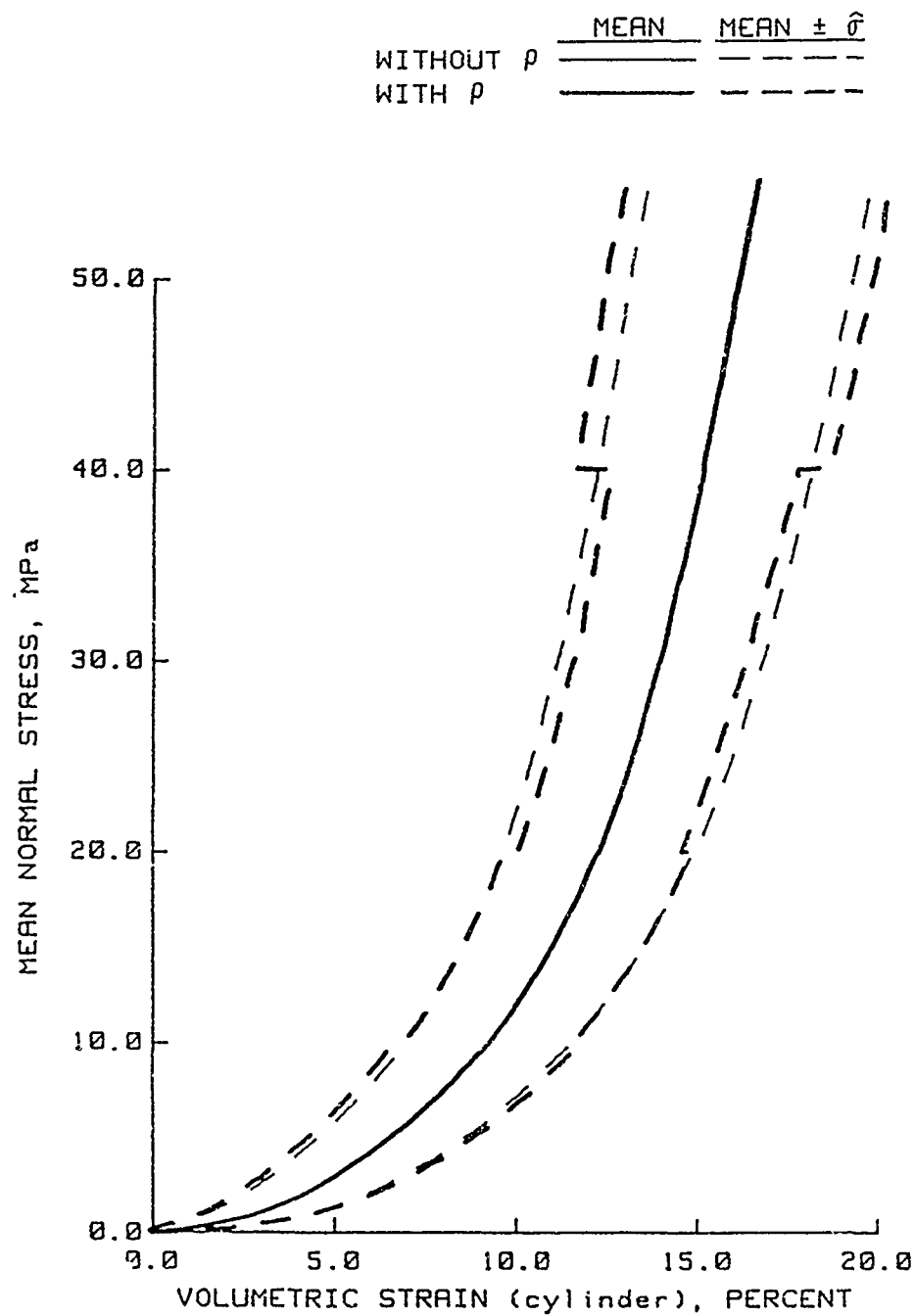


Figure 3.122. Results from applying the Rosenblueth procedure to constructed continuous results from the COV analysis of "measured" static HC test data.

	MEAN	MEAN $\pm \hat{\sigma}$
WITHOUT ρ	-----	-----
WITH ρ	-----	-----

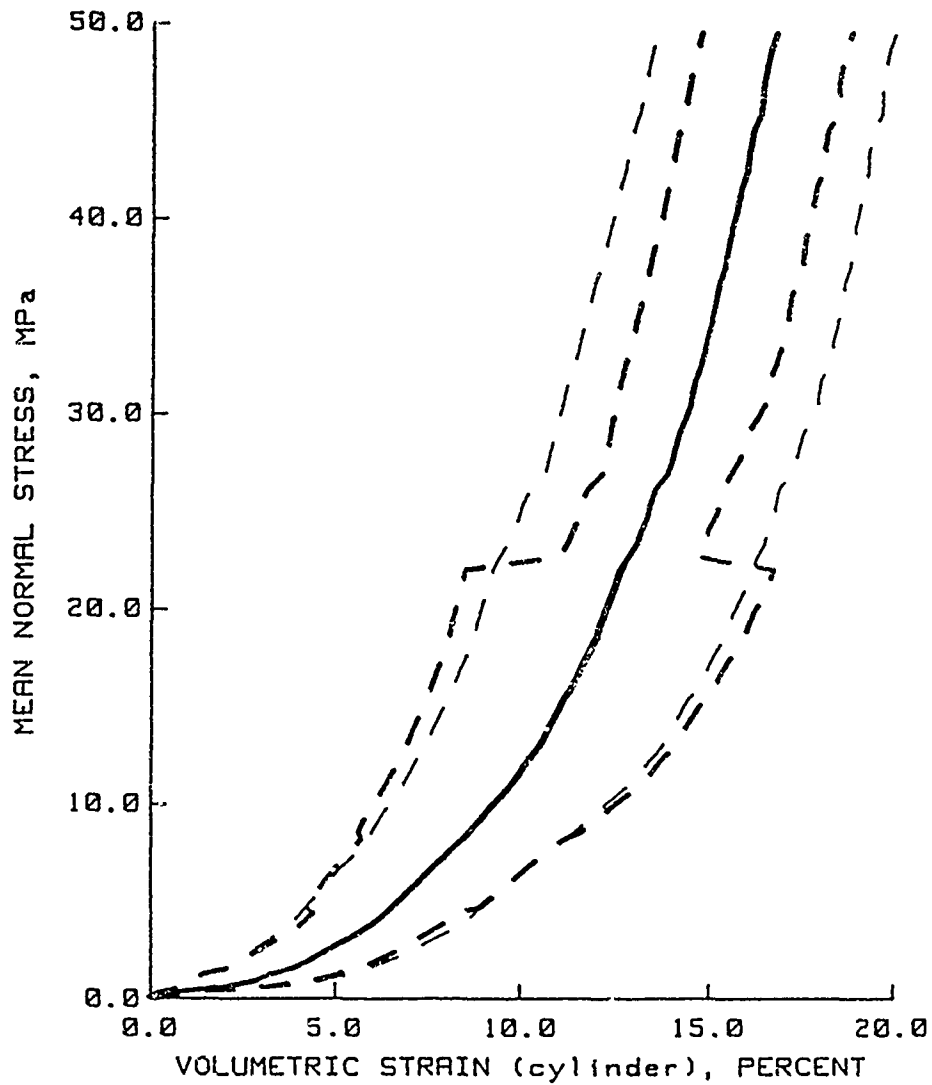


Figure 3.123. Results from applying the Rosenblueth procedure to constructed continuous results from the COV analysis of "measured" dynamic HC test data.

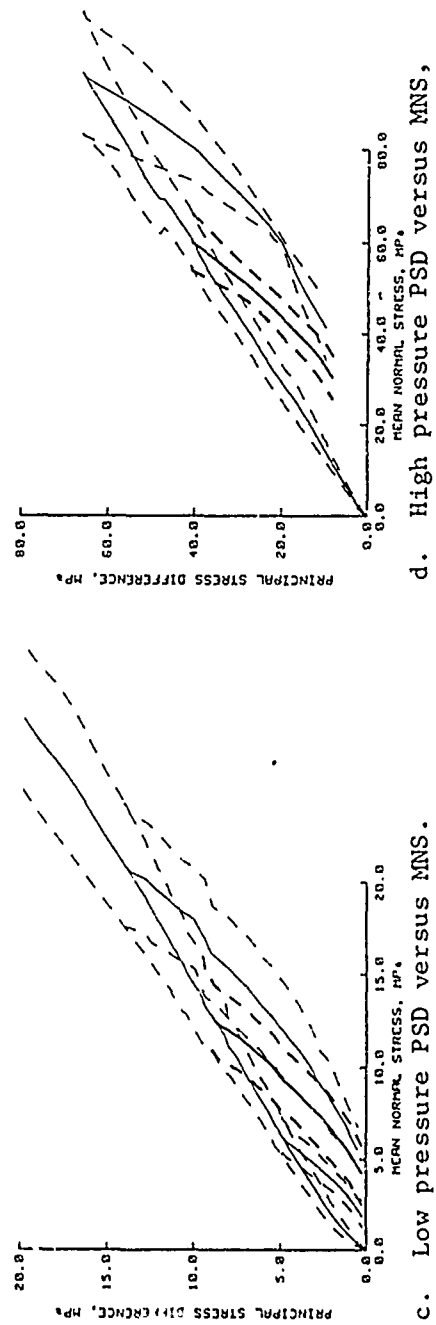
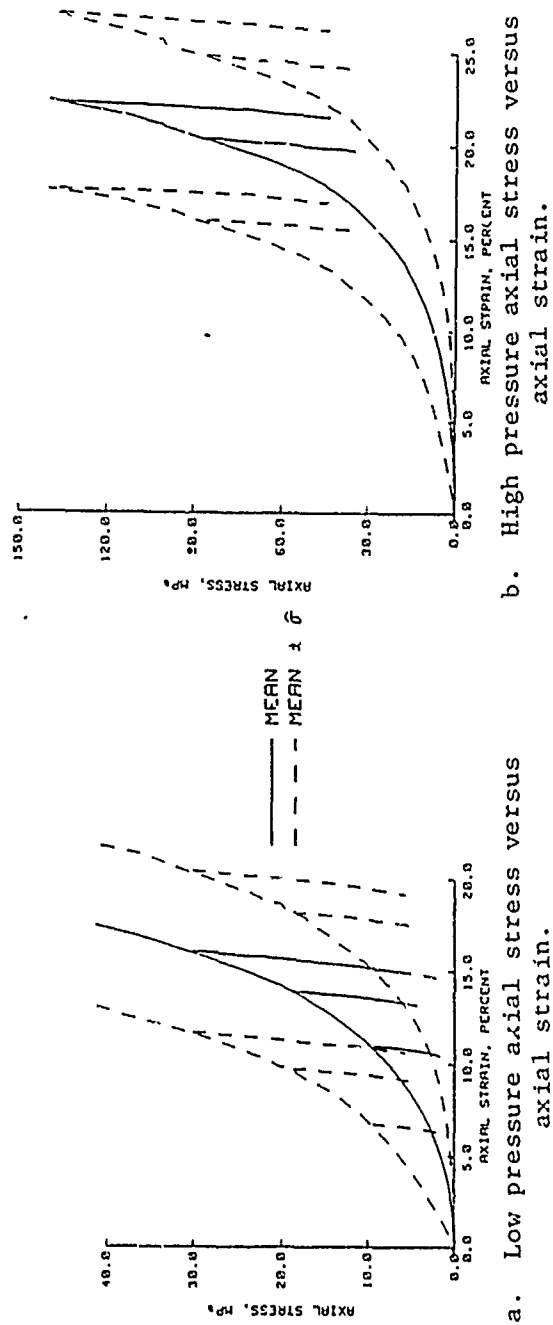
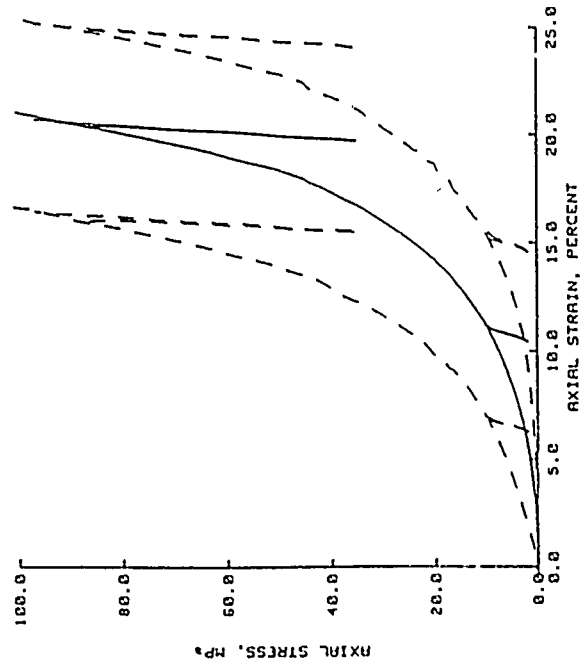
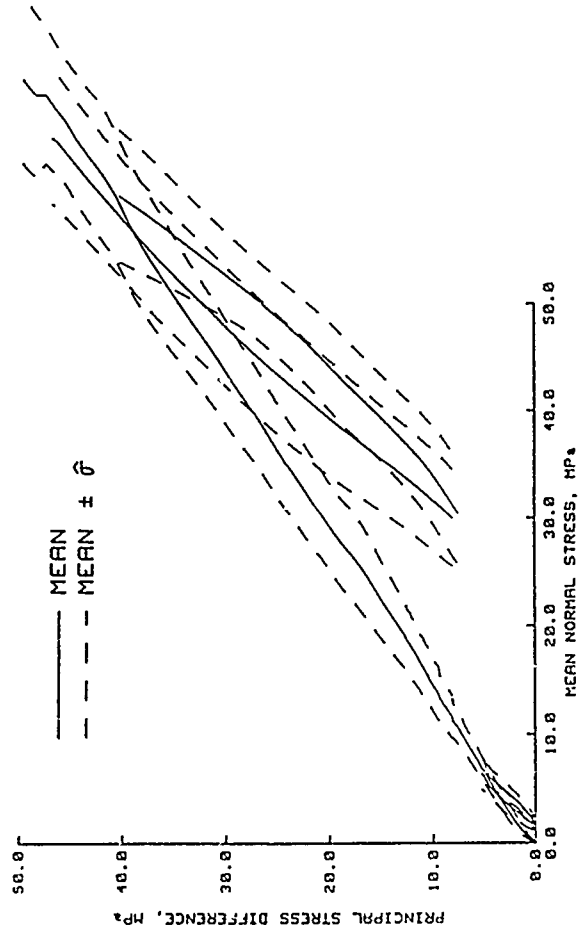


Figure 3.124. Load-unload responses constructed from the results of applying the Rosenbluth procedure to the results from the COV analysis of "measured" K_0 test data.

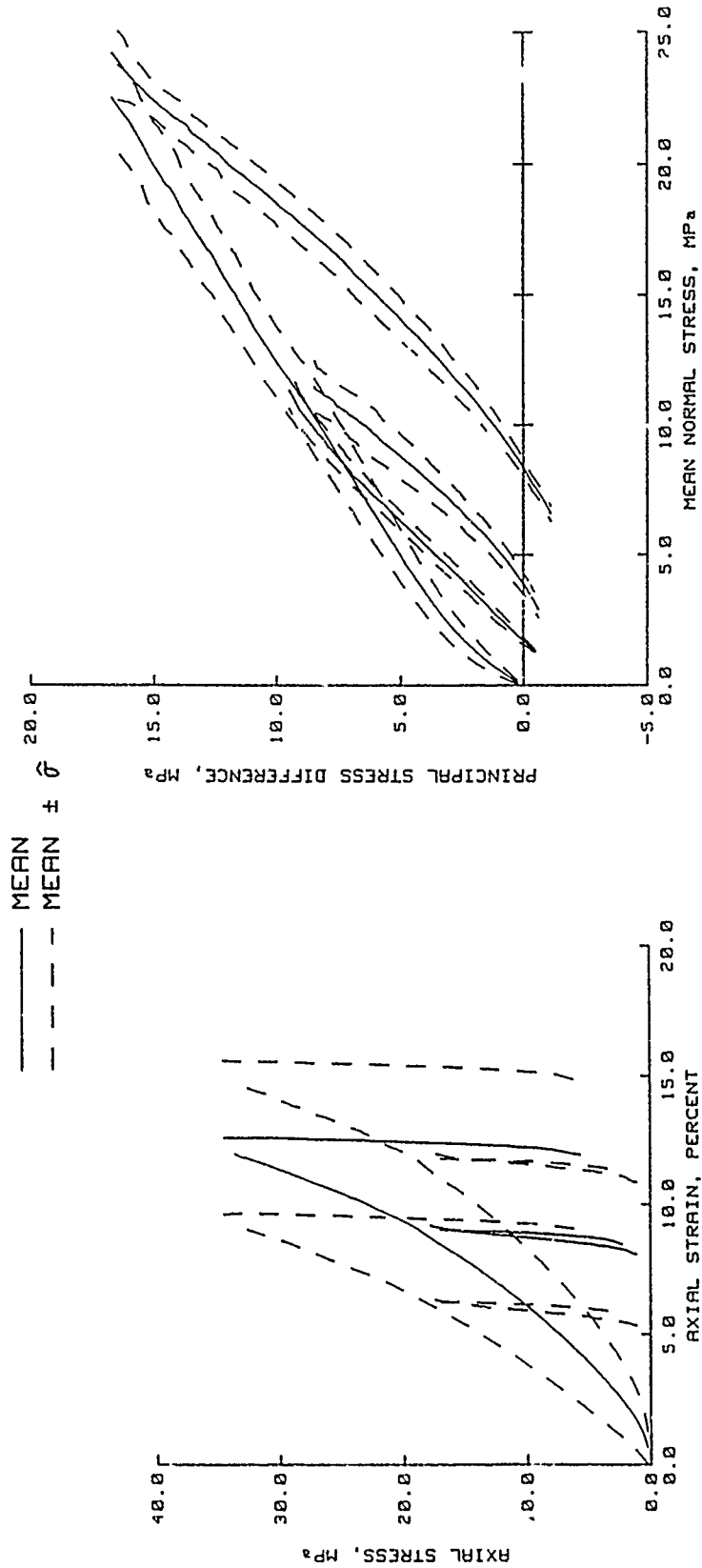


a. Axial stress versus axial strain.



b. p_{ij} versus MNS.

Figure 3.125. Load-unload-reload responses constructed from the results of applying the Rosenblueth procedure to the results from the COV analysis of "measured" K_0 test data.



a. Axial stress versus axial strain.

b. PSD versus MNS.

Figure 3.126. Load-unload-reload responses constructed from the results of applying the Rosenblueth procedure to the results from the COV analysis of "measured" EXT K_0 test data.

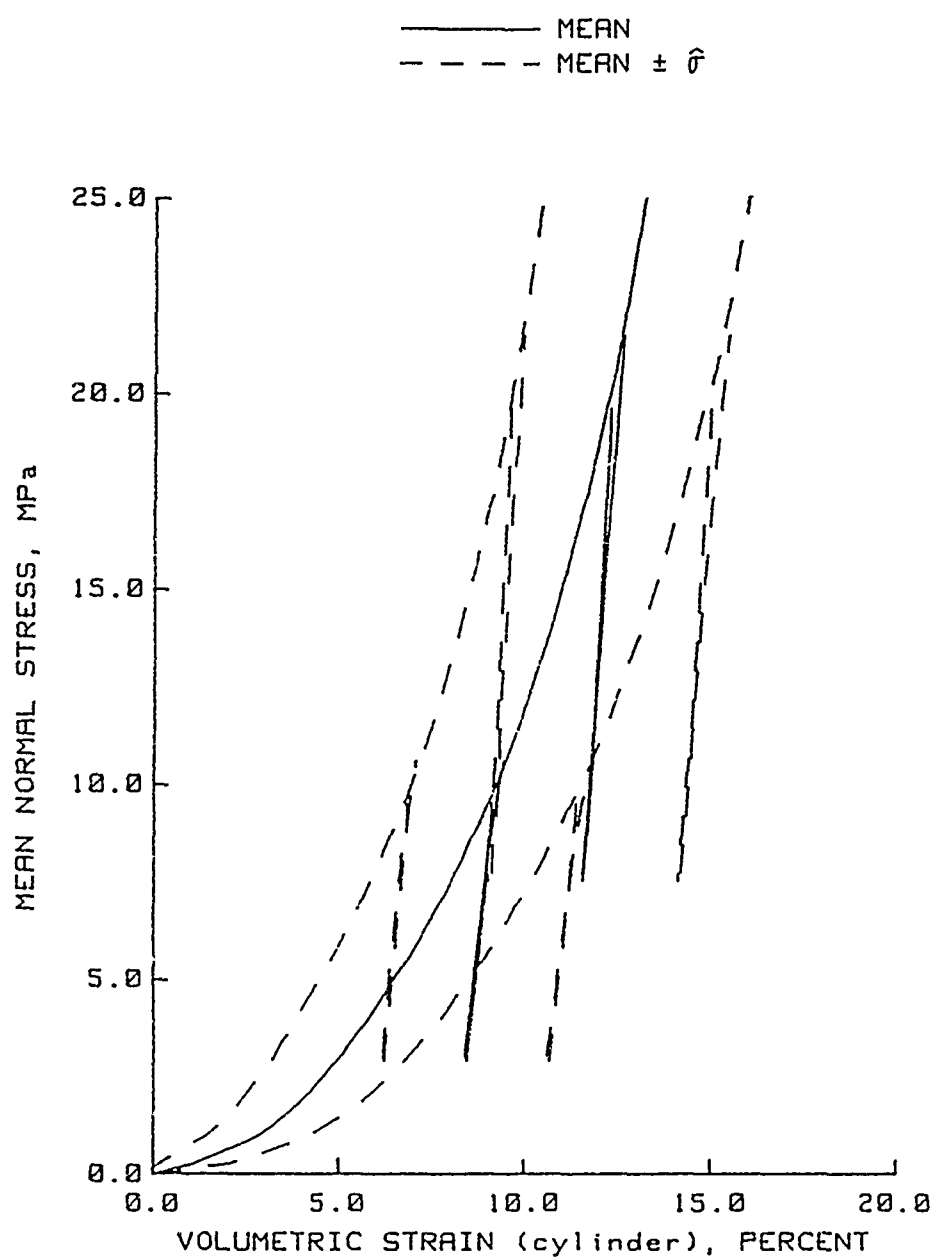


Figure 3.127. Load-unload-reload responses constructed from the results of applying the Rosenblueth procedure to the results from the COV analysis of "measured" static HC test data.

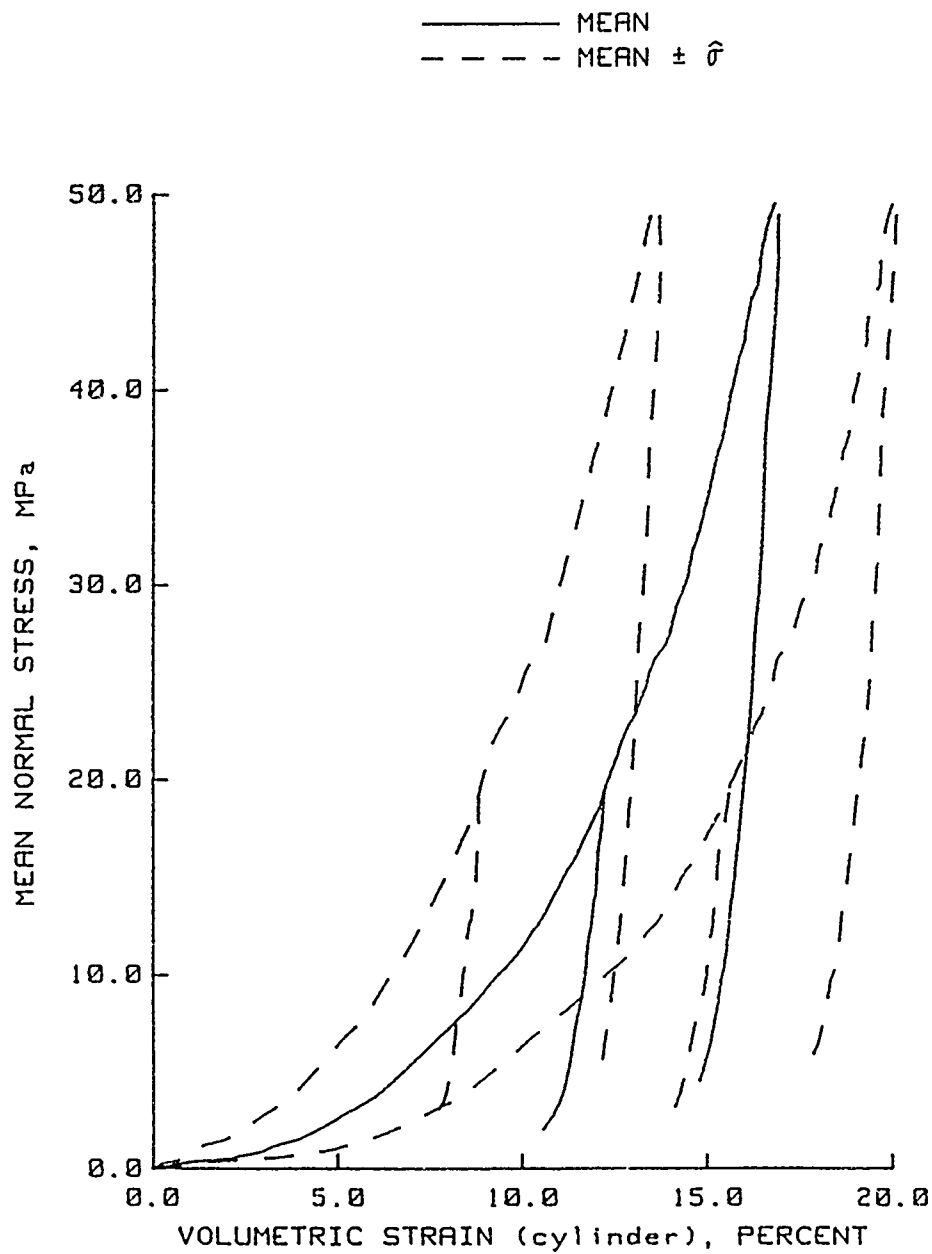


Figure 3.128. Load-unload responses constructed from the results of applying the Rosenblueth procedure to the results from the COV analysis of "measured" dynamic HC test data.

	MEAN	MEAN $\pm \sigma$
COV/ROSENBLUETH	---	---
COV	---	---

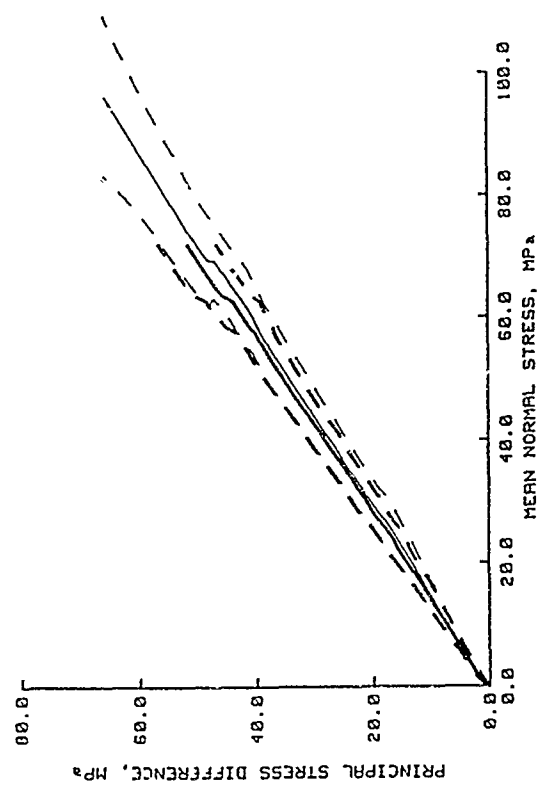
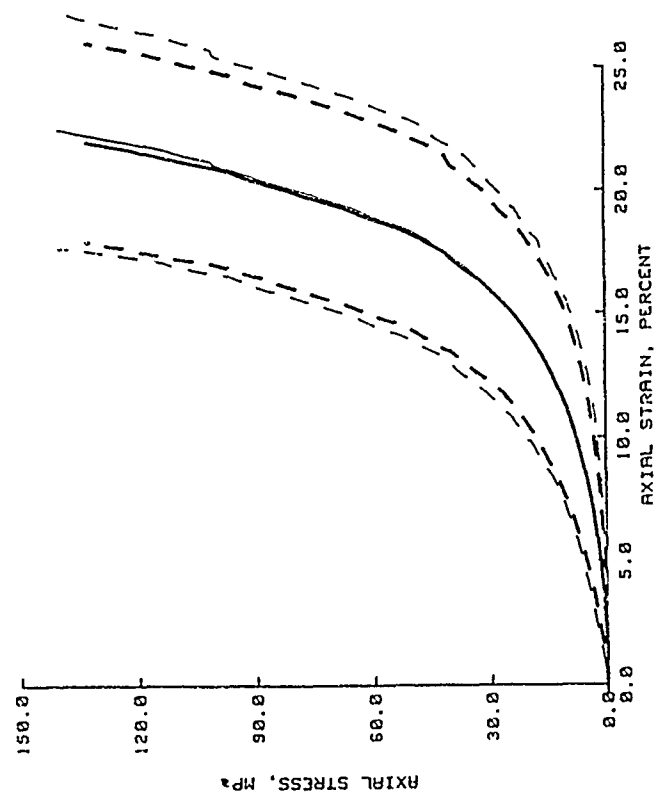


Figure 3.129. Comparison of the results from the COV and COV/Rosenblueth analysis techniques for the loading portion of K_0 test data.

	MEAN	MEAN $\pm \hat{\sigma}$
COV/ROSENBLUETH	---	---
COV	---	---

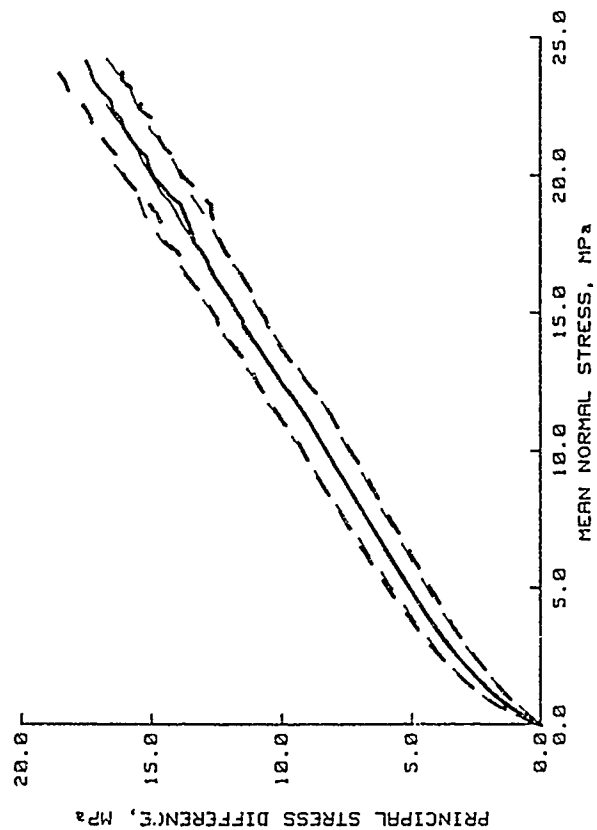
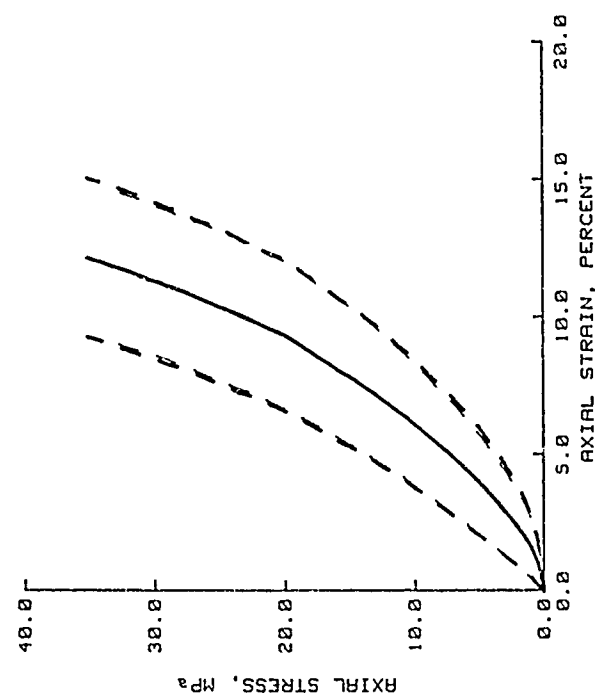


Figure 3.130. Comparison of the results from the COV and COV/Rosenblueth analysis techniques for the loading portion of EXT K₀ test data.

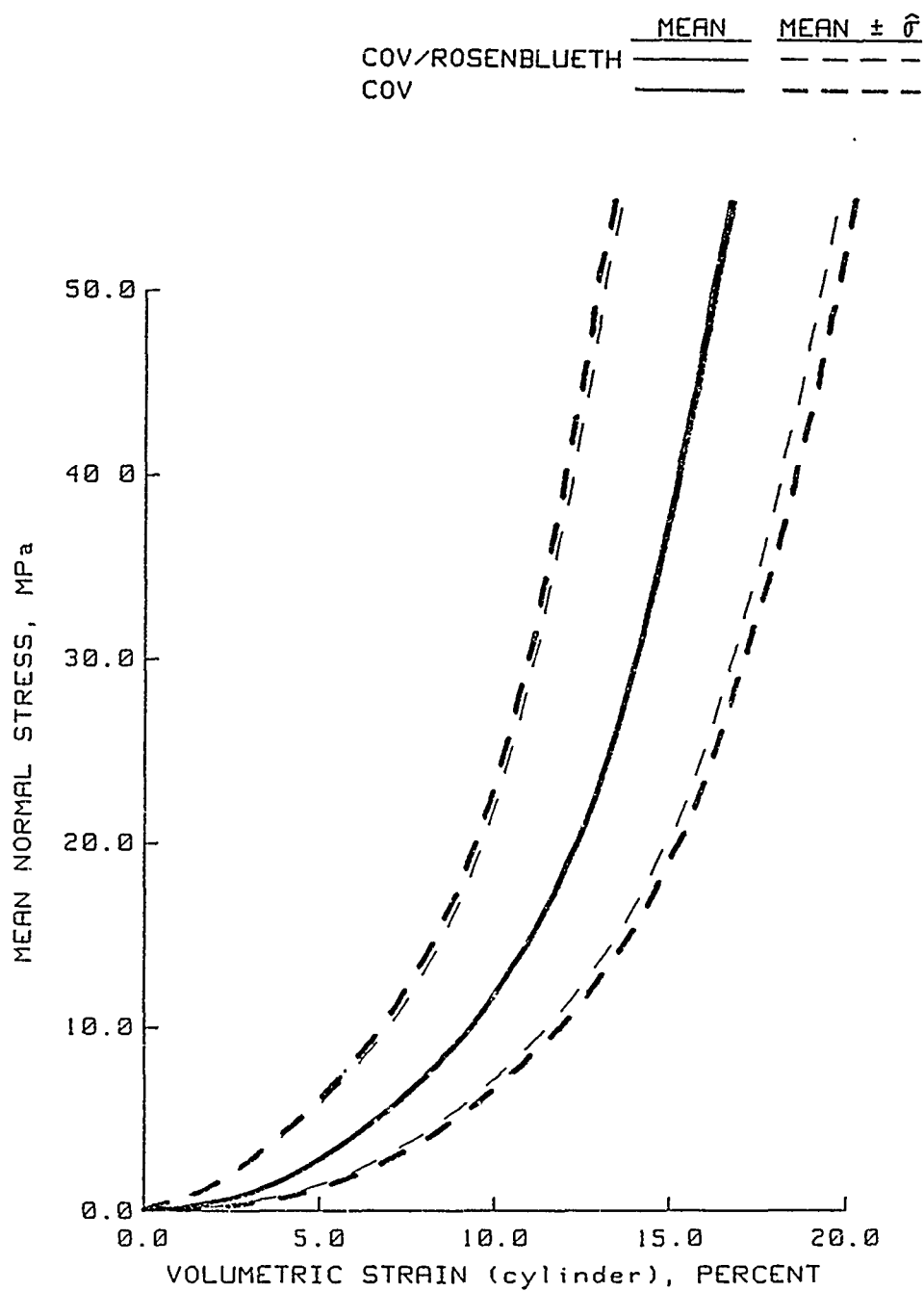


Figure 3.131. Comparison of the results from the COV and COV/Rosenblueth analysis techniques for the loading portion of static HC test data.

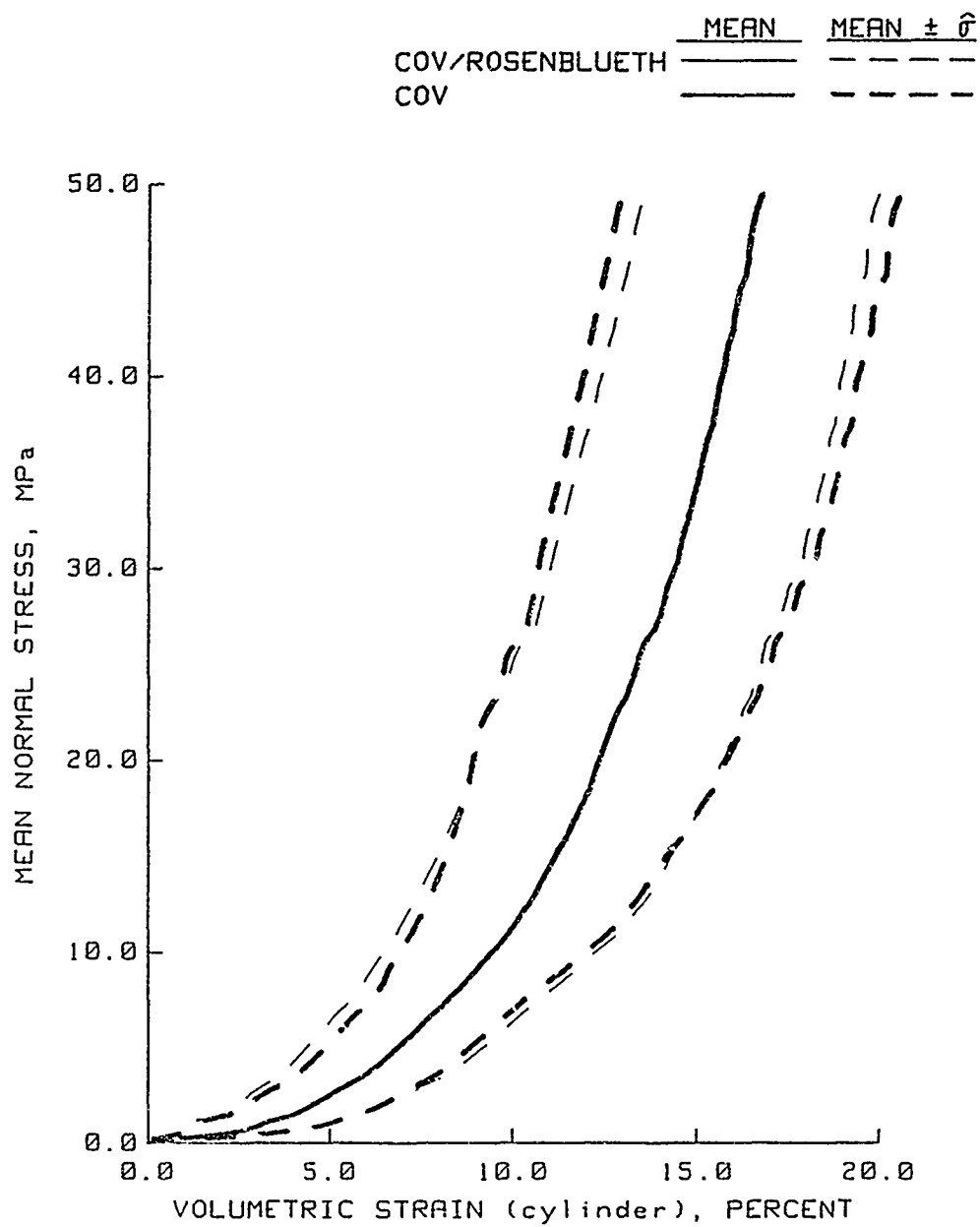


Figure 3.132. Comparison of the results from the COV and COV/Rosenblueth analysis techniques for the loading portion of dynamic HC test data.

	MEAN	MEAN $\pm \sigma$
COV/ROSENBLUETH	---	---
COV	---	---

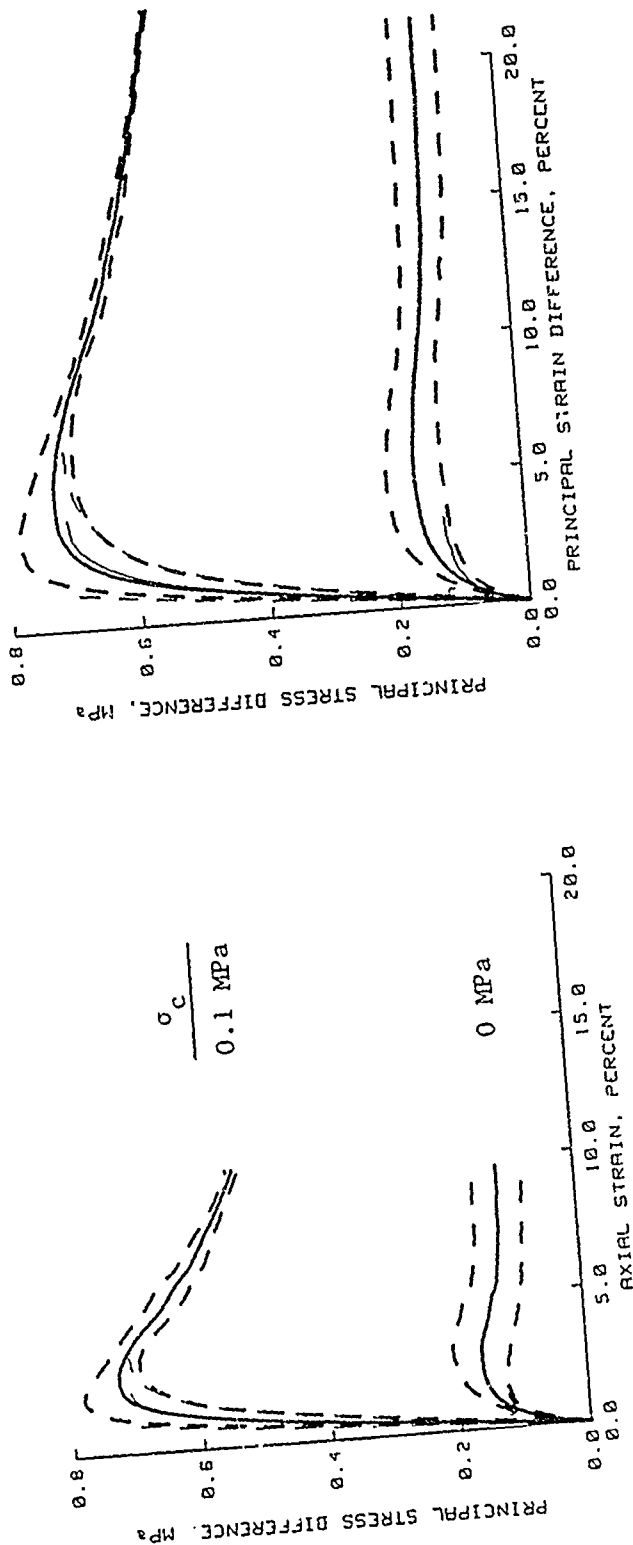


Figure 3.133. Comparison of the results from the COV and COV/Rosenblueth analysis techniques for the loading portion of static TXC test data at $\sigma_c = 0$ and 0.1 MPa.

	COV/ROSENBLUETH	MEAN	MEAN $\pm \hat{\sigma}$
	COV	---	---

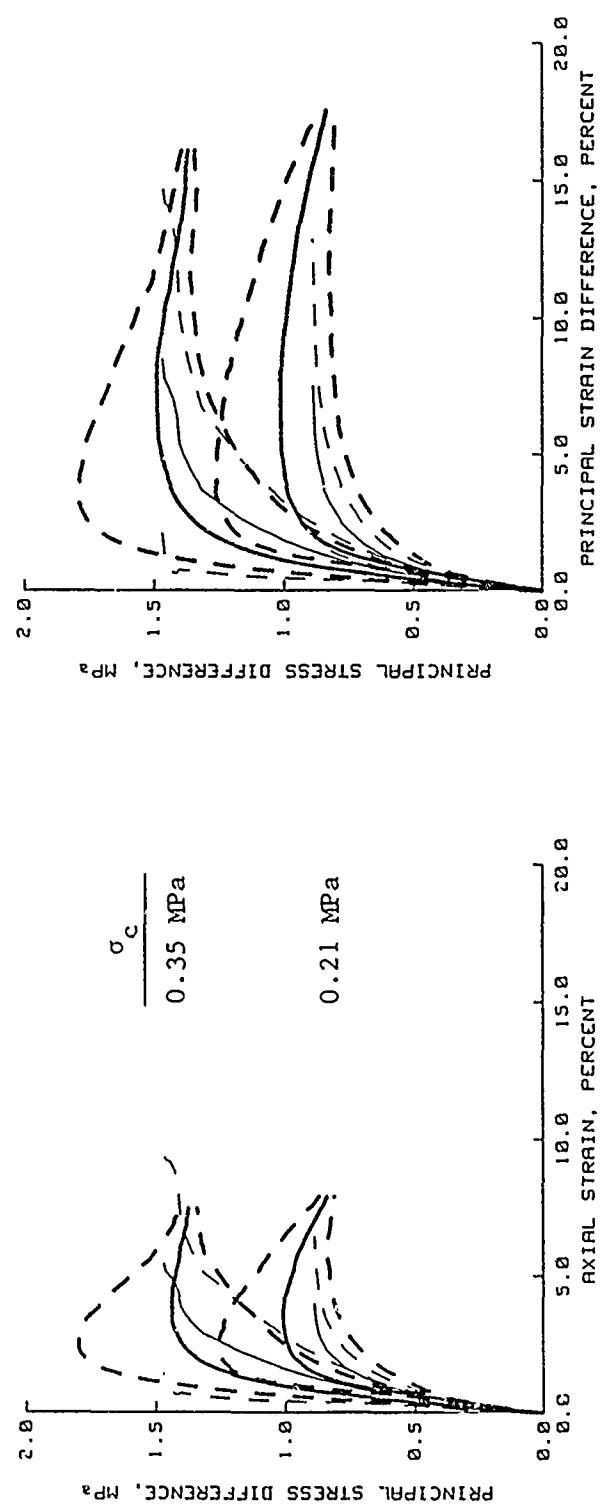


Figure 3.134. Comparison of the results from the COV and COV/Rosenblueth analysis techniques for the loading portion of static TXC test data at $\sigma_c = 0.21$ and 0.35 MPa.

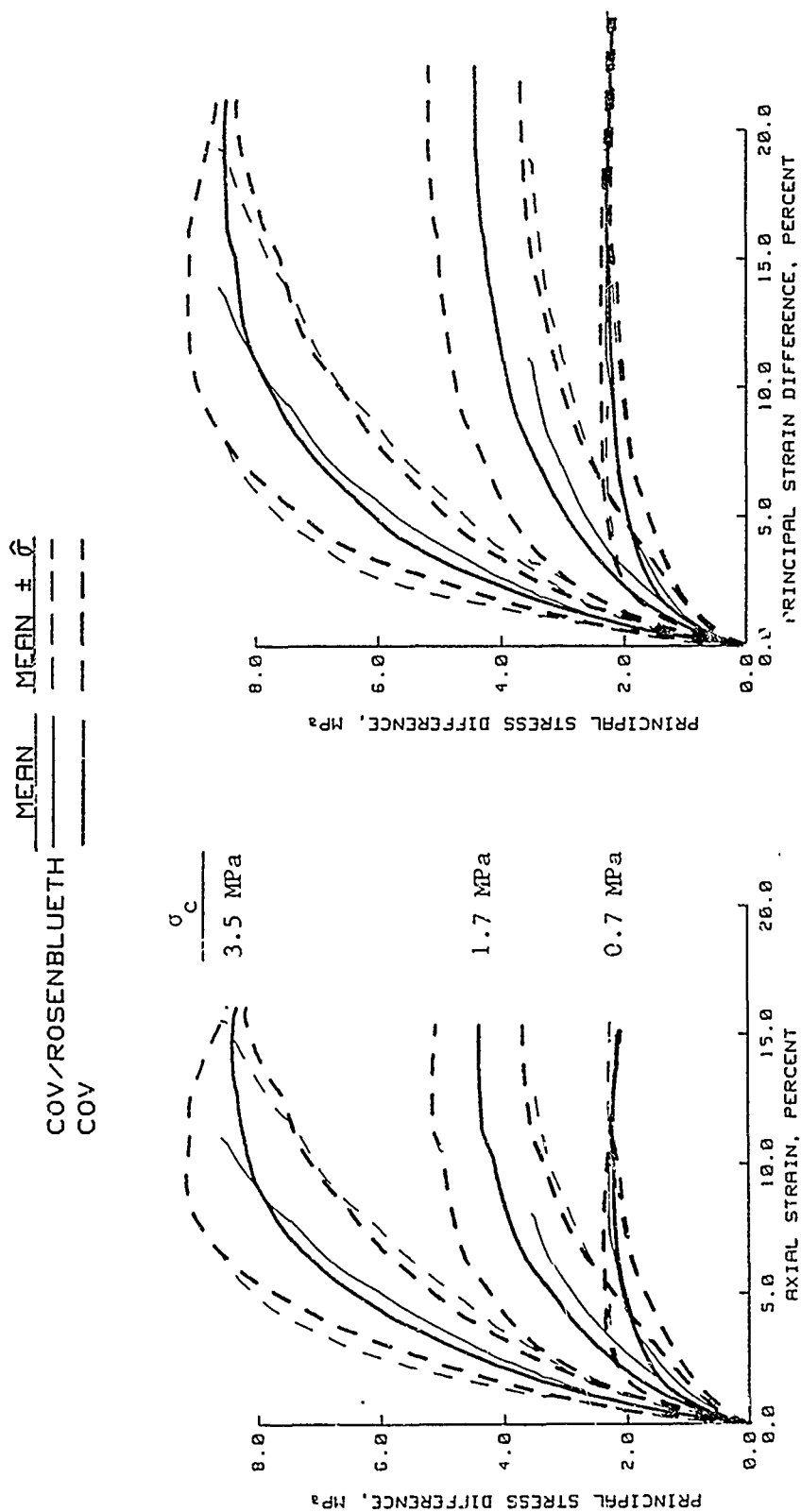


Figure 3 135. Comparison of the results from the COV and COV/Rosenblueth analysis techniques for the loading portion of static TXC test data at $\sigma_c = 0.7$, 1.7, and 3.5 MPa.

	MEAN	MEAN $\pm \hat{\sigma}$
COV/ROSENBLUETH	---	---
COV	---	---

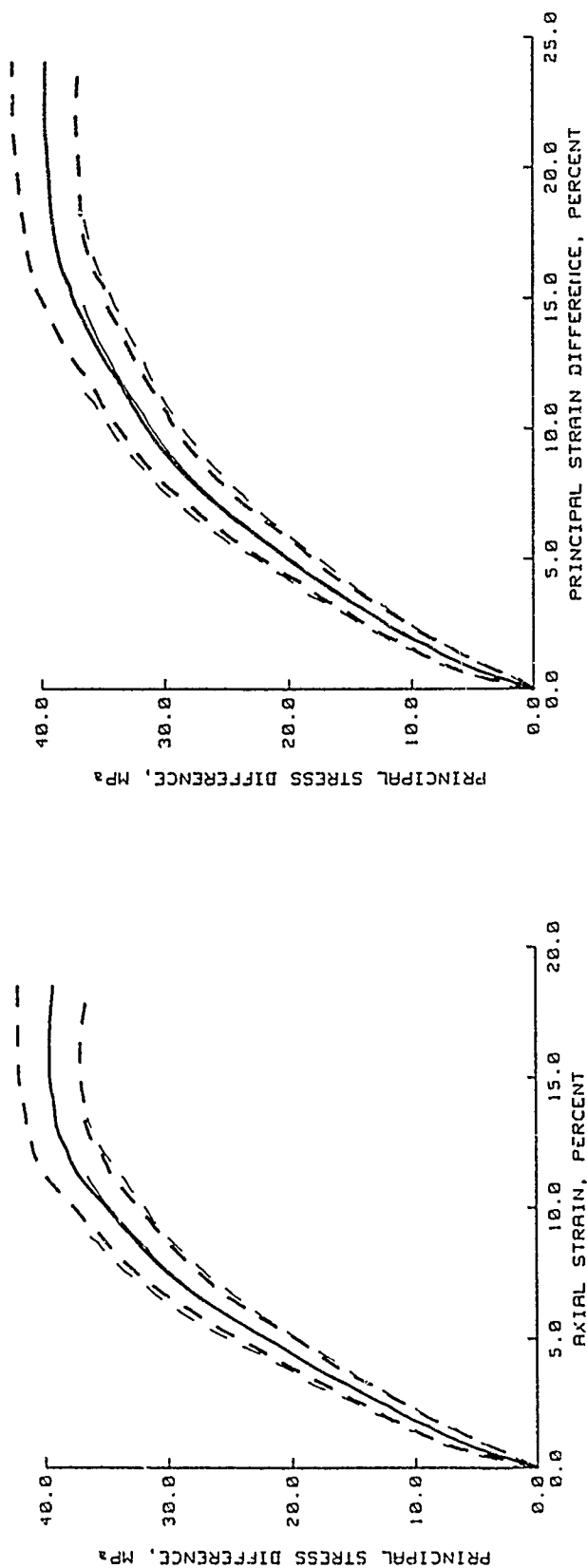


Figure 3.136. Comparison of the results from the COV and COV/Rosenblueth analysis techniques for the loading portion of static TXC test data at $\sigma_c = 17.5$ MPa.

	COV/ROSENBLUETH	MEAN	MEAN $\pm \hat{\sigma}$
	COV	---	---

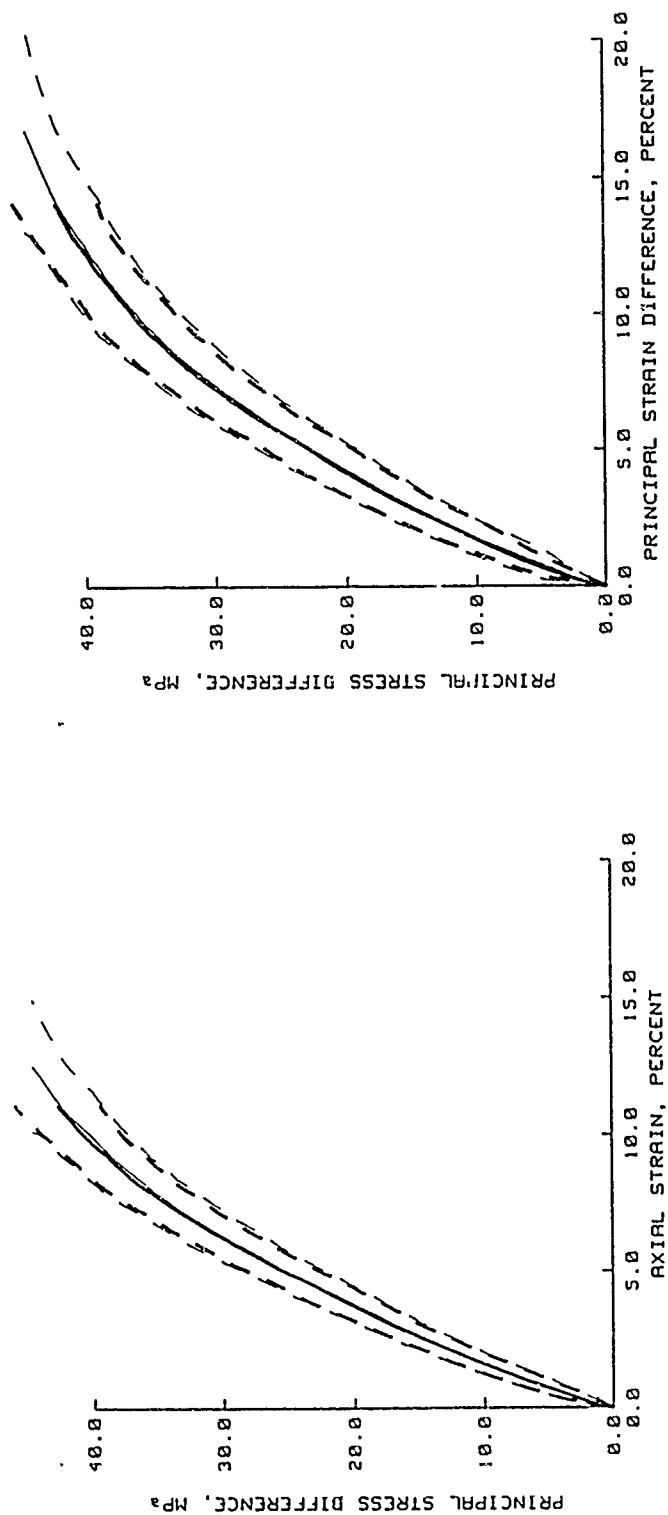


Figure 3.137. Comparison of the results from the COV and COV/Rosenblueth analysis techniques for the loading portion of static TXC test data at $\sigma_c \approx 20.0$ MPa.

COV/ROSENBLUETH
 COV

MEAN
 MEAN $\pm \hat{\sigma}$

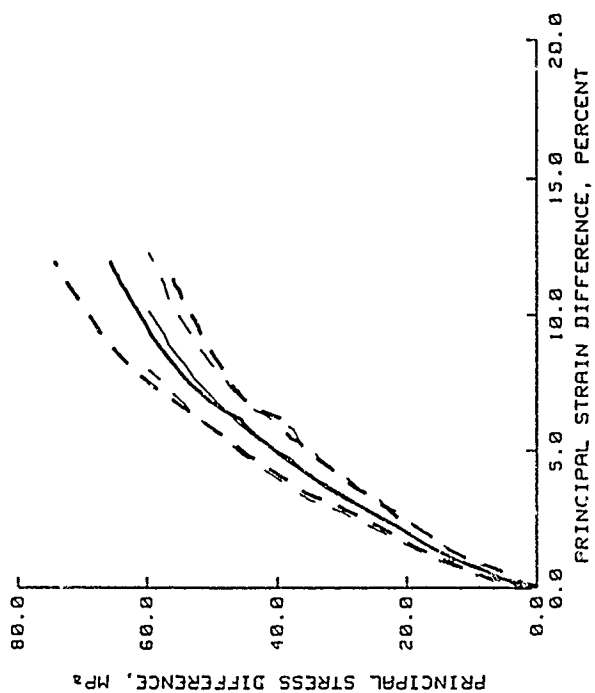
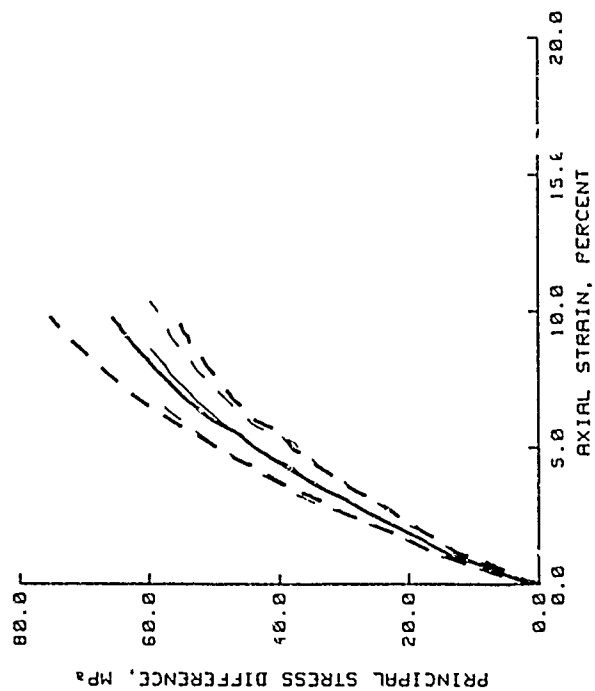


Figure 3.138. Comparison of the results from the COV and COV/Rosenblueth analysis techniques for the loading portion of static TXC test data at $\sigma_c = 40.0$ MPa.

	MEAN	MEAN $\pm \hat{\sigma}$
COV/ROSENBLUETH	---	---
COV	---	---

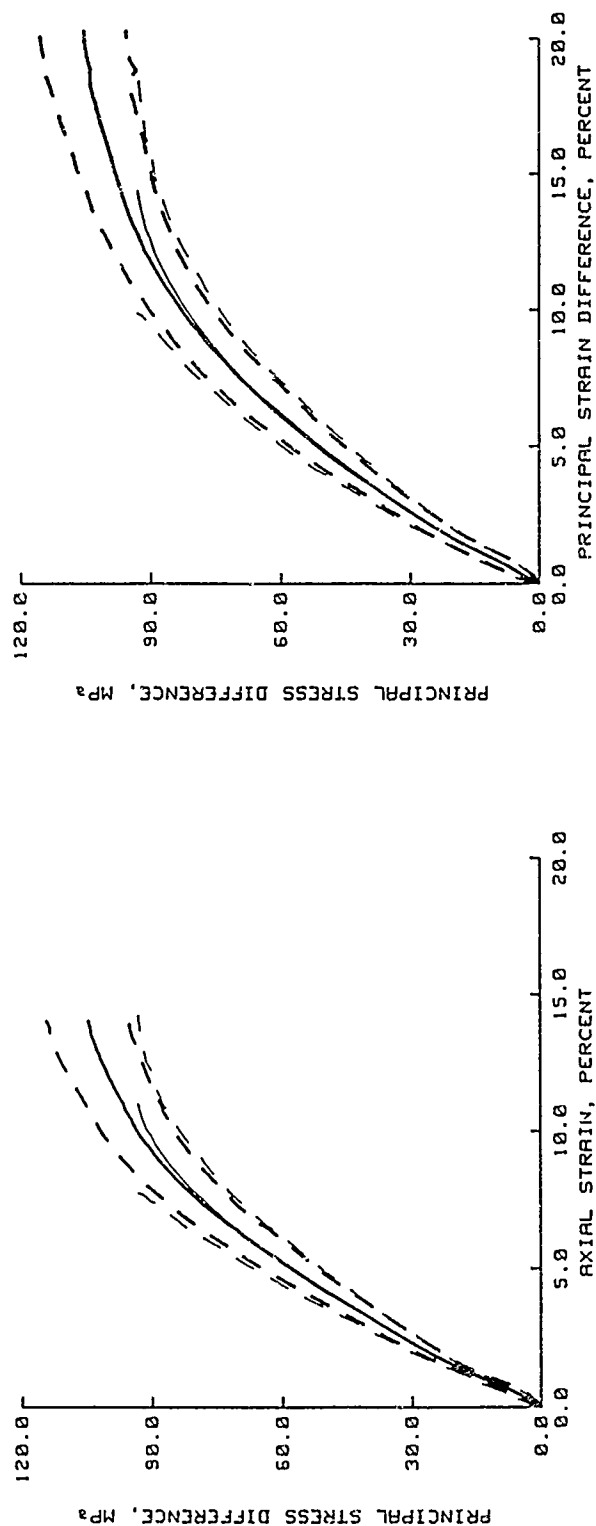


Figure 3.139. Comparison of the results from the COV and COV/Rosenblueth analysis techniques for the loading portion of static TXC test data at $\sigma_c = 55.0$ MPa.

	MEAN	MEAN $\pm \hat{\sigma}$
COV/ROSENBLUETH	---	---
COV	---	---

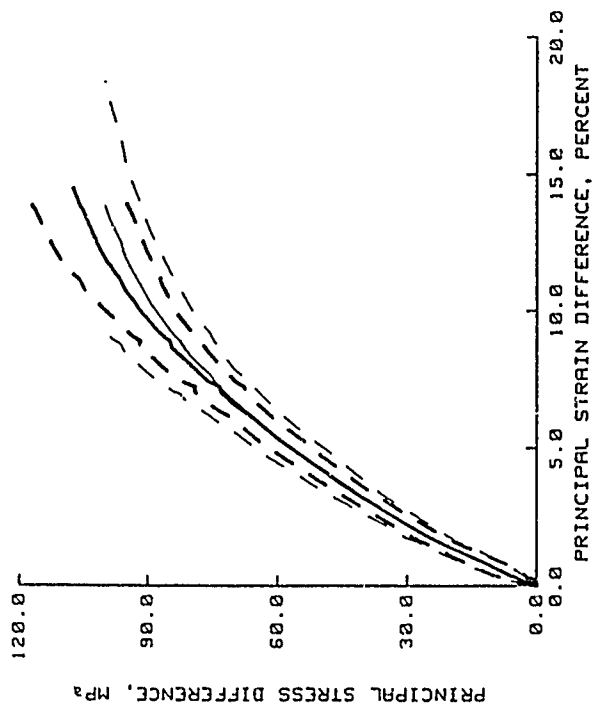
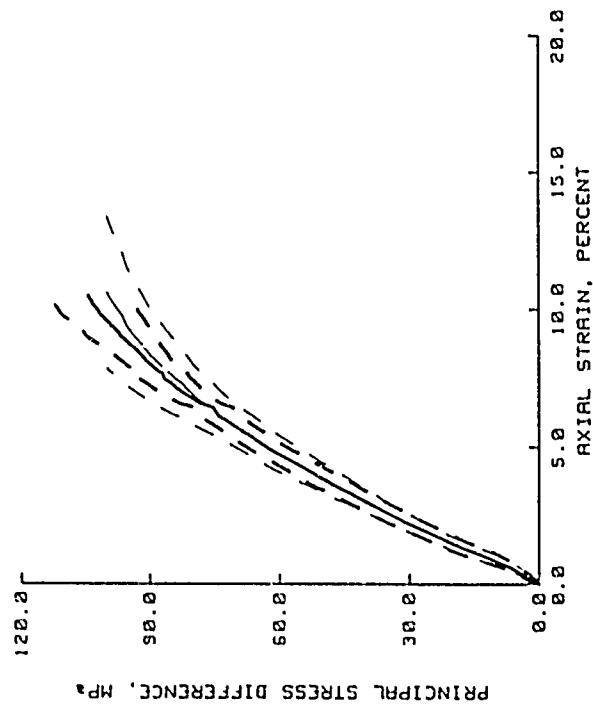


Figure 3.140. Comparison of the results from the COV and COV/Rosenblueth analysis techniques for the loading portion of static TXC test data at $\sigma_c = 60.0$ MPa.

	MEAN	MEAN $\pm \sigma$
COV/ROSENBLUETH	---	---
COV	---	---

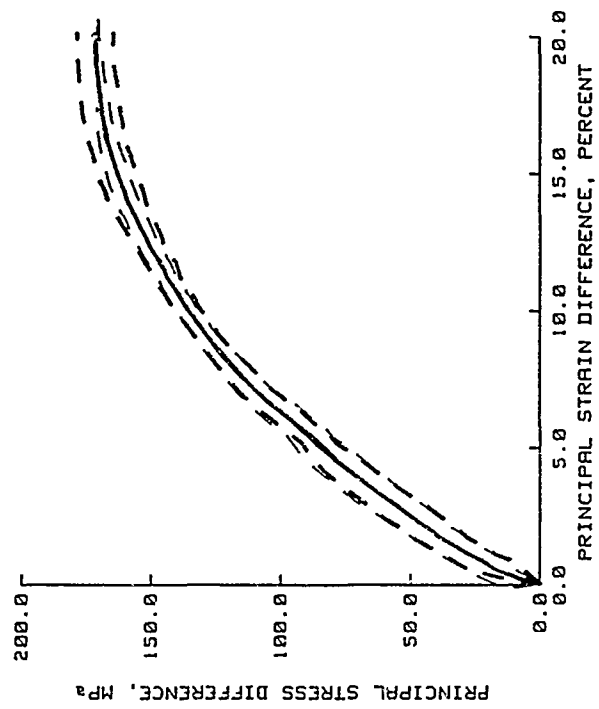
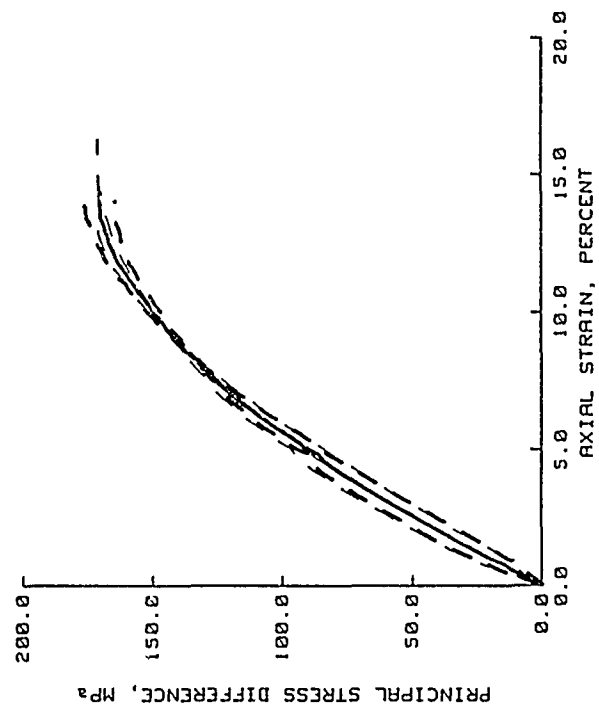


Figure 3.141. Comparison of the results from the COV and COV/Rosenblueth analysis techniques for the loading portion of static TXC test data at $\sigma_c = 80.0$ MPa.

CHAPTER 4

FINAL PROBABILISTIC MECHANICAL PROPERTIES

4.1 APPLICABILITY OF THE PROBABILISTIC MECHANICAL PROPERTIES TO AREA A

The applicability of the probabilistic mechanical properties from Chapter 3 to the first dry density-based layer of the subsurface profile for Area A is assessed by conducting one-way analysis of variance tests on the dry density data for the test specimens versus the dry density data for the layer. The results of the analysis for each test type are shown in Table 4.1. The mean dry density for the test specimens used in the dynamic uniaxial strain (UX) and hydrostatic compression (HC) tests and static UX with lateral stress measurements (Ko), HC, and triaxial compression (TXC) tests are not significantly different from the mean dry density for the layer. The mean dry density for test specimens used in the Ko tests conducted in the extension test device (EXT Ko) is statistically different from the mean dry density for the layer. Therefore, except for the EXT Ko test data, probabilistic mechanical properties based directly on the results from the analysis of the test data are assumed to be adequate for the layer. The results from the analysis of the EXT Ko test data will be used only as a guide for developing the negative principal stress difference (PSD) regime of the Ko stress path unloading.

4.2 PROBABILISTIC MECHANICAL PROPERTIES DEVELOPED FROM TEST RESULTS

In Section 3.2.5, it was shown that the results from applying covariance analysis to test data plotted in forms that are conducive to constitutive modeling (COV technique) and the results from applying the Rosenblueth procedure to the results from the covariance analysis of "measured data" (CCV/Rosenblueth technique) were essentially the same. Hence, the recommended probabilistic laboratory responses will be based on the results from the COV analysis technique. Unrealistic responses from the analysis of the laboratory test data are not included in the recommended responses.

The recommended probabilistic laboratory UX compressibility and the results from the COV analysis technique are plotted in Figure 4.1 as thick and thin lines, respectively. Since the axes form limits to the

possible loading UX compressibility response, the mean ± 1 standard deviation ($\hat{\sigma}$) responses are constructed such that the mean - $3\hat{\sigma}$ values are 0 or positive. The recommended probabilistic response does not include the unrealistic responses from the COV analysis, i.e., the softening of the loading response above an axial stress of approximately 80 MPa and the unusual "hook" in the unloading response that begins at an axial stress of approximately 95 MPa.

In Figure 4.2, the recommended probabilistic laboratory loading UX stress path (thick line) is drawn slightly below the results from the analysis of the Ko test data (thin line). From Figure 3.15, some of the test data shifted in an increasing principal stress difference (PSD) direction at values for mean normal stress (MNS) of approximately 25 and 55 MPa. The unloading and reloading stress path responses are constructed by drawing the mean response first. Then, the mean $\pm \hat{\sigma}$ unloading responses are drawn by laterally shifting the mean unloading to begin at the appropriate point on the mean $\pm \hat{\sigma}$ loading response. The response is extended or shortened as necessary. From Section 3.2.3.2, there is very little variance in the unloading or reloading Ko stress paths from a given stress level. The reloading responses are constructed in the same way but begin at the appropriate point on the corresponding unloading response. The results from the probabilistic analysis of the second set of EXT Ko unloading responses is used as a guide for developing the negative PSD region of the recommended response (Figure 4.3).

The recommended probabilistic laboratory static HC compressibility response is slightly softer and has a greater variance than the probabilistic response from the COV analysis of the static HC test data (Figure 4.4). The recommended response is the same as the results from the COV analysis of the dynamic HC test data (Figure 4.5). Since the results from the COV analysis of static HC test data are within the mean $\pm \hat{\sigma}$ response for the dynamic HC test data, there is no apparent dynamic effect. This material does exhibit a slight rate effect in UX compressibility for static to dynamic times to peak stress of several minutes to less than 10 milliseconds. Therefore, the recommended probabilistic laboratory HC response is applicable to static loadings but may not be applicable to fast dynamic loadings.

The results from applying the COV analysis technique to the loading static TXC shear responses at constant confining pressures less than 10 MPa are used as the recommended probabilistic laboratory responses (Figures 4.6 and 4.7). The recommended responses and the results from the COV analysis on comparable test data for constant confining pressures of 20.0, 40.0, 60.0, and 80.0 MPa are shown in Figures 4.8-4.11, respectively. Since there is very little variation in the unloading and reloading responses, only a mean recommended unloading that begins at the end of the mean loading response is shown for each confining pressure.

Recommended probabilistic laboratory "peak" strength envelopes are presented in Figure 4.12. The envelopes are eyeball fits through the "peak" strength data from Table 3.12. Slight undulations in the envelopes are generated by the spline fits through the digitized curves. The "peak" strengths from the probabilistic shear responses presented in Figures 4.6-4.11 are plotted as solid circles. The probabilistic shear responses for some confining pressures have "peak" strengths that do not follow a mean $\pm \hat{n}\hat{\sigma}$ criteria. However, all of the "peak" strengths from the shear responses are close to the probabilistic strength envelope except for the "peak" strengths at a confining pressure of 80 MPa.

The probabilistic shear response for a confining pressure of 80.0 MPa will be adjusted based on the probabilistic "peak" strength envelope. The mean shear response is developed using the mean value for "peak" strength from Figure 4.12b as a target value, and the recommended responses for confining pressures of 20.0, 40.0, and 60.0 MPa as a guide to the shape of the response. The variance is based on the coefficient of variation for the tests at confining pressures of 17.5, 20.0, and 55.0 MPa and the recommended responses at 20.0 and 60.0 MPa (Figures 4.13 and 4.14). The coefficient of variation starts at a value of approximately 50 percent and decreases to a fairly constant value of 10 percent. Using these criteria, a new recommended shear response for a confining pressure of 80.0 MPa is shown in Figure 4.15.

An estimated in situ effect will be added to the recommended laboratory dynamic UX compressibility response using an undocumented procedure based on the analyses of two dynamic in situ compressibility tests. A relationship was observed between axial stress and the ratio

of seismic strain to in situ strain (see Figure 4.16). The seismic strain is calculated as

$$\epsilon_s = \frac{\sigma_z g}{\gamma_d (1+\omega) C^2} \quad (4.1)$$

where ϵ_s is the seismic axial strain, σ_z is the axial stress, g is acceleration due to gravity, γ_d is the dry density, ω is the water content, and C is the seismic compression wave velocity. The in situ strain is calculated as

$$\epsilon_{IN\ SITU} = \frac{\epsilon_s}{\beta_{STRAIN}} \quad (4.2)$$

where $\epsilon_{IN\ SITU}$ is the in situ axial strain and β_{STRAIN} is obtained from Figure 4.16. The Rosenblueth procedure is used since probabilistic values for dry density (114.7 ± 5.1 pcf) and water content (3.8 ± 1.6 percent) were developed in Section 3.1. Mean and standard deviation values for C of 2675 and 100 fps, respectively, are typical for the area. The probabilistic in situ dynamic UX compressibility response is shown as a thick line in Figure 4.3. Since the procedure for calculating the in situ axial strain is only valid to an axial stress of 8 MPa, the response above 8 MPa is connected to the recommended laboratory response (thin line) using a French curve and the author's judgment.

Methods for determining the in situ and static to dynamic effects for the UX stress path of this material are not available at this time. Small variations in the UX compressibility response do not appear to significantly effect the UX stress path. Therefore, the in situ and dynamic effects incorporated into the UX compressibility response will probably have little effect on the UX stress path. There was no significant difference observed between the results from the available static and dynamic TXC tests.

4.3 METHODS FOR EXTRAPOLATING THE VARIANCE OF MECHANICAL PROPERTIES TO HIGHER STRESSES

Ground shock calculations require mechanical properties of the

earth materials to stresses higher than those generally applied in the laboratory tests. Two methods for extrapolating the variance of the recommended responses to higher stresses will be examined. The mean high pressure responses were extrapolated using engineering knowledge.

The coefficient of variation and values of alpha (α) and beta (β) for a beta distribution will be calculated for the recommended probabilistic laboratory UX compressibility, UX stress path, and TXC "peak" strength envelope. The trends for these parameters will be used to determine the variance about the extrapolated mean responses. The coefficient of variation is calculated as the standard deviation divided by the mean and is presented as a percentage. The α and β parameters for the beta distribution are calculated as

$$\alpha = \frac{\tilde{x}^2}{\tilde{v}} (1 - \tilde{x}) - (1 + \tilde{x}) \quad (4.3)$$

$$\beta = \frac{\alpha + 1}{\tilde{x}} - (\alpha + 2) \quad (4.4)$$

$$\text{where, } \tilde{x} = \frac{\bar{x} - a}{b - a} \text{ and } \tilde{v} = \left(\frac{\hat{\sigma}}{b - a} \right)^2$$

These equations are based on the assumption that the absolute minimum (a) and maximum (b) values are zero and mean + $3\hat{\sigma}$, respectively.

Plots of coefficient of variation, α , and β versus stress are shown in Figures 4.18-4.23. The values for the recommended probabilistic laboratory responses and the results from the COV analysis of the test data are shown as thick and thin lines, respectively. The plots tend to become parallel to the X-axis as stress increases. Values for coefficient of variation, α , and β of 20 percent, 8.5, and 5, respectively, for the UX compressibility, 10 percent, 22, and 6.7, respectively, for the UX stress path, and 5 percent, 55, and 7.8, respectively for the TXC "peak" strength envelope will be used.

The extrapolated responses are shown in Figures 4.24-4.26. For the UX compressibility and stress path, extrapolating the variance using coefficient of variation and the beta distribution parameters provide the same mean $\pm \hat{\sigma}$ responses; therefore, coefficients of variation of 20

and 10 percent will be used to extrapolate the variance to higher stresses since it is the simplest to apply and requires no assumptions. For the TXC "peak" strength envelope (Figure 4.26), a coefficient of variation of 5 percent will be used since it provided a slightly larger variance than the beta distribution parameters.

4.4 FINAL PROBABILISTIC MATERIAL PROPERTIES

The low stress portion of the recommended probabilistic dynamic UX compressibility and stress path, laboratory HC compressibility, TXC "peak" strength envelope, and TXC shear responses are shown in Figures 4.27-4.32. They are the same as those shown in Figures 4.1-4.10, 4.12, 4.15, and 4.17. A deterministic triaxial extension "peak" strength envelope is shown in Figure 4.29. The HC response will not be extrapolated to higher stresses since there is no available data to use as a guide.

A major concern with developing the probabilistic high stress properties is the correct handling of the full saturation portion of the responses, i.e., when the air voids content is zero and the degree of saturation is 100 percent. The UX compressibility response, UX stress path, and TXC "peak" strength envelope will have slopes that are nearly constant for stress greater than or equal to the stress at full saturation (the "lockup" stress). First consider the results of applying the covariance analysis technique to a set of test data that achieve full saturation at different stress levels. Since the slope of the responses is analyzed, a constant slope for the probabilistic response will not be reached until all of the responses in the data set have a constant slope. This indicates that the "lockup" stress for the probabilistic response is the highest "lockup" stress for the data set and is not probabilistic.

The high stress probabilistic dynamic in situ UX compressibility response is shown in Figure 4.33. Below an axial stress of 93 MPa, the response is the same as that shown in Figure 4.27. The mean $\pm \hat{\sigma}$ response above an axial stress of 93 MPa was determined by multiplying the mean axial strain at a given value of axial stress by a coefficient of variation of 20 percent. The mean $- \hat{\sigma}$, mean, and mean $+ \hat{\sigma}$ responses have constant moduli of 50, 45, and 40 GPa above a "lockup" axial stress

of 700 MPa. The mean unloading response from an axial stress of 700 MPa was determined using engineering judgment. From the lower pressure probabilistic unloading responses, the coefficient of variation for axial strain at the end of an unloading set is 20 to 23 percent. A coefficient of variation of 23 percent is used to determine the strain at zero axial stress for the final mean $\pm \hat{\sigma}$ unloadings.

The high stress probabilistic dynamic in situ UX stress path and TXC "peak" strength envelope are shown in Figure 4.34. A deterministic triaxial extension "peak" strength envelope is also shown. The UX stress path below a MNS of 70 MPa is the same as that shown in Figure 4.29; the TXC "peak" strength envelope below a MNS of 160 MPa is the same as that shown in Figure 4.14. Values for coefficient of variation of 10 and 5 percent were used to extrapolate the variance of the UX stress path and TXC "peak" strength envelope, respectively. Constant loading and unloading slopes that imply values for Poisson's ratio of 0.487, 0.490, and 0.493 are used for the mean - $\hat{\sigma}$, mean, and mean + $\hat{\sigma}$ UX stress paths, respectively, for MNS greater than or equal to 572 MPa. The probabilistic TXC "peak" strength envelope becomes flat at a MNS of 500 MPa. On the mean responses, these values of MNS coincide with the "lockup" axial stress of 700 MPa. The mean UX stress path unloadings are developed using engineering judgment. A coefficient of variation of 10 percent was used to determine the initial slopes for the mean $\pm \hat{\sigma}$ unloadings. The unloadings were completed by attaching the mean unloading response to the initial portions.

Table 4.1. One-way analysis of variance test for dry density of layer 1 at Area A versus dry density for test specimens from each test type.

Test Type	Mean Dry Density pcf	Dry Density Standard Deviation pcf	Number of Dry Density Points	Value of F for Layer 1 Versus Test Type*
Layer 1	114.72	5.11	400	---
Dynamic UX	113.48	2.96	21	1.21
Static Ko	113.08	5.84	26	2.47
Static EXT Ko	111.97	7.19	15	4.05
Static HC	115.12	4.82	32	0.18
Dynamic HC	116.40	4.51	12	1.27
Static TXC	113.99	6.28	70	1.13

* $F_{0.05}$ for $N > 400$ is between 3.92 and 3.84.

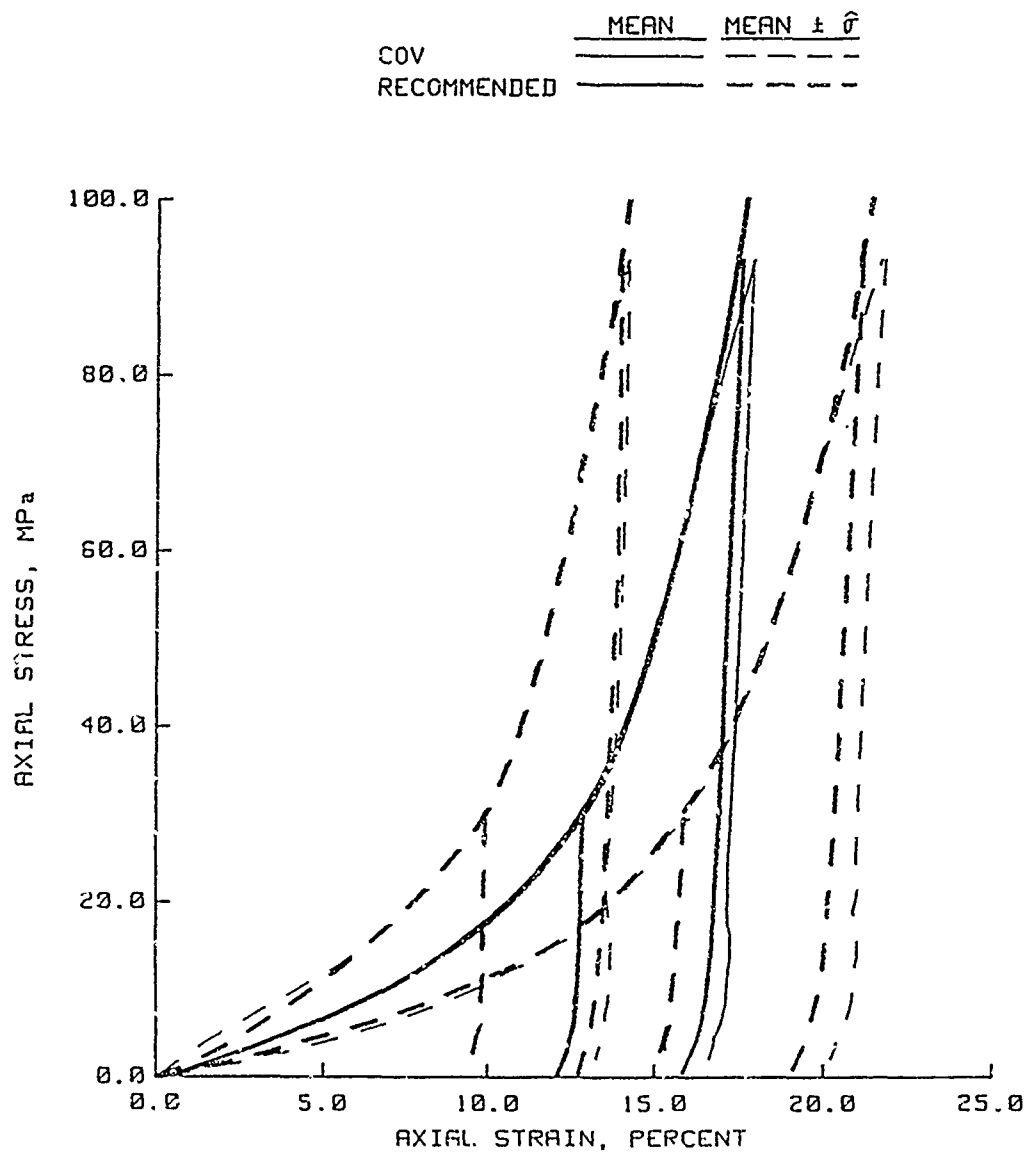


Figure 4.1. Comparison of the results from the COV analysis of dynamic UX test data and the recommended laboratory response.

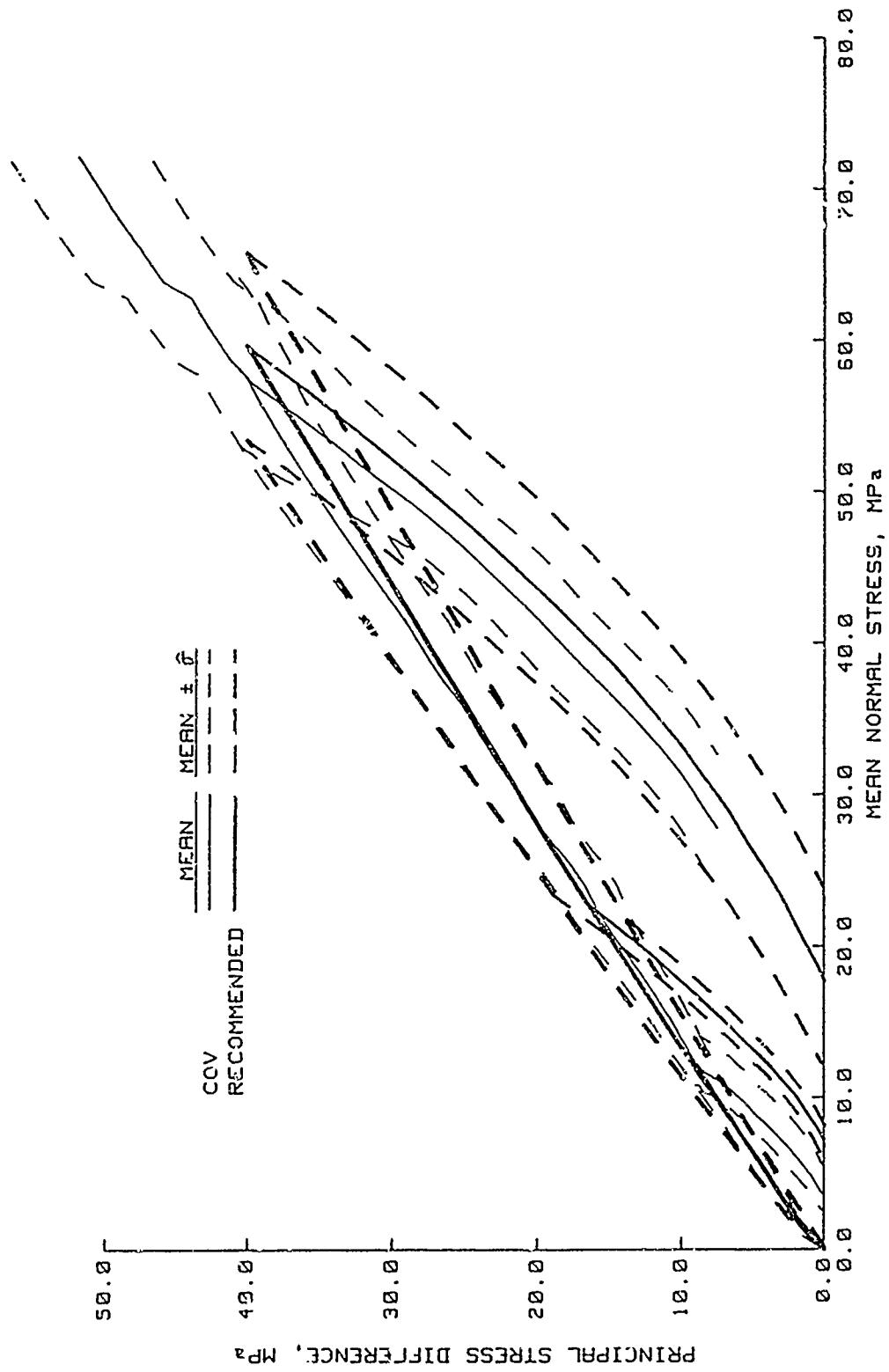


Figure 4.2. Comparison of the results from the COV analysis of K_o test data and the recommended laboratory UX stress path.

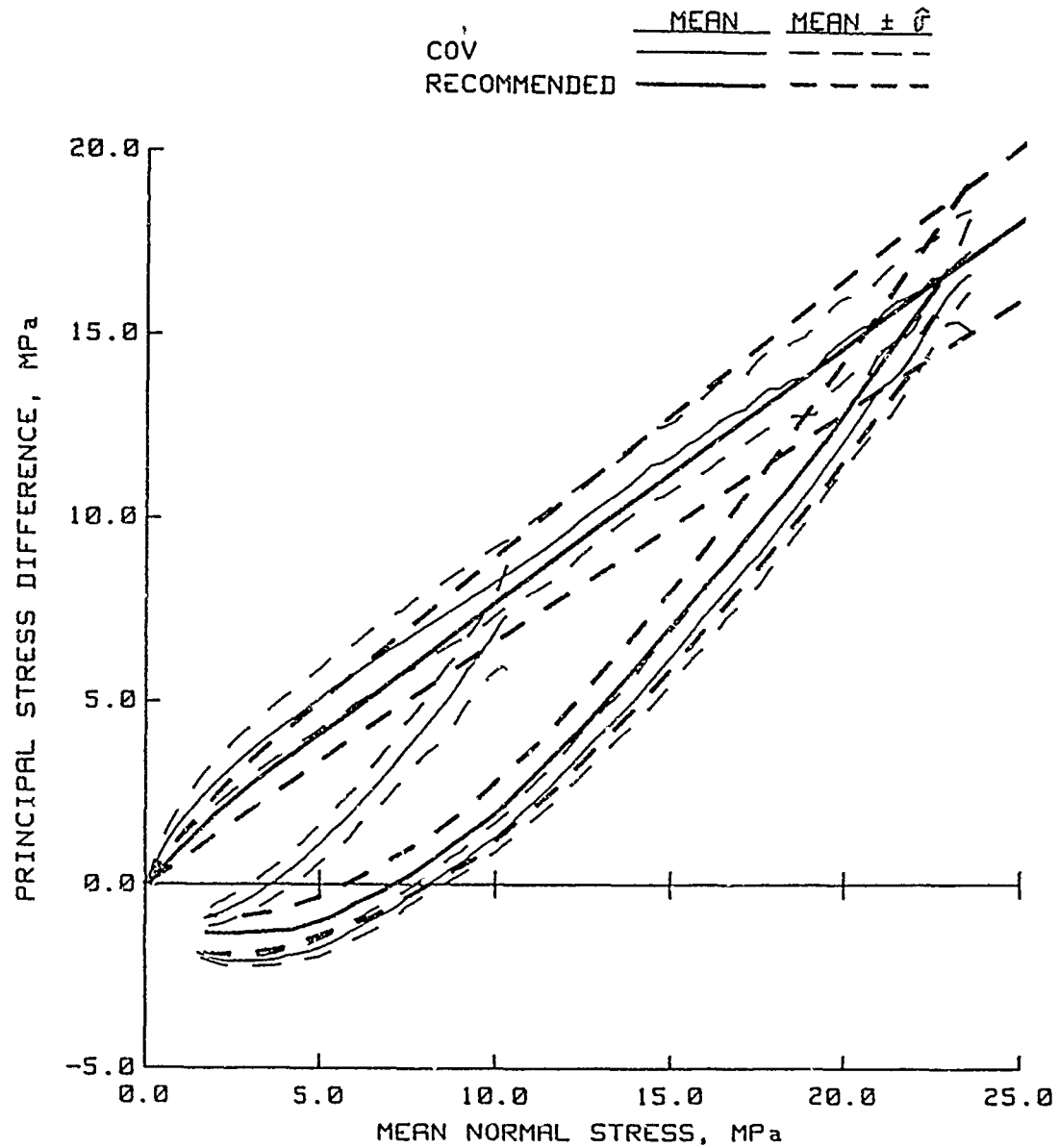


Figure 4.3. Comparison of the results from the COV analysis of EXT K_0 test data and the recommended laboratory UX stress path.

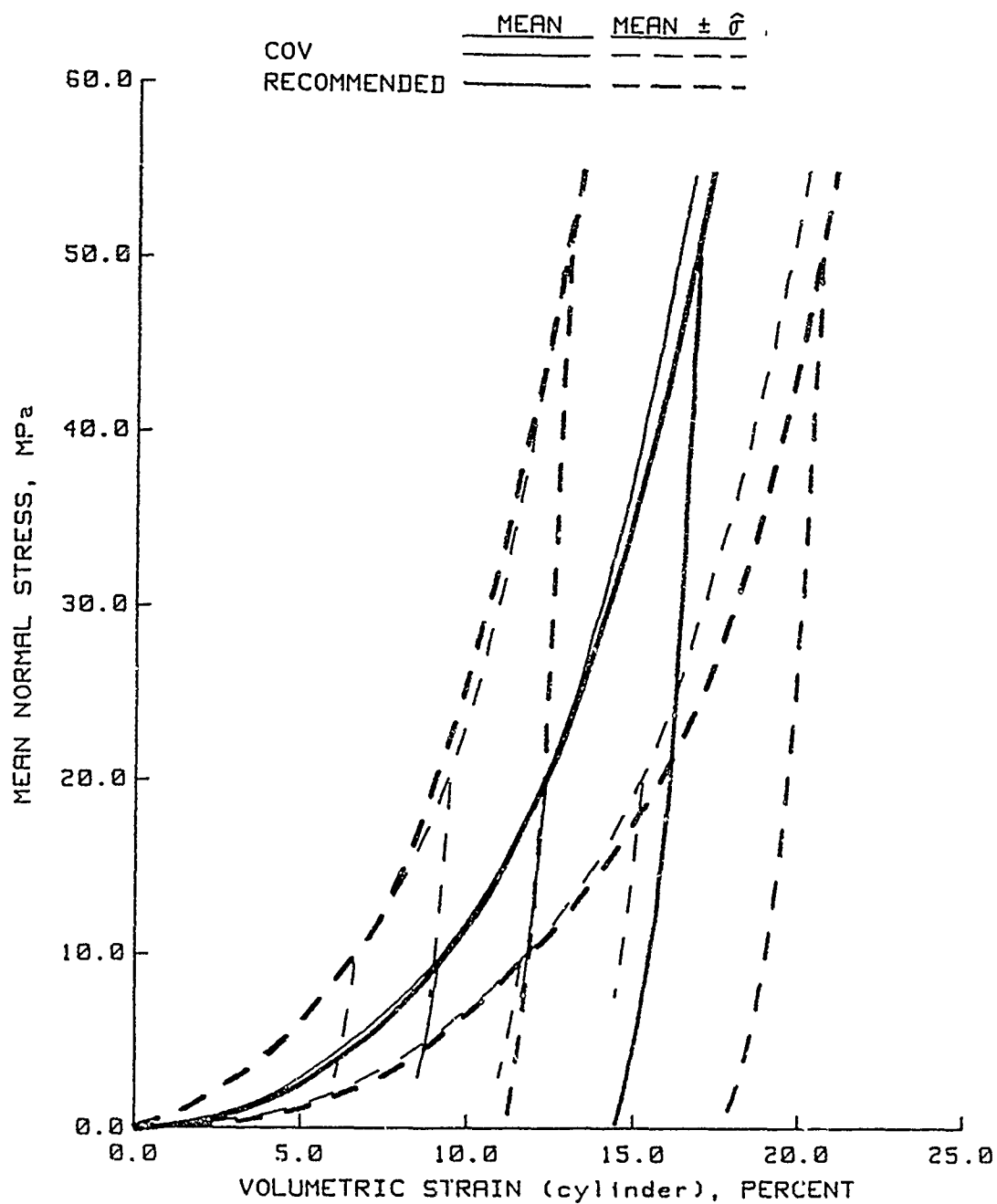


Figure 4.4. Comparison of the results from the COV analysis of static HC test data and the recommended laboratory HC compressibility response.

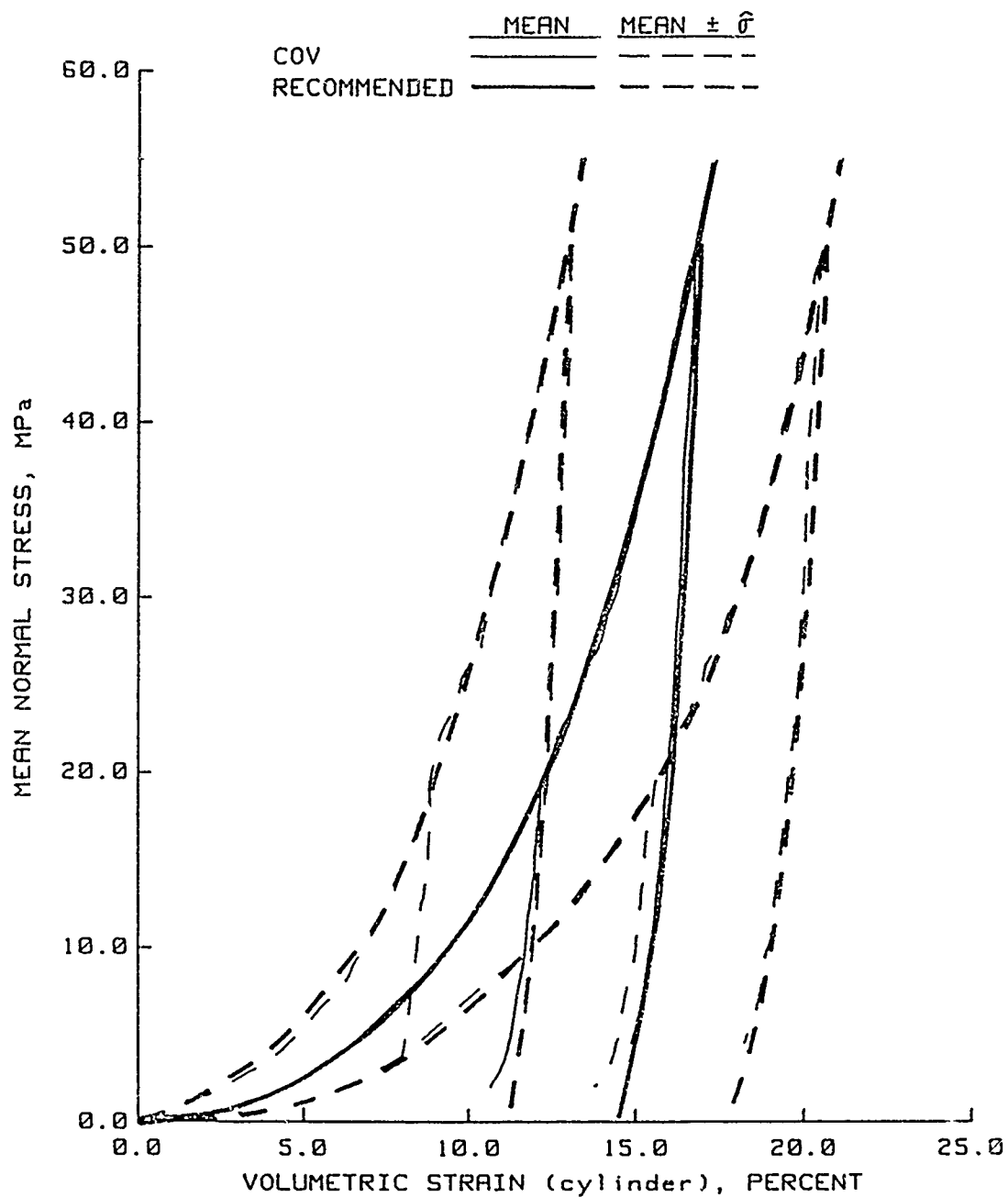


Figure 4.5. Comparison of the results from the COV analysis of dynamic HC test data and the recommended laboratory HC compressibility response.

— MEAN
 - - - MEAN $\pm \hat{\sigma}$
 — RECOMMENDED UNLOADING

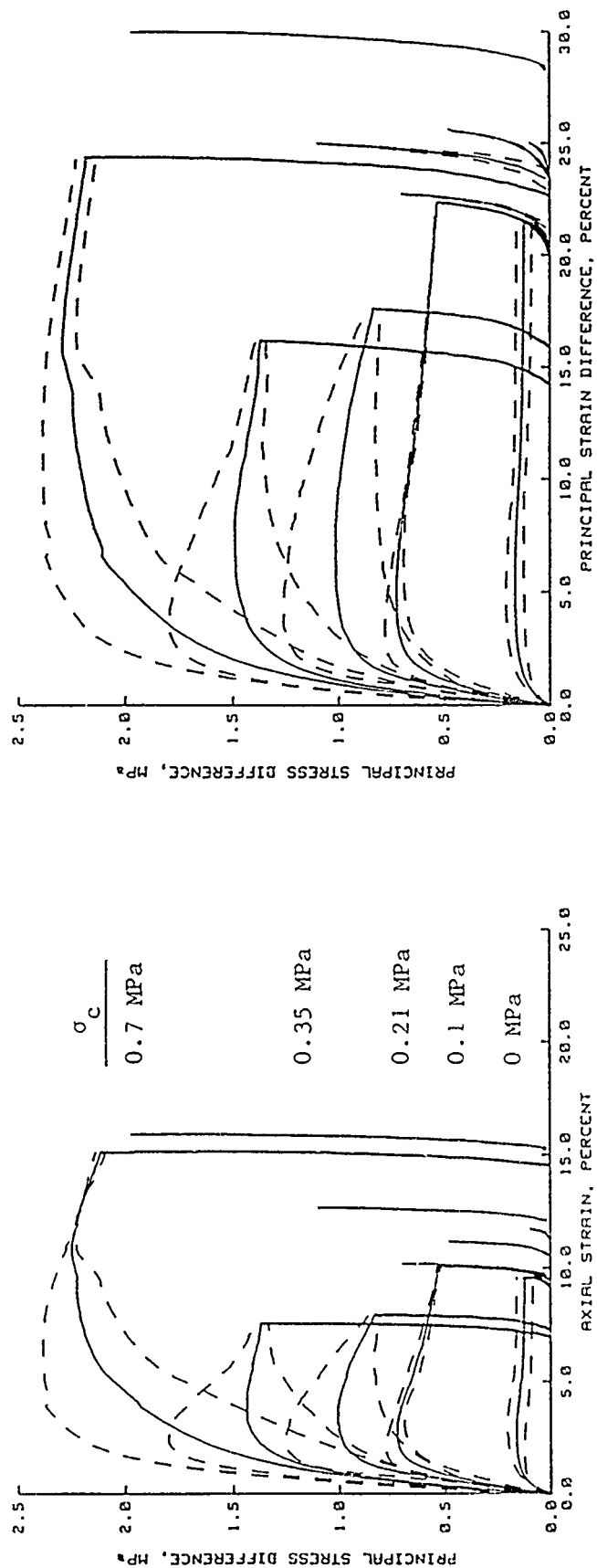


Figure 4.6. Results from the COV analysis of the static TXC test data and the recommended unloading response for $\sigma_c = 0, 0.1, 0.21, 0.35$, and 0.7 MPa.

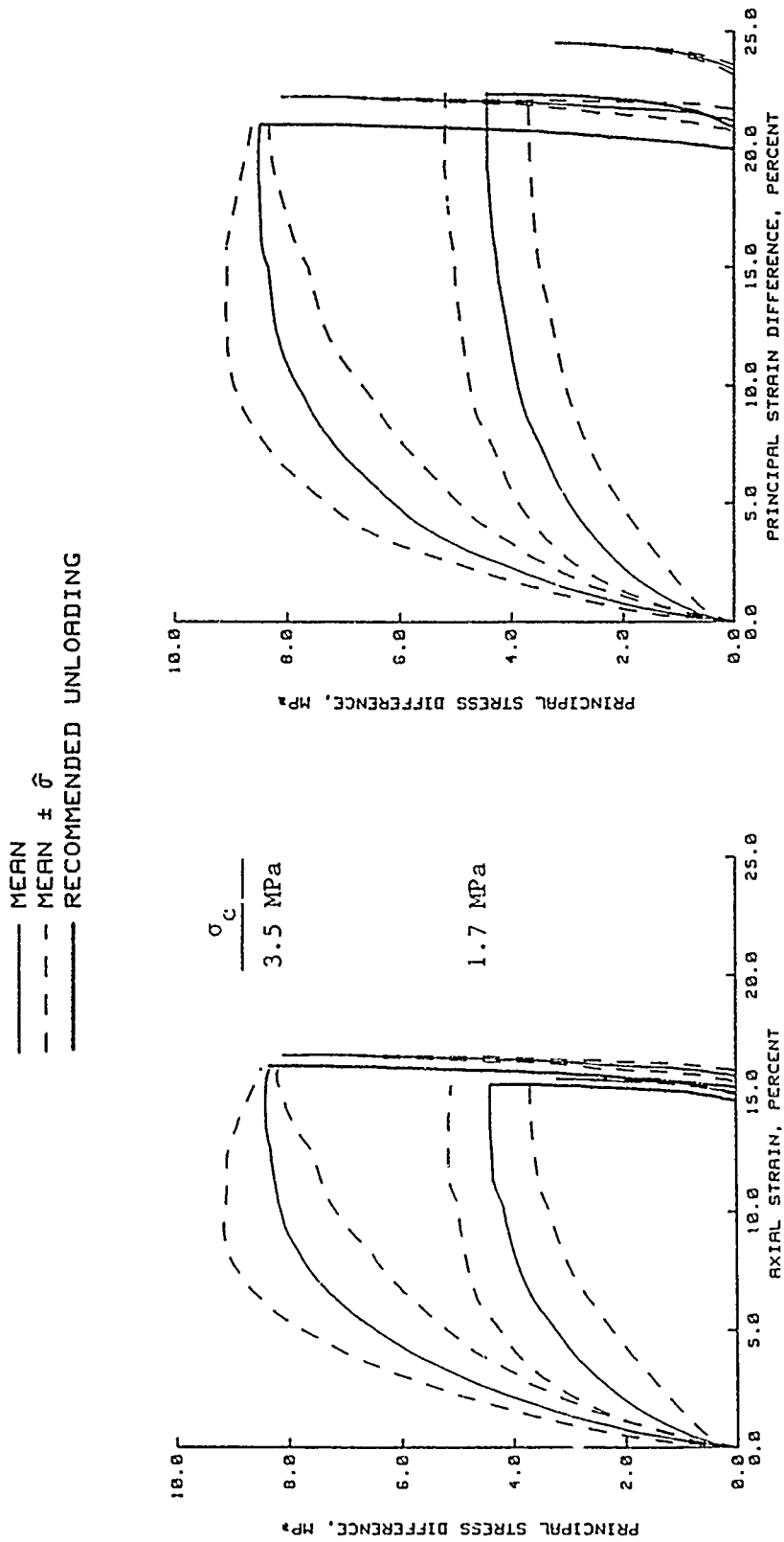


Figure 4.7. Results from the COV analysis of the static TXC test data and the recommended unloading response for $\sigma_c = 1.7$ and 3.5 MPa.

COV
RECOMMENDED

MEAN

MEAN $\pm \hat{\sigma}$

Test Data
at $\sigma_c =$
20.0 MPa
17.5 MPa

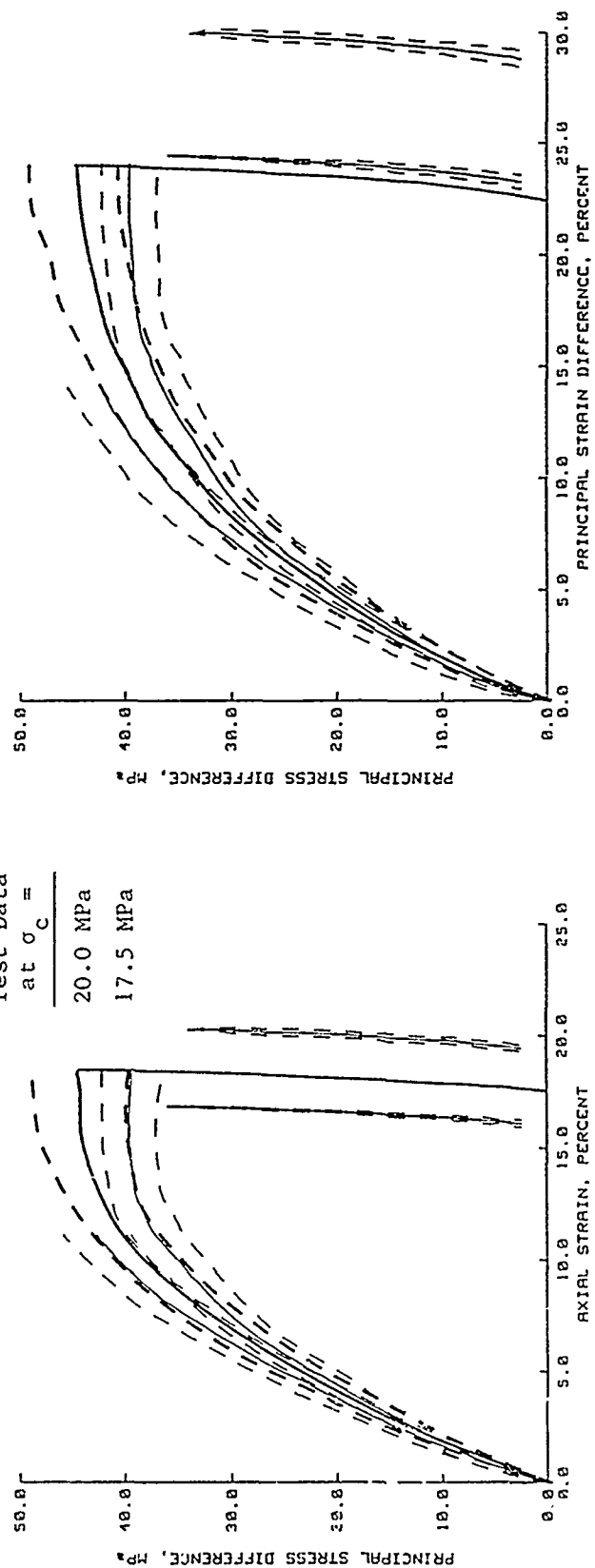


Figure 4.8. Comparison of the results from the COV analysis of the static TXC test data for $\sigma_c = 17.5$ and 20.0 MPa and the recommended laboratory response for $\sigma_c = 20.0$ MPa.

COV
 RECOMMENDED
 MEAN
 MEAN $\pm \sigma$

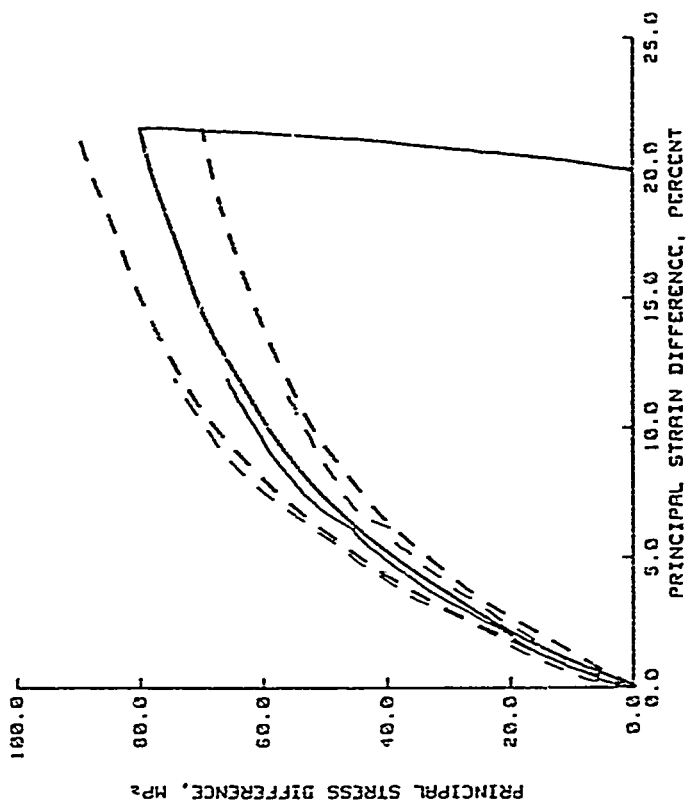
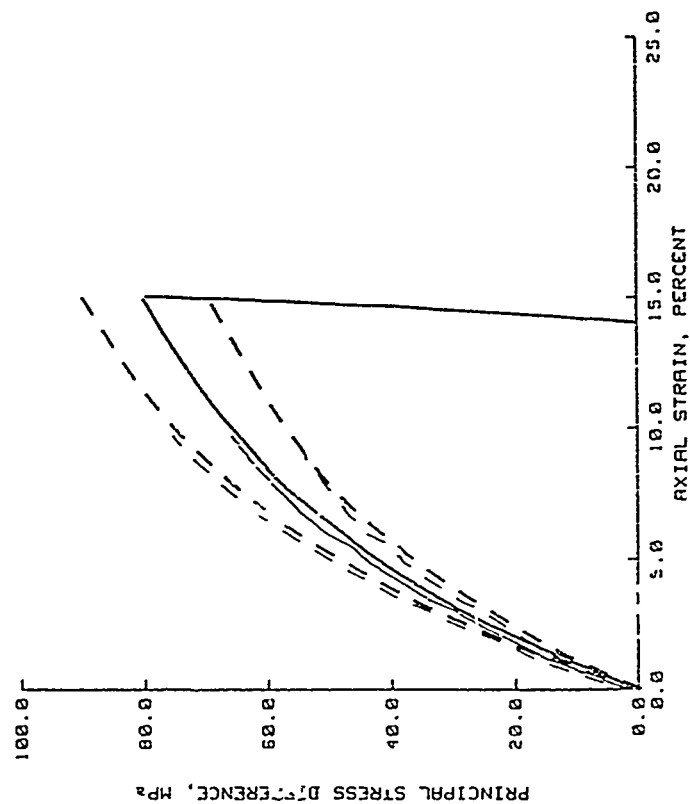


Figure 4.9. Comparison of the results from the COV analysis of the static TXC test data and the recommended laboratory response for $\sigma_c = 40.0$ MPa.

MEAN MEAN $\pm \sigma$
 COV ---
 RECOMMENDED ---

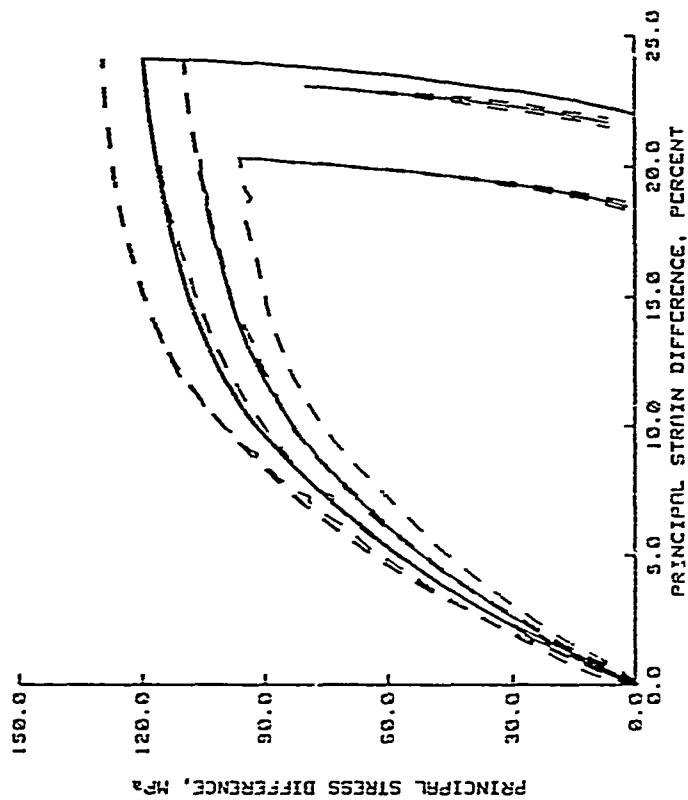
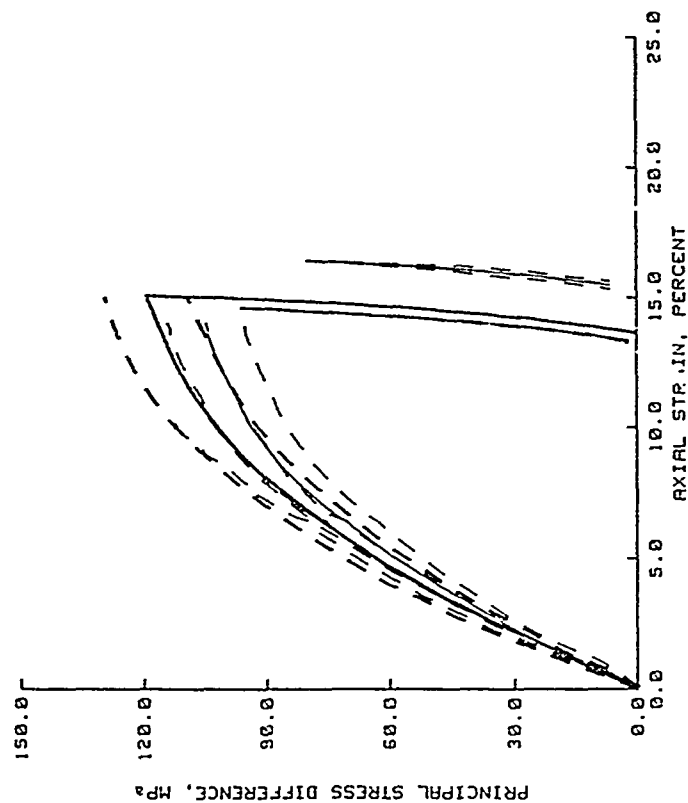


Figure 4.10. Comparison of the results from the COV analysis of the static TXC test data for $\sigma_c = 55.0$ and 60.0 MPa and the recommended laboratory response for $\sigma_c = 60.0$ MPa.

	MEAN	MEAN $\pm \sigma$
COV	---	---
RECOMMENDED	---	---

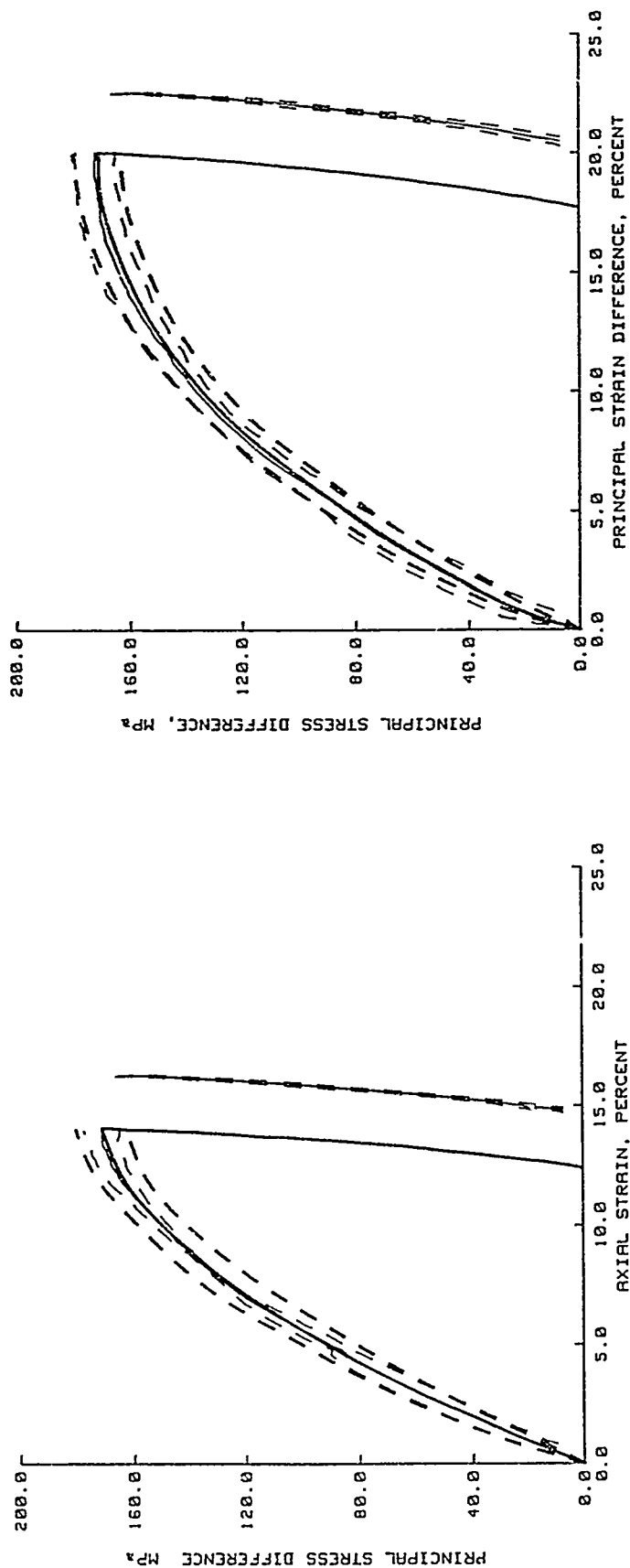


Figure 4.1i. Comparison of the results from the COV analysis of the static TXC test data and the recommended laboratory response for $\sigma_c = 80.0$ MPa.

——— MEAN
 - - - MEAN $\pm \sigma$
 O TEST DATA
 ● FIGURES 4.6-4.11

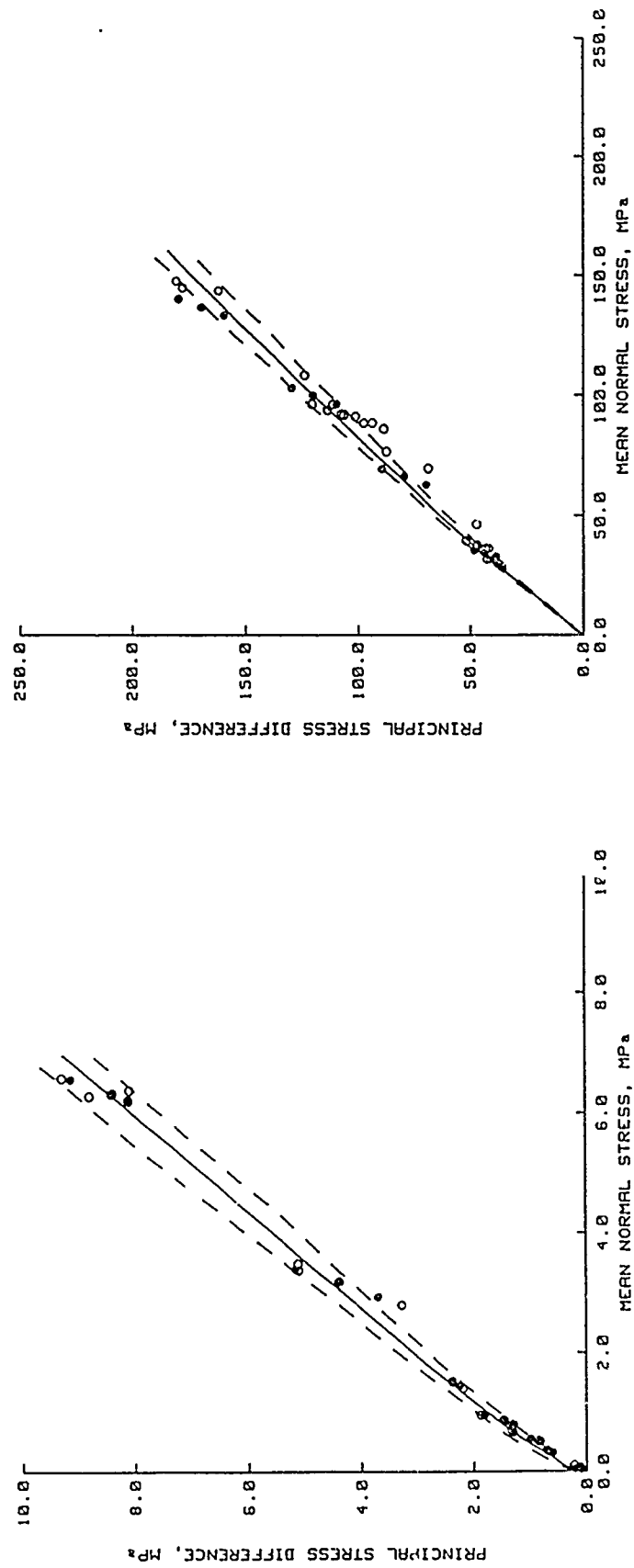


Figure 4.12. Static TXC "peak" strength test data, "peak" strength values from Figures 4.6 - 4.11, and recommended laboratory "peak" strength envelope.

— 17.5 MPa
 - - - 20.0 MPa
 — RECOMMENDED AT 20.0 MPa

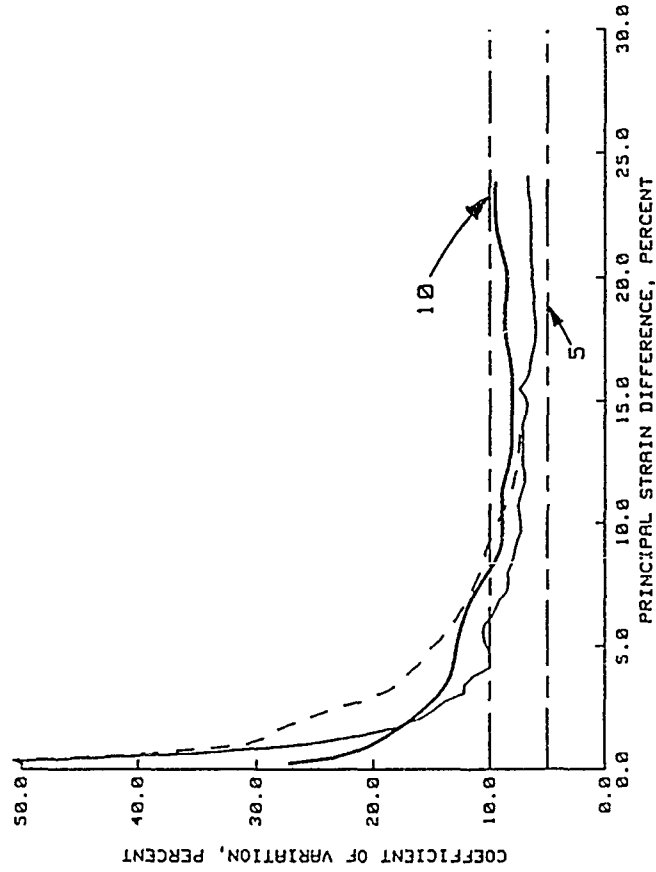
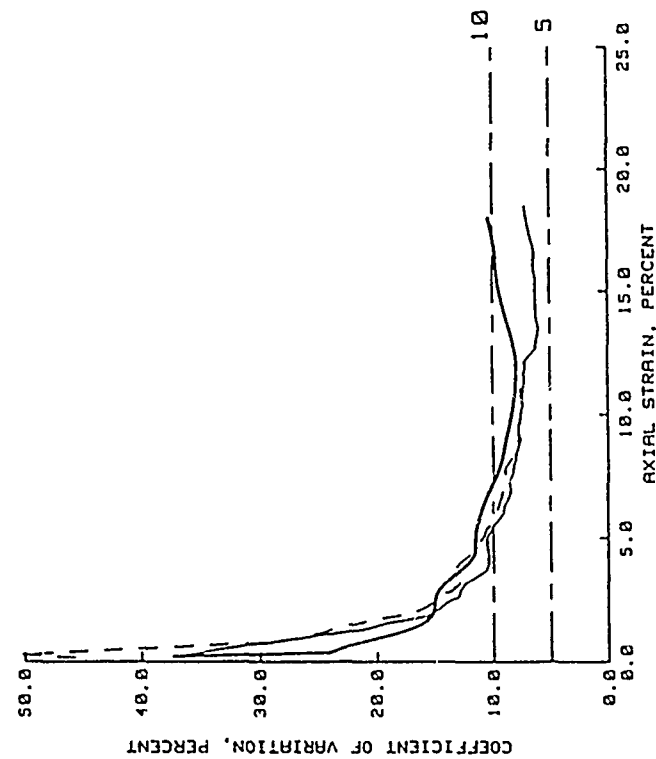


Figure 4.13. Coefficient of variation for the results from the COV analysis of static TXC test data for $\sigma_c = 17.5$ and 20.0 MPa and the recommended laboratory response for $\sigma_c = 20.0$ MPa.

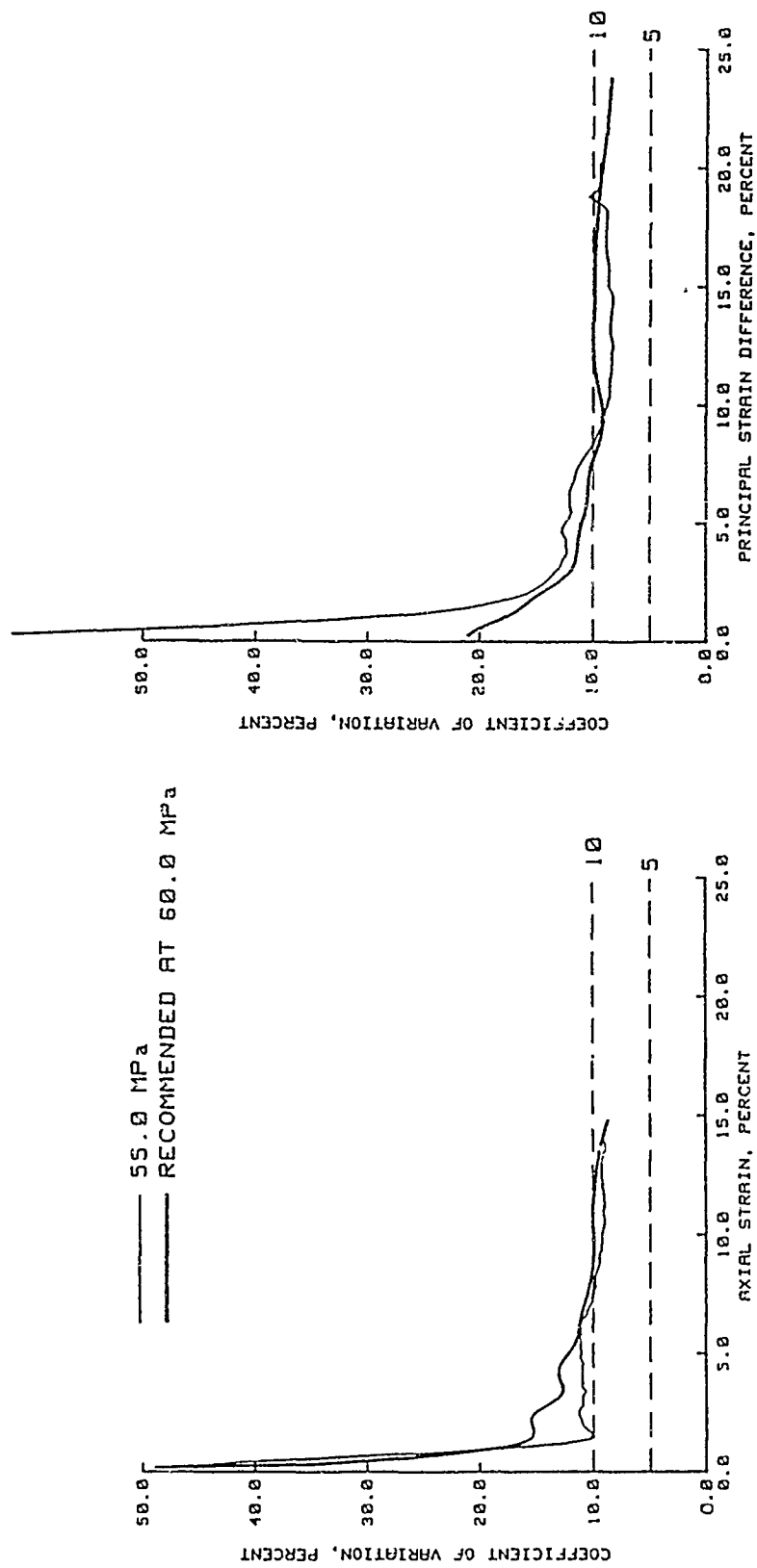


Figure 4.14. Coefficient of variation for the results from the COV analysis of static TXC test data for $\sigma_c = 55.0$ MPa and the recommended laboratory response for $\sigma_c = 60.0$ MPa.

MEAN	MEAN $\pm \hat{\sigma}$
COV	---
NEW	---

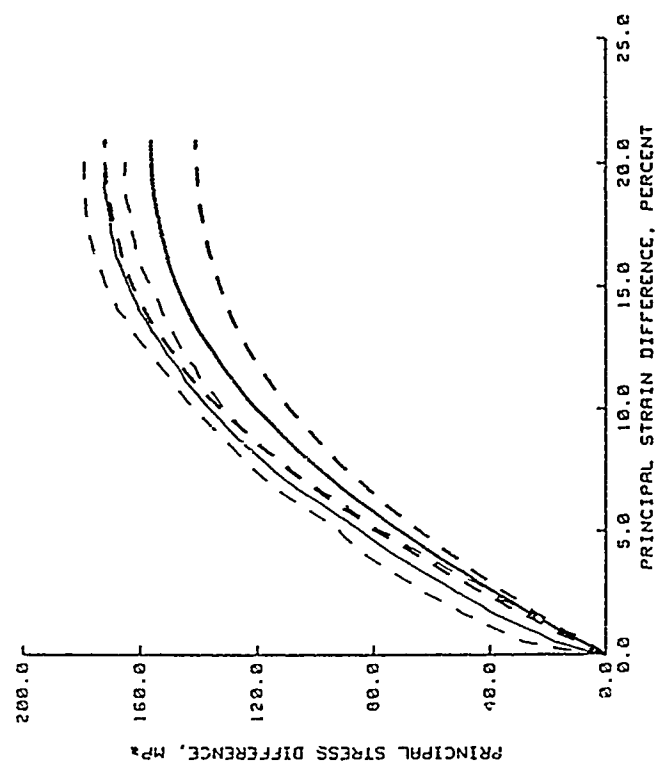
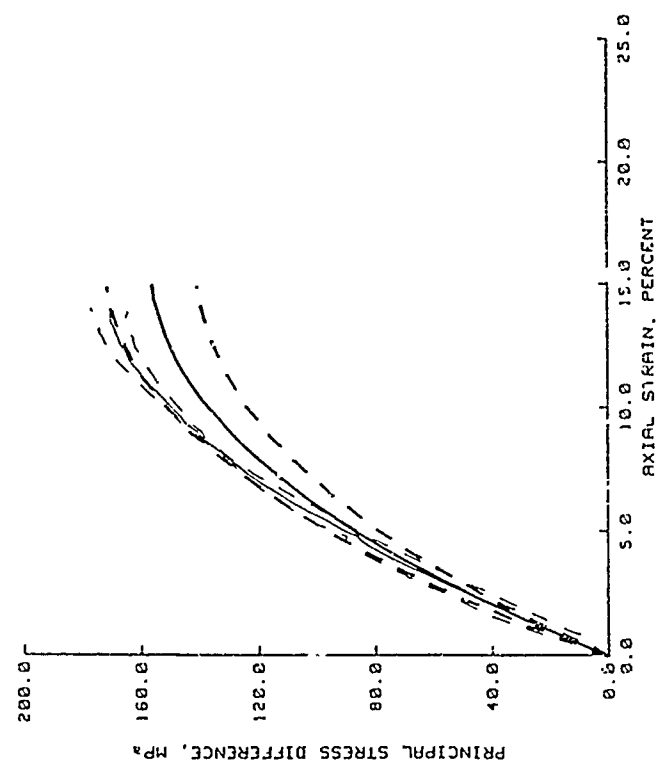


Figure 4.15. Comparison of the results from the COV analysis of the TXC test data and the new recommended response for $\sigma_c = 80.0$ MPa.

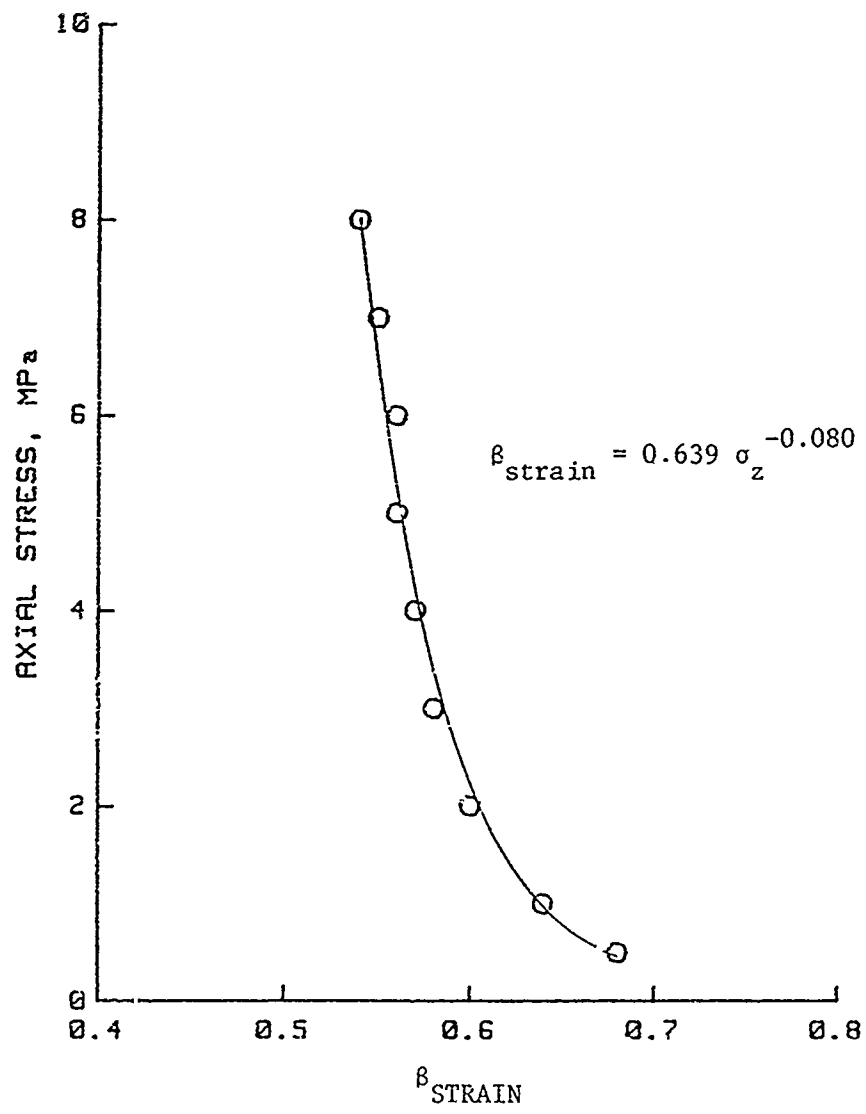


Figure 4.16. Correlation between in situ axial strain and seismic axial strain.

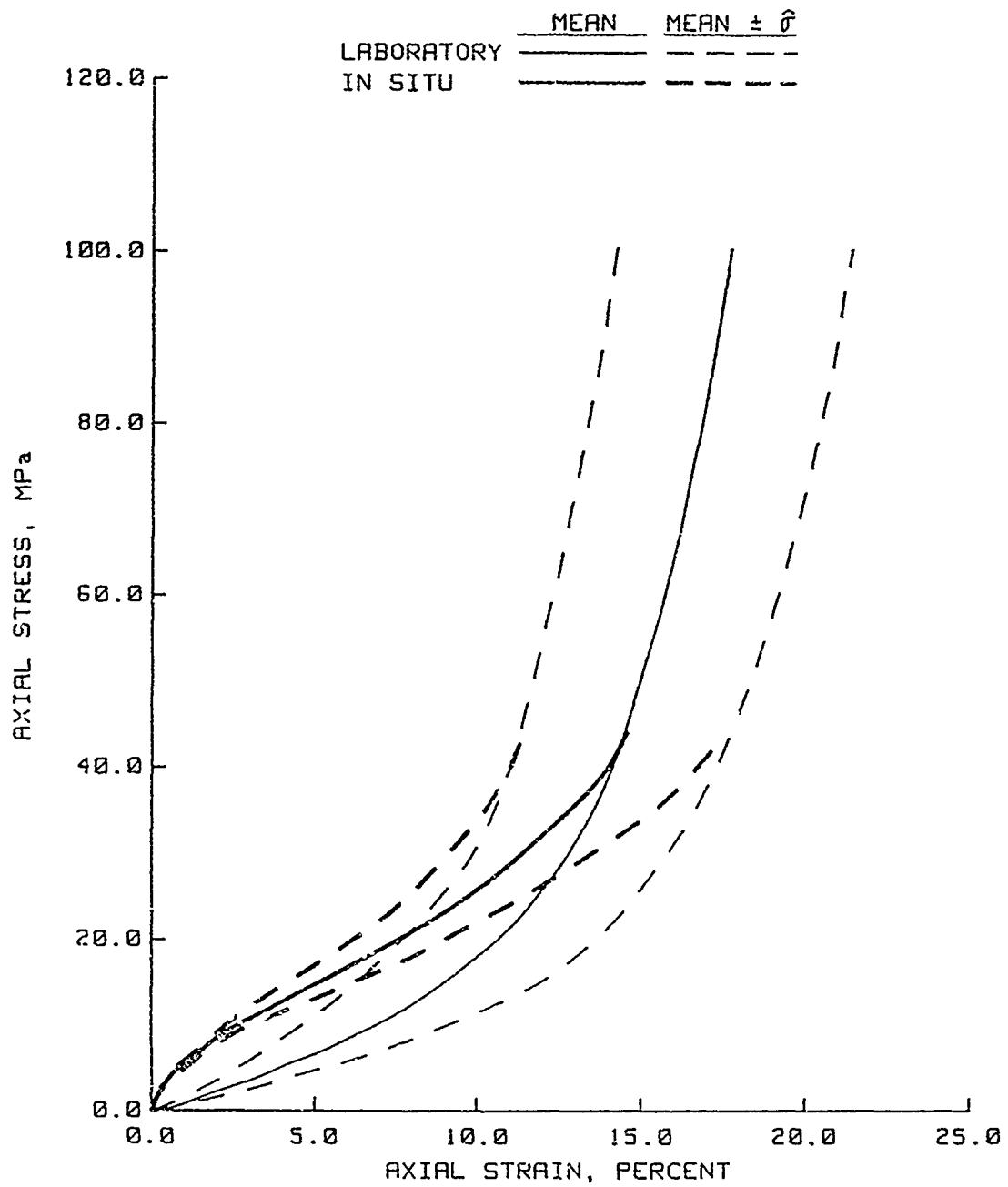


Figure 4.17. Recommended laboratory and in situ dynamic UX compressibility responses.

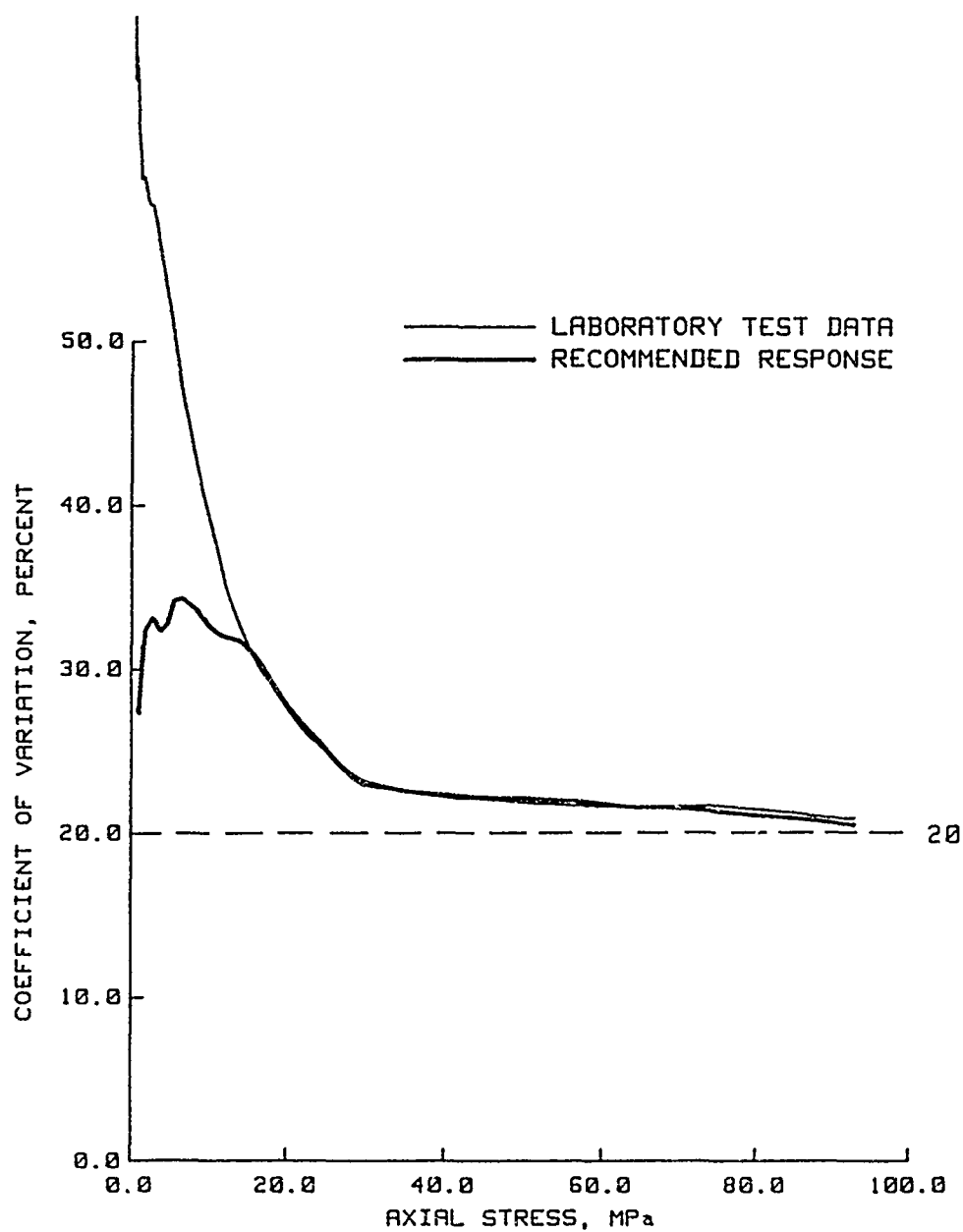


Figure 4.18. Coefficient of variation for the results from the COV analysis of dynamic UX test data and the recommended laboratory UX compressibility response.

——— LABORATORY TEST DATA
 ——— RECOMMENDED RESPONSE

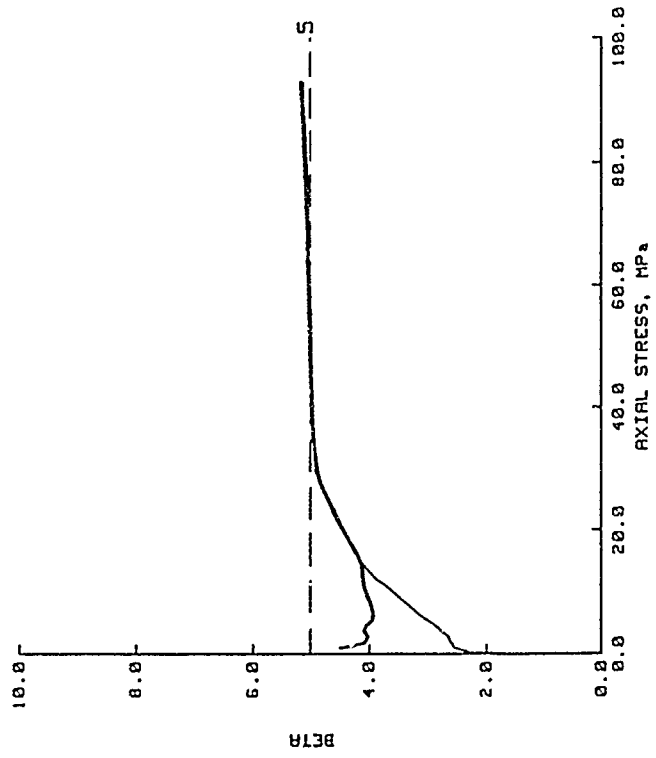
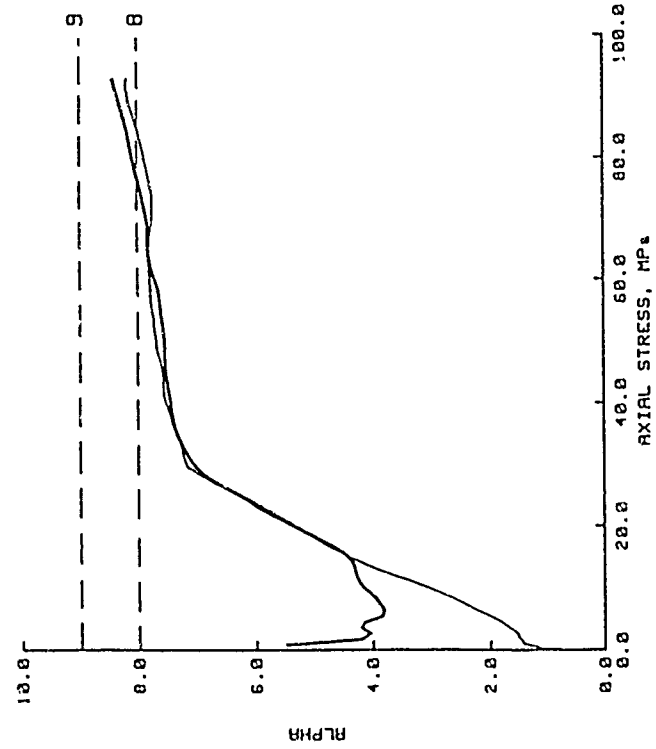


Figure 4.19. Beta distribution parameters α and β for the results from the COV analysis of dynamic UX test data and the recommended laboratory UX compressibility response.

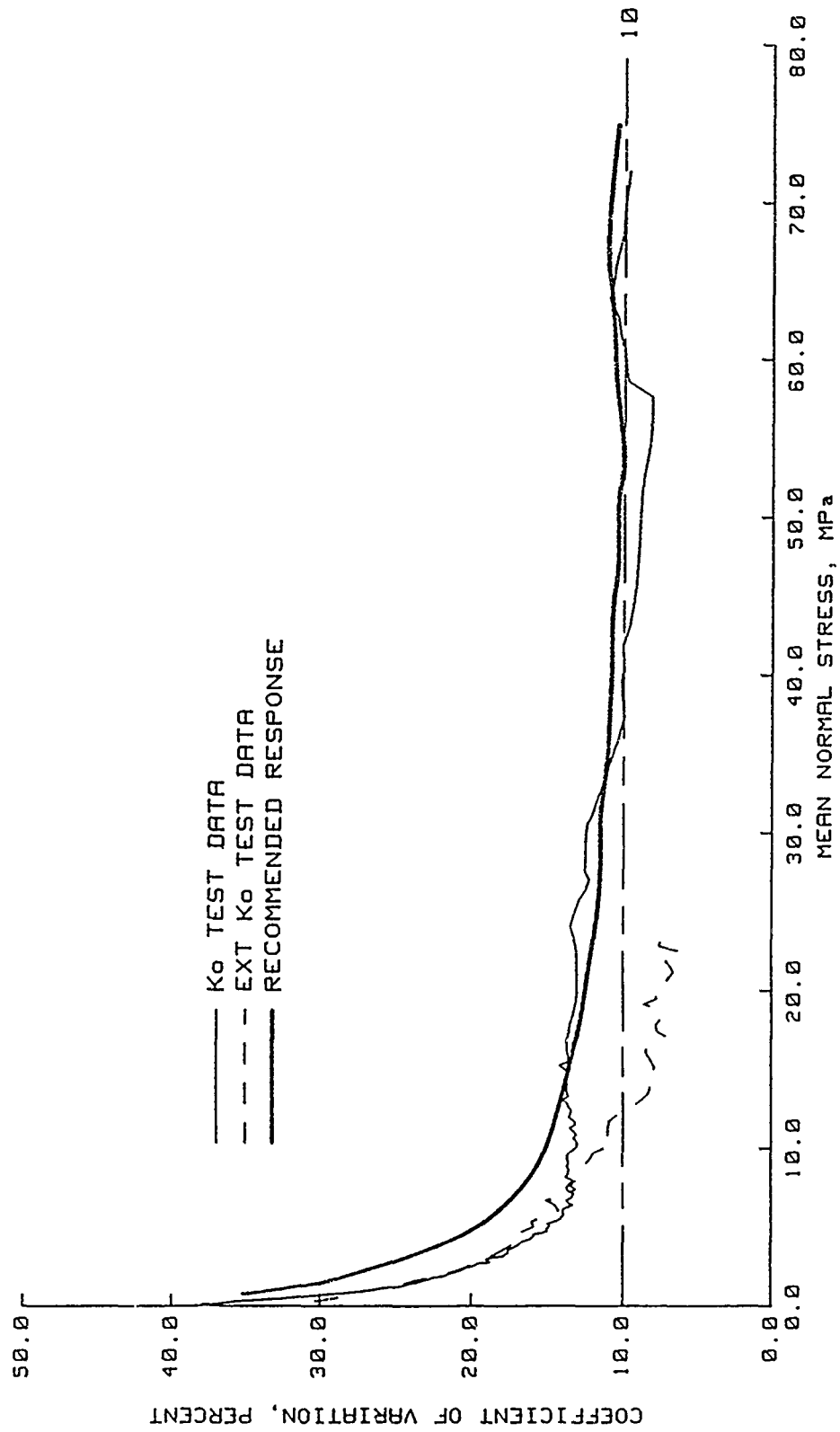
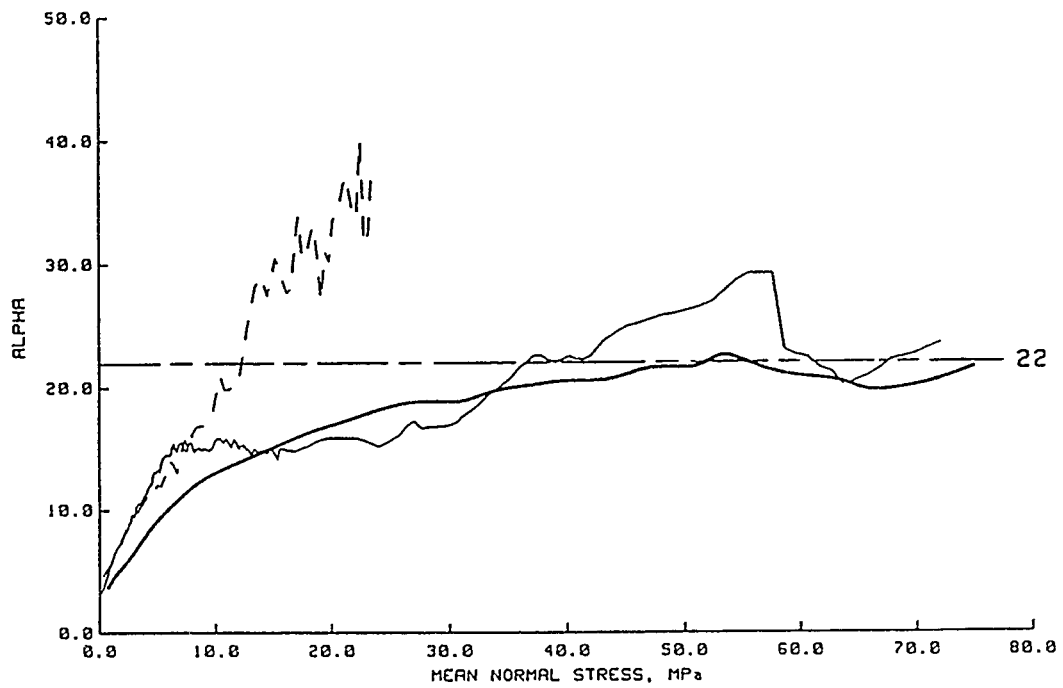


Figure 4.20. Coefficient of variation for the results from the COV analysis of K₀ and EXT K₀ test data and the recommended laboratory stress path.



— K₀ TEST DATA
 - - - EXT K₀ TEST DATA
 — RECOMMENDED RESPONSE

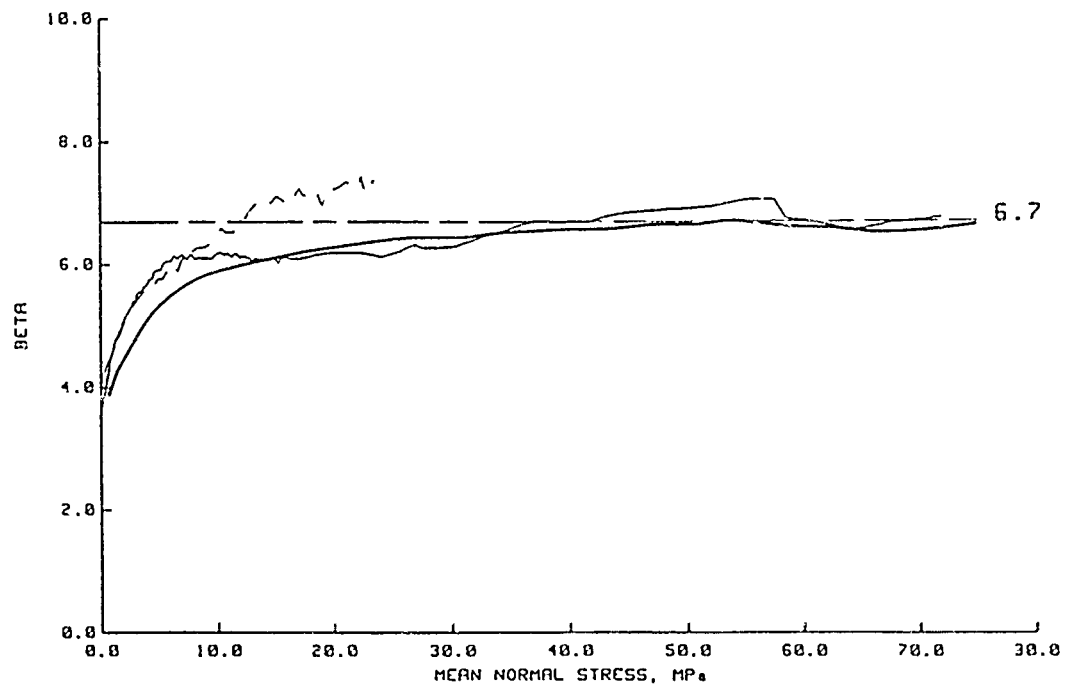


Figure 4.21. Beta distribution parameters α and β for the results from the COV analysis of K_0 and EXT K_0 test data and the recommended laboratory stress path.

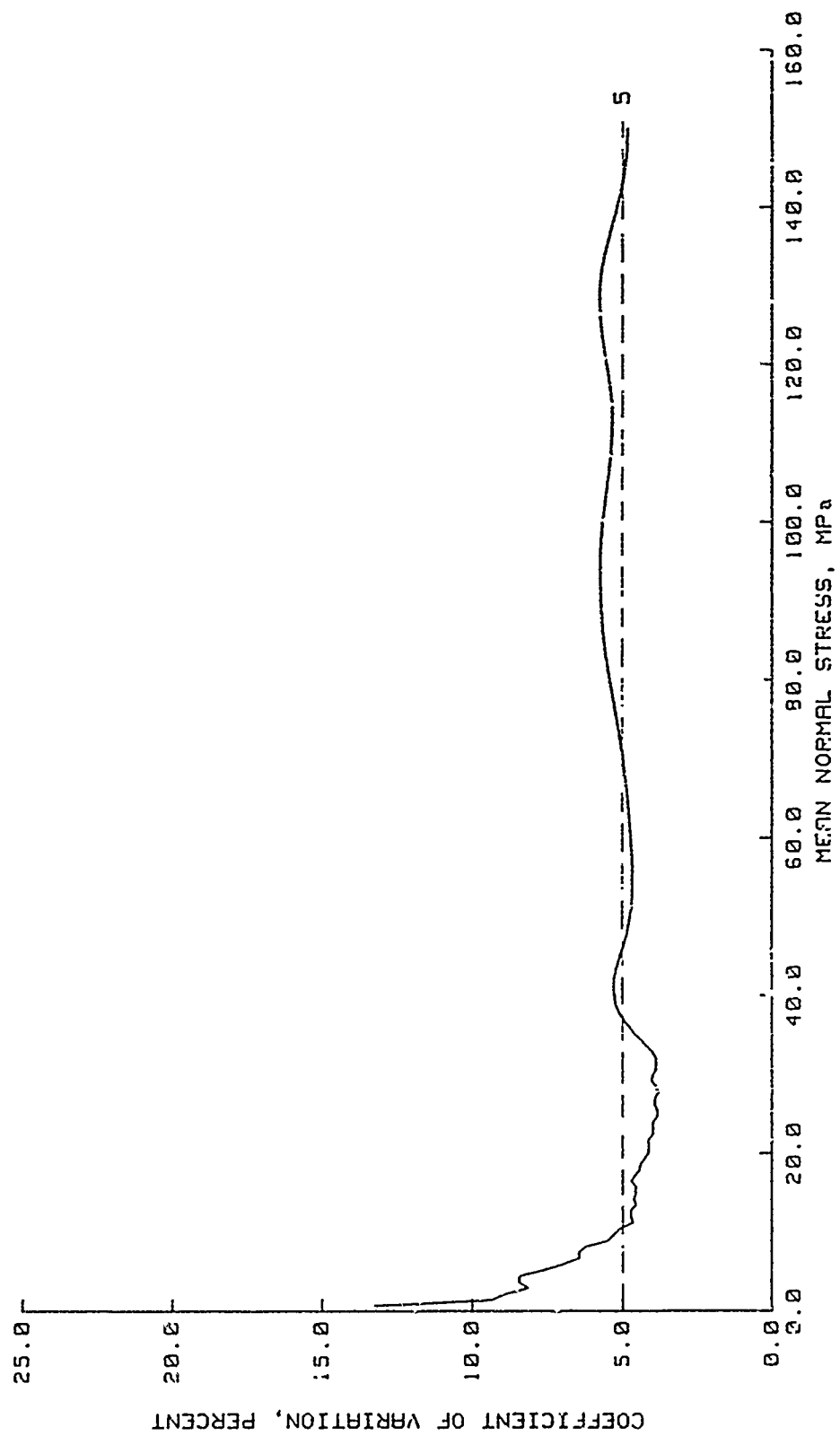


Figure 4.22. Coefficient of variation for the recommended laboratory TXC "peak" strength envelope.

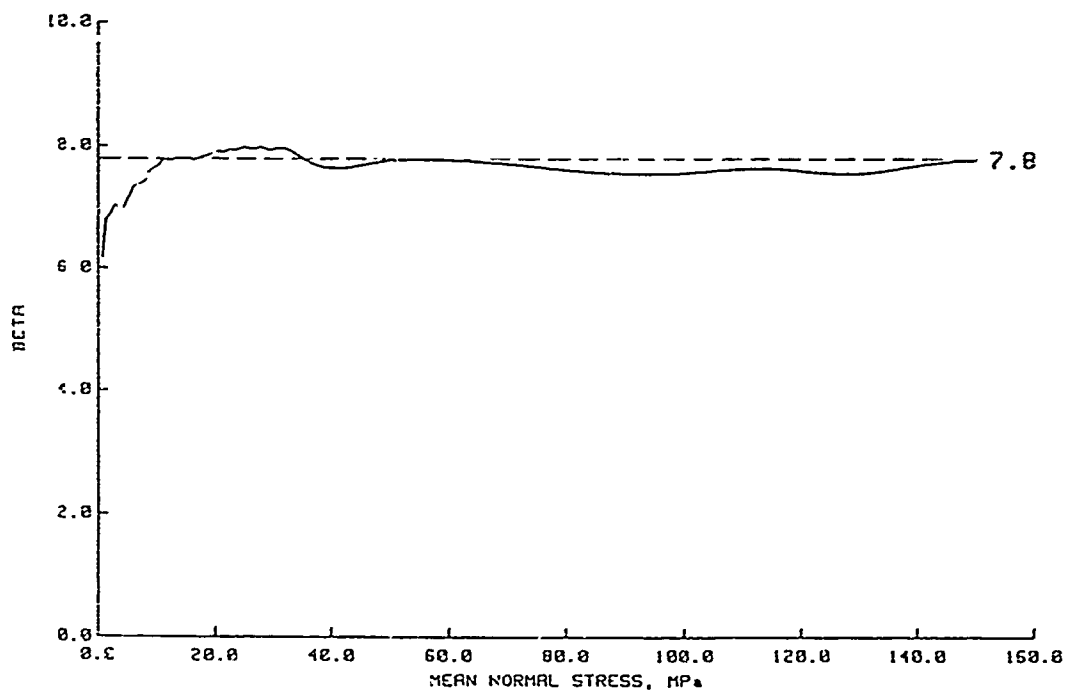
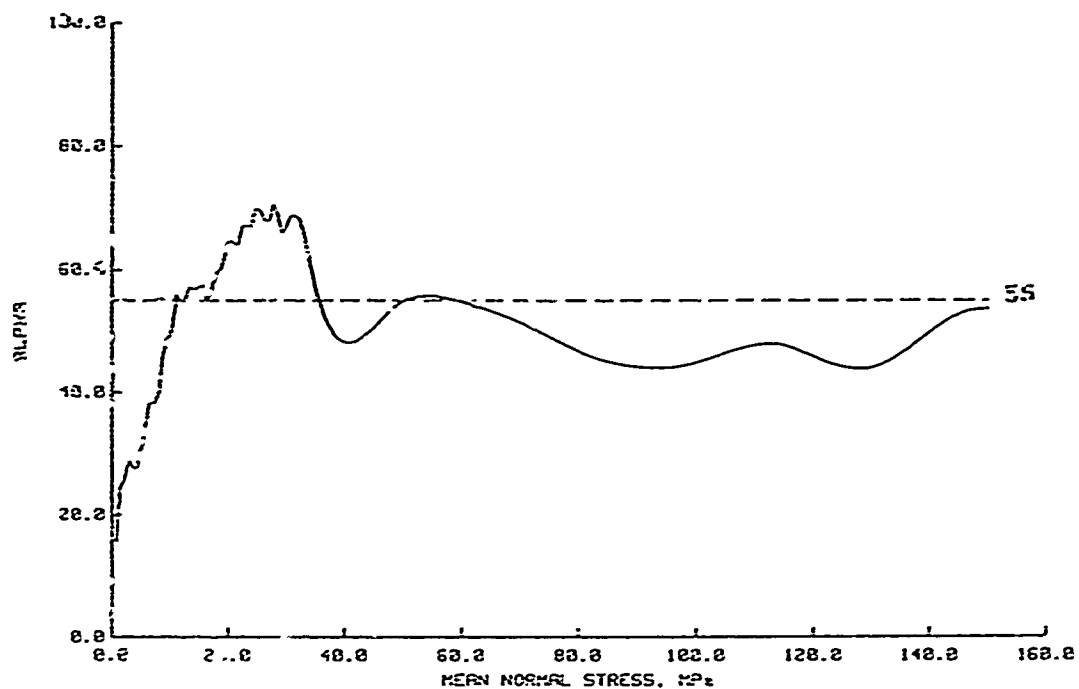


Figure 4.23. Beta distribution parameters α and β for the recommended laboratory TXC "peak" strength envelope.

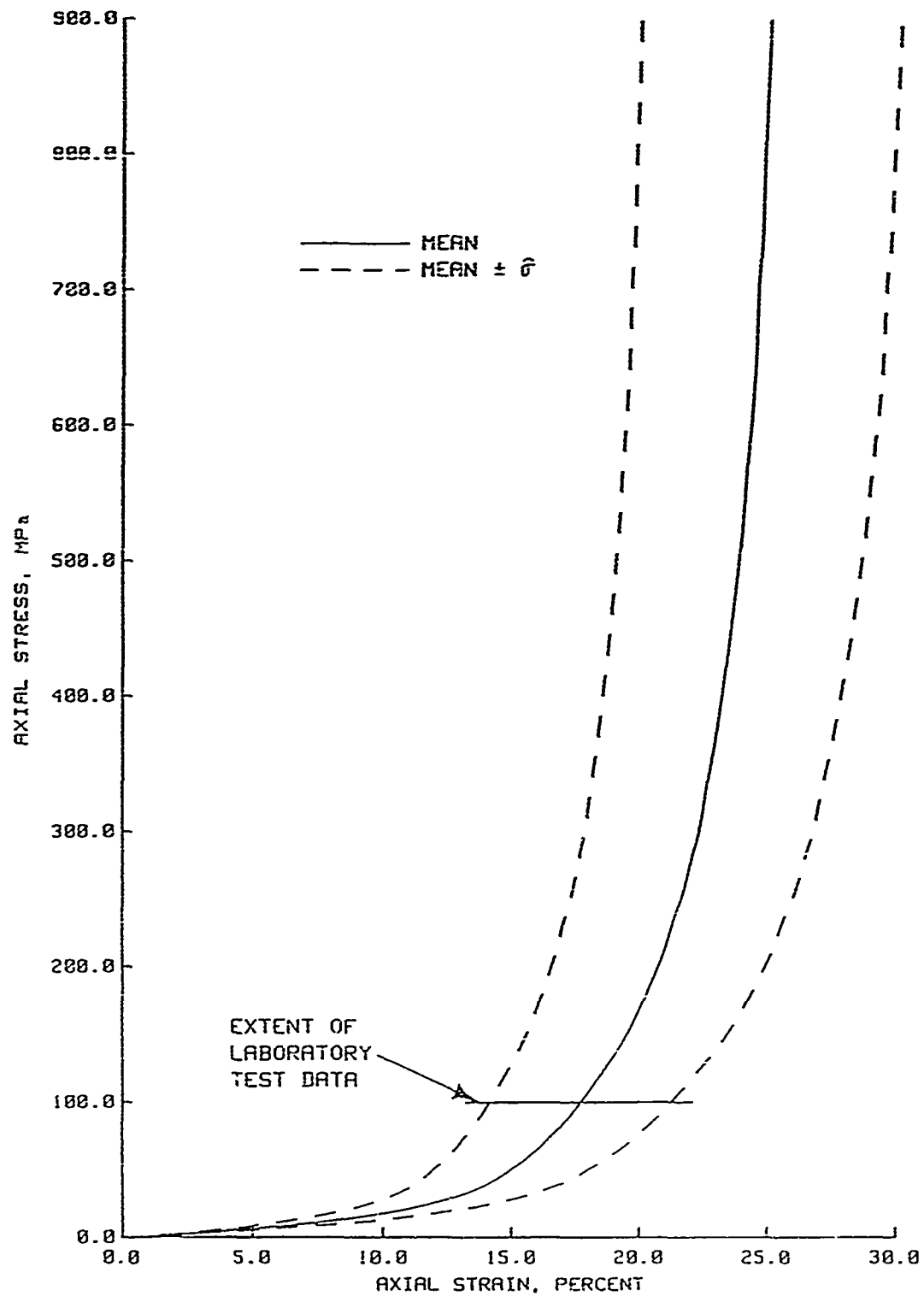


Figure 4.24. Recommended laboratory dynamic UX compressibility loading response extrapolated to higher stresses.

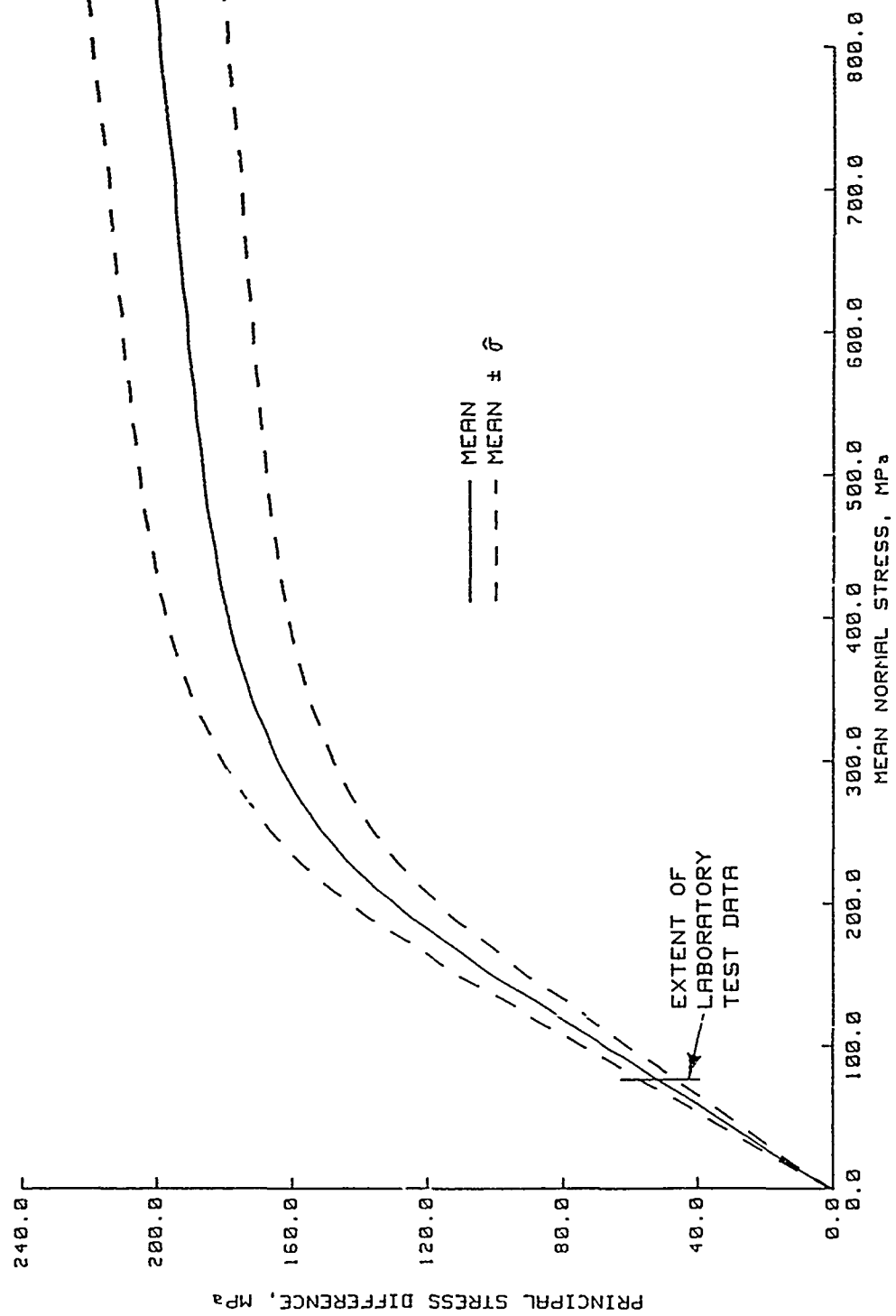


Figure 4.25. Recommended JX stress path extrapolated to higher stresses.

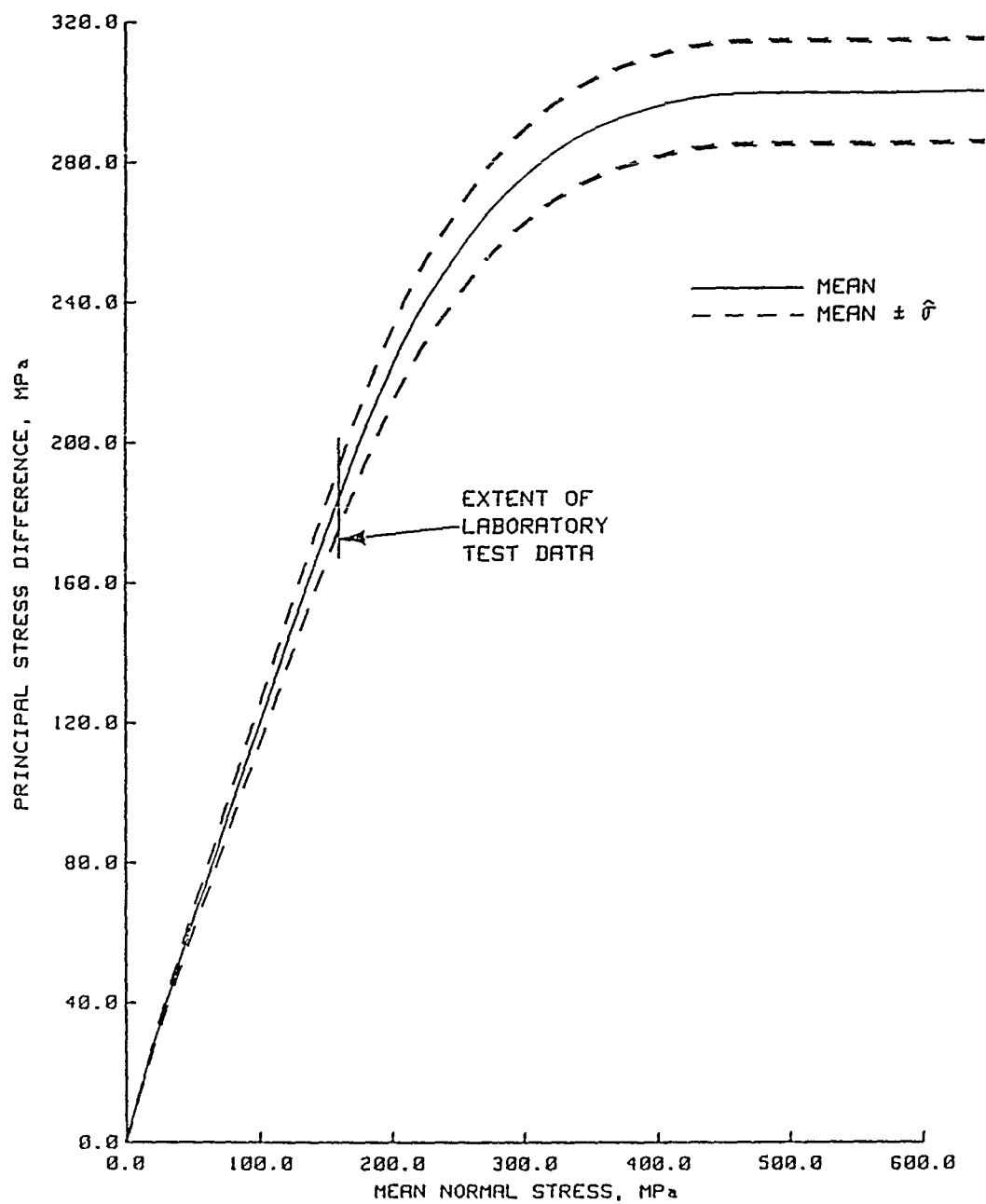


Figure 4.26. Recommended TXC "peak" strength envelope extrapolated to higher stresses.

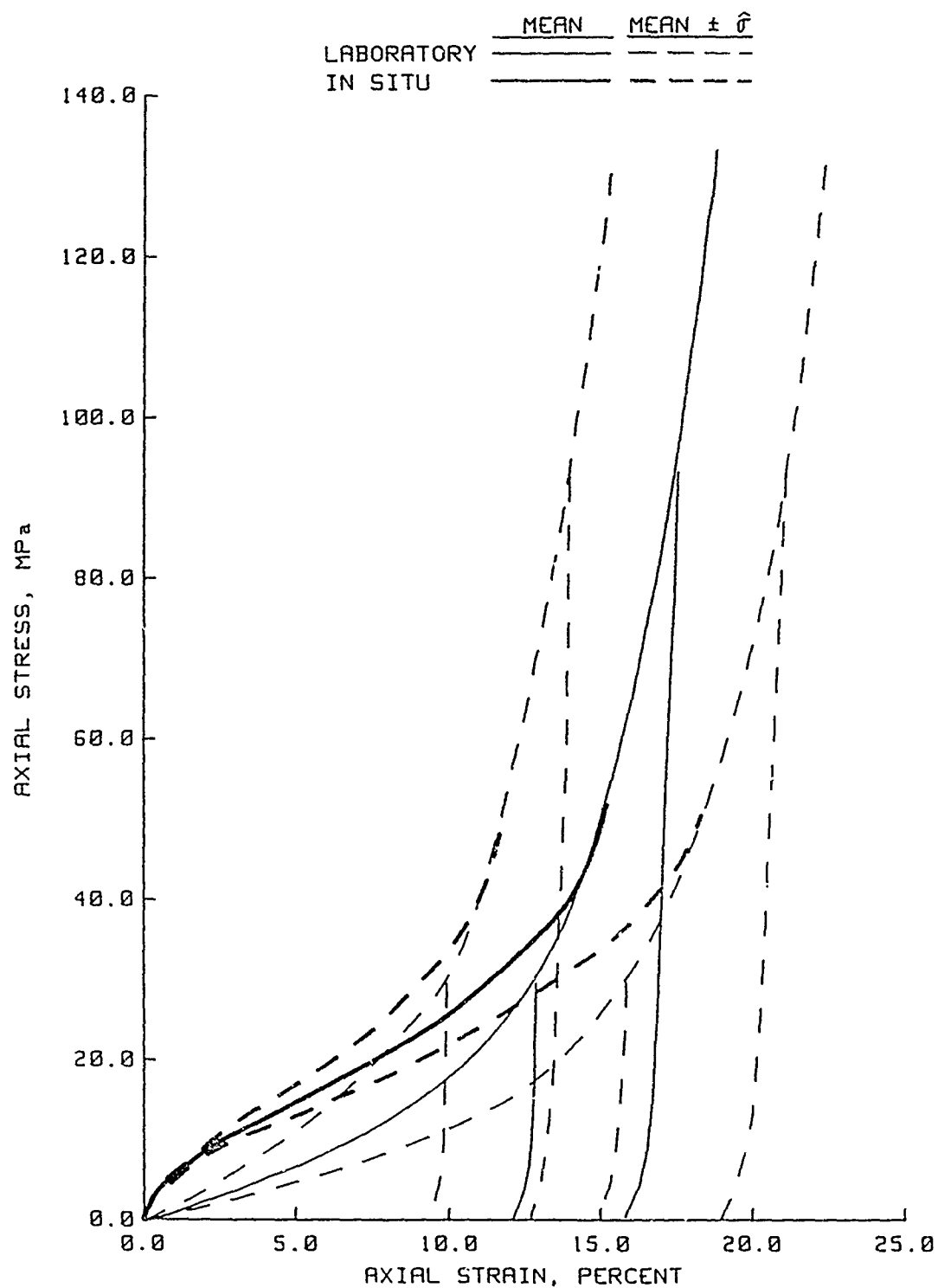


Figure 4.27. Low-stress laboratory and in situ probabilistic dynamic UX compressibility responses.

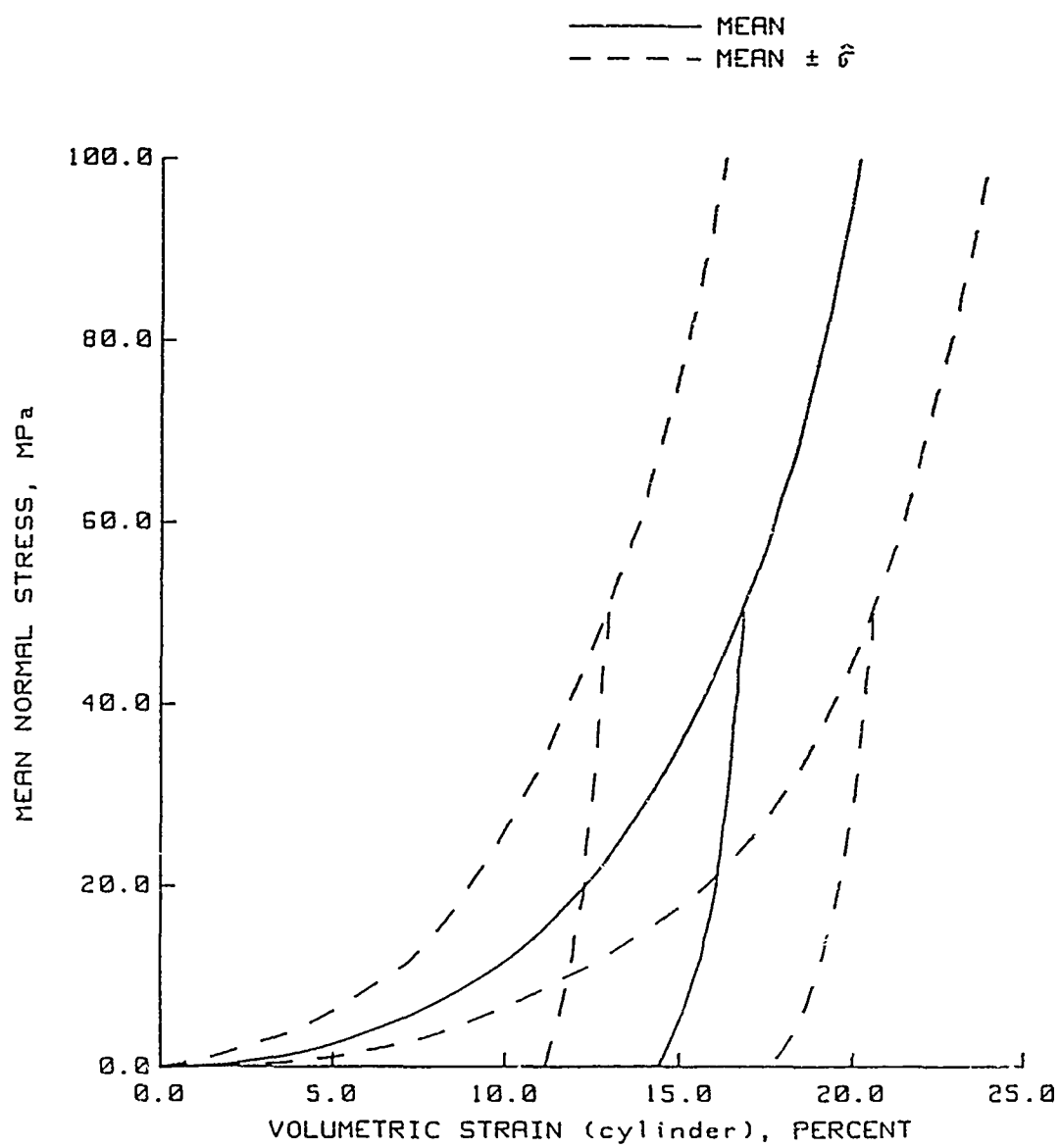


Figure 4.28. Laboratory probabilistic static HC compressibility response.

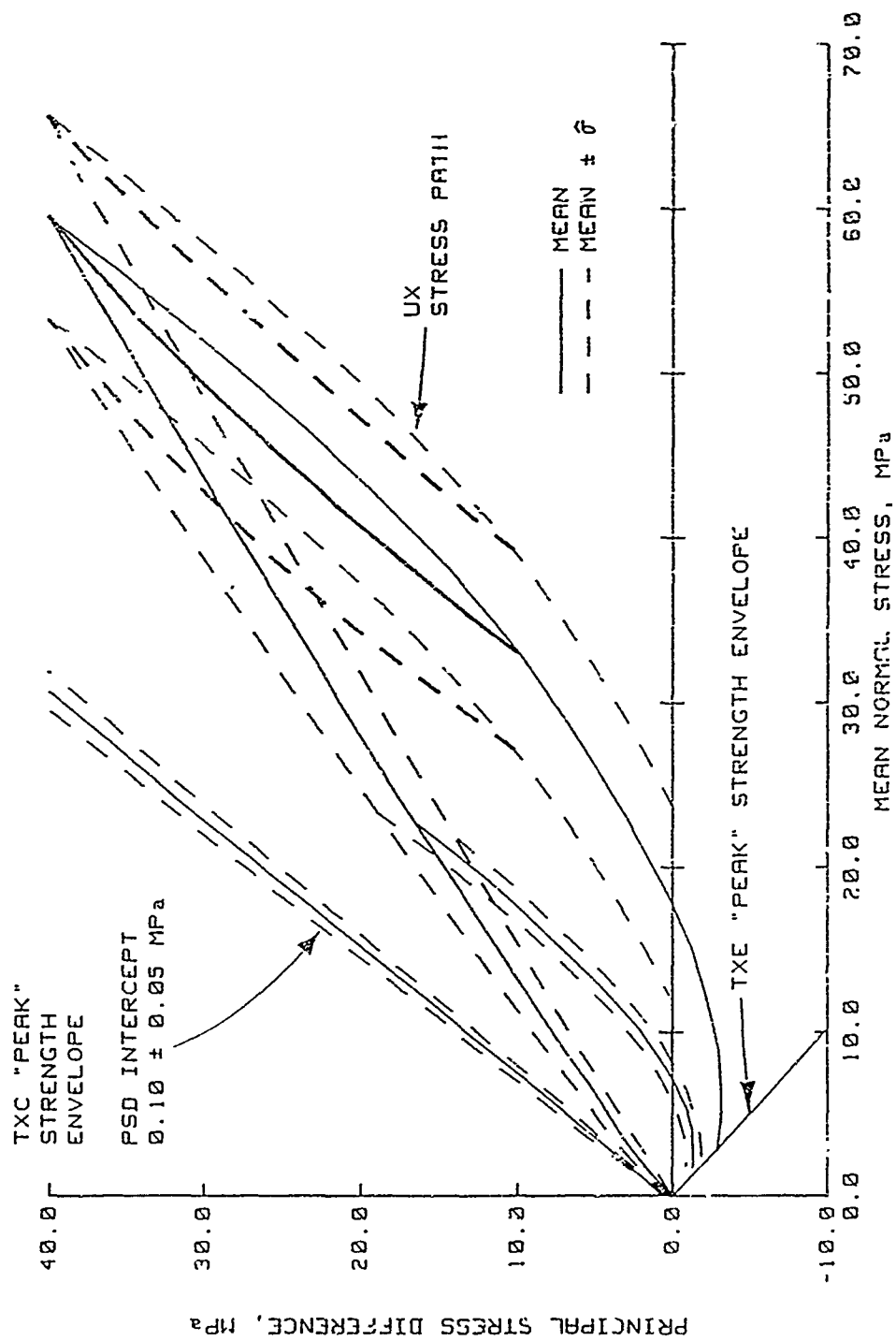


Figure 4.79. Low-stress in situ dynamic deterministic TXE "peak" strength envelope and probabilistic TXC "peak" strength envelope and UX stress path.

— MEAN
 - - - MEAN $\pm \sigma$

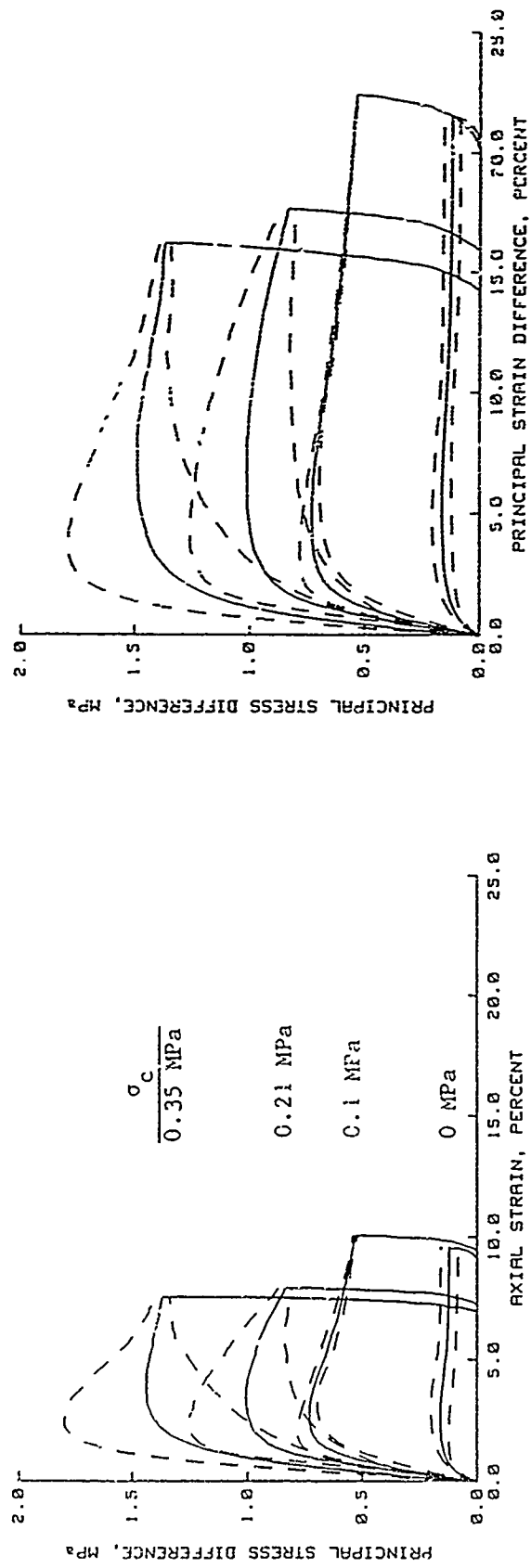


Figure 4.30. Probabilistic in situ dynamic TXC shear responses for $\sigma_c = 0, 0.1, 0.21$, and 0.35 MPa.

——— MEAN
 - - - MEAN $\pm \sigma$

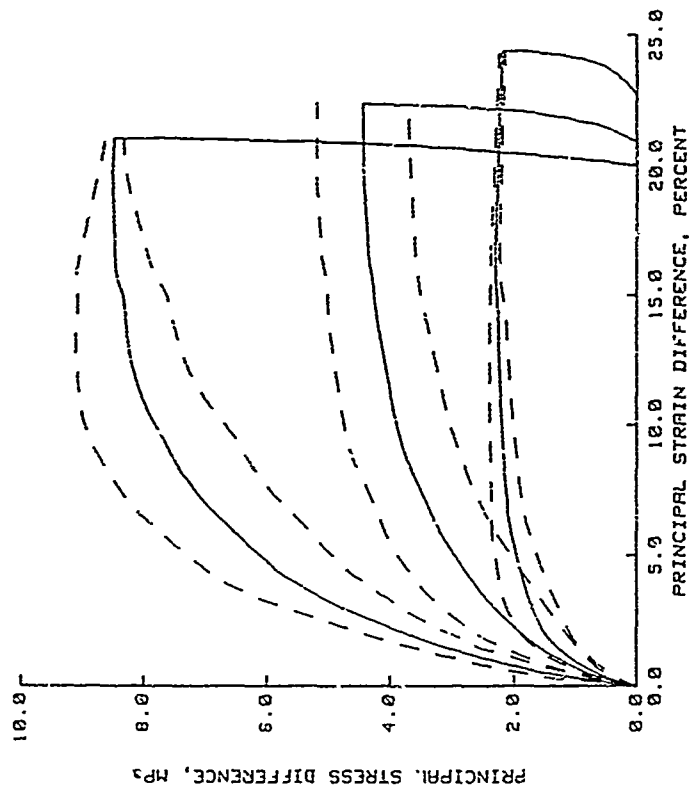
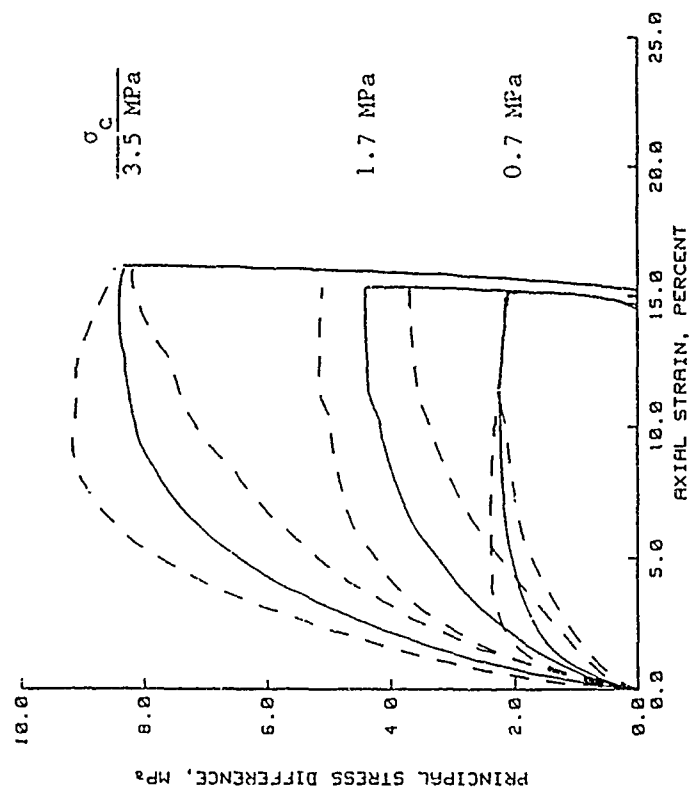


Figure 4.31. Probabilistic in situ dynamic TXC shear responses for $\sigma_c = 0.7, 1.7$, and 3.5 MPa.

——— MEAN
 - - - MEAN $\pm \hat{\sigma}$

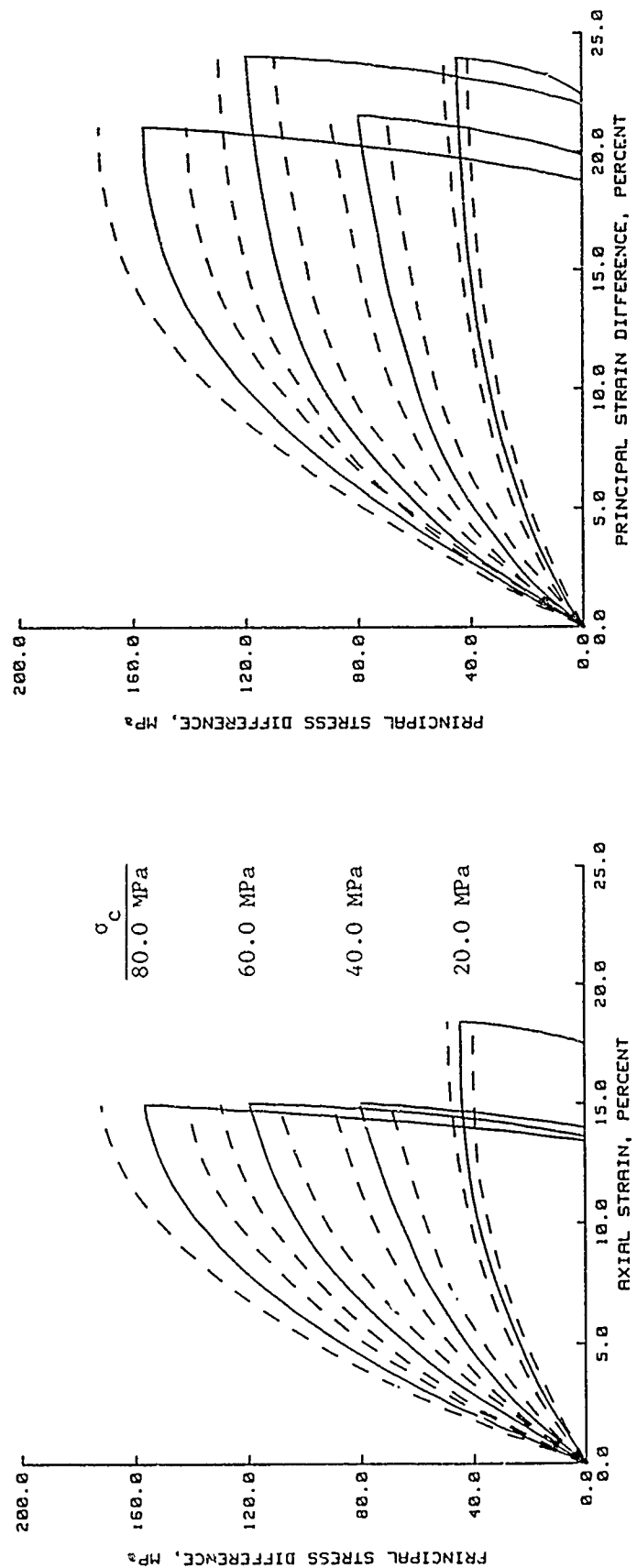


Figure 4.32. Probabilistic in situ dynamic TXC shear responses for $\sigma_c = 20.0, 40.0, 60.0, \text{ and } 80.0 \text{ MPa}$.

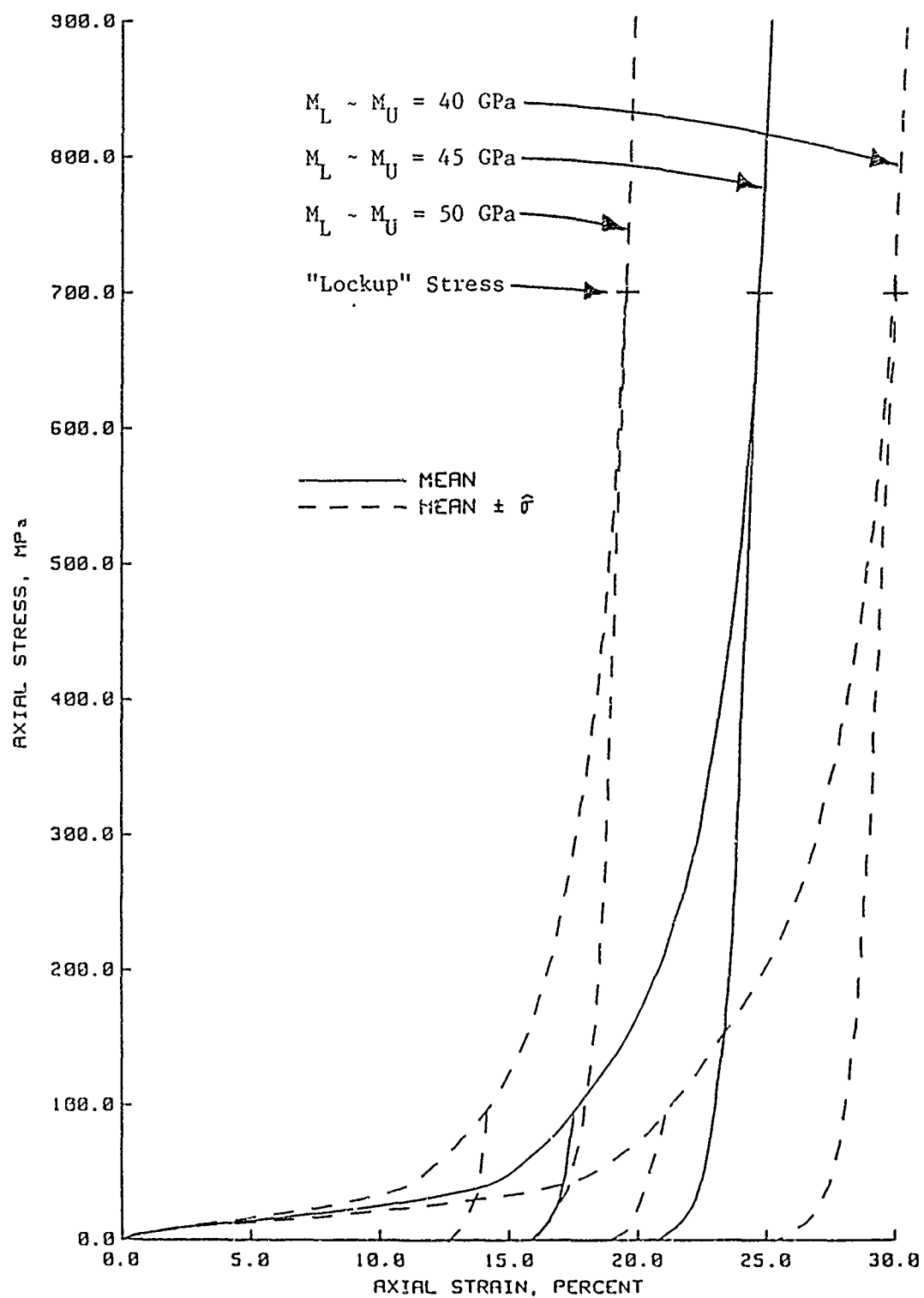


Figure 4.33. High-stress probabilistic in situ dynamic UX compressibility responses.

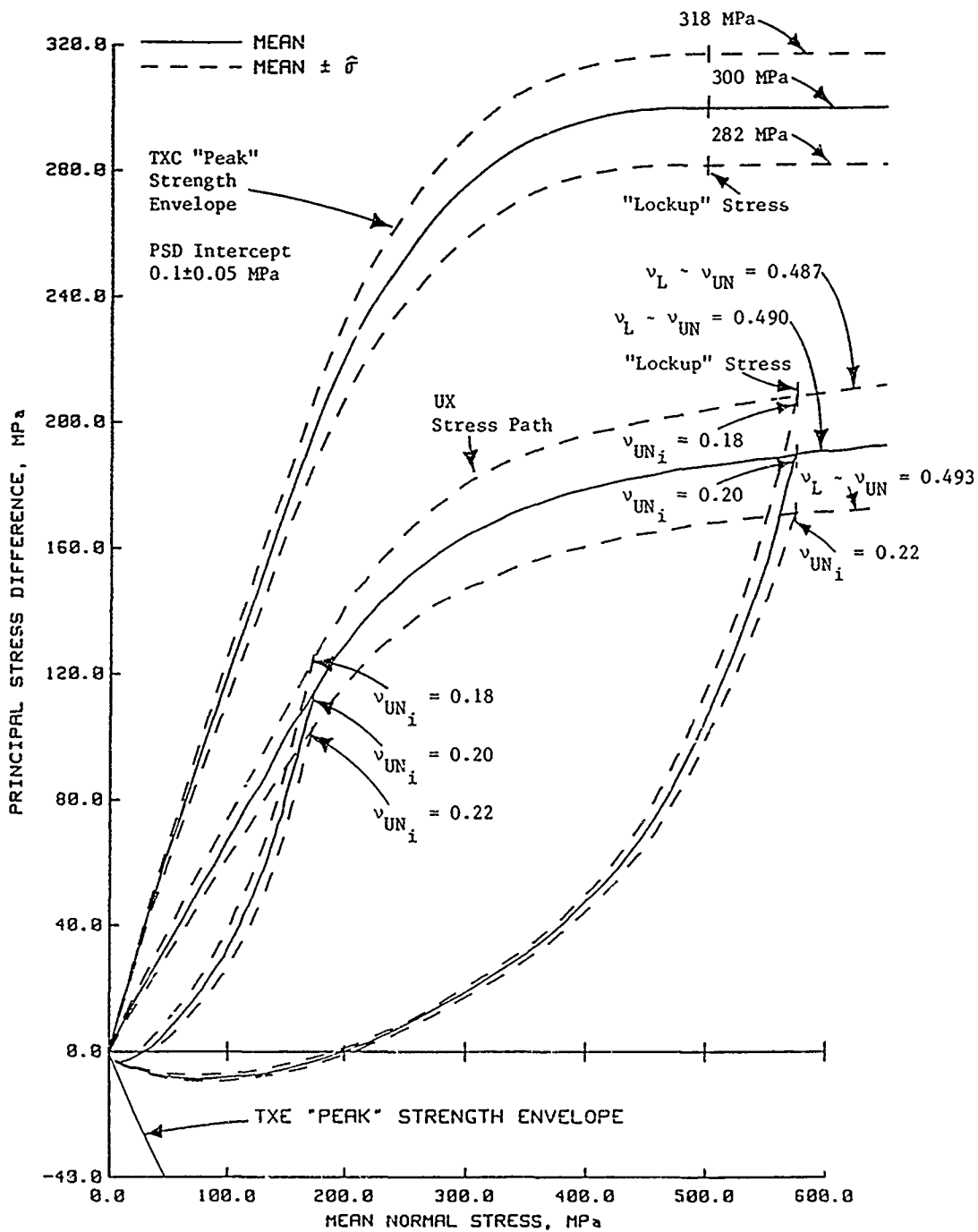


Figure 4.34. High-stress in situ dynamic deterministic TXE "peak" strength envelope and probabilistic TXC "peak" strength envelope and UX stress path.

SUMMARY, CONCLUSIONS, AND RECOMMENDATIONS

5.1 SUMMARY

A procedure for developing probabilistic properties of earth materials for use in probabilistic ground shock calculations was presented in Chapter 2. In this procedure, the subsurface profile of a given area was based on material type, mass-volume relations, index values, and seismic velocity. Probabilistic values for the mass-volume relations, index parameters, and seismic velocity were determined using simple statistical procedures. Probabilistic mechanical properties (i.e., strength and compressibility relations) were developed based on the results of laboratory tests conducted on undisturbed samples from each layer of the subsurface profile and on field experiments and engineering judgment. Data obtained from two adjacent areas located near Yuma, Arizona were used to illustrate the application of the procedure.

Because the basic material type at the two areas does not change significantly in the upper 150 feet, the subsurface profile was based on mass-volume relations, index parameters, and seismic velocity. Several probable zones were identified from plots of dry density data versus depth (Section 3.1). The apparent difference in the data was evaluated by conducting one-way analysis of variance tests. If the test results indicated no statistically significant difference, the trends were reevaluated and the test repeated. Probabilistic values for wet density, degree of saturation, and air voids content were calculated using a procedure developed by Rosenblueth (Section 2.2.3).

The results from uniaxial strain (UX), UX with lateral stress measurement (K_0), hydrostatic compression (HC), and triaxial compression (TXC) tests conducted on undisturbed samples from the first dry density-based layer at Area A were used to illustrate the procedure for developing probabilistic mechanical properties. The data base was supplemented by tests on undisturbed samples obtained from the upper 49 feet of Area B and with values of dry density within one standard deviation of the mean dry density for Area A.

A procedure for removing electrical noise from the data (Section 2.2.1) was applied to most of the UX test data and the higher pressure Ko and TXC test data. The mean and variance of incremental slopes from plots of the smoothed data were analyzed using the covariance technique (Section 2.2.2). The covariance (COV) analysis was conducted on (a) smoothed data plotted in a way that was conducive to constitutive modeling, i.e., axial stress, mean normal stress, principal stress difference, axial strain, volumetric strain, and principal strain difference, and (b) smoothed data plotted in a way that was as close as practical to the responses actually measured during the test, i.e., stress, load, and deflection. The results from the second analysis were converted into the conducive forms for constitutive modeling by applying the Rosenblueth procedure. The load, unload, and reload portions of the data were analyzed separately since the COV analysis requires that the individual responses be monotonic.

In the Rosenblueth procedure (Section 3.2.4), the mean and mean ± 1 standard deviation ($\hat{\sigma}$) secant slopes were calculated using the results from the COV analysis of the "measured" mechanical property test data. The probabilistic target responses were constructed by multiplying these values by the mean value for the denominator of the slope. Since the slopes of the desired plots were calculated, it was necessary to investigate the effect of including correlation coefficients (ρ). The values for ρ were estimated by linear regression analysis conducted on the random variables. Including ρ had the greatest effect on the variance and little to no effect on means. Whether the variance was increased, decreased, or unchanged depended on the sign of ρ and the rank of the ++, +-, -+, and -- calculations.

The results from applying the two analysis techniques to loading test data were compared in Section 3.2.5. Both techniques provided similar results for the Ko, EXT Ko, and HC test data. For TXC test data, the results were slightly different since the stress-axis was incremented in the COV analysis of the "measured data." The unloading and reloading responses from both analysis techniques were essentially the same for all test types.

Low stress probabilistic mechanical properties for the layer were developed by using the results from the COV analysis. analyses of

dynamic in situ compressibility tests, and engineering judgment (Section 4.2). The variance of the low stress probabilistic UX compressibility, UX stress path, and TXC "peak" strength envelope was extrapolated to higher stresses by examining the coefficients of variation and beta distribution parameters for the lower stress responses (Section 4.3); constant values were approached as stress increased.

The final probabilistic mechanical properties for the layer were presented in Section 4.4. The low stress responses were extended past the stress level at which the material became fully saturated ("lockup" stress). The "lockup" stress was not treated probabilistically since a single value would have resulted from the COV analysis of a set of test results that achieved different values for "lockup" stress.

5.2 CONCLUSIONS

The following conclusions can be made as a result of this investigation:

1. The one-way analysis of variance test is very useful for developing the subsurface profile of a given area based on plots of mass-volume, index, and seismic velocity data versus depth.

2. The COV analysis of mechanical property test data for earth materials plotted in forms that are conducive to constitutive modeling and applying the Rosenblueth procedure to the results from the COV analysis of "measured data" provide similar probabilistic responses.

3. The uniqueness of a soil specimen's response during a mechanical property test must be maintained when plotting measured data. This is accomplished by normalizing the measured data based on the specimen dimensions. A hypothetical example illustrating the effect of using the measured deflection is shown in Figure 5.1. Assuming that the variance in the strain of two test specimens of different size is the result of random scatter and not size effect, the average strain should be 12.5 percent and not 13.0 percent as calculated using the measured deflection.

4. When using the Rosenblueth procedure to transform the results from the COV analysis of the "measured data" into the forms that are more conducive to constitutive modeling, the effect of correlation coefficients ρ must be evaluated.

5. The procedure used to extrapolate the laboratory-based probabilistic mechanical properties maximized the variance about the extrapolated mean. Tests to higher stresses are needed to substantiate the extrapolation procedure.

6. The mean values for the mass-volume relations, index parameters, UX compressibility, UX stress path, TXC shear responses, and TXC "peak" strength envelope are coupled, i.e., they would be used in a deterministic ground shock calculation to obtain mean values for the output. Since there was no apparent tie between the mean $\pm \hat{\sigma}$ properties, the mean $+\hat{\sigma}$ or mean $-\hat{\sigma}$ values for one material property cannot be coupled with the mean $+\hat{\sigma}$ or mean $-\hat{\sigma}$ value for the other material properties. This results in many possible combinations.

5.3 RECOMMENDATIONS

Recommendations for further study are:

1. Include spatial variability in the determination of probabilistic properties of earth materials.

2. Correlate the probabilistic mass-volume, index, and mechanical properties of earth materials with the results from easily obtained field tests such as cone penetration tests.

3. Examine the true distribution of mass-volume, index, and mechanical property data to quantify the effect of assuming a symmetrical distribution in the analysis technique.

4. Complete the analysis for all layers of the profile for a given site and determine if the differences in the mass-volume, index, and seismic velocity data is translated into different mechanical responses. A method such as one-way analysis of variance could be used to determine if the apparent differences are significant.

Sample A is 2" high

Sample B is 3" high

Assume that during a UX strain test,

at $\sigma_z = 20 \text{ MPa}$,

$\epsilon_A = 10\%$ and $\epsilon_B = 15\%$

The average strain is $\frac{10 + 15}{2} = 12.5\%$

$$\Delta H_A = 2(0.10) = 0.2"$$

$$\Delta H_B = 3(0.15) = 0.45"$$

$$\text{The average } \Delta H = \frac{0.2 + 0.45}{2} = 0.325"$$

$$\text{The average } H = \frac{2 + 3}{2} = 2.5"$$

The average strain using the average ΔH

$$\text{and the average } H \text{ is } \frac{0.325}{2.5} = 13\%.$$

Since the sample heights are different, strain must be used.

Figure 5.1. Discrepancy created by varying sample size.

REFERENCES

1. Chou, Yu T. September 1981. "Probabilistic Modeling of Subgrade Soil Strengths," Miscellaneous Paper GL-81-5, US Army Engineer Waterways Experiment Station, Vicksburg, MS.
2. Diaz-Padilla, Jorge, and Vanmarcke, Erik H. August 1975. "Settlement Prediction: A Probabilistic Approach," Research Report R73-40, Department of Civil Engineering, Massachusetts Institute of Technology, Cambridge, MA.
3. Gilbert, Lawrence W. July 1977. "A Probabilistic Analysis of Embankment Stability Problems," Miscellaneous Paper S-77-10, US Army Engineer Waterways Experiment Station, Vicksburg, MS.
4. Vanmarcke, Erik H. "Reliability of Earth Slopes," Journal of the Geotechnical Engineering Division, Proc. ASCE, Vol. 103, No. GT11, November 1977, pp 1247-1265.
5. Jackson, J. G. July 1982. "Site Characterization for Probabilistic Ground Shock Predictions," Miscellaneous Paper SL-82-8, US Army Engineer Waterways Experiment Station, Vicksburg, MS.
6. Vanmarcke, Erik H. December 1979. "Probabilistic Soil Sampling Program for MX-Related Site Characterization," Miscellaneous Paper SL-79-26, US Army Engineer Waterways Experiment Station, Vicksburg, MS.
7. Vanmarcke, Erik H. "Probabilistic Modeling of Soil Profiles," Journal of the Geotechnical Engineering Division, Proc. ASCE, Vol. 103, No. GT11, November 1977, pp 1227-1246.
8. Benjamin, Jack R., and Cornell, C. Allen. "Probability, Statistics, and Decision for Civil Engineers," McGraw-Hill Book Company, 1970.
9. Rohani, Behzad. June 1982. "Probabilistic Solution for One-Dimensional Plane Wave Propagation in Homogeneous Bilinear Hysteretic Materials," Miscellaneous Paper SL-82-7, US Army Engineer Waterways Experiment Station, Vicksburg, MS.
10. Rohani, Behzad, and Cargile, James D. April 1984. "A Probabilistic One-Dimensional Ground-Shock Code for Layered Nonlinear Hysteretic Materials," Miscellaneous Paper SL-84-6, US Army Engineer Waterways Experiment Station, Vicksburg, MS.
11. Baladi, George Y., and Barnes, Donald E. October 1983. "An Objective Waveform Comparison Technique," Technical Report SL-83-4, US Army Engineer Waterways Experiment Station, Vicksburg, MS.

12. Vanmarcke, Erik H., Jackson, Andrew E. Jr., and Akers, Stephen A. September 1986. "Ralston Valley Soil Compressibility Study: Correlation of Laboratory Uniaxial Strain Compressibility with Field Seismic Refraction Data," Technical Report SL-86-14, US Army Engineer Waterways Experiment Station, Vicksburg, MS.
13. Jackson, A. E. Jr. December 1984. "Statistical Variation of Laboratory Soil Properties," Miscellaneous Paper SL-84-14, US Army Engineer Waterways Experiment Station, Vicksburg, MS.
14. Miller, Irwin, and Freund, John E. "Probability and Statistics for Engineers," Prentice-Hall, Englewood Cliffs, New Jersey, 1977.
15. Baladi, G. Y., and Rohani, B. June 1987. "A Method for the Statistical Analysis of the Stress-Strain Properties of Earth Materials," Proceedings of the Thirty-Second Conference on the Design of Experiments, Report No. 87-2, U. S. Army Research Office, Research Triangle Park, North Carolina.
16. Rosenblueth, E. October 1975. "Point Estimates for Probability Moments," Proceedings of the National Academy of Sciences, Vol 72, No. 10, pp 3812-3814.
17. Rosenblueth, E. October 1961. "Two-Point Estimates in Probabilities," Applied Mathematical Modeling, Vol 5, pp 329-335.
18. Bowles, Joseph E. "Physical and Geotechnical Properties of Soils," McGraw-Hill Book Company, 1979.
19. Akers, S. A., Reed, P. A., and Ehrgott, J. Q. August 1986. "WES High-Pressure Uniaxial Strain and Triaxial Shear Test Equipment," Miscellaneous Paper SL-86-11, US Army Engineer Waterways Experiment Station, Vicksburg, MS.
20. Ehrgott, J. Q. May 1971. "Calculation of Stress and Strain from Triaxial Test Data on Undrained Soil Specimens," Miscellaneous Paper S-71-9, US Army Engineer Waterways Experiment Station, Vicksburg, MS.

DISTRIBUTION LIST

DEPARTMENT OF DEFENSE

Director
 Defense Nuclear Agency
 ATTN: DFTD (Dr. D. A. Linger)
 DFSP (Dr. G. W. Ullrich)
 SPWE (Mr. C. B. McFarland)
 SPSD (Dr. K. L. Goering)
 SPSD (MAJ M. A. Reed)
 SPWE (MAJ Mike Pelkey)
 SPWE (Dr. E. J. Rinehart)
 Technical Library
 Washington, DC 20305-1000

Director
 Defense Nuclear Agency
 Nevada Operations Office
 ATTN: TDNV (Mr. J. W. LaComb)
 P.O. Box 98518
 Las Vegas, NV 89193-8518

Defense Nuclear Agency
 ATTN: TDTT
 TDCT
 Kirtland AFB, NM 87115-5000

Director
 Defense Advanced Research Project Agency
 ATTN: Technical Library
 1400 Wilson Blvd.
 Arlington, VA 22209

Director
 Defense Intelligence Agency
 ATTN: Technical Library
 Washington, DC 20301-6111

Defense Technical Information Center
 ATTN: TC
 Cameron Station
 Alexandria, VA 22314

DEPARTMENT OF THE ARMY

Commander
 US Army Corps of Engineers
 ATTN: CERD-L
 CERD-M (Mr. B. O. Benn)
 CEEC-ET (Mr. R. L. Wight)
 CEIM-SL
 Washington, DC 20314-1000

Division Engineer
 US Army Engineer Division, Huntsville
 ATTN: CEHND-SR
 P.O. Box 1600
 Huntsville, AL 35807-4301

Director
 US Army Construction Engineering Research
 Laboratory
 ATTN: Technical Library
 P.O. Box 4005
 Champaign, IL 61820-1305

DEPARTMENT OF THE ARMY (CONTINUED)

District Engineer
 US Army Engineer District, Omaha
 ATTN: CEMRO-ED-S (Mr. Bob Kelley)
 CEMRO-ED-SH (Mr. Bill Gaube)
 215 N. 17th Street
 Omaha, NE 68102-4978

Commander/Director
 US Army Cold Regions Research and
 Engineering Laboratory
 ATTN: Technical Library
 72 Lyme Road
 Hanover, NH 03755-1290

Commandant
 US Army Engineer School
 ATTN: ATZA-CD (COL Fred Parker)
 Technical Library
 Fort Belvoir, VA 22060-5281

Commander
 Harry Diamond Laboratories
 Department of the Army
 ATTN: Technical Library
 2800 Powder Mill Road
 Adelphi, MD 20783-1197

Director
 US Army Ballistic Research Laboratory
 ATTN: Technical Library
 Aberdeen Proving Ground, MD 21005-5066

Commander
 US Army Nuclear and Chemical Agency
 ATTN: Technical Library
 7500 Backlick Road, Bldg. 2073
 Springfield, VA 22150

DEPARTMENT OF THE NAVY

Naval Civil Engineering Laboratory
 ATTN: Technical Library
 Port Hueneme, CA 93043

Naval Facilities Engineering Command
 200 Stoval Street
 ATTN: Technical Library
 Alexandria, VA 22332

DEPARTMENT OF THE AIR FORCE

Air Force Institute of Technology
 Air University
 ATTN: Technical Library
 Wright-Patterson AFB, OH 45433

Air Force Office of Scientific Research
 ATTN: Technical Library
 Bolling AFB, DC 20332

DEPARTMENT OF THE AIR FORCE (CONTINUED)

Air Force Weapons Laboratory (AFSC)
ATTN: NTESG (CPT C. W. Felice)
NTEDC (Mr. J. N. Thomas)
Technical Library
Kirtland AFB, NM 87117-6008

Air Force Engineering and Services Center
(AFSC)
ATTN: Technical Library
Tyndall AFB, FL 32403

Commander
Ballistic Missile Office (AFSC)
ATTN: MYEB (LTC D. H. Gage)
ENSS (LT K. R. Hirlinger)
Technical Library
Norton AFB, CA 92409-6468

DEPARTMENT OF ENERGY

Lawrence Livermore National Laboratory
ATTN: Technical Library
P.O. Box 808
Livermore, CA 94550

Los Alamos National Laboratory
ATTN: Technical Library
P.O. Box 1663
Los Alamos, NM 87545

Sandia National Laboratories
ATTN: Technical Library
P.O. Box 5800
Albuquerque, NM 87185

Sandia National Laboratories
ATTN: Technical Library
Livermore, CA 94550

DEPARTMENT OF DEFENSE CONTRACTORS

Mr. J. L. Bratton
Applied Research Associates, Inc.
4300 San Mateo Blvd., NE, Suite A220
Albuquerque, NM 87110

Mr. S. E. Blouin
Applied Research Associates, Inc.
Box 120A, Waterman Road
South Royalton, VT 05068

Mr. J. L. Drake
Applied Research Associates, Inc.
3202 Wisconsin Avenue
Vicksburg, MS 39180

Dr. J. G. Trulio
Applied Theory, Inc.
930 S. LaBrea Avenue
Los Angeles, CA 90036

Dr. Y. Marvin Ito
Mr. S. H. Schuster
California Research & Technology, Inc.
20943 Devonshire Street
Chatsworth, CA 91311-2376

Dr. Hon-Yim Ko
Department of Civil, Environmental, and
Architectural Engineering
University of Colorado at Boulder
Boulder, CO 80309

Dr. K. C. Valanis
Endochronics, Inc.
8605 Northwest Lakecrest Court
Vancouver, WA 98665

New Mexico Engineering Research Institute
ATTN: Technical Library
University of New Mexico
Box 25, University Station
Albuquerque, NM 87131

Mr. J. G. Lewis
Dr. Don Simons
R&D Associates
P.O. Box 9695
Marina del Rey, CA 90291

Mr. L. S. Melzer
Science Applications International
Corporation
505 West Texas Street
First City Center, Tower 2, Suite 1335
Midland, TX 79701

Dr. John Schatz
Science Applications International
Corporation
P.O. Box 2351
La Jolla, CA 92038-2351

Dr. H. E. Read
Mr. Steve Peyton
S-Cubed
P.O. Box 1620
La Jolla, CA 92038-1620

Dr. Lynn Seaman
SRI International
333 Ravenswood Avenue
Menlo Park, CA 94025

Mr. S. J. Green
Mr. William Klauber
Terra Tek, Inc.
420 Wakara Way
Salt Lake City, UT 84108

Mr. Norman Lipner
Dr. M. G. Katona
TRW Defense Systems Group
P.O. Box 1310
San Bernardino, CA 92402

Dr. D. J. Neas
TRW Defense and Space Systems Group
One Space Park, Bldg. 134/Rm 9835
Redondo Beach, CA 90278

Dr. I. S. Sandler
Weidinger Associates
333 Seventh Avenue
New York, NY 10001

Dr. Jeremy Isenberg
Dr. Howard S. Levine
Weidinger Associates
620 Hansen Way, Suite 100
Palo Alto, CA 94304

Dr. J. F. Carroll
Department of Civil Engineering
and Environmental Sciences
University of Central Florida
Orlando, FL 32816

Dr. R. T. Allen
Pacifica Technology
P.O. Box 148
Del Mar, CA 92014

Dr. P. H. S. W. Kulatilake
University of Arizona
Building No. 12
Tucson, AZ 85721

Dr. Robert M. Schoites
Dr. Ralph Sarno
Mississippi State University
P.O. Drawer CE
Mississippi State, MS 39762